The 9th Laser Display and Lighting Conference

21–24 April 2020
Yokohama, Japan

Organized by
Laser Display Technology Group (LDT) of Optical Society of Japan (OSJ)

Sponsored by
The Optical Society of Japan
The Japan Society of Applied Physics

In cooperation with
The Laser Society of Japan

Consortium of Visible Laser Diode Applications

Conference Chairs

Kazuo Kuroda, Utsunomiya University (Japan)
Hiroshi Murata, Mie University (Japan)

Steering Committee
Co-Chairs
Kazuhisa Yamamoto, Osaka Univ. (Japan)
Norihiro Ohse, SONY (Japan)
Members
Masato Ishino, Osaka Univ. (Japan)
Makio Kurashige, Dai Nippon Printing (Japan)
Keizo Ochi, VLDAC (Japan)
Shouichi Ozawa, Techno Management Research Inst. (Japan)
Tsutomu Shimura, Univ. of Tokyo (Japan)
Shinji Saito, Toshiba Corp. (Japan)
Ichiro Sato, Bosch Corp. (Japan)
Tsuyoshi Suzudo, Ricoh Industrial Solutions (Japan)
Takunori Taira, National Inst. of Natural Science (Japan)

Y-Q Qin, Nanjing University (China)

Takuya Kushimoto, Kyoto Univ. (Japan)

Advisory Members

Ray-Hua Horng, National Chung Hsing Univ. (Taiwan)

Andreas Tünnermann, Fraunhofer Institute, IOF (Germany)

Yasuhiro Koike, Keio Univ. (Japan)

Shigeo Kubota, Oxide Corp. (Japan)

Takashige Omatsu, Chiba Univ. (Japan)

Brian Schowengerdt, Univ. of Washington (United States)

Hiroaki Sugiura, Mitsubishi Electric Corp. (Japan)

Toshiaki Suhara, Osaka Univ. (Japan)

Introduction

The LDC is an international conference on laser displays, laser lighting, and related technologies. The 1st, 2nd, 4th, and 6~8th LDC were held in Yokohama, Japan in 2012, 2013, 2015, and 2017~2019, respectively, the 3rd in Taichung, Taiwan in 2014, and the 5th in Jena, Germany in 2016. The 9th LDC, LDC 2020 is being held from 21st to 24th April 2020 at Pacifico Yokohama. The LDC2020 is intended to provide a central forum for the update and review of scientific and technical information on laser display and lighting covering a wide range of fields from fundamental research to systems and applications. The conference is sponsored by the Optical Society of Japan in cooperation with several academic societies and associations.

For details, please come to our web-site;
https://ldc.opicon.jp/

Kazuo Kuroda
Hiroshi Murata

LDC2020
CONFERENCE PROGRAM

Apr. 21rd to 24th, 2020
Pacifico Yokohama

Tue. Apr 21, 2020

301

LDC2020 | Oral Presentation

Opning
Session Chair: Sunao Kurimura(NIMS)
10:15 AM - 10:30 AM 301 (Conference Center)

[LDC-OP] Opening Remarks
　　　　10:15 AM - 10:30 AM

LDC2020 | Oral Presentation

Keynote 1
Session Chair: Sunao Kurimura(NIMS), Kazuo Kuroda(Utsunomiya University)
10:30 AM - 12:00 PM 301 (Conference Center)

[LDC1-01(Keynote)] AR/VR based technologies and their applications
　　　*Jyrki Saarine[1]　(1. Univ. of Eastern Finland)
　　　10:30 AM - 11:15 AM

[LDC1-02(Keynote)] Recent advances of InGaN laser diodes for high power applications
　　　*Stephan Haneder[1], Harald König[1], Sven Gerhard[1], Muhammad Ali[1], Urs Heine[1], Sönke Tautz[1], Christoph Eichler[1], Georg Brüderl[1], Matthias Peter[1], Alfred Lell[1], Martin Behringer[1], Markus Keidler[1], Tobias Haupeltshofer[1], Christoph Walter[1], Markus Baumann[2], Anne Balck[2], Volker Krause[2]　(1. OSRAM Opto Semiconductors, 2. Laserline Gesellschaft für Entwicklung und Vertrieb von Diodenlasern mbH)
　　　11:15 AM - 12:00 PM

LDC2020 | Oral Presentation

AR, MR, VR, ... XR technologies 1
Session Chair: Norihiro Ohse(Sony)
1:00 PM - 3:00 PM 301 (Conference Center)

[LDC2-01] Finnish flagship programme for Photonics
　　　*Juha Purmonen[1,2,3]　(1. Photonics Finland, 2. Institute of Photonics, 3. University of Eastern Finland)
　　　1:00 PM - 1:30 PM

[LDC2-02] Chaging World: What is the impact of VR/AR nowadays and in the future?
　　　*Shun Kubota[1]　(1. Mogura Inc.)

1:30 PM - 2:00 PM

[LDC2-03] Glass for see-through head-mounted display - High refractive index/High transparency glass wafer-
　　　*Satoko Konoshita[1], Hiroshi Sawasato[2], Shunsuke Fujita[1], Takashi Murata[1]　(1. Research Div., Nippon Electric Glass Co., Ltd., 2. Display Glass Div., Nippon Electric Glass Co., Ltd.)
　　　2:00 PM - 2:30 PM

[LDC2-04] FOV Expanding of Computer Generated Holograms with a Holographic Waveguide Combiner
　　　*Shao-Kui Zhou[1,2], Wen-Kai Lin[1,2], Bor-Shyh Lin [1], Wei-Chia Su[2]　(1. National Chiao Tung University, 2. National Changhua University of Education)
　　　2:30 PM - 2:45 PM

[LDC2-05] Overcoming the limitations of Spatial Light Modulators for holographic near-eye displays
　　　*Michal Makowski[1], Rafal Trybus[1], Szymon Fiderkiewicz[1], Joanna Starobrat[1]　(1. Warsaw University of Technology)
　　　2:45 PM - 3:00 PM

LDC2020 | Oral Presentation

AR, MR, VR, ... XR technologies 2
Session Chair: Masafumi Ide(MagicLeap)
3:15 PM - 4:45 PM 301 (Conference Center)

[LDC3-01(Invited)] Optical See-Through AR HMD with Spatial Tracking
　　　*Hiroshi Mukawa[1], Hiroyuki Aga[1], Atsushi Ishihara[1], Koichi Kawasaki[1]　(1. Sony Corporation)
　　　3:15 PM - 3:45 PM

[LDC3-02] MEMS system for AR HMDs
　　　Ran Gabai[1], Gil Cahana[1], Dan Nabel[1], Meni Yehiel[1], Avi Leibushor[1], Gady Yearim[1], *Matan Naftali[1]　(1. Maradin LTD)
　　　3:45 PM - 4:15 PM

[LDC3-03(Invited)] Why Light Field is an Important Fundamental Technology for Future XR Displays
　　　*Takafumi Koike[1]　(1. Hosei University)
　　　4:15 PM - 4:45 PM

Wed. Apr 22, 2020

301

LDC2020 | Oral Presentation

Imaging / Lighting -Speckle-
Session Chair: Hiroshi Murata(Mie University)
9:00 AM - 10:30 AM 301 (Conference Center)

[LDC4-01] Efficient speckle reduction using volume scattering crystals
*Shigeo Kubota[1], Koji Suzuki[1], Hisashi Masuda[1], Keisuke Nakagome[1], Yutaka Anzai[1] （1. Oxide Corporation）
9:00 AM - 9:30 AM

[LDC4-02] Speckle reduction within nanosecond-order pulse widths for flash lidar applications
*Fergal Shevlin[1] （1. DYOPTYKA）
9:30 AM - 9:45 AM

[LDC4-03] Error Analysis of Speckle Contrast by Image Subtraction Method
*Makio Kurashige[1], Kazutoshi Ishida[1], Shumpei Nishio[1] （1. Dai Nippon Printing Co., Ltd.)
9:45 AM - 10:00 AM

[LDC4-04] Improved Visual Resolution Measurement for Laser Displays Based on Eye-diagram Analysis of Speckle Noise
*Junichi Kinoshita[1], Akira Takamori[1], Kazuhisa Yamamoto[1], Kazuo Kuroda[2], Koji Suzuki[3], Keisuke Hieda[4] （1. Osaka Universitry, 2. Utsunomiya University, 3. Oxide Corporation, 4. HIOKI E.E.CORPORATION）
10:00 AM - 10:15 AM

[LDC4-05] Study on Projection Screen and Speckle Contrast in Laser Display Technology
*Yuwei Fang[1], Linxiao Deng[1], Chun Gu[1], Lixin Xu[1] （1. University of Science and Technology of China)
10:15 AM - 10:30 AM

LDC2020 | Oral Presentation

Imaging / Lighting -Display Technologies-
Session Chair: Satoshi Ouchi(Hitachi)
10:45 AM - 12:30 PM 301 (Conference Center)

[LDC5-01] A laser backlight liquid crystal display achieving a BT.2020 wide color gamut
*Koichi Okuda[1], Shinichi Komura[1], Ken Onoda[1], Hiroaki Kijima[1] （1. Japan Display Inc.)

10:45 AM - 11:15 AM

[LDC5-02] Aerial Display Opens a New Field of Biology
*Hirotsugu Yamamoto[1,2], Erina Abe[1], Masaki Yasugi[1,2], Eiji Watanabe[3], Hideaki Takeuchi[4] （1. Utsunomiya University, 2. JST, ACCEL, 3. National Institute for Basic Biology, 4. Tohoku University）
11:15 AM - 11:45 AM

[LDC5-03] Near-eye CGH display with Holographic Waveguide Element
*Wei-Chia Su[1], Wen-Kai Lin[2], Shao-Kui Zhou[2], Bor-Shyh Lin[2] （1. Graduate Institute of Photonics, National Changhua University of Education, 2. College of Photonics, National Chiao Tung University）
11:45 AM - 12:15 PM

[LDC5-04] Effective Speckle Reduction Method Based on a Rotating Ball Lens
*Linxiao Deng[1], Yuwei Fang[1], Yuhua Yang[1], Tianhao Dong[1], Chun Gu[1], Lixin Xu[1] （1. University of Science and Technology of China）
12:15 PM - 12:30 PM

LDC2020 | Short Oral Presentaion

Short Presentation for Poster Paper
Session Chair: Satoshi Ouchi(Hitachi)
12:30 PM - 12:33 PM 301 (Conference Center)

[LDCp-01] Reforming of Computer Generated Hologram Pattern through Angular Spectrum Domain Computation
*Chang Joo Lee[1], Woo Young Choi[1], Joong Ki Park[2], Kwan Jung Oh[2], Kee Hoon Hong[2], Ki Hong Choi[2], Seung Yeol Lee[1] （1. Kyungpook National University, 2. Electronics and Telecommunication Research Institute (ETRI)）
12:30 PM - 12:33 PM

Hall A

LDC2020 | Poster Presentation

Poster Session
2:00 PM - 3:30 PM Hall A (Exhibition Hall)

[LDCp-01] Reforming of Computer Generated Hologram Pattern through Angular Spectrum Domain Computation

*Chang Joo Lee[1], Woo Young Choi[1], Joong Ki Park[2], Kwan Jung Oh[2], Kee Hoon Hong[2], Ki Hong Choi[2], Seung Yeol Lee[1]　(1. Kyungpook National University, 2. Electronics and Telecommunication Research Institute (ETRI))

Thu. Apr 23, 2020

301

LDC2020 | Oral Presentation

Keynote 2
Session Chair: Tetsuya Yagi(Mitsubishi Electric.Co.,)
9:00 AM - 9:45 AM 301 (Conference Center)

[LDC6-01(Keynote)] Indication of current-injection lasing from an organic semiconductor

*Chihaya Adachi[1], Toshinori Matsushima[1], Fatima Bencheikh[1], Shinobu Terakawa[1], William J. Potscavage[1], Chuanjiang Qin[1], Takashi Fujihara[1], Kenichi Goushi[1], Jean-Charles Ribierre[1]　(1. Kyushu University)

9:00 AM - 9:45 AM

LDC2020 | Oral Presentation

Light sources and components 1
Session Chair: Tetsuya Yagi(Mitsubishi Electric.Co.,)
9:45 AM - 10:30 AM 301 (Conference Center)

[LDC7-01] Speckle Contrast Generated by 638-nm Broad Area Laser Diodes

*Kyosuke Kuramoto[1], Takuma Fujita[1], Takehiro Nishida[1], Tetsuya Yagi[1], Akira Takamori[2], Kazuhisa Yamamoto[2], Masahiko Kondow[3]　(1. Mitsubishi Electric Corporation, 2. Institute of Laser Engineering, Osaka University, 3. Graduate School of Engineering, Osaka University)

9:45 AM - 10:00 AM

[LDC7-02] Monolithic single-mode diode lasers at 633 nm with high coherence and reliability for holographic printing

*Katrin Paschke[1], G. Blume[1], J. Pohl[1], B. Sumpf[1], D. Feise[1], P. Ressel[1], A. Sahm[1], N. Werner[1], J. Hofmann[1]　(1. Ferdinand-Braun-Institut)

10:00 AM - 10:15 AM

[LDC7-03] High-direction and low-coherence semiconductor laser with dumbbell-type cavity

*Linhai Xu[1], Yufei Wang[1], Yufei jia[1], Wanhua Zheng[1]　(1. Institute of Semiconductors, CAS)

10:15 AM - 10:30 AM

LDC2020 | Oral Presentation

Light sources and components 2
Session Chair: Tatsushi Hamaguchi(Sony)
10:45 AM - 12:15 PM 301 (Conference Center)

[LDC8-01] Progress in semipolar GaN-based VCSELs

*Jared A Kearns[1], Joonho Back[2], Nathan C Palmquist[1], Daniel A Cohen[1], Steven P DenBaars[1,2], Shuji Nakamura[1,2]　(1. Materials Department University of California, Santa Barbara, 2. Department of Electrical and Computer Engineering, University of California, Santa Barbara)

10:45 AM - 11:15 AM

[LDC8-02] High Power Static Phosphor Light Source for Cinema Projectors

*Kenneth Li[1]　(1. Optonomous Technologies Inc.)

11:15 AM - 11:30 AM

[LDC8-03] Interference Pattern Generation of Multi-wavelength Yellow-Orange Lasers Using Chi$^{(2)}$ Nonlinear Photonic Crystals

Bai-Wei Wu[1], Kai-Hsun CHANG[1,2], Safia Mohand Ousaid[2], Azzedine BOUDRIOUA[2], Hiroyuki YOKOYAMA[3], Chih-Ming Lai[4], *Lung-Han Peng[1,2,3]　(1. National Taiwan University, 2. Université Paris 13, 3. Tohoku University, 4. Ming Chuan University)

11:30 AM - 11:45 AM

[LDC8-04] High-Frequency Modulation of RGB Semiconductor Lasers for High-Resolution Scanning Displays

*Kiyoshiro Yamanaka[1], Hiroshi Murata[1,2], Junichi Kinoshita[2], Kazuhisa Yamamoto[2]　(1. Mie University, 2. Osaka University)

11:45 AM - 12:00 PM

[LDC8-05] 645 nm lasers with a low vertical divergence angle for laser display

*Yufei Jia[1], Yufei Wang[1], Linhai Xu[1], Wanhua Zheng[1]　(1. Institute of Semiconductors, CAS)

12:00 PM - 12:15 PM

LDC2020 | Oral Presentation

Novel and emerging technologies and applications 1
Session Chair: Hirotsugu Yamamoto(Utsunomiya University), Shiro Suyama(Tokushima University)
1:30 PM - 3:00 PM 301 (Conference Center)

[LDC9-01] Warp Square: A 360-degree Visual Experience in 4K Ultra-short-throw Projector Cave

*Norihiro Ohse[1]　(1. Sony Corporation)

1:30 PM - 2:00 PM

[LDC9-02] Trends and Prospects of Systems and Applications of Wireless Power Transmission Using Laser Light

*Tomoyuki Miyamoto[1] （1. Tokyo Institute of Technology）

2:00 PM - 2:30 PM

[LDC9-03] Evaluation of the chromaticity of tricolor laser displays under the laser wavelength shifts depending on the operating currents

*Keisuke Hieda[1], Tomoyuki Maruyama[1], Fumio Narusawa[1] （1. HIOKI E.E. CORPORATION）

2:30 PM - 2:45 PM

[LDC9-04] Forming Aerial Signage in front of LED Panel by Use of Retro-Reflector with Square-Shaped Holes

*Daiki Nishimura[1], Masaki Yasugi[1,2], Hirotsugu Yamamoto[1,2] （1. The University of Utsunomiya, 2. JST, ACCEL）

2:45 PM - 3:00 PM

LDC2020 | Oral Presentation

Novel and emerging technologies and applications 2

Session Chair: Masato Ishino(Osaka University), Norihiro Ohse(Sony)

3:30 PM - 4:45 PM 301 (Conference Center)

[LDC10-01] Large and Long-Viewing Distance DFD (Depth-Fused 3D) Display by using Transparent Polyethylene Screens and Short-Focus Projectors

*Shiro Suyama[1], Haruki Mizushina[1] （1. Tokushima University）

3:30 PM - 4:00 PM

[LDC10-02] Subjective Super-Resolution by Use of High-Speed Multi-Color LED Display

*Kojiro Matsushita[1], Toyotaro Tokimoto[1,2], Hirotsugu Yamamoto[1,3] （1. Utsunomiya University, 2. DaoApp Technology Company Limited, 3. JST, ACCEL）

4:00 PM - 4:15 PM

[LDC10-03] Improvement of Visibility of Aerial Image in See-Through AIRR by Cutting Off Ambient Light Using Polarization Modulation

*Kengo Fujii[1], Masaki Yasugi[1,2], Hirotsugu Yamamoto[1,2] （1. Utsunomiya University, 2. JST ACCEL）

4:15 PM - 4:30 PM

[LDC10-04] Fabrication of SiO_2-based Binary Diffractive Lens with Controllable Focal Distribution for

High-Power Laser Applications

*Atsushi Motogaito[1], Kazuki Matsuo[1], Kazumasa Hiramatsu[1] （1. Mie University）

4:30 PM - 4:45 PM

Fri. Apr 24, 2020

301

LDC2020 | Oral Presentation

Laser Technology for Automotive Applications - Phosphor Light Source-

Session Chair: Masaru Kuramoto(Stanley Electric)
9:15 AM - 10:30 AM 301 (Conference Center)

[LDC11-01] AlInGaN laser diodes for automotive applications

*Takashi Miyoshi[1], Masanobu Tanaka[1], Shin-ichi Nagahama[1] (1. Nichia Corporation)

9:15 AM - 9:45 AM

[LDC11-02] Laser Light Sources for Automotive Front Lighting Applications

*Meng Han[1], Julian Carey[1], Paul Rudy[1] (1. SLD Laser)

9:45 AM - 10:00 AM

[LDC11-03] Design parameters for light engines with static ceramic luminescent converter assemblies

*Volker Hagemann[1], Albrecht Seidl[1] (1. SCHOTT AG)

10:00 AM - 10:15 AM

[LDC11-04] Ce:YAG composite ceramic phosphors for laser lighting

*Kenta Yagasaki[1], Hisashi Minemoto[1], Kana Fujioka[1], Hiroshi Fuji[1], Kazuhisa Yamamoto[1] (1. Osaka University)

10:15 AM - 10:30 AM

LDC2020 | Oral Presentation

Laser Technology for Automotive Applications - Systems-

Session Chair: Satoshi Ouchi(Hitachi)
10:45 AM - 12:15 PM 301 (Conference Center)

[LDC12-01] Automotive Laser Headlamps using DMD Technologies

*Kenneth Li[1], Yung Peng Chang[2] (1. Optonomous Technologies Inc., 2. Taiwan Color Optics, Inc.)

10:45 AM - 11:15 AM

[LDC12-02] Sokuiki-Sensor (LiDAR) System and Applications

*Keisuke Inoue[1], Katsumi Kimoto[1], Naohiro Shimaji[1], Masanori Hino[1], Toshihiro Mori[1] (1. Hokuyo Automatic co., ltd.)

[LDC12-03] Wide Angle Multi-Shift Stereo Camera with Monocular Detection

*Masayuki Kobayashi[1], Kazuyoshi Yamazaki[1], Felipe Gomez Caballero[2], Takuma Osato[2], Takeshi Endo[2], Masayuki Takemura[2], Takeshi Nagasaki[3], Takeshi Shima[3] (1. Central Research Laboratory, Hitachi Ltd., 2. Hitachi Research Laboratory, Hitachi Ltd., 3. Hitachi Automotive Systems Ltd.)

11:45 AM - 12:15 PM

LDC2020 | Oral Presentation

Visible light communication (VLC) technologies and systems

Session Chair: Hidekazu Hatanaka(Ushio)
1:00 PM - 2:30 PM 301 (Conference Center)

[LDC13-01] Location-based Services using Visible Light Communication

*Shinichiro Haruyama[1] (1. Keio University)

1:00 PM - 1:30 PM

[LDC13-02] Laser-based LiFi for 6G: Potential and Applications

*Volker Jungnickel[1], Julian Hohmann[1], Dominic Schulz[1], Peter Hellwig[1], Jonas Hilt[1], Christoph Kottke[1], Ronald Freund[1] (1. Fraunhofer Heinrich Hertz Institute)

1:30 PM - 2:00 PM

[LDC13-03] The Future Prospects of Robot-Photonics:Visible Light Communication and Sensing with the Plasmonic Mirror

*Kensuke Murai Murai[1] (1. National Institute of Advanced Industrial Science and Technology)

2:00 PM - 2:30 PM

LDC2020 | Oral Presentation

Smart Systems

Session Chair: Junichi Kinoshita(Osaka University)
3:15 PM - 4:30 PM 301 (Conference Center)

[LDC14-01] Vertical View Human Action Recognition from Range Images

*Akinobu Watanabe[1], Keiichi Mitani[1] (1. Hitachi, Ltd.)

3:15 PM - 3:45 PM

[LDC14-02] High-Speed Projection for Augmenting the World

*Yoshihiro Watanabe[1] (1. Tokyo Institute of Technology)

3:45 PM - 4:15 PM

[LDC14-03] Color LiDAR using RGB visible laser diodes

*Tomoyuki Ohashi[1], Masato Ishino[1], Kazuhisa

Yamamoto[1], Kana Fujioka[1]　(1. Institute of Laser

Engineering, Osaka University）

4:15 PM - 4:30 PM

LDC2020 | Oral Presentation

Post Deadline and Closing

Session Chair: Sunao Kurimura(NIMS)

4:30 PM - 5:00 PM 301 (Conference Center)

[LDC15-01] No peer review required Dummy submission

for PDP by the committee

*QWER ASDF[1]　(1. ZXCV)

4:30 PM - 4:45 PM

[LDC-CL] Closing Remarks

4:45 PM - 5:00 PM

LDC2020 | Oral Presentation

Keynote 1

Session Chair: Sunao Kurimura(NIMS), Kazuo Kuroda(Utsunomiya University)
Tue. Apr 21, 2020 10:30 AM - 12:00 PM 301 (Conference Center)

[LDC1-01(Keynote)] AR/VR based technologies and their applications

*Jyrki Saarine[1]　（1. Univ. of Eastern Finland）

10:30 AM - 11:15 AM

[LDC1-02(Keynote)] Recent advances of InGaN laser diodes for high power applications

*Stephan Haneder[1], Harald König[1], Sven Gerhard[1], Muhammad Ali[1], Urs Heine[1], Sönke Tautz[1], Christoph Eichler[1], Georg Brüderl[1], Matthias Peter[1], Alfred Lell[1], Martin Behringer[1], Markus Keidler[1], Tobias Haupeltshofer[1], Christoph Walter[1], Markus Baumann[2], Anne Balck[2], Volker Krause[2]　（1. OSRAM Opto Semiconductors, 2. Laserline Gesellschaft für Entwicklung und Vertrieb von Diodenlasern mbH）

11:15 AM - 12:00 PM

LDC2020 | Oral Presentation
# Keynote 1
2020年4月21日(火) 10:30 〜 12:00 301 (Conference Center)

[LDC1-01(Keynote)] AR/VR based technologies and their applications

*Jyrki Saarine[1] （1. Univ. of Eastern Finland）

AR/VR based technologies and their applications will be discussed.

AR/VR based technologies and their applications

Jyrki Saarine

Institute of Photonics, Univ. of Eastern Finland, Finland

Sorry. The abstract has not been submitted so far.

Keynote 1

[LDC1-02(Keynote)] Recent advances of InGaN laser diodes for high power applications

*Stephan Haneder[1], Harald König[1], Sven Gerhard[1], Muhammad Ali[1], Urs Heine[1], Sönke Tautz[1], Christoph Eichler[1], Georg Brüderl[1], Matthias Peter[1], Alfred Lell[1], Martin Behringer[1], Markus Keidler[1], Tobias Haupeltshofer[1], Christoph Walter[1], Markus Baumann[2], Anne Balck[2], Volker Krause[2] （1. OSRAM Opto Semiconductors, 2. Laserline Gesellschaft für Entwicklung und Vertrieb von Diodenlasern mbH）

The paper introduces OSRAM Opto Semiconductor laser portfolio and describes the recent progress for blue high power GaN lasers with focus on design optimization to improve lifetime for single emitters and efficiency and output power for laser bars.

Recent advances of InGaN laser diodes for high power applications

Stephan Haneder[1*], Harald König[1], Sven Gerhard[1], Muhammad Ali[1], Urs Heine[1], Sönke Tautz[1], Christoph Eichler[1], Georg Brüderl[1], Matthias Peter[1], Alfred Lell[1], Martin Behringer[1], Markus Keidler[1], Tobias Haupeltshofer[1], Christoph Walter[1], Markus Baumann[2], Anne Balck[2], Volker Krause[2]

[1]Osram Opto Semiconductors GmbH, Leibnizstrasse 4, 93055 Regensburg, Germany
[2]Laserline Gesellschaft für Entwicklung und Vertrieb von Diodenlasern mbH, Fraunhoferstrasse, Mülheim-Kärlich, Germany

ABSTRACT

The paper introduces OSRAM Opto Semiconductor and describes the recent progress for blue high power GaN lasers - with focus on design optimization to improve lifetime for single emitters and efficiency and output power for laser bars.

Since many years OSRAM Opto Semiconductors is setting innovations and trends in laser diode technology - historically strong in GaAs IR laser bars used for material processing and IR pulse laser diodes with peak powers up to 120W for LIDAR applications. Based on this expertise OSRAM Opto Semiconductors was one of first companies exploring the field of direct emitting green InGaN laser diodes. In recent years significant improvements have been made for transversal single mode green and blue laser diodes in respect of optical output power, efficiency and optical characteristics.

Besides low-power single mode InGaN lasers, blue high-power semiconductor lasers have increased greatly in optical power and efficiency over the recent decade enabling new application fields from high brightness projection up to materials processing beyond 1000W output power systems [1,2,3,4,5,6,7]. The basis to employ laser bars – an array of single emitters on one chip - for material processing is the underlying single emitter semiconductor technology. Optical power beyond 5W and efficiency higher than 40% have been demonstrated at room temperature [8]. Improved temperature performance was introduced, enabling automotive application like laser headlamp with required temperature range from -40°C up to 125°C and resulting in enhanced lifetime performance, that is discussed in this presentation by lifetime investigations of single emitters in TO-packages. The laser diodes were tested up to 5000h duration at different conditions in operating temperatures ranging from 64°C to 96°C and output power up to 3.5W. Dominating degradation mechanism is wear-out which is accelerated by optical output power and additional thermal activation. Extrapolation of the test results in combination with an acceleration model points towards a median lifetime of up to 65.000h for 25°C operation

For power scaling into the kilowatt range high-power laser bars as known from infrared lasers may ease power scaling and fiber coupling. First blue high-power laser bars were demonstrated and maximum output power of 107W was achieved [8] and based on that diode lasers with more than 1kW were demonstrated [4]. Motivated by this demonstration further effort was put into design optimization of the laser bars to find the best chip design for reliable high-power operation. First several designs were proposed from simulation and later on processed in the wafer fabrication. Main

factor on the performance is the fraction of actively pumped semiconductor area, the so-called fill factor. It is defined by the width of each emitter on the bar divided by the center-to-center pitch of the emitters, e.g. 40µm emitters with 400µm pitch correspond to 10% fill factor.

Finally, data of a fiber coupled diode laser system consisting of an optimum blue laser bar are shown. Each bar was mounted on microchannel heat sinks and collimated by a fast axis collimation lens. The diode laser consists of two polarization-combined laser stacks. After symmetric beam forming the light was coupled into a 600µm fiber with 0.22 NA. A maximum output power ex fiber of 1600W was demonstrated at 50A and previously published values exceeded by far [9]. This proves application of laser bars for fiber coupled diode lasers as a source for high-power material processing in the blue wavelength range and makes kW sources available to the market.

REFERENCES

[1] Balck, A., Baumann, M., Malchus, J., Chacko, R. V., Marfels, S., Witte, U., Dinakaran, D., Ocylok, S., Weinbach, M., Bachert, C., Kösters, A., Krause, V., König, H., Lell, A., Stojetz, B., Löffler, A., Strauss, U., "700 W blue Fiber-coupled Diode-laser emitting at 450 nm", Proc. SPIE 10514, 1051403 (2018).

[2] Köhler, B., Drovs, S., Stoiber, M., Dürsch, S., Kissel, H., Könning, T., Biesenbach, J., König, H., Lell, A., Stojetz, B., Löffler, A., Strauß, U., "Visible high power fiber coupled diode lasers", Proc. SPIE 10514, 1051408 (2018).

[3] J. P. Feve, M. Silva Sa, M. Finuf, R. Fritz, J-M. Pelaprat, M. Zediker, "500 watt blue laser system for welding applications," Proc. SPIE 10900, 1090004 (2019); https://doi.org/10.1117/12.2514465

[4] M. Baumann, A. Balck, J. Malchus, R. V. Chacko, S. Marfels, U. Witte, D. Dinakaran, S. Ocylok, M. Weinbach, C. Bachert, A. Kösters, V. Krause, H. König, A. Lell, B. Stojetz, M. Ali, U. Strauss, "1000 W blue fiber-coupled diode-laser emitting at 450 nm," Proc. SPIE 10900, 1090005 (2019); https://doi.org/10.1117/12.2511255

[5] T. Könning, S. Drovs, M. Stoiber, P. König, H. Kissel, F. Harth, B. Köhler, J. Biesenbach, H. König, A. Lell, B. Stojetz, M. Ali, U. Strauss, "High brightness fiber coupled diode lasers at 450 nm," Proc. SPIE 10900, 1090006 (2019). https://doi.org/10.1117/12.2507462

[6] M. Riva, G. Rossi, F. Pescarmona, A. Braglia, G. Perrone, "High-power and brightness 105-micron fiber coupled blue laser diode modules (Conference Presentation)," Proc. SPIE 10900, 1090007 (2019); https://doi.org/10.1117/12.2510535

[7] M. Suwa, N. Wakabayashi, T. Hiroki, K. Tojo, S. Masuno, R. Higashino, M. Tsukamoto, "Development of BLUE IMPACT, a 450nm-wavelength light source for laser processing," Proc. SPIE 10900, 109000A (2019); https://doi.org/10.1117/12.2515510

[8] König, H., Strauss, U., Ali, M., Bergbauer, W., Bruederl, G., Eichler, C., Gerhard, S., Heine, U., Lell A., Nähle, L., Peter, M., Ristic, J., Rossbach, G., Somers, A., Stojetz, B., Tautz, S., Wagner, J., Wurm, T., Baumann, M., Balck, A., Krause, V., "Visible GaN laser diodes: from lowest thresholds to highest power levels," Proc. SPIE 10939, 109390C (2019); https://doi.org/10.1117/12.2511976

[9] https://www.laserline.com/de-int/ldm-blue-blauer-diodenlaser/

LDC2020 | Oral Presentation

AR, MR, VR, ... XR technologies 1

Session Chair: Norihiro Ohse(Sony)
Tue. Apr 21, 2020 1:00 PM - 3:00 PM 301 (Conference Center)

[LDC2-01] Finnish flagship programme for Photonics

*Juha Purmonen[1,2,3] （1. Photonics Finland, 2. Institute of Photonics, 3. University of Eastern Finland）

 1:00 PM - 1:30 PM

[LDC2-02] Chaging World: What is the impact of VR/AR nowadays and in the future?

*Shun Kubota[1] （1. Mogura Inc.）

 1:30 PM - 2:00 PM

[LDC2-03] Glass for see-through head-mounted display -High refractive index/High transparency glass wafer-

*Satoko Konoshita[1], Hiroshi Sawasato[2], Shunsuke Fujita[1], Takashi Murata[1] （1. Research Div., Nippon Electric Glass Co., Ltd., 2. Display Glass Div., Nippon Electric Glass Co., Ltd.）

 2:00 PM - 2:30 PM

[LDC2-04] FOV Expanding of Computer Generated Holograms with a Holographic Waveguide Combiner

*Shao-Kui Zhou[1,2], Wen-Kai Lin[1,2], Bor-Shyh Lin [1], Wei-Chia Su[2] （1. National Chiao Tung University, 2. National Changhua University of Education）

 2:30 PM - 2:45 PM

[LDC2-05] Overcoming the limitations of Spatial Light Modulators for holographic near-eye displays

*Michal Makowski[1], Rafal Trybus[1], Szymon Fiderkiewicz[1], Joanna Starobrat[1] （1. Warsaw University of Technology）

 2:45 PM - 3:00 PM

LDC2020 | Oral Presentation
# AR, MR, VR, ... XR technologies 1
2020年4月21日(火) 13:00 〜 15:00 301 (Conference Center)

[LDC2-01] Finnish flagship programme for Photonics

*Juha Purmonen[1,2,3] （1. Photonics Finland, 2. Institute of Photonics, 3. University of Eastern Finland）

The Finnish Flagship Programme provides a new, unique way of doing R&D&I in Finland. The Programme promotes active collaboration between research, business and society in the field of each Flagship. Photonics Research and Innovation platform focusing on light-based solutions from scientific excellence to industrial and societal impact. PREIN partners are worldwide leaders in photonics that changes the world.

LDC2020 | Oral Presentation
# AR, MR, VR, ... XR technologies 1
2020年4月21日(火) 13:00 〜 15:00 301 (Conference Center)

[LDC2-02] Changing World: What is the impact of VR/AR nowadays and in the future?

*Shun Kubota[1] （1. Mogura Inc.)

Nowadays VR/AR technologies starts adopting in the society. As VR/AR specific journalist, I describe how VR/AR is changing the society, industry, daily life and how fast the adoption is in this early stage of adoption. Also I describe the future of these technologies.

Changing World: What is the impact of VR/AR nowadays and in the future?

Shun Kubota

CEO Mogura Inc., Iidabashi 1-9-5 SKB Building 3F, ChiyodaKu Tokyo Japan, +81362723551, sunkubo@moguravr.com

Abstract: *Nowadays VR/AR technologies starts adopting in the society. As VR/AR specific journalist, I describe how VR/AR is changing the society, industry, daily life and how fast the adoption is in this early stage of adoption. Also I describe the future of these technologies.*

1. Main text

VRHMD has released to the public in 2016 steadily increased. And yet, 4 years later, there are still plenty of early adopters. It remains a far from being adopted. On the other hand, in 2016, it was hardly publicized by manufacturers at all, but it is undoubtedly the industrial application that is making a great impact both at home and abroad. And at the same time, 2016-2017 new generation of AR will start.

Corporate investment in VR is growing, and adoption is accelerating, especially for training purposes, according to figures released by US research firm Superdata at the end of 2018. Full-scale introduction cases by large enterprises have begun to appear. Training alone could save as much as $13.5 billion a year in the future.

In my session, I describe these below.

1) Market statistics
2) VR/AR technologies now
3) Increasing Industry usage
4) Emerging consumer market of VR
5) Major players of the industry and their approach to VR/AR
6) The future of VR/AR

2. Conclusions

The adoption of VR/AR gradually goes. And hardware technologies are one of the key factor. Furthermore the most important is the harmony of hardware, software (usage development) and tools.

3. Bio

Mr Kubota is the founder of Mogura Inc. and founder and editor in Chief of Mogura VR, VR/AR specific news outlet in Japan. Mogura VR is the main source for the industry in Japan. Executive Director of XR Consortium / Auditor of Location-based VR Association / Auditor of VRM Consortium

After graduating from Keio University, Faculty of Law, he joined the Ministry of the Environment. He founded Mogura VR in 2015 as his personal business. Mogura Inc was founded in 2016. He believes that VR/AR evolves the perception of the reality perceived by humans, feels the infinite possibilities of changing society. He is dedicated himself to spread these technologies. Specializes in gathering information and consulting in the VR / AR industry. The network is also expanding, including visiting domestic and overseas events.

Author of Japanese Virtual Reality Society Journal Vol.24 No.2 Special Issue "VR Applications and Startups"

LDC2020 | Oral Presentation
# AR, MR, VR, ... XR technologies 1
2020年4月21日(火) 13:00 ～ 15:00 301 (Conference Center)

[LDC2-03] Glass for see-through head-mounted display -High refractive index/High transparency glass wafer-

*Satoko Konoshita[1], Hiroshi Sawasato[2], Shunsuke Fujita[1], Takashi Murata[1] （1. Research Div., Nippon Electric Glass Co., Ltd., 2. Display Glass Div., Nippon Electric Glass Co., Ltd.）

High index and high transparency glass with ϕ300mm and 0.3mm has developed for the see-through head-mounted display. This glass will realize a wider FOV and higher brightness as a light guide in AR/MR glasses.

Glass for see-though head-mounted display
-High refractive index / High transparency glass wafer -

Satoko Konoshita[1], Hiroshi Sawasato[2], Shunsuke Fujita[1], Takashi Murata[1]

[1]Research Div., Nippon Electric Glass Co. Ltd., [2]Display Glass Div., Nippon Electric Glass Co. Ltd.,

7-1, Seran 2 chome, Otsu, Shiga 520-8639, +81-77-537-8772, +81-77-534-3572(FAX), skonoshita@neg.co.jp

Abstract: *High refractive index, nd 2.00, and high internal transmittance, 98% at 500nm, glass with Φ300mm and 0.3mm thick has successfully developed for the see-through head-mounted display. This glass wafer will realize a wider field of view and higher brightness as a light guide plate in the AR/MR glasses.*

1. Introduction

A see-through head-mounted display using augmented reality (AR) or mixed reality (MR) technology is attracting attention as one of the next-generation display device, and market of glass for the AR / MR is expected to grow rapidly in a few years. The development trends of AR/MR technology are expected to compact and lightweight device.[1]The AR/MR device generally consists of a combination of a micro display device (LCOS, DLP, OLED, μLED etc.) and a light guide plate using glass. Many types of light guide plate [2, 3] are demonstrated and the light guide plate using a half mirror are the currently the mainstream. However, since this method has a limitation in device size, a light guide plate using diffractive optical elements (DOEs) or holographic optical elements (HOEs) is expected to realize thinner and compact AR/MR devices.

Glass or resin could be a candidate for the material of light guide plate. Glass has an advantage for high - definition DOEs and wide field of view (FOV) due to the higher rigidity and higher refractive index, respectively compared with resin. Also, high transmittance is required for a brighter image in AR/MR devices. However, transmittance generally tends to decrease with increasing the refractive index. In our recent research, we have successfully developed the glass wafer that has both high refractive index and high transmittance by glass composition and process design techniques. Also, smooth surface is required to form nano-scale DOEs. In this report, the excellent performance of the developed glass for the light guide plate will be shown.
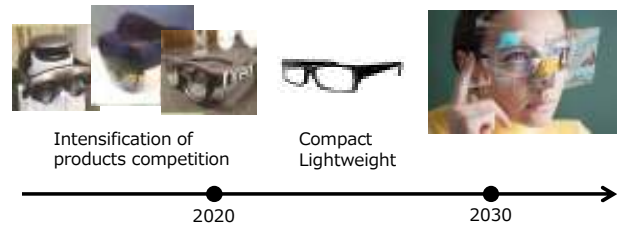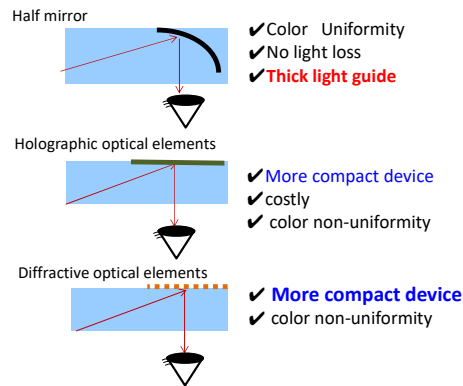

Fig.1. Development trends of AR/MR device.[1]

Fig.2. Waveguide systems for AR/MR devices.[2, 3]

2. Developments

Developed glass showed high refractive index, n_d 2.00 with the composition containing Nb_2O_5 giving high refractive index to the glass (figure 3). High internal transmittance (98% at 500nm) was obtained by controlling valence number of Nb-ion since Nb-ion absorbs visible light [6, 7]. Also, process-technology in thin glass production line at NEG enable glass to be thinner, 0.3mm, and φ300mm (12 inches) with enough planarity for the high-definition gratings.

3. Summary

The glass with high refractive index of n_d 2.00 and high transmittance of 98% (at 500 nm) was successfully developed for a composition system containing a high content of Nb_2O_5. By applying this glass to the light

guide plate for AR/MR glasses, it is expected that a smart glass having both a wider FOV and a brighter image will be realized.

Furthermore, we succeeded in processing the largest and thinnest glass wafers with a diameter of 300 mm and a thickness of 0.3 mm, which can contribute to the weight reduction of AR / MR devices.
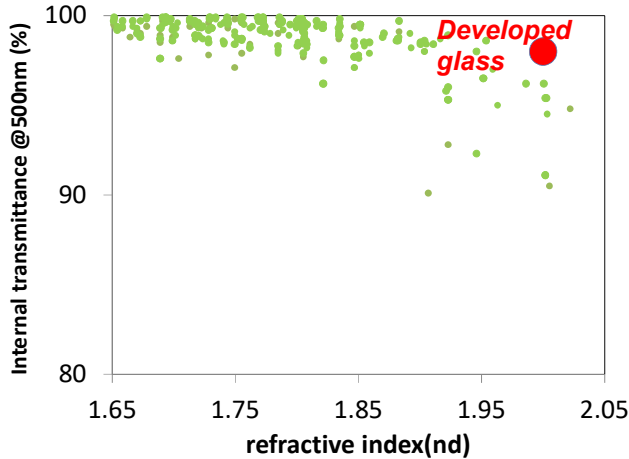

Fig. 3. Correlation between refractive index and internal transmittance of glass for optics.[4.5]

Fig.4. Appearance of developed glass wafer (Φ300mm, 0.3mm thickness).

References

[1] Shota Azuma, Nikkei Electronics, Feb.(2020) 42-45

[2] Totani Takahiro, Nikkei Electronics, Dec. (2014) 55

[3] Yue Zhang and Fengzhou Fang, Precision Engineering, 60(2019) 482-496

[4] Interglad 8.0 data

[5] Optical glass catalogue

[6] L. Ghussn, R.M.C.V.Reis, R.K.Brow, D.B. Baker, J. Non-Crystal. Sol., 401 (2014) 96-100

[7] R. R. Rakhimov, V. J. Turney, D. E. Jones, S. N. Dobryakov, Yu. A. Borisov, A. I. Prokof'ev and A. I. Aleksandrov, J. Chemical physics, 118 [13] (2003)

LDC2020 | Oral Presentation
AR, MR, VR, ... XR technologies 1
2020年4月21日(火) 13:00 ～ 15:00 301 (Conference Center)

[LDC2-04] FOV Expanding of Computer Generated Holograms with a Holographic Waveguide Combiner

*Shao-Kui Zhou[1,2], Wen-Kai Lin[1,2], Bor-Shyh Lin [1], Wei-Chia Su[2] （1. National Chiao Tung University, 2. National Changhua University of Education）

The field of view of computer-generated –hologram from spatial light modulator is expanded by using a holographic waveguide combiner. The aberration of the diffraction images at 50 cm behind the waveguide is analysed and then are compensated. Through experimental verification, virtual images with larger FOV can be obtained without aberrations.

FOV Expanding of Computer Generated Holograms with a Holographic Waveguide Combiner

Shao-Kui Zhou [1,2)], Wen-Kai Lin [1,2)], Bor-Shyh Lin [1)], Wei-Chia Su [*2)]

[1)] College of photonics, National Chiao Tung University, Tainan, 71150, Taiwan

[*2)] Graduate Institute of Photonic, National Changhua University of Education, Changhua, 50007, Taiwan

wcsu@cc.ncue.edu.tw

Abstract: *The field of view of computer-generated –hologram from spatial light modulator is expanded by using a holographic waveguide combiner. The aberration of the diffraction images at 50 cm behind the waveguide is analysed and then are compensated. Through experimental verification, virtual images with larger FOV can be obtained without aberrations.*

1. Introduction

The see-through display is an important characteristic for augmented reality (AR) techniques [1] in recently years. For the conventional case, see-through function is usually achieved by using a half silvered mirror and an eyepiece [1, 2]. However, these components let the system become heavy and bulky. In recent years, many studies proposed see-through display system that replacing traditional elements with holographic waveguide elements to reduce the volume of the device [3,4]. Using the holographic waveguide elements can make the AR head-mounted displays (HMDs) become compact.

Computer generated holograms (CGHs) is also a very popular topic for AR HMD display. These CGHs are displayed on the spatial light modulator (SLM) to offer holographic images. The holographic image can be reconstructed successfully by using a coherence reading beam to incident the CGHs on SLM [5, 6]. The dynamic holographic displays were generated by displaying the different CGHs on SLM sequentially. Generally, the field of view (FOV) of CGH is limited by the SLM pixel size.

In this paper, a CGH reconstruction system is used as the image source of the HMD system. Then the image is coupled into the holographic waveguide under the condition of the total internal reflection (TIR). In our designed, the virtual image will locate behind the combiner with a distance of 50 cm. Through the function of holographic lens on the waveguide combiner, FOV of the CGH will be extended and will not be limited by the SLM pixels size.

2. Experiment

The schematic diagram of the proposed HMD device is shown in Fig. 1. The device can be divided into two parts, one is the CGH reconstruction system and the other one is the holographic lens based on waveguide combiner. The CGH reconstruction a virtual image behind the SLM, and the HOE of this system is seen as a lens. The HOE is attached on the waveguide. The CGH reconstruction system will redirect the propagation direction of the virtual image to the eye. The image location in front of the eye is modified by adjusting the location of the diffracted image behind the SLM.
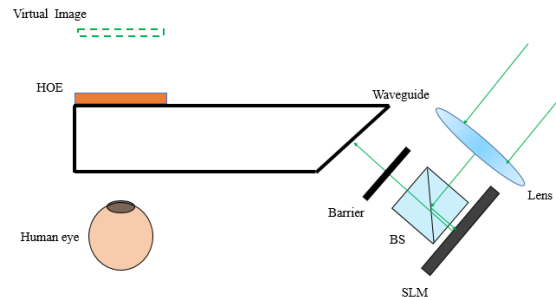

Fig. 1. HMD display with a CGH system and a holographic lens based on waveguide combiner.

The recording process for generating the HOE device is shown as Fig. 2. In this system, the Diode-Pump Solid-State (DPSS) laser which wavelength is 532nm was used. First, an unexposed hologram was attached on the glassy waveguide, and then the half-wave plate (HWP) and polarized beam splitter (PBS) were used to generate two S-polarized beams and to control the light intensity ratio. And then, these two beams were turned into collimation waves by using the spatial filters (SF) and collimating lenses (CL). One collimation wave was coupled into the waveguide and its incident angle fit the conditions of the TIR. Another collimation wave is turned into converged wave by propagating through the lens with 5 cm focal length. The hologram recorded the interference fringe which was generated by the collimation wave and the converged spherical wave.
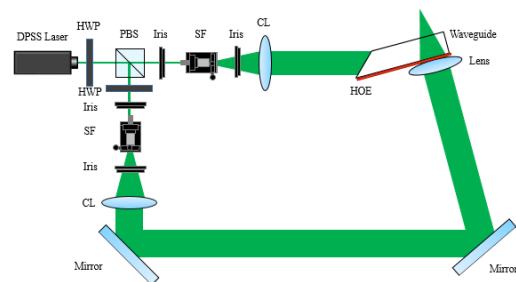

Fig. 2. The experimental system for generating the holographic lens. HWP: half-wave plate, PBS: polarized beam splitter, SF: spatial filter, CL: collimating lens

Related studies have presented CGH display systems with a convergent readout beam instead of a collimation

readout beam for the CGH reconstruction [7, 8]. It has been proven that fewer optical elements will be used in such kind of systems. Therefore, the CGH reconstruction system probed by a convergence beam is employed in our system. Fig. 3 shows the observation system in our experiments. A convergence beam will probe the SLM and the diffraction including the image information and DC term noises will be obtained. The DC term diffraction will be blocked by a barrier, and then the reconstructed image will be coupled into the waveguide under the condition of the TIR. The reconstructed image will be imaged by the holographic lens again and then the final image will locate behind the waveguide with 50 cm.
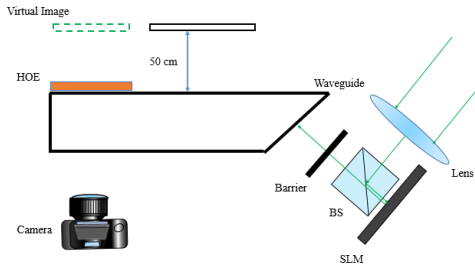

Fig. 3. The observation system. The camera focuses at 50 cm behind the waveguide.

3. Results

The image quality from this device is shown as Fig. 4. From the image shown in Fig. 4, the astigmatism can be observed.
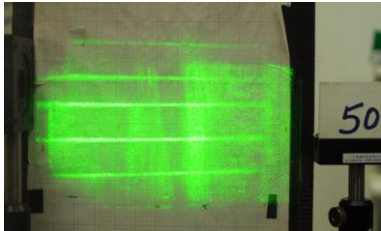

Fig. 4. The diffraction image shows astigmatism effect in the proposed system.

In previous research, the astigmatism can be suppressed by adding an inverse astigmatism phase on the CGH algorithm [8]. After astigmatism correction, the final image is shown as Fig. 5. The astigmatism effect is suppressed.
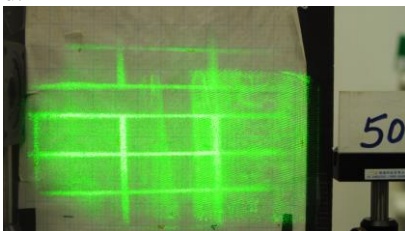

Fig. 5. The diffraction image with astigmatism correction.

The theoretical FOV of the CGH is calculated by the Eq. (1) shows in the following. Among Eq. (1), p represents the SLM pixel size, and λ represents the wavelength. The theoretical FOV is ±2.38° when pixel size is 6.4 μm and λ is 532 nm.

$$\theta = 2\sin^{-1}\frac{\lambda}{2p} \quad\ldots\ldots\ldots\ldots(1)$$

The practical FOV in this system can be decided by Eq. (2), where d represents the distance from the observer to the final diffraction image, and w represents the dimension of the final diffraction image.

$$\theta = \tan^{-1}\frac{w}{d} \quad\ldots\ldots\ldots\ldots(2)$$

Based on Eq. (2), the practical FOV is ±13.28°×±6.67° (horizontal × vertical).

4. Conclusion

In this study, the image of the HMD system is located at 50 cm behind the waveguide combiner. This system shows the astigmatism effect but it can be suppressed by the proposed CGH algorithm. The FOV of the CGH is expanded by the holographic lens on waveguide combiner. In our system, the FOV of CGH will not be limited by the pixel size of the SLM. The final horizontal FOV is ±13.28° and the vertical FOV is ±6.67° in our demonstrated system.

References

[1] Azuma, Ronald T., "A Survey of Augmented Reality," Teleoperators and Virtual Environments, 6(4), 355-385 (1997).
[2] K. Kiyokawa, Y. Kurata, H. Ohno, "An Optical See-through Display for Mutual Occlusion of Real and Virtual Environments," Computers and Graphics 12(3), 369-380 (2010)
[3] Piao, J.A., Li, G., Piao, M. L., Kim, N., "Full color holographic optical element fabrication for waveguide-type head mounted display using photopolymer," Journal of the Optical Society of Korea, 17(3), 242-248 (2013).
[4] H. Yeom, H. Kim, S. Kim, H. Zhang, B. Li, Y. Ji, S. Kim, J. Park, "3D holographic head mounted display using holographic optical elements with astigmatism aberration compensation," Optics express 23(25), 32025–32034 (2015).
[5] Y. Ogihara, Y. Sakamoto, "Fast calculation method of a CGH for a patch model using a point-based method," Applied optics 54(1), A76–A83 (2015).
[6] Y. Takaki, M. Nakaoka, "Scalable screen-size enlargement by multi-channel viewing-zone scanning holography," Optics express 24(16), 18772–18781 (2016).
[7] E. Murakami, Y. Oguro, Y. Sakamoto, "Study on compact head mounted display system using electro-holography for augmented reality," IEICE transactions on electronics 100(11), 965–971 (2017).
[8] W.-K Lin, O. Matoba, B.-S. Lin, W.-C. Su, "Astigmatism and deformation correction for a holographic head-mounted display with a wedge-shaped holographic waveguide," Applied optics, 57(25), 7094-7101. (2018)

LDC2020 | Oral Presentation
# AR, MR, VR, ... XR technologies 1
2020年4月21日(火) 13:00 ～ 15:00 301 (Conference Center)

[LDC2-05] Overcoming the limitations of Spatial Light Modulators for holographic near-eye displays

*Michal Makowski[1], Rafal Trybus[1], Szymon Fiderkiewicz[1], Joanna Starobrat[1]　(1. Warsaw University of Technology）

Among the limitations of Spatial Light Modulators for computer holography there are regular pixel arrays, causing the formation of spurious higher diffractive orders. We address this problem by two-dimensionally tilted SLM configuration and by pixel-level engineering involving apodizing masks and irregular sampling. We show the experimental cancellation of higher orders.

Overcoming the limitations of Spatial Light Modulators for holographic near-eye displays

M. Makowski[1], R. Trybus [1], S. Fiderkiewicz[1], J. Starobrat [1]

[1] Warsaw University of Technology, Faculty of Physics, 75 Koszykowa, 00-662 Warsaw, Poland, +48222347267,
dziekan.wf@pw.edu.pl

Abstract: *Among the limitations of Spatial Light Modulators for computer holography there are regular pixel arrays, causing the formation of spurious higher diffractive orders. We address this problem by two-dimensionally tilted SLM configuration and by pixel-level engineering involving apodizing masks and irregular sampling. We show the experimental cancellation of higher orders.*

1. Introduction

Spatial Light Modulators have opened the possibilities of animated computer holography, allowing the growth of exciting applications like holographic projection and holographic near-eye AR/VR displays. The use of phase modulation has allowed unprecedented energetic efficiencies, practically unlimited brightness and full control over the 3-D shape of the projected fields [1].

On the other hand, liquid-crystal-on-silicon SLMs exhibit some intrinsic hardware limitations, which compromise the quality of the output intensity patterns. Among them there can be named the regular pixel array with non-100% fill factor. Simple mathematics shows that any intensity pattern projected with an SLM must be repeated angularly in a tile-like structure all over the viewing zone, which is especially problematic in near-eye displays. In this paper we approach this problem by enlarging the angular separation of the mentioned orders by a highly-tilted SLM configuration [2] and especially by pixel-engineering of the SLM with the use of intensity-apodizing masks and additionally irregular-sampling masks.

2. The origin of higher diffractive orders

All the diffractive orders formed by the methods of computer holography with the use of an SLM are attenuated by the so called *sinc* envelope.
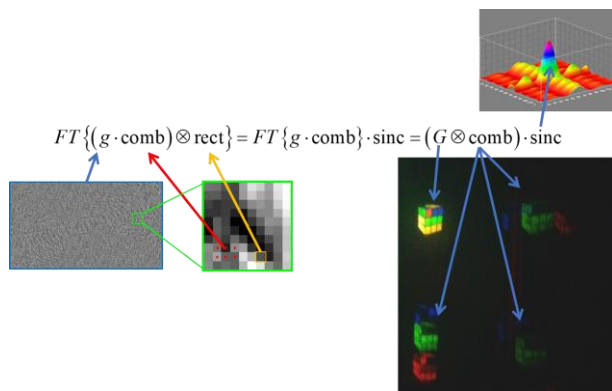
This is the result of the fundamental equation of the Fourier optics adapted to Fraunhofer-type holograms, as shown in Fig. 1.

The signal (G) is reconstructed from the hologram as the Fourier transform of the input g signal, as shown in Fig. 1, but is convolved with a comb function, resulting from the regular placement of the SLM pixels in a cartesian matrix. Moreover, the signal G is multiplied with a *sinc* envelope, being the Fourier transform of the individual pixel of the SLM. Since the pixels are generally square-shaped, the resulting envelope is sinc-shaped. In principle, changing the shape of the pixels could result in another profile of the envelope. Ideally such engineered shape should emphasize the useful, first diffractive order and cancel out all the others.

3. Pixel-level apodizing mask

We have performed the simulations of holographic reconstructions with apodizing per-pixel masks attached to the surface of the SLM (Holoeye Pluto, 8um pixel pitch). This means that each physical SLM pixel was simulated with 8x oversampling to include the gaussian-shaped mask in the process. Fig. 2 shows the cross-sections of the original (non-apodized) and apodized envelopes, showing that the higher diffractive orders could potentially be efficiently attenuated without a significant suppression of the useful central order, as seen in Fig. 3.

$$FT\{(g \cdot \mathrm{comb}) \otimes \mathrm{rect}\} = FT\{g \cdot \mathrm{comb}\} \cdot \mathrm{sinc} = (G \otimes \mathrm{comb}) \cdot \mathrm{sinc}$$

Fig. 1. Signals in the image formation process in Fourier-type holograms.
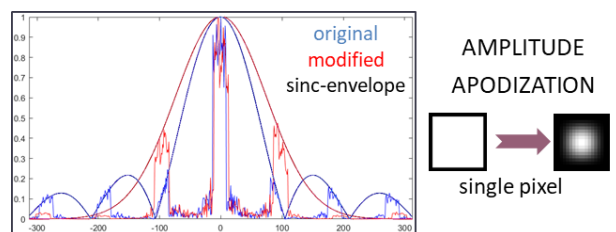

Fig. 2. Simulated original and modified (gaussian) envelope achieved by per-pixel apodizing masks of the gaussian shape.
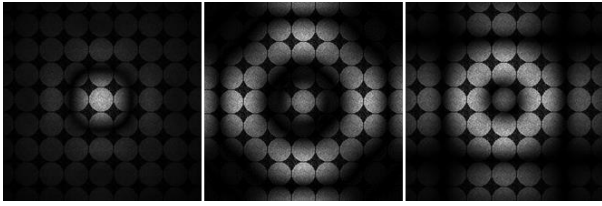
Fig. 3 The use of exemplary apodizing masks on the visibility of diffractive orders.
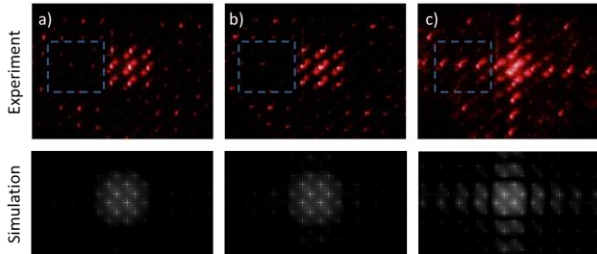

Fig. 4. The use of per-pixel apodization in a) gaussian and b) cosine shaped profile allows the suppression of the normally visible 3, 4, 5th diffractive orders (c).

Fig. 4 shows the results of initial experiments with simple apodizing filters. As clearly seen in the marked area, the spurious diffractive orders normally strongly visible are suppressed thanks to the use of the per-pixel apodization. This happens without any notable attenuation of the useful central part of the field, where the useful lower diffractive orders are located. Obviously, the used intensity filters take some of the light energy through absorption, nevertheless in AR/VR applications the elimination of ghost images from the field of view is the main goal, putting the energetic aspects in the second row.

4. Pixel-level irregular sampling mask

The other possibility of eliminating spurious signals from the equation shown in Fig. 1 is making the sampling (or positioning of the phase-modulating samples) irregular.

Although it is not feasible by physical shifting of the SLM pixels, one can use sampling filters with apertures smaller than the pixel size and placed in various (random) positions within the pixels. Effectively such a filter array transmits the phase-modulated field only through tiny holes located without any regularity, as shown in Fig. 5. The growing randomization of the positioning of the samples in the filter efficiently suppresses the formation of the ghost images in the upper orders, as seen in Fig. 6. The marked region should normally show the -2nd order of diffraction, but with strong randomization of the samples in the hologram its existence is no longer supported by the regularity of phase-modulating pixels.
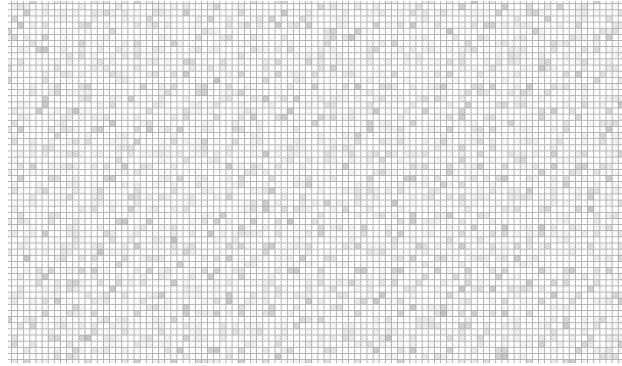

Fig. 5. Close-up of an exemplary bitmap displayed on the SLM with oversampling, showing randomized samples transmitting the holographic signal.
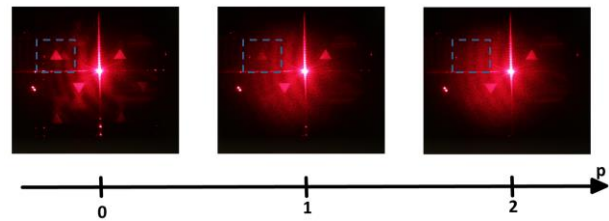

Fig. 6 The experimental playback of the signal showing a triangle with a growing randomization parameter (p) of the used sampling mask.

5. Conclusions

The initial results shown here exhibit the possibilities of limiting the visibility of spurious higher diffractive orders by pixel-level intensity masks. One approach exploits the gaussian-like apodization leading to the optimally attenuated envelope of projected fields. The second presented approach destroys the regularity of the pixel grid by randomized sampling with adaptive phase correction. Both methods were proven useful in initial experiments.

References

[1] J. Starobrat, P. Wilczynska, and M. Makowski, "Aberration-corrected holographic projection on a two-dimensionally highly tilted spatial light modulator," Opt. Express **27(14)**, 19270-19281 (2019).

[2] M. Makowski, A. Kowalczyk, M. Bieda, J. Suszek, I. Ducin, T. Shimobaba, Y. Nagahama, T. Ito, "Miniature holographic projector with cloud computing capability," Appl. Opt. **58**, A156-A160 (2019).

LDC2020 | Oral Presentation

AR, MR, VR, ... XR technologies 2

Session Chair: Masafumi Ide(MagicLeap)
Tue. Apr 21, 2020 3:15 PM - 4:45 PM 301 (Conference Center)

[LDC3-01(Invited)] Optical See-Through AR HMD with Spatial Tracking

*Hiroshi Mukawa[1], Hiroyuki Aga[1], Atsushi Ishihara[1], Koichi Kawasaki[1]　(1. Sony Corporation)

 3:15 PM - 3:45 PM

[LDC3-02]　　　　　MEMS system for AR HMDs

Ran Gabai[1], Gil Cahana[1], Dan Nabel[1], Meni Yehiel[1], Avi Leibushor[1], Gady Yearim[1], *Matan Naftali[1]　(1. Maradin LTD)

 3:45 PM - 4:15 PM

[LDC3-03(Invited)] Why Light Field is an Important Fundamental Technology for Future XR Displays

*Takafumi Koike[1]　(1. Hosei University)

 4:15 PM - 4:45 PM

LDC2020 | Oral Presentation
# AR, MR, VR, ... XR technologies 2
2020年4月21日(火) 15:15 ～ 16:45 301 (Conference Center)

[LDC3-01(Invited)] Optical See-Through AR HMD with Spatial Tracking

*Hiroshi Mukawa[1], Hiroyuki Aga[1], Atsushi Ishihara[1], Koichi Kawasaki[1]　(1. Sony Corporation)

An optical see-through AR HMD prototype with a small temporal registration error between virtual and real objects was developed. The prototype employs micro-OLED displays to achieve high image quality despite the challenge to reduce the temporal registration error. Our latency compensation technique can minimize the temporal registration error small enough for practical use.

Optical See-Through AR HMD with Spatial Tracking

Hiroshi Mukawa, Hiroyuki Aga, Atsushi Ishihara, Koichi Kawasaki
R&D Center, Sony Corporation, Japan

Abstract: *An optical see-through AR HMD prototype with a small temporal registration error between virtual and real objects was developed. The prototype employs micro-OLED displays to achieve high image quality despite the challenge to reduce a temporal registration error. Our latency compensation technique can minimize the temporal registration error small enough for practical use.*

1. Introduction

AR HMDs capable of accurate spatial registration between virtual objects and the physical world are necessary for both entertainment use cases requiring a sense of reality and enterprise use cases requiring accurate positioning between virtual and real objects. There are two types of see-through AR HMDs: optical see-through (OST) and video see-through (VST). OST systems usually provide a wider see-through field of view and more precise depth sense than VST systems. However, achieving accurate spatial registration is more challenging especially during a user's head motion.

A registration error due to a user's head motion (a temporal registration error) is mainly caused by system latency. In VST systems, the error can be eliminated as these systems capture the physical world by cameras, then render it after aligning it with virtual images. However, in OST systems, it is difficult to align those two images because users see the physical world with no delay. Therefore, reducing system latency is inevitable to achieve an acceptable registration error.

In this paper, the design and implementation of a latency compensation system to reduce a temporal registration error are presented. We employ a time-warp technique for latency compensation. With this approach, the error is reduced small enough not to be clearly perceived by users in normal usage.

2. Related Work

Reducing registration errors of virtual objects in AR systems has been a critical issue and there are lots of prior research. Holloway explained that system delay, optical distortion, and tracker measurement errors are the main causes of registration errors [1]. Other existing research has been devised systems that compensate for latency by transforming 2D rendered images right before frame buffer read-out. Regan et al. introduced a post-rendering warp stage between a graphic processor and a display [2].

Kijima et al. developed an HMD that modulated a signal of LCDs and shifted a viewport within an image by measuring rotations of a user's head using a gyroscope [3]. Jerald et al. integrated predictions and post-rendering image corrections for raster scan displays into his hardware [4, 5]. However, the errors due to roll and translation of a user's head were not minimized so far.

3. System Overview

Our goal is to develop a standalone OST AR HMD system with a spatial tracking function capable of pinning virtual objects in the physical world even when a user's head is moving.

Our HMD system uses two inside-out cameras and inertial measurement units (IMUs) for sensors. A custom SoC was developed for low latency signal processing. Micro-OLED panels are employed for display modules to avoid color breakup although they require more complex control in the latency compensation process than plane sequential micro-displays such as LCoS panels. The entire system data flow is shown in Fig. 1.
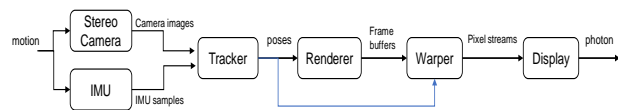

Fig. 1. System dataflow

3.1 Sensors

The stereo camera block captures real scenes periodically. It generates raw image data using the image signal processor (ISP) and writes out the undistorted and rectified stereo images with exposure timestamps. The IMU block captures raw data streams from a gyro sensor and accelerometer and writes out corrected angular velocity and linear acceleration with a timestamp.

3.2 Tracker

The tracker consists of a pose estimation block and a pose prediction block. The estimation block estimates a current user's head pose by the stereo camera images and IMU data stream. The prediction block predicts a user's head pose when the light comes out from micro-OLEDs based on the current pose and its derivative.

3.3 Renderer

The renderer renders virtual objects to a frame buffer viewed from the predicted head pose by the tracker.

3.4 Time-warper

The actual head pose at t_d, the time when the rendered image is shown on the display, is most likely different from which the tracker predicted at the timing just before the renderer starts rendering (i.e. t_g) shown in Fig. 2. The later the tracker predicts a head pose, the smaller the prediction error becomes. The time-warp is a technique to generate the latest virtual image by transforming an

already rendered image based on the latest predicted head pose. The image transformation is done in a 2D plane by shifting, skewing, expanding and shrinking an original image according to the latest head pose. This simplifies the signal process and minimizes the prediction-to-photon latency from (t_g to t_{d_1}) to (t_{r_1} to t_{d_1}). Due to the nature of micro-OLED as a line-sequential display, it takes some time to emit light from a top line to a bottom line, therefore, the time-warp is carried out several times per frame using the latest IMU data at $t_{r_1}\ldots t_{r_n}$ targeting the light emissions at $t_{d_1}\ldots t_{d_n}$.
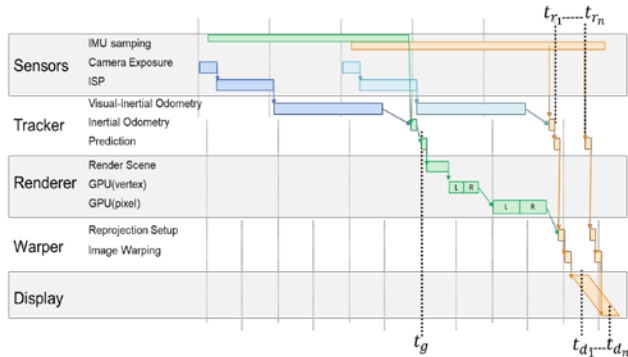

Fig. 2. System timing chart

3.5 Display

Image light from a micro-OLED is collimated and projected to a waveguide combiner by an optical engine. Then, the light is combined with light from the physical world and projected to an observer's eye.

4. Implementation

The developed prototype is shown in Fig. 3. Sony IMX388 image sensors with a resolution of 640x480 at 60Hz frame rate are used for the stereo cameras. The sensor array operates with a global-shutter mode. The diagonal field of view of the camera is 100°. Bosch BMI160 and ST Microelectronic LIS3DHH were used as

Fig. 3. Photo of prototype

a gyroscope at 1600Hz and an accelerometer at 1100Hz respectively. The micro OLED has a 1280x768 resolution and 120Hz frame rate. The field of view of the display is 40°x20° with 20°x20° overlap.
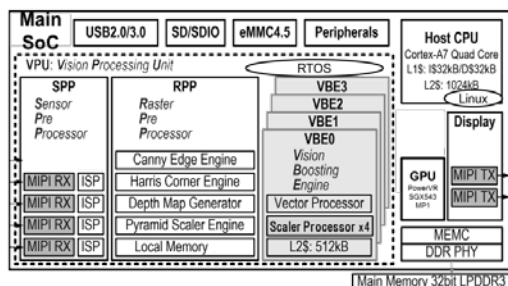

Fig. 4. Block diagram of main SoC

Fig. 4 shows a block diagram of the main SoC. It consists of an ARM core CPU which runs Linux, Vision Processing Unit (VPU) which runs a proprietary Real-Time Operating System (RTOS) as well as a GPU and display controller. All the tracking algorithms and time-warp control are implemented in the RTOS on the VPU to reduce the overall system latency and time jitter. The rendering function is performed on the CPU and GPU at 60Hz using OpenGL ES 2.0 graphics API.

5. Experimental result

We measured registration errors of virtual objects while rotating the HMD along the roll axis with a sine wave whose period is 5 Hz and amplitude is ±1°. The measured result is shown in Fig. 5. The blue line is the real object position, and the red cross is the virtual object position. When latency compensation is enabled, the registration error improves from 0.832° to 0.074°.
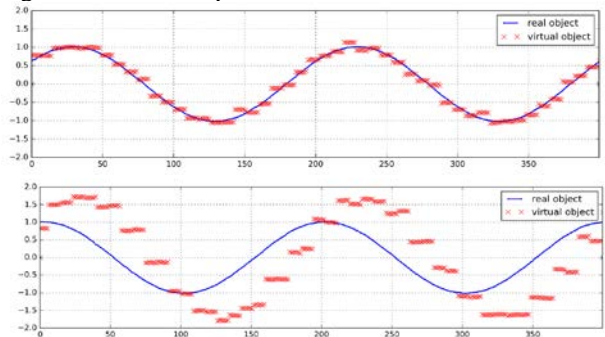

Fig. 5. Registration errors with and without the latency compensation

6. Conclusion

It was shown that the latency compensation technique with our time-warp approach can reduce a temporal registration error of OST AR HMDs with micro-OLEDs to less than one-tenth of the error without the technique, which would be small enough for many use cases.

References
[1] R.L. Holloway, Registration errors in Augmented Reality Systems, Ph. D. thesis, University of North Carolina at Chapel Hill (1995).
[2] J.M.P. van Waveren, "The asynchronous time warp for virtual reality on consumer hardware," in Proceedings of the 22nd ACM Conference on Virtual Reality Software and Technology, 37-46 (2016).
[3] M. Regan, R. Pose, "Priority rendering with a virtual reality address recalculation pipeline," in Proceedings of the 21st Annual Conference on Computer Graphics and Interactive Techniques, 155-162 (1994).
[4] R. Kijima, E. Yamada, T. Ojika, "A development of Reflex HMD -HMD with time delay compensation capability," in Proceedings of International Symposium on Mixed Reality 2001, 1-8 (2001).
[5] J. Jerald, A. Fuller, A. Lastra, M. Whitton, L. Kohli, F. Brooks, "Latency compensation by horizontal scanline selection for head-mounted displays," in Proceedings of Stereoscopic Displays and Virtual Reality Systems, 6490, 64901Q–64901Q–11, (2007).

LDC2020 | Oral Presentation
# AR, MR, VR, ... XR technologies 2
2020年4月21日(火) 15:15 ～ 16:45 301 (Conference Center)

[LDC3-02] MEMS system for AR HMDs

Ran Gabai[1], Gil Cahana[1], Dan Nabel[1], Meni Yehiel[1], Avi Leibushor[1], Gady Yearim[1], *Matan Naftali[1] （1. Maradin LTD）

MEMS-based projectors are attractive to use for AR HMDs for their high-resolution, small-footprint, and low-power properties. High dynamics capabilities are required to achieve the desired image quality. These achieved by a combination of innovative mechanical design with break-through feedback control. Key design points of such MEMS devices are presented.

MEMS system for AR HMDs

Ran Gabai[1], Gil Cahana[1], Dan Nabel[1], Meni Yehiel[1], Avi Leibushor[1], Gady Yearim[1], Matan Naftali[1]

[1] Maradin LTD., 2 HaCarmel St. Yokneam, ISRAEL, 972 (4) 627 3653, ran.gabai@maradin.co.il,

Abstract: *MEMS based projectors are attractive to use for AR HMDs for their high-resolution, small-footprint, and low-power properties. High dynamics capabilities are required to achieve the desired image quality. These achieved by a combination of innovative mechanical design with break-through feedback control. Key design points of such MEMS devices are presented.*

1. Introduction

Head Mount Display (HMD) devices require a high capability projecting system to produce high resolution, high frame-rate images. Tiny projectors, based on Micro-Electro-Mechanical System (MEMS) mirror, are attractive to use for this purpose. The small dimensions, low-cost, low power requirements properties suit HMDs requirements [1]. Designing a high performances projector based on a MEMS scanning mirror involves innovative mechanical design combined with sophisticated driving electronics and control such as demonstrated at [2]. While there are several feedback loops required to operate a MEMS mirror, a unique feedback loop designed to tune the resonance frequency is shown. It is common to drive the mirror at ist resonance frequency due to power considerations. Commonly this is done by resonance tracking. Here, a different approach is suggested in which the system's resonance frequency is tuned to match the required frequency of scan.

Human vision can maintain a wide Field of View (FOV) with increased resolution in a small section of the image that falls on the fovea [3]. This can be achieved using a projector based on a MEMS scanning mirror, with no additional hardware.

The following work presents key points in designing a MEMS based projector system. Showing the mechanical design, control design and demonstrating the generation of a foveated image.
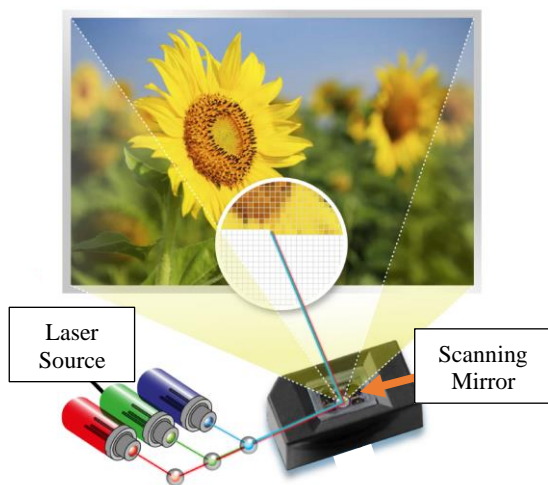

Fig. 1 An image projected by a scanning mirror operating in raster scan

2. MEMS scanning mirror principle of operation

A scanning laser projector is steering a laser beam on the projected surface by a moving mirror. The motion of the scanning mirror is controlling the location of the light on the projected surface and the light source is controlling the intensity of the image. A common operating mode for such a scanning mirror is a raster scan [4] in which a rectangle image of M lines having N pixels each (a frame of $N \times M$ pixels) is projected line by line. This is illustrated in Fig. 1. The spatial pattern of pixels is translated into a series of timings marks, marking the time for each pixel.

A common design of micro-projectors based on a MEMS scanning mirror with a diameter of ~1[mm]. The mirror is gimbaled in two perpendicular axes allowing it to scan in the horizontal and vertical directions simultaneously. The amplitude of the scanning in each direction defines the FOV of the scanning projector. A possible design of a dual-axis MEMS scanning mirror is depicted in Fig. 2.
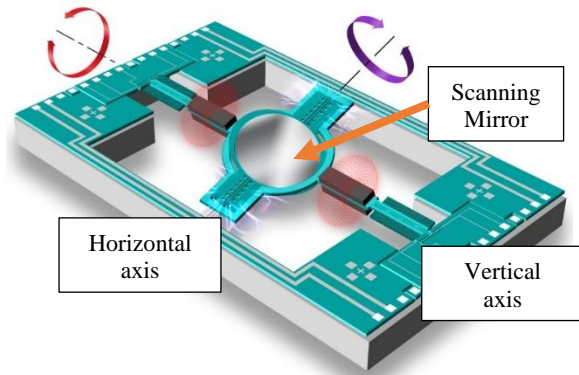
Fig. 2 A dual-axis MEMS Scanning mirror. Mirror diameter is 1[mm].

Operating a scanning mirror to generate a rasterized image a single horizontal scan generates a single line and a single vertical scan creates the entire frame. This requires the horizontal scan frequency to be considerably faster than the vertical scan frequency. This means that for a desired frame rate, creating an image of M lines requires the horizontal scanning frequency to be:

$$f_{horizontal} = 2M \cdot (frame\ rate) \qquad (1)$$

The mechanical design of the MEMS mirror is guided by the required image and video properties of the projector.

3. MEMS mirror design challenges

The growing demand from MEMS scanning mirrors for higher projection resolutions and higher frame rate leads designers to increase the resonance frequencies of the mirrors to accomplish these demands. In general, this is achieved by increasing the stiffness of the supporting structure of the mirror. Several technological challenges arise from stiffening the structure. (a) The stresses the structure experiences during operation are becoming critical and may lead to mechanical failures. (b) The dynamic deflection of the mirror itself becomes significant in high frequencies. (c) The power required to achieve decent FOV increases significantly.

The solution must be combined from both innovative geometric/mechanic design of the MEMS, the use of vacuum packaging and sophisticated active closed-loop control effort closing some of the gaps the (passive) design cannot cope with. Non-linear structures that allow large deflections with low strains and internal stress.

In order to reduce the dynamic deflections, some solutions were presented [5] to increase the mirror's plate stiffness. Nevertheless, a novel approach presents an ever-stiffer mirror with reduced inertia. The reduction of inertia is crucial for the reduction of actuating power.

Vacuum package enables the reduction of actuation power for large deflections due to low damping (Q>100). Yet, such a system is very sensitive to working out of its resonance. As the resonance frequency of MEMS is determined by its geometry, a novel control approach is used to modify the resonance frequency for a given mechanical structure by applying additional electrical forces that tune the system stiffness toward the desired resonance frequency.

4. Scanning mirror frequency control

It is desired to maintain the system's resonance frequency at the required scanning frequency. A unique method based on modifying the stiffness to move the resonance frequency to the desired frequency is presented. By applying a feedback loop, that applies additional torque to the mirror which is proportional to the scanning mirror angle. Acting as an additional virtual spring that modifies scanning mirror stiffness. The result is an augmented scanning system with resonance frequency shifted from the mechanical resonance. The equation of motion for one of the axes of a scanning mirror is given by:

$$J_y \ddot{y} + C_d \dot{y} + K_y y = T_{drive} + T_{fshift} \quad (2)$$

whereas y is the mechanical angle, J_y, C_d, K_y are the inertia, damping, and stiffness respectively. T_{drive} is the driving torque and T_{shift} is the feedback control force. Define an internal feedback loop $T_{fshift} = F \cdot y$ and substitute into (2):

$$J_y \ddot{y} + C_d \dot{y} + (K_y - F)y = T_{drive} \quad (3)$$

From (3) it is shown that tuning the feedback gain F can affect the total stiffness of the axis. Thus, tuning the resonance frequency of the system:

$$\omega_y = \sqrt{(K_y + F)/J_y} \quad (4)$$

By tuning F, the resonance frequency of the mirror can be tuned toward the required scanning frequency. Moreover, this can be carried out adaptively during the mirror operation allowing real-time adjustment in reaction to system changes.

5. High capability example: Foveated imaging

A foveated image requires a non-uniform resolution of pixels. Projecting a rasterized image using a scanning mirror, the horizontal non-uniform density of pixels is controlled per line by timing the projection of each pixel relative to the uniform location. The vertical density is controlled per frame by controlling the actual vertical position of each line. In this way, straight lines remain straight but columns of pixels are distorted to increase local resolution. Fig. **3** shows a real foveated image projected by Maradin DM3102 MEMS projecting system.
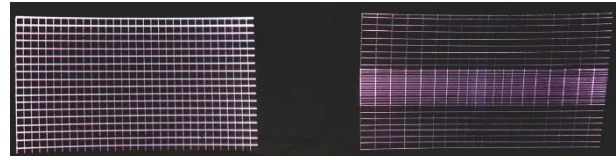

Fig. 3 A non foveated (left) and foveated (right) image, projected by Maradin DM3102 MEMS projecting system.

Applying synchronization and control algorithms, the foveated image can be tuned in each frame.

6. Conclusions

The use of projectors based on MEMS scanning mirrors in AR HMDs is attractive. However, the MEMS system requires special mechanical design coupled with the control algorithms to provide the required performances. This work presents some of the aspects involved.

References

[1] Urey, Hakan, David W. Wine, and Thor D. Osborn. "Optical performance requirements for MEMS-scanner-based microdisplays." In MOEMS and Miniaturized Systems, **vol. 4178**, pp. 176-185. International Society for Optics and Photonics, (2000).

[2] Qian, Rong-rong, Zhi-yu Wen, Li Chen, Zhongquan Wen, and Biao Luo. "Closed-loop control of a MOEMS mirror integrated with angle sensor." In International Symposium on Photoelectronic Detection and Imaging 2011: Sensor and Micromachined Optical Device Technologies, vol. 8191, p. 81911S. International Society for Optics and Photonics, (2011).

[3] R. Gabai, G. Yearim, M. Yehiel, G. Cahana, A. Baram, M. Naftali, Foveated display by laser scanning, Foveated display by laser scanning, SPIE Photonic West conference, San Francisco, California, 1-6 Feb (2020).

[4] Yalcinkaya, Arda & Urey, Hakan & Brown, Dean & Montague, Tom & Sprague, Randy. Two-Axis Electromagnetic Microscanner for High Resolution Displays. Microelectromechanical Systems, Journal of. **15**. 786 - 794. (2006).

[5] US7034370B2, Advanced Nano Systems Inc, MEMS scanning mirror with tunable natural frequency, (2005)

LDC2020 | Oral Presentation
AR, MR, VR, ... XR technologies 2
2020年4月21日(火) 15:15 〜 16:45 301 (Conference Center)

[LDC3-03(Invited)] Why Light Field is an Important Fundamental Technology for Future XR Displays

*Takafumi Koike[1]　（1. Hosei University）

Light field is a concept that describes light by position and direction. At present, the light field is an important concept for displays and computer graphics. I describe why the light field is important also for AR and VR.

Why Light Field is an Important Fundamental Technology for Future XR Displays

Takafumi Koike[1)]

[1)] Hosei University, 3-7-2 Kajino-cho, Koganei-shi, Tokyo, Japan, +81-42-387-7203, takafumi@hosei.ac.jp

Abstract: *Light field is a concept that describes light by position and direction. At present, the light field is an important concept for displays and computer graphics. I describe why the light field is important also for AR and VR.*

1. Introduction

The concept of light field has spread to 3D displays and cameras, computer graphics, and computer vision as its applications. We describe a brief introduction of light field and the importance of light fields to XR and how it affects them.

2. Light Fields

Light field is a concept that considers light as a field and expresses the brightness of light at an arbitrary position in three-dimensional space by position and direction. As shown in Fig. 1, three-dimensional (x, y, z) for the light emission position, two-dimensional (θ, φ) for the direction, and one-dimensional information for wavelength (λ) and time (t) are used. Thus, any light intensity can be described as the following [1].
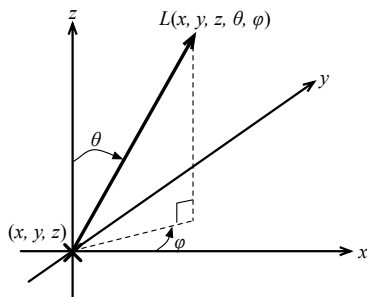
$$P(x, y, z, \theta, \phi, \lambda, t)$$

Fig. 1. Light field and its parameters

3. Light Field Display

The display that reproduces the light field described above is a light field display. Therefore, in a broad sense, even a normal display is considered to be a limited light field display. However, here we describe two typical light field displays, which are well-known methods and have substantial differences, with reference to Fig. 2.

First, the principle of integral photography invented in 1908 by Lippmann is called the ray sampling method or the lens array method. The second type uses multiple display panels such as liquid crystal, and is called a stacked type, stack type, or tensor display.

3.1 Ray sampling display

The ray sampling method combines a two-dimensional display such as a liquid crystal display with an optical system such as a lens array or a barrier to achieve directivity of light. The optical system is equivalent to the original integral photography proposed by Lippmann [2], which is also the principle of general naked-eye stereoscopic displays. Integral imaging is often referred to as an imaging technology that has an optical system equivalent to integral photography.

3.2 Stacked display

The second method is to stack multiple transmission type liquid crystal panels etc. in the normal direction, and here we will call it the stacked type [3]. As for the stacked type 3D display, DFD (Depth Fused 3D) by Suyama et al. [4], Which can perceive a 3D image even if the number of layers is reduced to two, is well known. Although there is no significant difference in hardware between the DFD and the tensor product method, the general stacked 3D display including DFD thinks that there is an image at the panel position or the space between both end panels, whereas the tensor display method The major difference is that in principle, images can be displayed in a range beyond the space between the panels at both ends.

3.3 Classification of light field displays

Fig. 3 shows the classification of light field displays. In this figure, many types of displays are classified based on the concept of light field displays.

For example, an ordinary 2D display can be regarded as a display that reproduces the two-dimensional information of the light field. In this way, it is possible to arrange displays in terms of the dimensions of the light field, and to qualitatively and quantitatively compare displays between different systems [5].

As a display in XR, 5D light field playback is the final goal, but using an HMD with head tracking, etc., we have a possibility that the display itself can reduce the dimension to be played.

4. XR Applications by LF

4.1 Hardware

Since a general HMD is a virtual imaging optical system, the eye focuses on the virtual image position. Therefore, at the viewing distance of a general HMD, the convergence and the accommodation mismatch often occur. The discrepancy between convergence and accommodation is known to be one of the causes of visual fatigue and discomfort [6]. The state where two or more rays are incident on the pupil is called super multi-view,

and it has been shown that super multi-view reduces the mismatch between focus and accommodation [7]. If a light field display with a high light beam reproduction density is used, two or more rays will be incident on the pupil, so the focal point will be at an arbitrary position.

In addition, it has been shown that by using a light field display to perform the optical focus changing function of general glasses, it is possible to correct even myopia or hyperopia [8]. Eye information such as eyesight needs to be known in advance, but with a light field display, glasses can be realized simply by changing the light field to be displayed. In order for AR glasses to spread, such eye-friendly functions are indispensable.

In other words, using an HMD or glasses-type display as a light-field display has the potential to reduce eye fatigue and support myopia and hyperopia.

4.2 Software and contents
In the future XR Display, software and content will become more important than hardware. LF has been conventionally used for generating free viewpoint images. For example, an actual light field is photographed using a camera array. Overbeck et al. indicate that LF reproduce specular and the like more accurately by capturing LFs sufficiently densely [9].

7. Conclusions
We briefly describe the concept of the light field and the light field display, and the possibility of the light field display as a display for future XR. We hope this paper will help you in the future direction of display R&D.

References

[1] E. H. Adelson and J. R. Bergen, "The plenoptic function and the elements of early vision, " Computational Models of Visual Processing, MIT Press, pp. 3-20 (1991).

[2] M. G. Lippmann, "Epreuves reversibles donnant la sensation du relief," J. Phys. 7(4), pp. 821-825 (1908).

[3] G. Wetzstein, D. Lanman, M. Hirsch, and R. Raskar, "Tensor displays: compressive light field synthesis using multilayer displays with directional backlighting," ACM Transactions on Graphics, 31(4) (2012).

[4] S. Suyama, H. Takada, and S. Ohtsuka, "A direct-vision 3-D display using a new depth-fusing perceptual phenomenon in 2-D displays with different depths," IEICE Transactions on Electronics, E85-C, 11, pp. 1911-1915 (2002).

[5] T. Koike, "Future of 4D light field display," 15th International Meeting on Information Display, 45-3 (2015).

[6] D.M. Hoffman, A.R. Girshick, K. Akeley, and M.S. Banks "Vergence-accommodation conflicts hinder visual performance and cause visual fatigue," J. Vision 8, 3, 33, pp.1-30 (2008).

[7] Y. Kajiki, H. Yoshikawa, and T. Honda "Hologram-like video images by 45-view stereoscopic display," Proc. SPIE 3012, pp.154-166 (1997).

[8] F.-C. Huang, G. Wetzstein, B. Barsky, and R. Raskar, "Eyeglasses-free display: Towards correcting visual aberrations with computational light field displays, " ACM Transactions on Graphics, 33(4), pp. 59 (2014).

[9] R. S. Overbeck, D. Erickson, D. Evangelakos, M. Pharr, and P. Debevec, "A system for acquiring, processing, and rendering panoramic light field stills for virtual reality, " ACM Transactions on Graphics, 37(6), Article 197 (2018)
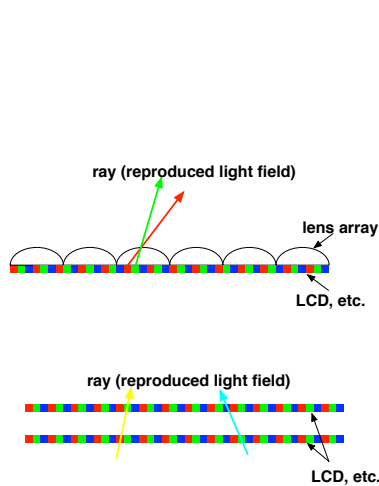
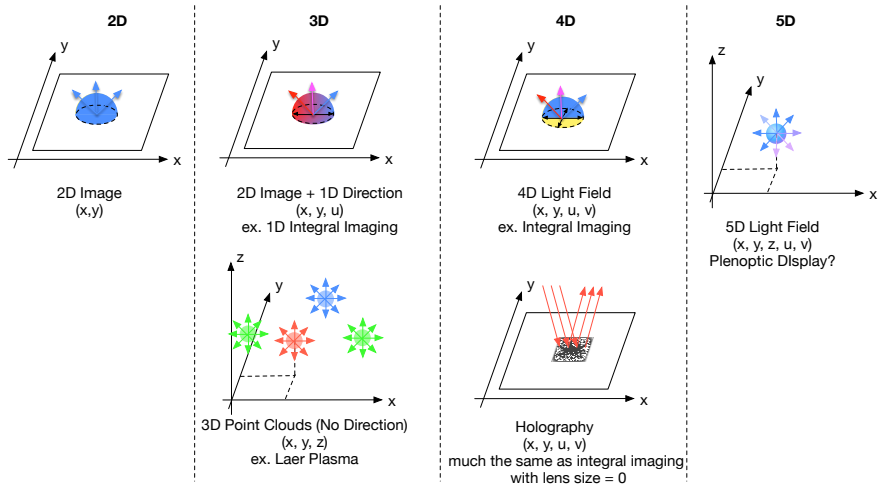Fig. 2. Two typical light field displays

Fig. 3. Classification of light field displays by sampling dimension of light field.

LDC2020 | Oral Presentation

Imaging / Lighting -Speckle-
Session Chair: Hiroshi Murata(Mie University)
Wed. Apr 22, 2020 9:00 AM - 10:30 AM 301 (Conference Center)

[LDC4-01] Efficient speckle reduction using volume scattering crystals

*Shigeo Kubota[1], Koji Suzuki[1], Hisashi Masuda[1], Keisuke Nakagome[1], Yutaka Anzai[1] （1. Oxide Corporation）

9:00 AM - 9:30 AM

[LDC4-02] Speckle reduction within nanosecond-order pulse widths for flash lidar applications

*Fergal Shevlin[1] （1. DYOPTYKA）

9:30 AM - 9:45 AM

[LDC4-03] Error Analysis of Speckle Contrast by Image Subtraction Method

*Makio Kurashige[1], Kazutoshi Ishida[1], Shumpei Nishio[1] （1. Dai Nippon Printing Co., Ltd.）

9:45 AM - 10:00 AM

[LDC4-04] Improved Visual Resolution Measurement for Laser Displays Based on Eye-diagram Analysis of Speckle Noise

*Junichi Kinoshita[1], Akira Takamori[1], Kazuhisa Yamamoto[1], Kazuo Kuroda[2], Koji Suzuki[3], Keisuke Hieda[4] （1. Osaka Universitry, 2. Utsunomiya University, 3. Oxide Corporation, 4. HIOKI E.E.CORPORATION）

10:00 AM - 10:15 AM

[LDC4-05] Study on Projection Screen and Speckle Contrast in Laser Display Technology

*Yuwei Fang[1], Linxiao Deng[1], Chun Gu[1], Lixin Xu[1] （1. University of Science and Technology of China）

10:15 AM - 10:30 AM

LDC2020 | Oral Presentation
# Imaging / Lighting -Speckle-
2020年4月22日(水) 09:00 ～ 10:30 301 (Conference Center)

[LDC4-01] Efficient speckle reduction using volume scattering crystals

*Shigeo Kubota[1], Koji Suzuki[1], Hisashi Masuda[1], Keisuke Nakagome[1], Yutaka Anzai[1]　（1. Oxide Corporation）

Volume scattering diffusers are overwhelmingly efficient in speckle reduction in laser displays than surface scattering diffusers. We report a eutectic crystal is potential stationary diffuser for speckle reduction using the volume scattering, based on simulations and experiments.

Efficient Speckle Reduction Using Volume Scattering Crystals

Shigeo Kubota[1], Koji Suzuki[1], Hisashi Masuda[1], Keisuke Nakagome [1], and Yutaka Anzai [1]

[1] Oxide Corporation, #203 Kawasaki Business Incubation Center, 7-7, Shin-kawasaki, Saiwai-ku, Kawasaki 212-0032 Japan
kubota@opt-oxide.com

Abstract: Volume scattering diffusers are overwhelmingly efficient in speckle reduction in laser displays than surface scattering diffusers. We report eutectic crystals are potential stationary diffusers for speckle reduction using the volume scattering, based on simulations and experiments.

1. Introduction

A monochromatic laser light scattered on a roughened screen surface is, after free space propagation, diffracted by an aperture of the eye lens to form an image on the retina, which is accompanied with a random interference intensity noise pattern, so-called speckle. If any speckle is developed, it will severely degrade the resolution of the total imaging system. Therefore, several ways for speckle suppression have been tried, such as polarization diversity, moving screen, specially designed screen, wavelength diversity, angle diversity, over-design projection lens and moving diffuser. [1]   If stationary diffusers be used for speckle reduction, the volume scattering diffusers will be overwhelmingly advantageous in speckle control than the surface scattering diffusers. Previous works on the volume scattering diffuser demonstrated speckle contrast down to 0.31 on a stationary 12 mm-thick white acrylic. [2,3] On the other hand, usage of surface scattering diffusers has been limited to ones for the moving diffusers, where the hypothesis of the ergodicity is automatically established. Very recently, we measured speckle contrast as low as 0.04 on a stationary, 1.2 mm-thick eutectic crystal diffuser, that is categorized into volume scattering diffusers from its nature.

2. Lamellar and rod structure in eutectic crystal

Examples of common eutectic materials are seen in metal alloys such as Pb-Sn, Al-Si, and Cu-Ag. The eutectic reaction process is best understood by the binary eutectic phase diagram. Analogous to the metal alloys, following the eutectic reaction process, two immiscible crystal components of eutectic oxide crystal are grown from a high temperature melt. The domain structure of eutectic material is characterized by the well-defined lamellar and rod structure depending on the composition ratio [4,5]. It is in our case the composite domain structure, of which sectional view is shown in Fig.1. Due to the difference in the refractive indices and high transmittances in visible wavelength region of two domains contained in the randomized structure, the ray direction changes very frequently at the Fresnel reflection and refraction points on the 3-dimensional domain boundary surfaces. This fact is quite beneficial in view of prolongation in the total optical path length (OPL) of ray within the crystal of a

certain thickness and is most crucial part to understand the speckle reduction in the volume scattering.
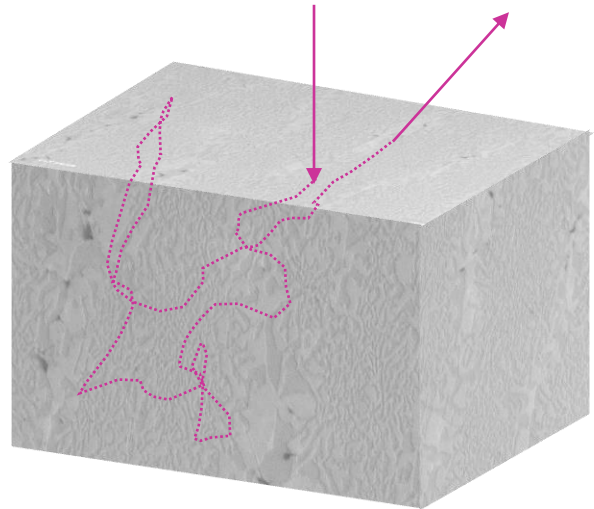

Fig. 1.   Computer graphics of a snake ray generated by ray trace through multiple refractions and reflections in composite random domain structure of a binary eutectic crystal.

3. Monte Carlo simulation and experiment

3.1 Stochastic model of eutectic domain structure
The stochastic model of such distinct random domain boundary surface in the volume scattering media is an ensemble of microfacets, of which tangential plane are repeatedly generated on the computer program. The simulation program was initially developed for the laser phosphor crystal analysis. [6]
Composite domain structure model:
- ✓ For each tangential plane of microfacet, pseudo random numbers are given to set the distributions of the surface-to-surface separation and orientational angle of the surface normal vector.
- ✓ Up to two refractive indices as well as small absorption coefficients, are definable for alternating multiple domains.

Ray tracing:
Let us start with a ray incident on the incoming plane on the bulk eutectic crystal. The orientation of a ray is redirected at every event of refraction and reflection on the domain boundary surfaces and such stochastic processes to produce a snake ray shown in Fig.1. A series

of 'time of flight' from surface to surface creates a time sequence to be integrated. A goal of the Markov chain, Monte Carlo (MC-MC) ray trace is to obtain the average impulse response for the diffusion approximation of the volume scattering, which is expressed by the path integral, in other words, OPL. A histogram of OPL is shown in Fig.2, where the vertical axis shows the number of occurrences for the OPL travelled from input to output in the volume scattering medium. Normalized by the area under the fitting function of plots, probability density function (PDF) for the OPL is defined. For the PDF to be stationary, it is necessary that a snake ray is well developed on the computer, which is ensured by proper construction of stochastic model for eutectic domain structures. In next section, it is described that we succeeded in constructing the stochastic model for our eutectic material. Resulted PDF of OPL will allow prominent speckle reduction to be compared with experimental results.
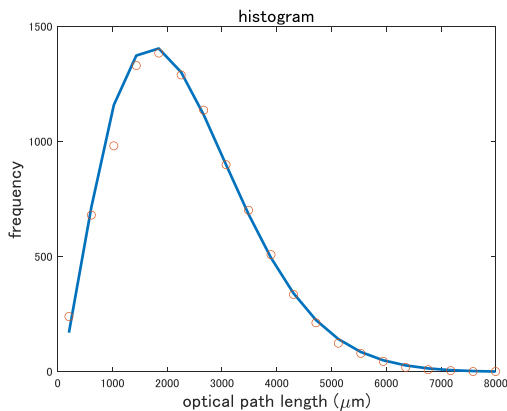

Fig.2 A histogram of the total optical path length from input to output in the volume scattering medium. Vertical axis shows the number of occurrences.

3.2 Speckle contrast calculation and measurement.
Speckle contrast C is calculated from replacing $M_h(\Delta q_z)$ in

$$C = \sqrt{\int_{-\infty}^{\infty} K_{\hat{g}}(\Delta \nu)|M_h(\Delta q_z)|^2 d\Delta \nu} \qquad (1)$$

by the characteristic function of the OPL probability density function $p_l(l)$:

$$M_l(\Delta q_z) = \int_0^{\infty} p_l(l)e^{j\Delta q_z l}dl \qquad (2)$$

Here, $K_{\hat{g}}(\Delta \nu)$ is the autocorrelation function of the normalized power spectrum for laser projector source. Assuming the linewidth in the projector source with its line spacing around 0.07 nm, since it is used for a raster-scan system, the initial speckle contrast calculated by Eq.

(1) must be calibrated against the calculated or measured values on the reference screen which is raster scanned by the projector. [7] In such a way calibrated speckle contrast on the eutectic crystal illuminated by the raster-scanned projector showed 0.04 at green, which agreed well with the measurement using a speckle contrast measurement system, Oxide corporation's model SM01VS09.

4. Conclusions
We have demonstrated the advantages of the volume scattering diffuser in terms of efficiency in speckle reduction by using a 1.2 mm-thick eutectic oxide crystal, which is characterized by composite lamellar and rod domain structure, numerically and experimentally. It is promising for a speckle-free laser back-lighting and will lead to a speckle-free, stationary screen for laser projection in very near future.
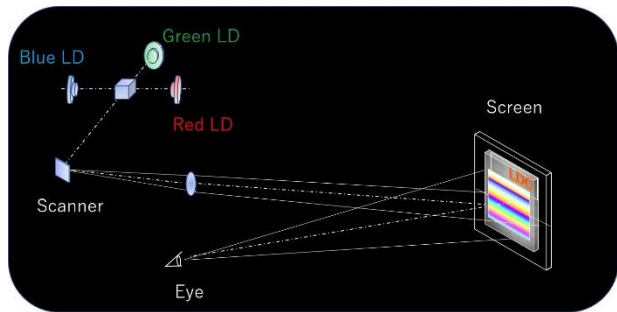

Fig.3 A schematic drawing of the screen employing stationary volume scattering diffusers for a laser projection system.

References
1. Joseph W. Goodman, *Speckle Phenomena in Optics*, (2007 Roberts).
2. C.A. Thompson, K.J. Webb, and A.M. Weiner, "Diffusive media characterization with laser speckle," Appl. Opt. vol.36 (1997) 3726-3734.
3. M.A. Webster K.J. Webb, A.M. Weiner, J. Xu, and H. Cao, "Temporal response of a random medium from speckle intensity frequency correlations," J. Opt. Soc. Am vol.20 (2003) 2057-2070.
4. K.A. Jackson and J.D. Hunt, "Lamellar and rod eutectic growth," Trans. Met. Soc. AIME vol.236 (1966) 1129-1142.
5. W. Kurz and D.J. Fisher, *Fundamentals of Solidification*, Reprinted Fourth Revised Ed. (2017 Trans Tech, Switzerland).
6. S. Kubota, K. Nakagome, M. Matsukura, Y. Anzai, and Y. Furukawa, "Micro Grain Analysis in the Ce: YAG and Sapphire Co-Crystal Phosphors," in digest of IDW2017, PH2-1.
7. S. Kubota, "Spatial Coherence Measurement of a Scanning Laser System and Applicability of Zernike's Approximation to the Exit Pupil on the Scan Mirror," Optical Review vol.19 No.6 (2012) 432-435.

Imaging / Lighting -Speckle-

2020年4月22日(水) 09:00 〜 10:30 301 (Conference Center)

[LDC4-02] Speckle reduction within nanosecond-order pulse widths for flash lidar applications

*Fergal Shevlin[1] （1. DYOPTYKA）

Our innovative deformable mirror technology is shown to be effective for the reduction of speckle contrast within pulse
durations of approximately 6 ns. It can be used to improve the spatial and temporal resolution of flash lidar distance measurements.

Speckle reduction within nanosecond-order pulse widths for flash lidar applications

Fergal Shevlin

DYOPTYKA, 7 Westland Court, South Cumberland St., Dublin 2, Ireland.
Phone: +353-85-1423747; Email: fshevlin@dyoptyka.com

Abstract: Our innovative deformable mirror technology is shown to be effective for the reduction of speckle contrast within pulse durations of approximately 6 ns. *It can be used to improve the spatial and temporal resolution of flash lidar distance measurements.*
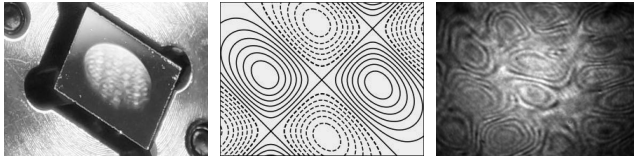
Fig. 1: [Left] Small deformable mirror in an active state. Randomly-distributed surface deformations are excited at very high frequencies in the 3 mm × 4.5 mm elliptical region. Reflection efficiency is approx. 99% and damage threshold is approx. 6 W. [Center] Contour plot of simulated deformations. As heights change over time the curvature of each region is reversed such that directions of reflection are changed. [Right] Microscope interferometer image showing fringes resulting from actual mirror deformations.

1 Introduction

To achieve good spatial and temporal resolution of range estimation, flash lidar systems illuminate the scene with pulses of ns-order duration. For consumer applications, arrays comprising thousands of coherent VCSEL emitters on a single small chip are used at kHz repetition rates. Although their pulses are mutually-incoherent, inhomogeneity and speckle are evident in acquired imagery. The cause is insufficient angular separation of emitters relative to the angular extent of the sensor pupil [1]. An effective technique for improvement is to generate multiple uncorrelated speckle patterns that are integrated at the sensor. For time-of-flight measurement, these patterns should be generated within the durations of single pulses so as to preserve temporal resolution. The high speed required precludes the use of conventional approaches such as moving diffusers.

DYOPTYKA has developed an innovative phase-randomizing deformable mirror technology [2], see Figure 1. It can be used to reduce speckle contrast and to improve homogeneity with excellent optical efficiency and at very high speed.

2 Objectives

To demonstrate how our deformable mirror can be used to improve the spatial and temporal resolution of flash lidar distance measurements through the reduction of speckle contrast by generating multiple uncorrelated speckle patterns within ns-order pulse widths.
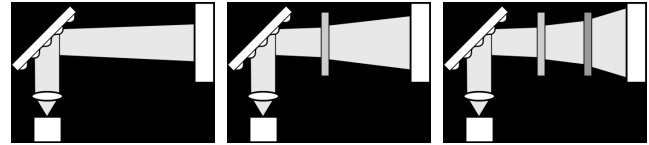

Fig. 2: [Left] Multimode 520 nm laser diode: Thorlabs NPL52C generating approx. 6 ns pulses at 2 Hz; collimating lens; Deformable mirror operating at approx. 1.67 MHz; Thorlabs BC106-VIS beam profiler. [Center] With RPC Photonics EDS 10 deg square light-shaping diffuser at approx. 20 mm distance from mirror. [Right] With additional 1500 grit ground glass diffuser, Thorlabs DG10.

3 Apparatus

Several configurations of the experimental apparatus are shown in Figure 2. Although a visible wavelength was used for convenience, similar performance is expected with the NIR of typical lidars. The light-shaping diffuser is similar to those used with VCSEL arrays for compact and efficient homogenization of illumination. The purpose of the ground glass diffuser is to simulate a rough surface on an illuminated target.

The actuation frequency of the deformable mirror is sufficient for local changes of slope to sweep reflected light across the diffuser(s) over distances greater than the correlation length of surface roughness. If separation between diffuser and mirror is reduced, the magnitude of local slope change should be increased. This is possible through operating the mirror at different frequencies and/or amplitudes.

4 Results

Imagery acquired with different configurations are shown in Figures 3–6. In each [top, left] image, the deformable mirror is inactive and some undesirable consequences of coherent illumination are evident. Each [top, right] image is an average of a large number acquired when mirror active. Their homogeneity is due mainly to uncorrelated speckle patterns being generated at a frequency at least equal to the pulse repetition rate. Speckle contrast C is quantified as the ratio of standard deviation of pixel intensity to mean intensity.

The [bottom, left] images of figures 4–6 are extracts from full images when mirror inactive such that individual pixels are easily visible. The C values of extracts and full images
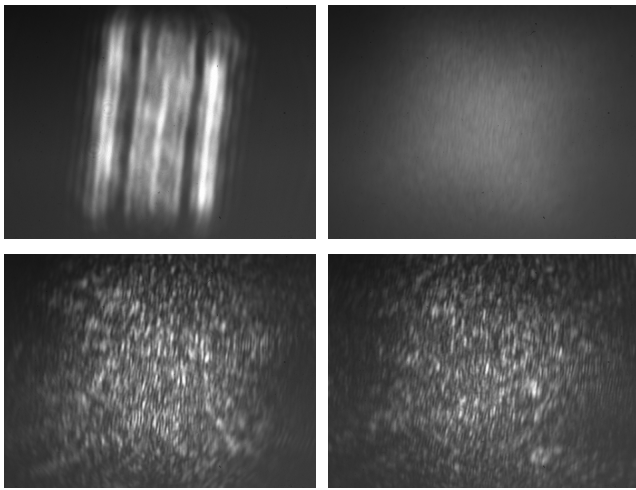
Fig. 3: Without diffuser(s.) [Top, left] Multimode emission pattern when deformable mirror inactive; [Top, right] Average of 88 images when mirror active. Demonstrates that mirror effects on different pulses are relatively uncorrelated. [Bottom] Effects of active mirror on two 6 ns pulses.
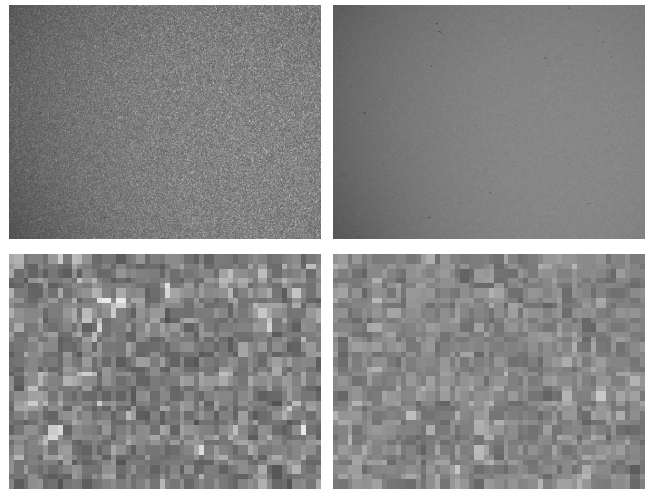

Fig. 5: With ground glass diffuser at distance of 10 mm from sensor. [Top, left] When deformable mirror inactive, $C \approx 20\%$. [Top, right] Average of 80 images when mirror active, $C \approx 9\%$. [Bottom, left] Central region when inactive, $C \approx 18\%$. [Bottom, right] Region when active, $C \approx 12\%$.
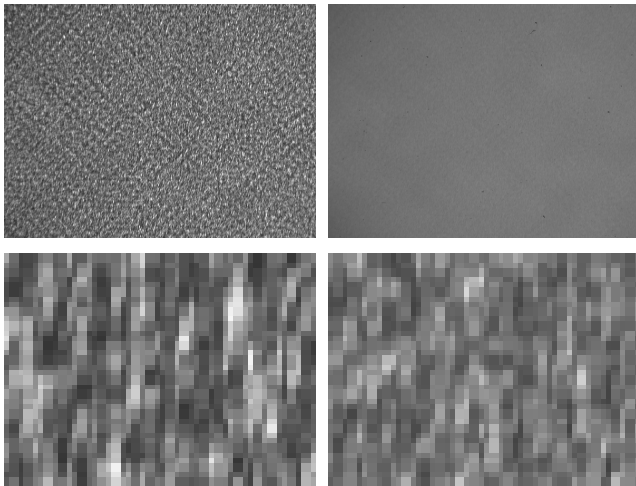

Fig. 4: With light-shaping diffuser. [Top, left] Light-shaping diffuser pattern when deformable mirror inactive, $C \approx 28\%$. [Top, right] Average of 86 images when mirror active, $C \approx 5\%$. [Bottom, left] Central region when inactive, $C \approx 32\%$. [Bottom, right] Region when active, $C \approx 21\%$.

Fig. 6: With ground glass diffuser at distance of 100 mm from sensor. [Top, left] When deformable mirror inactive, $C \approx 17\%$. [Top, right] Average of 89 images when mirror active, $C \approx 2\%$. [Bottom, left] Central region when inactive, $C \approx 16\%$. [Bottom, right] Region when active, $C \approx 12\%$.

are different due to variations of mean intensity across the field. Note that the spatial frequency of speckle is lower when diffuser is further from sensor. The corresponding [bottom, right] images show a relative reduction of speckle contrast by at least 25% when mirror active.

5 Conclusions

The observed reduction in speckle contrast confirms that our deformable mirror leads to the generation of uncorrelated speckle patterns within a 6 ns pulse duration. Further reduction can be expected through relatively straightforward modifications to device design and control electronics. We are not aware of any other compact, optically efficient
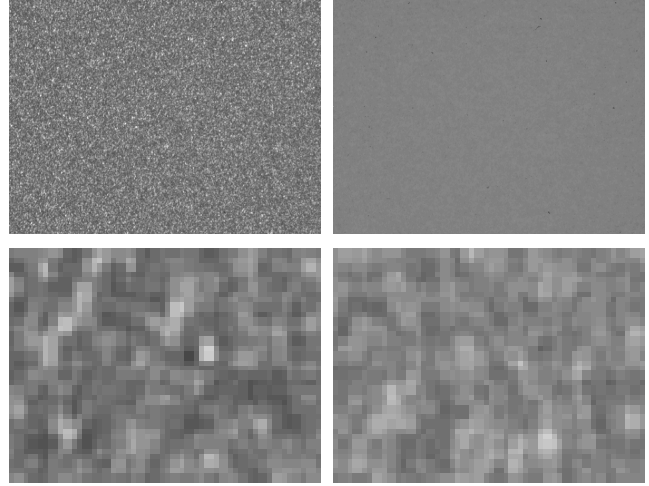
approach that can achieve such performance.

In addition to improvement of transverse spatial resolution through the mitigation of speckle artifacts, flash lidar systems should benefit from improvement of longitudinal spatial and temporal resolution since the averaging of images from many different pulses would not be necessary.

[1] Goodman, J., [*Speckle phenomena in optics*], Roberts and Company, Colorado, USA (2007).
[2] Shevlin, F., "Phase randomization for spatio-temporal averaging of unwanted interference effects arising from coherence," *Applied Optics* **57**(22), E6–E10 (2018).

LDC2020 | Oral Presentation

Imaging / Lighting -Speckle-

2020年4月22日(水) 09:00 〜 10:30 301 (Conference Center)

[LDC4-03] Error Analysis of Speckle Contrast by Image Subtraction Method

*Makio Kurashige[1], Kazutoshi Ishida[1], Shumpei Nishio[1] （1. Dai Nippon Printing Co., Ltd.）

Measurement error of speckle contrast was analysed in terms of the size of measurement field and imaging condition. The images from the different area of the original image were subtracted to check the randomness.

Error Analysis of Speckle Contrast by Image Subtraction Method

Makio Kurashige, Kazutoshi Ishida, Shumpei Nishio

Dai Nippon Printing Co., Ltd., 250-1 Wakashiba, Kashiwa-shi, Chiba-ken, 277-0871, JAPAN, +81-4-7134-1213

Abstract: *Measurement error of speckle contrast was investigated by using image subtraction method. The statistical error was suppressed enough when the sampling pixels were around 200×200 pixels. The parameter as an indicator of both statistical error by insufficient sampling pixels and low- frequency intensity variation within the sampling field was proposed.*

1. Introduction

Speckle pattern is an intensity distribution which is statistically random, then speckle contrast Cs is introduced to estimate how speckle is strongly observed by calculating the standard deviation of the intensity distribution σ, divided by its average $\overline{I}$.

$$C_S = \frac{\sigma}{\overline{I}} \qquad (1)$$

Speckle contrast is dependent on by various parameters. Theoretical and experimental approaches were reported to clarify the influence of each parameter, such as characteristics of the light source, measurement geometries, imaging conditions. At the same time, there are several sources of "possible error", such as focusing, low-frequency intensity variation, and the number of sampling pixels. Regarding the sufficient sampling pixels for the speckle contrast calculation, there has not been enough information from the experimental viewpoint, because multiple sources of error might be overlapped at once. In this report, "image subtraction method" was proposed to separate the error from insufficient sampling pixels and low-frequency intensity variation.

2. Image subtraction method

Assume that two different speckle patterns which is extracted from the different location of a single speckle pattern, shown in Figure 1. Standard deviation and mean value of each extracted image are σ_1, $\overline{I_1}$ for the image 1 and σ_2, $\overline{I_2}$ for the image 2 respectively.
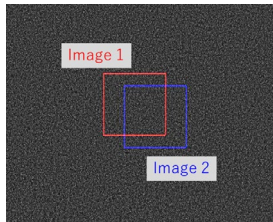

Fig.1. An example of images of speckle pattern used for subtraction process.

Then, the subtracted image, which has standard deviation of σ_{sub}, can be obtained by subtracting the intensity data matrix of the image 1 from the image 2. If both two images have uniform local intensity over the whole area of the image and same standard deviation, σ_{sub} is expressed as formula (2).

$$\sigma_{sub} = \sqrt{\sigma_1^2 + \sigma_2^2} = \sqrt{2}\sigma_1 \qquad (2)$$

This estimation can be established under the conditions; 1) Each speckle pattern is statistically random and independent, 2) in each local area of the image, the local average intensity is same, 3) the number of sampling pixels (i.e. the number of detector element to calculate the speckle contrast) is enough to reduce statistical error. Regarding 1), the theory to calculate the average speckle grain size is useful to estimate the minimum requirement of the displacement of each image. The average speckle size R is represented by the formula (3),

$$R = \frac{4}{\pi} F\#_{image}\, \lambda \qquad (3)$$

where, $F\#_{image}$ is an effective f-number of the imaging lens, λ is wavelength of the laser. R is defined as the FWHM of the auto-correlation function of the speckle pattern. Therefore, almost $3R$ of the distance between each extracted image would be enough to regard both extracted images independent. For the condition 2), the calibration method to suppress the local intensity variation was already established. Or, when such calibration is not applied, the deviation from the factor $\sqrt{2}$ in the formula (2) would occur. As for the condition 3), if the relative ratio of σ_2 to σ_1 is introduced as a statistical sampling factor α, the formula (2) would be changed as,

$$\sigma_{sub} = \sqrt{\sigma_1^2 + (\alpha\sigma_1)^2} = \sqrt{1+\alpha^2}\,\sigma_1 \qquad (4)$$

where, α is non-linear function and it would vary according to the imaging conditions and sampling pixels. α falls to 1 when the number of the sampling pixels is sufficiently large.

3. Experiments

3.1 Measurement setup

The measurement setup under suppressed speckle condition is shown in Figure 2. SHG laser (wavelength 533 nm) illuminated the rotating diffuser, making a spot about 1 cm diameter at 1.2 m away from the diffuse reflectance target, SRT-99-050 (Labsphere, Inc.). The measurement distance was fixed at 0.62m. The focal length of the imaging lens was 50mm at infinity, and imaging f-number was changed from 2.1 to 33.3. The cooled-CCD with 9 μm pixel pitch was used. In the section 3.2, low-frequency intensity variation was corrected by the method described in IEC 62906-5-4 to eliminate the influence from non-random components. The displacement of each extracted image was 30 pixels,

i.e. 270 μm on the CCD. The size of the extracted images was changed from 10×10 pixels to 200×200 pixels. As increasing the extracted image size, each image was partially overlapped.
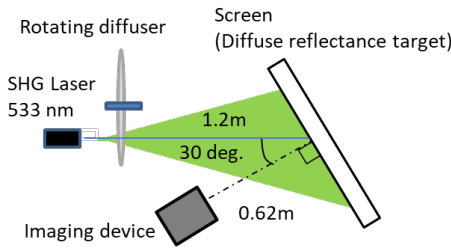

Fig.2. Measurement configuration of speckle contrast under suppressed speckle condition.

3.2 Measurement of suppressed speckle

Figure 3 shows the speckle contrast from each extracted image with various f-number. The factor σ_{sub} / σ_1 was also shown.
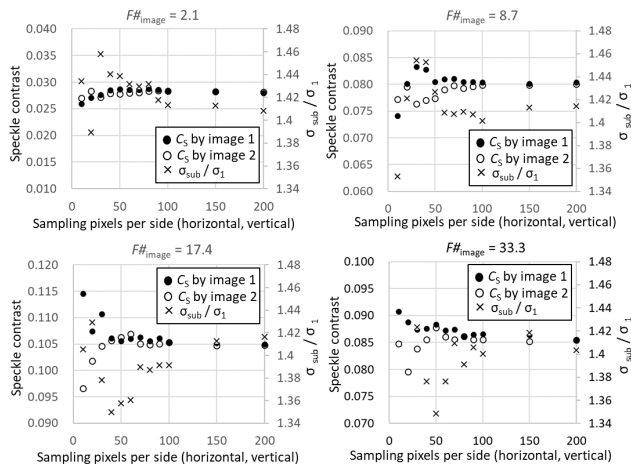

Fig.3. Speckle contrast and the factor σ_{sub} / σ_1 under different sampling pixels and f-numbers.

In all the cases, speckle contrast converged to the certain value around 200×200 pixels. At the same time, the factor σ_{sub} /σ_1 was also getting close to 1.414 ($\sqrt{2}$) in all f-numbers, i.e. α was close to 1. However, in terms of speckle contrast, the variation was different in each condition. To investigate this point in more detail, the relative deviation percentage to the converged value of speckle contrast C_{S-C} was investigated by using the formula (4),

$$\frac{C_{S-E} - C_{S-C}}{C_{S-C}} \times 100 (\%) \qquad (5)$$

where, C_{S-E} was speckle contrast under evaluation. As a value of C_{S-C}, average at 200×200 pixels was used. Figure 4 shows the results. In all the cases, relative deviation percentage was converged within 1% around 200×200 pixels, like the factor σ_{sub} /σ_1. These results showed that the statistical error of speckle contrast regarding the number of sampling pixels has a similar trend in all speckle contrast level, and the factor σ_{sub} /σ_1 can be used as an indicator of statistical error from the insufficient sampling pixels.
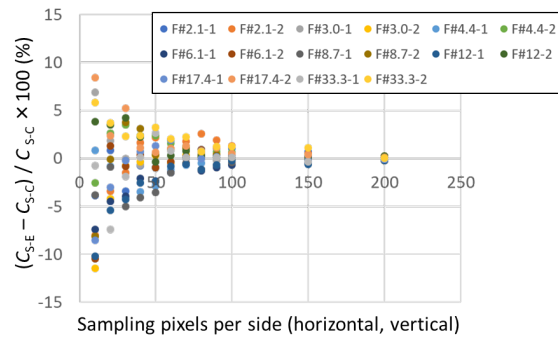

Fig.4. Relative deviation percentage of speckle contrast against its average value at 200 pixels per side.

3.3 Measurement of suppressed speckle without correcting low-frequency intensity variation

In this case, the condition 1) and 2) in the section 2.1 were not satisfied, even if the statistical error in condition 3) could be reduced enough. Figure 5 shows the speckle pattern (a) and speckle contrast (b) from each extracted image with f-number of 17.4 without correcting low-frequency intensity variation. The factor σ_{sub} / σ_1 was also shown in Figure 5 (b).
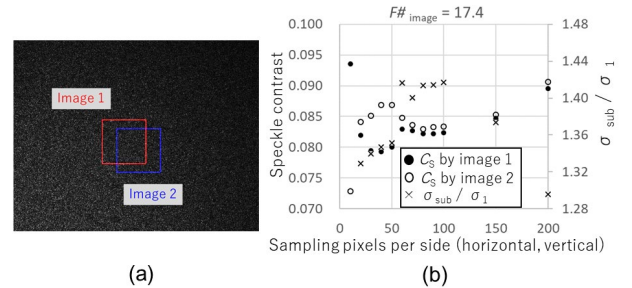

(a)　　　　　　　　　(b)

Fig.5. Speckle pattern without correcting low-frequency intensity variation (a), and speckle contrast and the factor σ_{sub} / σ_1 under different sampling pixels at f-number of 17.4 (b).

In this case, both speckle contrast and the factor σ_{sub} / σ_1 kept changing with increasing the sampling pixels. This is because the gradual intensity variation was counted in the standard deviation σ_1, although it was almost cancelled in σ_{sub} by the subtraction operation when each extracted image was close enough. In this case, the factor σ_{sub} /σ_1 could be used as an indicator of low-frequency intensity variation within the sampling field when the number of sampling pixels was large enough.

4. Conclusion

The measurement error of speckle contrast was investigated by using image subtraction method. The statistical error was suppressed enough when the sampling pixels were around 200×200 pixels. The factor σ_{sub} / σ_1 could be used as an indicator of both statistical error by insufficient sampling pixels and low- frequency intensity variation within the sampling field.

References
[1] J.W. Goodman, "Speckle Phenomena in Optics: Theory and Applications" (Roberts and Company Publishers, Colorado, 2006).
[2] IEC 62906-5-4, Laser display devices - Part 5-4: Optical measuring methods of colour speckle (2018).

LDC2020 | Oral Presentation
Imaging / Lighting -Speckle-
2020年4月22日(水) 09:00 〜 10:30　301 (Conference Center)

[LDC4-04] Improved Visual Resolution Measurement for Laser Displays Based on Eye-diagram Analysis of Speckle Noise

*Junichi Kinoshita[1], Akira Takamori[1], Kazuhisa Yamamoto[1], Kazuo Kuroda[2], Koji Suzuki[3], Keisuke Hieda[4]　(1. Osaka Universitry, 2. Utsunomiya University, 3. Oxide Corporation, 4. HIOKI E.E.CORPORATION）

Visual resolution measurement method under the effect of speckle noise is improved by considering eye-diagram analysis. Measurement is carried out using a raster-scan mobile laser projector. The speckle effects can be expressed more clearly.

Improved Visual Resolution Measurement for Laser Displays Based on Eye-diagram Analysis of Speckle Noise

Junichi Kinoshita[1], Akira Takamori[1], Kazuhisa Yamamoto[1],
Kazuo Kuroda[2], Koji Suzuki[3], Keisuke Hieda[4],
[1]Institute of Laser Engineering, Osaka University, 2-6 Yamada-oka, Suita, Osaka 565-0871, Japan,
phone number +81-6-6879-8958, fax number +81-6-6879-8958, and email jun1-istd@ile.osaka-u.ac.jp
[2] Center for Optical Research and Education, Utsunomiya University, [3] Oxide Corporation, [4] HIOKI E.E. CORPORATION

Abstract: *Visual resolution measurement method under the effect of speckle noise is modified and improved by considering eye-diagram analysis. Measurement results are discussed by comparing with the previous method using a raster-scan mobile laser projector. As a result, the speckle effects can be expressed more clearly harmonized with the eye-diagram analysis.*

1. Introduction

Monochromatic and color speckle measurements for display and lighting applications have been established and standardized [1-5]. Recently, visual resolution under effect of speckle noise has been discussed and measured in our previous works [6]. The term, "visual" is used because speckle is observed as a kind of random interference patterns on human retina, depending on human-eye optics. In other words, speckle is not patterns projected on a screen.

In our previous works, the contrast modulation, C_M under the effect of speckle for obtaining visual resolution was simply formulated using the averages of speckle along the grille pattern. From a viewpoint of noise analysis, a condition was added as C_M value must be set zero if the C_M is buried in speckle noise. However, we have found this formulation is not good enough from a viewpoint of error-rate analysis. The error-rate of distinguishing the white or the black level must be formulated considering how much narrowing eye diagram.

In this work, an improved formulation harmonized with narrowing eye-diagram is presented. The measured visual resolution data using a raster-scan mobile laser projector are also presented here. Grille patterns of equi-width line-pairs are projected in turn changing the width.

2. Measurement of speckled grille patterns

2.1 Measurement setup

Measurement setup is shown in Fig.1. The grille patterns of equi-width line-pairs were projected on a standard diffusive screen, SRT-99-120 (Labsphere) using a raster-scan RGB mobile laser projector, Celluon PicoBit (R: 644nm, G: 519nm, B: 446nm).

Three grille patterns of vertical line pairs with widths corresponding to 3.77, 1.88, and 1.0 pixels were prepared based on the pixel resolution of the laser projector, 16:9, 1280×720 pixels (for input signal).

The 2D data (300×300) of the projected speckled grille patterns were obtained by speckle measurement equipment, SM01VS11 (Oxide Corporation) [7]. The layout dimensions are L=390mm, D=710mm, and θ=20.6º.
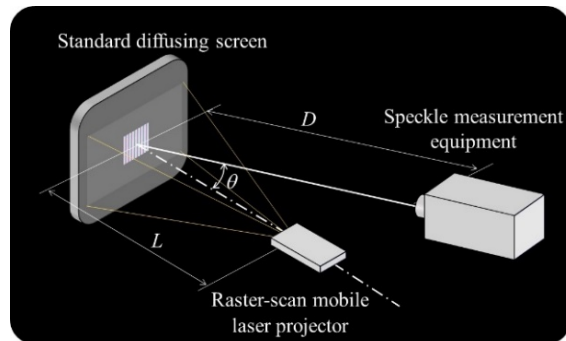

Fig. 1. Measurement setup.

2.2 Measured results

CIE 1931 white chromaticity (x, y) = (0.3059, 0.2964), photometric speckle contrast C_{ps}= 0.038 (where C_{s-R} = 0.072, C_{s-G} = 0.041, C_{s-B} = 0.111) were obtained in the central large window area using an RGB laser-meter, TM6102 (HIOKI E.E. CORPORATION). The 2D-grille pattern illuminance data are shown in Fig.2 for 3.77, 1.88, and 1.0 pixels.
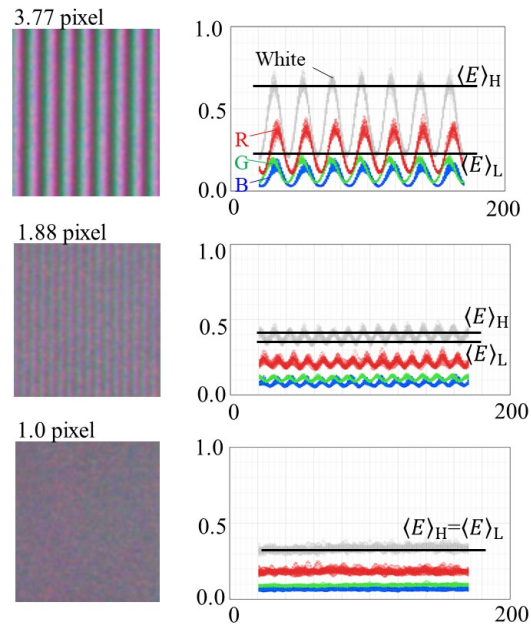

Fig. 2. Speckled 2D grille pattern data for 3.77, 1.88, and 1.0 pixels.

The averages of the local maxima and the local minima of the measured grille pattern plots in Fig.2 are defined as $\langle E \rangle_H$ and $\langle E \rangle_L$, respectively. The eye-diagram plots of the right-side plots in Fig.2 are shown in Fig. 3. The graph-plots of white/black in Fig.2 are expressed together with their antiphase black/white plots. Most of the speckle noise exit within $\pm \langle E \rangle_{H,L} C_{ps}$ because C_{ps} is standard deviation. From a viewpoint of white/black error-rate, the eye-diagram in Fig.3 must be more widely open for lower error rate, distinguishing the 2D data whether white or black. For 1.0 pixel, the white/black levels could not be distinguished.
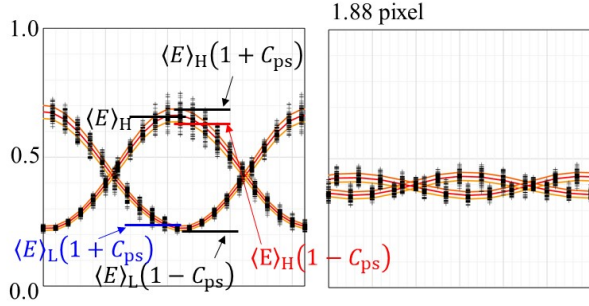

Fig. 3. Eye-diagram plots.

3. Formulation of modulation contrast C_M

3.1 Previous formulation

In our previous work [6], contrast modulation C_M under speckle effects was defined as:

$$C_M = \frac{\langle E \rangle_H - \langle E \rangle_L}{\langle E \rangle_H + \langle E \rangle_L}$$

$$C_M = 0, \ for \ C_M \leq C_{ps}$$

(1)

The second line of the above equation implies that contrast modulation C_M is buried in the speckle noise.

3.2 Modified formulation

The previous definition of C_M under speckle effects is modified considering the eye-diagram analysis method in Fig.3. The new definition is expressed as follows.

$$C_{M(New)} = \frac{\langle E \rangle_H (1 - C_{ps}) - \langle E \rangle_L (1 + C_{ps})}{\langle E \rangle_H (1 - C_{ps}) + \langle E \rangle_L (1 + C_{ps})} = \frac{C_M - C_{ps}}{1 - C_M C_{ps}}$$

(2)

The above formulation is consistent with the condition of Equation (1) ($C_M = 0$ for $C_M = C_{ps}$) as well as harmonized with the eye-diagram analysis.

4. Results of C_M-plot and visual resolution

The $C_{M(New)}$ values calculated by Equation (2) are plotted a thick solid line in the graph on the left side of Fig.4. The C_M values calculated by Equation (1) are plotted as a thin solid line also in the same graph. The C_M values without speckle effects are plotted in the graph on the right side of Fig.4. The unspeckled data were obtained by fully opening the iris of the speckle measurement equipment [3]. It should be noted that those data do not mean visually

sensed by human-eye optics because the MTF of the optics of the measurement equipment is not equivalent to human-eye anymore. The graph on the right side is just for reference.
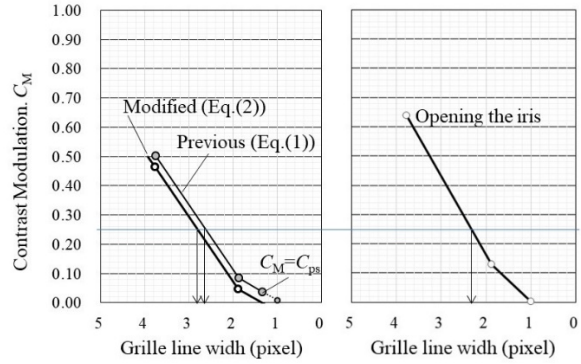

Fig. 4. C_M-plots
(Speckled: Left, Unspeckled: Right).

For image displays, the resolution criterion was $C_M=0.25$. The modified visual resolution was estimated to be 2.80 pixel, a little worse than the previous estimation of 2.63 pixel. For reference, the resolution when opening the iris was estimated to be 2.33 pixel.

5. Conclusions

The modified formulation of contrast modulation C_M under speckle effects is harmonized with white/black error-rate analysis using eye-diagram, including the previous noise-buried case. As a result, visual resolution is successfully obtained.

References

[1] K. Kuroda, T. Ishikawa, M. Ayama, S. Kubota, "Color speckle", Optical Review **21** (1), 83-89 (2014).

[2] S. Kubota, "Simulating the human eye in measurements of speckle from laser-based projection displays", App. Opt. **53**(17), 3814 (2014).

[3] J. Kinoshita, K. Ochi, A. Takamori, K. Yamamoto, K. Kuroda, K. Suzuki, K. Hieda, "Color speckle measurement of white laser beam emitted from fiber output of RGB laser modules", Optical Review **26** (6), 720-728 (2019).

[4] IEC 62906-5-2: Laser display devices - Part 5-2: Optical measuring methods of speckle contrast (2016).

[5] IEC 62906-5-4: Laser display devices - Part 5-4: Optical measuring methods of colour speckle (2018)

[6] J. Kinoshita, K. Yamamoto, A. Takamori, K. Kuroda, K. Suzuki, "Visual resolution of raster-scan laser mobile projectors under effects of color speckle", Opt. Rev. **26**(1), 187–200 (2019).

[7] K. Suzuki, S. Kubota, "Understanding the exposure-time effect on speckle contrast measurements for laser displays", Optical Review **25** (1), 131-139 (2018).

Imaging / Lighting -Speckle-

2020年4月22日(水) 09:00 ～ 10:30 301 (Conference Center)

[LDC4-05] Study on Projection Screen and Speckle Contrast in Laser Display Technology

*Yuwei Fang[1], Linxiao Deng[1], Chun Gu[1], Lixin Xu[1]   (1. University of Science and Technology of China)

We have promoted and demonstrated a relationship between speckle contrast and the fluctuation of the screen surface. We used the step profiler to measure the height and surface topography of 12 kinds of screens and meanwhile built a speckle testing platform to simulate human eye.

Study on Projection Screen and Speckle Contrast in Laser Display Technology

Yuwei Fang [1], Linxiao Deng [1], Chun Gu [1], Lixin Xu [1]

Author	Yuwei Fang	Linxiao Deng	Chun Gu	Lixin Xu (Corresponding author)
Email address	ywfang@mail.ustc.edu.cn	dlx2988@mail.ustc.edu.cn	guchun@ustc.edu.cn	xulixin@ustc.edu.cn
Affiliation	[1]Department of Optics and Optical Engineering, University of Science and Technology of China, Hefei, China			

Abstract: *We have promoted and demonstrated a relationship between speckle contrast and the fluctuation of the screen surface. We used the step profiler to measure the height and surface topography of 12 kinds of screens and meanwhile built a speckle testing platform to simulate human eye.*

1. Introduction

Since laser has been invented 60 years ago, its applications has been entered in plenty of fields, such as laser communication, spectroscopy, optical imaging and display technology. For many years, Laser Display Technology (LDT), has been the focus of many scientist. LDT used laser as light source which had remarkable advantages such as high saturation, big color gamut, high luminance and long life [1, 2]. Nevertheless, there are also a lot of problems corresponding to LDT, and one of the most annoying issues was laser speckle. Laser speckle was an inevitable problem in laser projection display due to its high coherence. The appearance of laser speckle would make the original gorgeous and clear picture appear irregular "particles", which would seriously affect the quality of the projection picture [3].

In LDT, the viewer obtains the image by receiving the diffuse light on the screen, so the screen has a great influence on the quality of the projected image [4]. In this paper, we simulated the human eye by building a testing platform, and studied the speckle characteristics of the screen used for LDT by measuring the height and surface topography of 12 kinds of screens.

2. Experimental setup

As an important part of LDT, projection screen could be divided into many types. According to the material of the surface, the screens are divided into Glass Theater Curtain (GTC), Metal Screen (MS), White Plastic Curtain (WPC), etc. In LDT, the roughness of the screen affects the speckle contrast. If the speckle contrast is too large, there would be obvious grainy noise on the picture, which could seriously reduce the projection quality. In our experiment, we measured the surface characteristics of different types of screens and focused on their surface topography and fluctuation height.

3. Results and discussions

In measurement, we selected 12 different screens and numbered them separately. As shown in Table 1, screens from No. 1 to No. 6 were low gain WPCs. Screens from No. 7 to No. 12 were high gain screens, in which screens from No. 7 to No. 10 were GTCs while No. 11 and No.12 represented MSs. In order to accurately measure the surface topography and fluctuation height of the above screens, we chose the Dektak XT step profiler as the measuring instrument. With this step profiler, we could

Table 1. Screen numbers and Gain values

Low Gain (WPC)		High Gain (GTC & MS)		
Number	Gain	Number	Gain	
1	0.85	7	2.2	GTC
2	0.9	8	1.7	
3	0.9	9	1.8	
4	0.8	10	2.4	
5	1	11	1.8	MS
6	1.2	12	1.4	

measure the surface roughness of nanoscale samples, as well as measure and analyze the three-dimensional topography of the samples.

We have analyzed the fine surface height data in a certain area on each 12 screens and obtained the 3D surface topography characteristic graphs. The measuring results of part of the testing screens was shown below. Fig. 1, Fig. 2 and Fig. 3 provided the results of three screens numbered 3, 8 and 12 separately. As illustrated in these figures, it could be seen that the surface topography of different types of screens varied greatly. The surface of the low gain WPC was typical random fluctuation topography, which meant that the raised "particles" appeared evenly on the surface. However, the surface topography of high gain GTC was obviously different from that of WPC. The
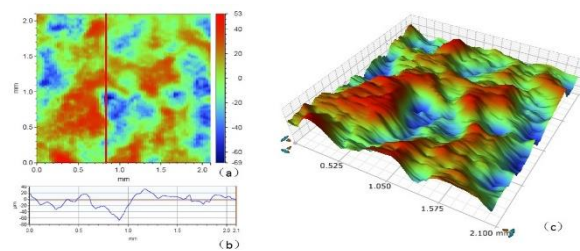

Fig. 1. The testing graph of No. 3 screen. a) 2D profile; b) 1D height graph at the red line; c) 3D surface topography.
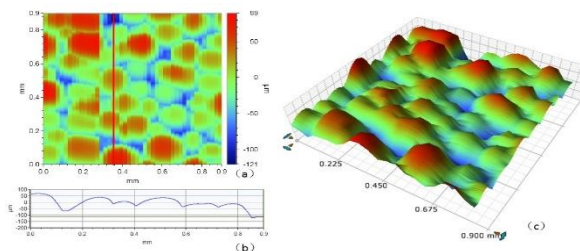

Fig. 2. The testing graph of No. 8 screen. a) 2D profile; b) 1D height graph at the red line; c) 3D surface topography.
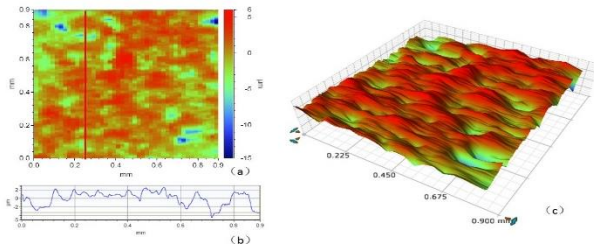
Fig. 3. The testing graph of No. 12 screen. a) 2D profile; b) 1D height graph at the red line; c) 3D surface topography.

surface was covered with microspheres of different sizes, namely glass beads. As for high gain MS, its surface fluctuation was relatively average, and a large area of same color appeared in 2D profile. So as a conclusion, we could say that the surface topography of different screens varied greatly, due to different substrate, spraying way, spraying material and other physical characteristics of the screens.

These properties mentioned above affected not only the performance parameters of the screen, but also influenced the speckle contrast of the image in laser display system. For studying the relationship between surface topography of screens and speckle contrast, we established a speckle measuring system simulating human eye to obtain the speckle contrast of each screen. As shown in Fig. 4(a), we chose ARTCAM-274KY-C CCD
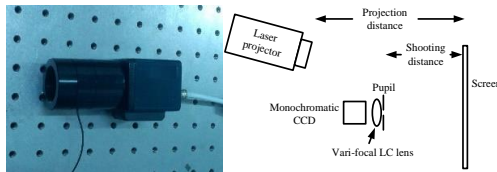

Fig. 4. a) CCD camera with liquid crystal lens; b) Speckle measuring system.

camera as speckle detector, with pixel size of 4.4 μm × 4.4μm and integration time of 40 ms. Fig. 4(b) showed that the projection distance, the detection distance and the lens distance was 3m, 1m and 40 mm, respectively.

Using this measuring system, we have obtained the relationship between speckle contrast and standard deviation of surface fluctuation height of 12 screens. As illustrated in Table 2, C represented the speckle contrast

Table 2. Speckle contrast and standard deviation of surface fluctuation height of 12 screens

Number	C/%	σ_h	Number	C/%	σ_h
1	2.77	12.05	7	3.14	36.55
2	2.90	15.03	8	3.35	32.96
3	2.98	19.67	9	4.67	37.60
4	3.11	17.37	10	3.55	40.83
5	5.05	1.57	11	4.84	11.11
6	6.29	1.77	12	7.81	2.12

of each screen and calculated by:

$$C = \frac{\sigma_s}{\bar{I}_s} = \frac{\sqrt{\frac{1}{N}\sum(I_n - \bar{I})^2}}{\bar{I}} \qquad (1)$$

in which N, I_n and $\bar{I}$ stand for total pixels, light intensity measured at each pixel and average light intensity, respectively. σ_h was calculated by:

$$\sigma_h = \sqrt{\frac{1}{N}\sum(h_i - \bar{h})^2} \qquad (2)$$

where N, h_i and $\bar{h}$ represented the total number of measuring points, the surface height of each pixel and the average height of all pixels. From Table 2 we could get that in WPCs and MSs, screen with smaller σ_h should correlate to higher C. While in GTCs, their smaller σ_h didn't reduce C, which could be attributed to the structure of glass beads. Therefore, the GTCs were excluded from the following analysis.

While σ_h was larger than the wavelength scale, there would be an approximate linear relationship between C and $\sqrt{\sigma_h}$ [4]. Fig, 5 showed the linear fitting of C and $1/\sqrt{\sigma_h}$, which would provide an estimation method of speckle characteristics of different screens.
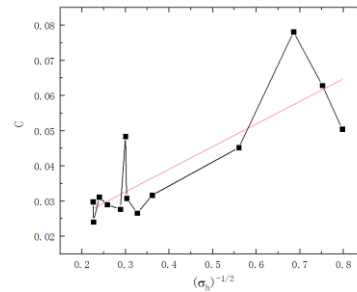

Fig. 5. Linear fitting of C and $1/\sqrt{\sigma_h}$.

4. Conclusions

In conclusion, we used a precise step profiler to measure the surface fluctuation and topography of three kinds of projection screens: WPC, GTC and MS, and established a speckle contrast testing system simulating human eye, and consequently obtained the relationship between speckle contrast and surface fluctuation of 12 screens. Therefore, under the guidance of theory, we could choose a more optimal projection screen suitable for laser display technology.

References

[1] E. C. Baker, "Laser display technology", IEEE Spectrum, 1968, 5(12): 39-50.
[2] A. Neumann, J. J. Wierer, W. Davis, Y. Ohno and J. Y. Tsao, "Four-color laser white illuminant demonstrating high color-rendering quality", Opt. Express. 19(S4): 982-990 (2011).
[3] J. W. Goodman, "Some fundamental properties of speckle", JOSA, 66(11): 1145-1150 (1976).
[4] J. W. Goodman, "Statistical properties of laser speckle patterns: Laser Speckle and Related Phenomena", Vol 9. Heidelberg: Springer Berlin, 9-75 (1975).

LDC2020 | Oral Presentation

Imaging / Lighting -Display Technologies-

Session Chair: Satoshi Ouchi(Hitachi)

Wed. Apr 22, 2020 10:45 AM - 12:30 PM 301 (Conference Center)

[LDC5-01] A laser backlight liquid crystal display achieving a BT.2020 wide color gamut

*Koichi Okuda[1], Shinichi Komura[1], Ken Onoda[1], Hiroaki Kijima[1] (1. Japan Display Inc.)

10:45 AM - 11:15 AM

[LDC5-02] Aerial Display Opens a New Field of Biology

*Hirotsugu Yamamoto[1,2], Erina Abe[1], Masaki Yasugi[1,2], Eiji Watanabe[3], Hideaki Takeuchi[4] (1. Utsunomiya University, 2. JST, ACCEL, 3. National Institute for Basic Biology, 4. Tohoku University)

11:15 AM - 11:45 AM

[LDC5-03] Near-eye CGH display with Holographic Waveguide Element

*Wei-Chia Su[1], Wen-Kai Lin[2], Shao-Kui Zhou[2], Bor-Shyh Lin[2] (1. Graduate Institute of Photonics, National Changhua University of Education, 2. College of Photonics, National Chiao Tung University)

11:45 AM - 12:15 PM

[LDC5-04] Effective Speckle Reduction Method Based on a Rotating Ball Lens

*Linxiao Deng[1], Yuwei Fang[1], Yuhua Yang[1], Tianhao Dong[1], Chun Gu[1], Lixin Xu[1] (1. University of Science and Technology of China)

12:15 PM - 12:30 PM

LDC2020 | Oral Presentation

Imaging / Lighting -Display Technologies-

2020年4月22日(水) 10:45 ～ 12:30 301 (Conference Center)

[LDC5-01] A laser backlight liquid crystal display achieving a BT.2020 wide color gamut

*Koichi Okuda[1], Shinichi Komura[1], Ken Onoda[1], Hiroaki Kijima[1] （1. Japan Display Inc.）

The developed laser backlight liquid crystal display covers 98% of the color gamut of BT.2020. In addition, the speckle problem is solved by applying an AC voltage to the laser diodes.

A laser backlight liquid crystal display achieving a BT.2020 wide color gamut

Koichi Okuda, Ken Onoda, Hiroaki Kijima, Shinichi Komura

R&D Division, Japan Display Inc., 3300, Hayano, Mobara-shi, Chiba-ken, 297-8622 Japan
Tel: +81-475-25-9009, Fax: +81-475-26-3990
E-mail: koichi.okuda.dt@j-display.com

Abstract: *A BT.2020 wide color gamut is obtained using a laser backlight liquid crystal display (LCD). The developed laser backlight LCD covers 98% of the color gamut of BT.2020. In addition, the speckle problem is solved by applying an AC voltage to the laser diodes.*

1. Introduction

In Japan, Nippon Hoso Kyokai (NHK) began broadcasting Super Hi-Vison with ultra-high-definition videos in December 2018. The specifications of the Super Hi-Vison are defined by the International Telecommunication Union Radiocommunication Sector (ITU-R), Recommendation BT.2020 [1]. The BT.2020 color gamut covers 99.9% of the Pointer's color gamut, which is the maximum gamut of real object colors [2].

The BT.2020 color gamut is defined by the three primary colors of a monochrome. Therefore, changing the light source of a liquid crystal display (LCD) from conventional LEDs to lasers is necessary, because the three primary colors are only possible through lasers. Previous studies indicate that LCDs containing laser backlights with laser diodes as the light source satisfy the BT.2020 color gamut [3-6].

2. Laser backlight

We developed a double light guide plate laser backlight illustrated in Fig.1. In this side-edge laser back light, the two light guide plates are stacked. The light emitted from each laser diode is transmitted in the x direction. The light incident surface of each light guide plate is concave. The light guide plate comprises light-mixing, and light-emitting areas. Two issues arise if a conventional light guide plate is utilized for a laser backlight [5,6]. First, the luminance gradually increases from the light incident side to the opposite side, thereby introducing a luminance gradient. Secondly, dark spots appear periodically near the laser diodes. In our laser backlight, the luminance gradient is eliminated by the concave shape, while dark spots are prevented by the light-mixing area. Each light-mixing area overlaps the light-emitting area of other light guide plates. Therefore, the double light guide plate laser backlight does not require a wide bezel for the light-mixing area. The same
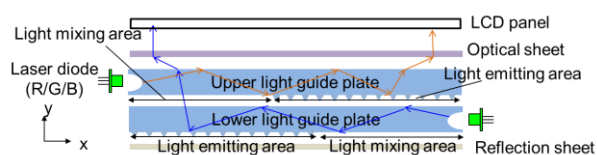
light guide plates overlap in the opposite direction in the developed laser backlight.

In the developed laser backlight, the light emitted from the lower light guide plate is transmitted to the upper light guide plate. The upper light guide plate may, therefore, affect the light emitted from the lower light guide plate, especially in the middle part along the x direction of the backlight where prisms are present in the upper light guide plate. These may affect the light emitted from the lower light guide plate. To assess this, we performed a numerical simulation. We designed the luminance distribution due to each light guide plate with line symmetry and uniform summation. The results are shown in Fig. 2. The luminance distributions due to the upper light guide plate (1), lower light guide plate (2), both light guide plates, and the summation of (1) and (2) are plotted as a function of position x. The luminance distribution due to both light guide plates is almost identical to the summation of the luminance distributions of the upper and lower light guide plates. This suggests that the upper light guide plate does not affect the light emitted from the lower light guide plate. Light emitted from the lower light guide plate is considered unaffected by the prism of the upper light guide plate, since the prisms are fabricated with low density.
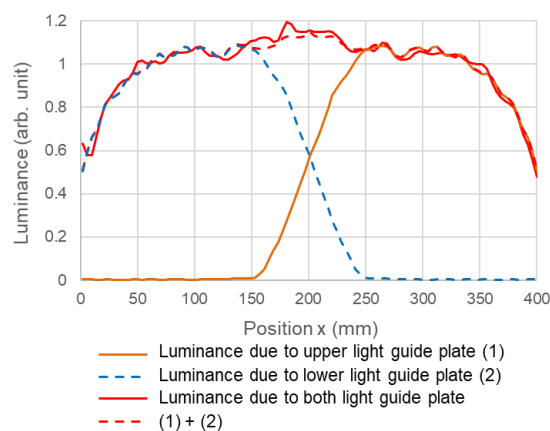

Fig.2. Simulation results of the luminance distribution.

Fig.1. Side view of the developer laser backlight.

3. Speckle

One of the problems of a laser backlight is speckle. Speckle is a glare generated by the coherence of laser light, which degrades display quality. Previous studies suggest that speckles are suppressed by AC driving because it decreases the coherence of lasers [7]. We confirmed that speckles depend on the frequency of the voltages applied to laser diodes. With DC driving, the speckles become worse, and improved as the frequency changed from 50 to 300 Hz but deteriorated again above 1kHz. Fig.3 shows the measured chromaticity of a red laser diode driven at different frequencies. The chromaticity shifts while the speckle is better, suggesting that the spectrum changes and coherence decreases from 50 to 300 Hz.
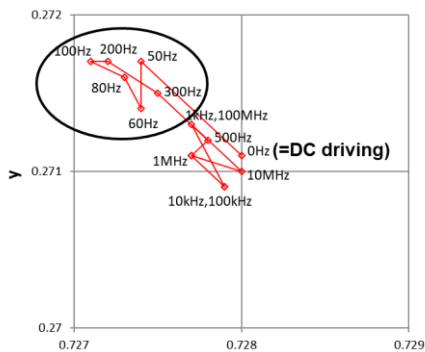

Fig.3. Chromaticity for a red laser with AC driving.

Since the flicker occurred at a frequency below 100 Hz, we selected 100 Hz as the frequency. Fig.4 shows observation results for the developed laser backlight with DC driving and 100 Hz driving, respective. These photographs taken with green lasers show that speckles are reduced by applying 100 Hz driving.
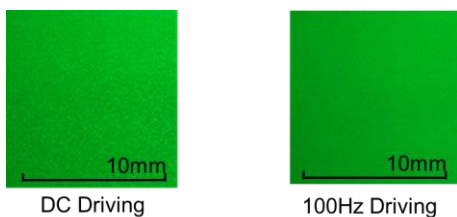

Fig.4. Results for observation of speckles
for the laser backlight with DC and 100 Hz driving.

4. Laser backlight LCD

Fig.5 shows the color gamut in CIE 1931 color coordinates of the developed laser backlight LCD and BT.2020. The developed laser backlight LCD covers 98% of the color gamut of BT.2020 with a narrow bezel, using the developed laser backlight and appropriate color filters [5,6].
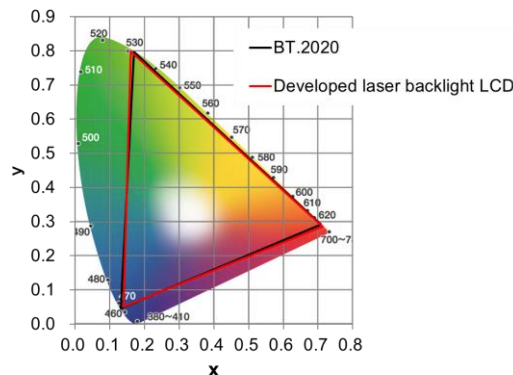

Fig.5. Color gamut in CIE 1931 color coordinates.

5. Conclusions

A laser backlight LCD is necessary for achieving a BT.2020 wide color gamut. We introduced a double light guide plate type laser backlight LCD in this study. We achieved a narrow-bezel laser backlight with uniform luminance. The developed laser backlight LCD covers 98% of the color gamut of BT.2020. In addition, the speckle problem was solved by applying an AC voltage to the laser diodes.

References

[1] Rec. ITU-R BT.2020, "Parameter Values For Ultra-High Definition Television Systems For Production And International Programme Exchange," (2012).

[2] K. Masaoka, Y. Nichida, M. Sugawara, and E. Nagasu, "Design of Primaries for a Wide-Color Gamut Television Colorimetry," IEEE Trans. Broadcast., Vol. 56, No. 4, pp.452-457 (2010).

[3] I. Hiyama, R.Oke, K. Miyazaki, J. Maruyama, N. Sato, T. Kato, and A. Hirota, "The latest IPS-LCD Technology realizing Super High Resolution and Wide Color Gamut," Proc. IDW'15, pp.8-11(2015).

[4] E. Niikura, N. Okimoto, S. Maeda, H. Yasui, A. Heishi, S. Yamanaka, T. Sasagawa, Y. Nishida, Y. Kusakabe, "Development RGB Laser Backlit Liquid Crystal Display," Proc. IDW'15, pp.1096-1099(2015).

[5] Y. Asakawa, K. Onoda, H. Kijima, S. Komura, "17-inch 8K 120-Hz driving and BT.2020 color gamut LCDs with laser backlights," Proc. SPIE 10943 (2019).

[6] Y. Asakawa, K. Onoda, H. Kijima, S. Komura, "17-inch Laser Backlight LCD with 8K, 120-Hz Driving and BT.2020 Color Gamut," Proc. IDW'19, pp.265-268 (2019).

[7] T. Nishida, T. Yagi, H. Murata, A. Koizumi, "Speckle Reduction by Optimizing Pulse Width of Drive Current for Red Laser Diodes," Proc. IDW '14, pp.1098-1101 (2014).

LDC2020 | Oral Presentation
# Imaging / Lighting -Display Technologies-
2020年4月22日(水) 10:45 ～ 12:30 301 (Conference Center)

[LDC5-02] Aerial Display Opens a New Field of Biology

*Hirotsugu Yamamoto[1,2], Erina Abe[1], Masaki Yasugi[1,2], Eiji Watanabe[3], Hideaki Takeuchi[4] （1. Utsunomiya University, 2. JST, ACCEL, 3. National Institute for Basic Biology, 4. Tohoku University）

This paper introduces our developments on aerial displays. We have realized an omni-directional aerial display with aerial imaging by retro-reflection. The developed display is utilized for behavioral biology experiments, such as optomotor reaction.

Aerial Display Opens a New Field of Biology

Hirotsugu Yamamoto*[1, 2)], Erina Abe[1)], Masaki Yasugi[1, 2)], Eiji Watanabe[3)], Hideaki Takeuchi[4)]

[1)] Utsunomiya University, 7-1-2 Yoto, Utsunomiya, Tochigi 321-0904, Japan,
[2)] JST, ACCEL, 7-1-2 Yoto, Utsunomiya, Tochigi 321-0904, Japan,
[3)] National Institute for Basic Biology, 38 Nishigonaka, Myodaiji, Okazaki, Aichi 444-8585, Japan,
4) Tohoku University, 2-1-1 Katahira, Aoba-ku, Sendai, Miyagi 980-8577, Japan.
* Tel: +81-28-689-7074; email: hirotsugu@yamamotolab.science

Abstract: *This paper introduces our developments on aerial displays. We have realized an omni-directional aerial display with aerial imaging by retro-reflection. The developed display is utilized for behavioural biology experiments, such as optomotor reaction. A medaka in the water tank followed to the rotating stripes shown on the surrounding screen.*

1. Introduction

This paper proposes a novel application of aerial display, which forms information screen in the mid-air. The information screen is formed with aerial imaging by retro-reflection (AIRR) [1]. AIRR features a wide viewing angle, a large-size scalability, and a low cost with mass-productive process. Aerial 3D display can be realized by use of multi-layered images [2, 3]. By use of a cone-shaped beam splitter and a flat panel display (FPD), we have formed an omni-directional information screen that surrounds a cylindrical water tank. We have utilized this omni-directional display to show visual stimuli for fish in a cylindrical water tank. We have conducted experiments on optomotor reaction and also fighting reaction of fish.

2. Aerial Imaging by Retro-Reflection (AIRR)

AIRR employs three elements, which are a light source, a beam splitter, and a retro-reflector. We have utilized retro-reflector to converge the lights emitted from a display in the mid-air. Fundamental setups of AIRR is shown in Fig. 1. The light emitted from a light source is reflected on a beam splitter and impinges the retro-reflector. Retro-reflected light reversely travels the optical paths. The retro-reflected light that transmits through the beam splitter converges to the aerial image position, which is the plane-symmetrical position of the light source position regarding the beam splitter.
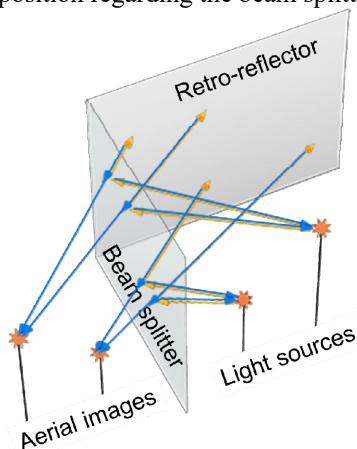
3. Omni-Directional Aerial Display

Our proposed optical design employs a cone-shape beam splitter to form an omnidirectional aerial image. As illustrated in Fig. 2, a cross-section of the optical system is consisted of the conventional AIRR. Thus, an aerial image formed cylindrically and surrounds the central viewing region. The light transmitted through the beam splitter also converges to the aerial image when we install a retro-reflector on the upper surface. Thereby, the luminance of the aerial image increases. In addition, the retro-reflector on the upper surface also performs a barrier to block the ambient light and improves the contrast of the aerial image.

A liquid-crystal display (LCD) panel can be used for the light source on the bottom of the optical system, as shown in Fig. 3. In order to observe the omnidirectional image from the central region, we used an omnidirectional camera (RICOH THETA). Fig. 4 shows observed results. Note that the displayed image on the LCD panel is shown in Fig. 3. We have successfully confirmed omnidirectional aerial image formation.

Because the cone-shaped beam splitter maps the FPD surface to a cylindrical surface, geometrical transformation has been performed to show images on the cylindrical surface [4]. The transformation is expressed by polar coordinate system.

For the experiments, two crossed-louver filters covered the LCD panel so that the displayed image surface is invisible inside the cylindrical screen (Fig. 5).

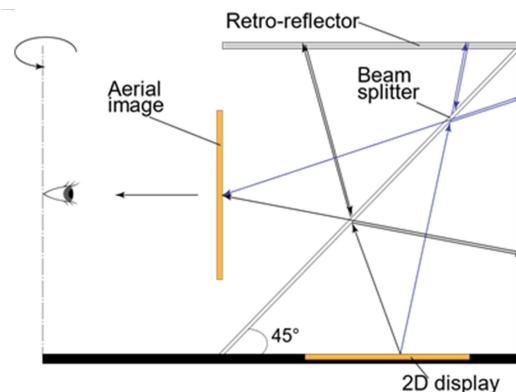Fig. 1. Principle of aerial imaging by retro-reflection.

Fig. 2 Principle of omni-directional aerial display.
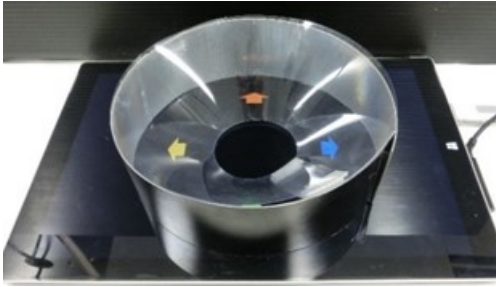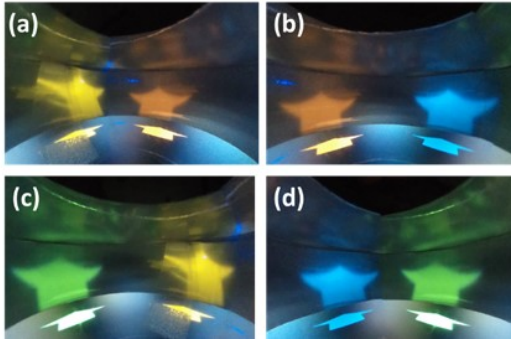
Fig. 3 Developed omnidirectional display apparatus.

Fig. 4. Viewed results in the four shooting directions.

Fig. 5. Viewed images (a) without and (b) with crossed crossed-louver filters.

4. Application of Aerial Display for Behavioural Biology Experiments

The formed omni-directional aerial screen surrounds a cylindrical water tank where fish swims. We have performed opto-motor reaction experiments on Medaka (Japanese rice fish), which is a model organism and is extensively used in many areas of biological research, most notably in toxicology. Medaka have a short gestation period. Nearly all aspects of the life cycle of medaka have been analyzed by researchers including sexual behavior, genetic inheritance of coloration, spawning habits, feeding, pathology, embryological development, ecology, etc.

We showed stripes on the omni-directional aerial display. The stripes rotated clockwise and counter-clockwise. Fig. 6 (a) and (b) show the opto-motor reaction of Medaka. The Medaka followed the rotation.

Furthermore, we have investigated reactions of Betta (Siamese fighting fish) to the aerial images. Experimental results are shown in Fig. 7. The male Betta showed a fighting behavior called flaring when he was surrounded by male Betta images rotating around the water tank.

Our developed system enables researchers to make the stimulus image in 2D image format. For example, it is possible to investigate the boundary of a female Betta and a male Betta with computer graphics.

Fig. 6. Opto-motor reactions of Medaka when stripes (a) in clockwise rotation and (b) in counterclockwise rotation were shown on the omni-directional aerial display.
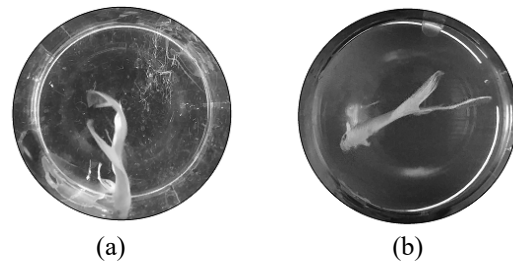

Fig. 7. Reactions of male Betta when (a) female Betta images and (b) male Betta images were shown on the omni-directional aerial display.

5. Conclusion
We have realized an omni-directional aerial display by mapping a FPD image to a cylindrical shape with AIRR. The developed aerial display has been utilized for behavioral biology experiments.

References
[1] H. Yamamoto, Y. Tomiyama, and S. Suyama, "Floating aerial LED signage based on aerial imaging by retro-reflection (AIRR)," *Optics Express* **22**, 26919-26924 (2014).
[2] K. Uchida, S. Ito, H. Yamamoto, "Multi-Functional Aerial Display by Use of Polarization-Processing Display," *Optical Review* **24**, 72-79 (2017).
[3] Y. Terashima, S. Suyama, H. Yamamoto, "Aerial depth-fused 3D image formed with aerial imaging by retro-reflection (AIRR)," *Optical Review* **26**, 179–186 (2019).
[4] E. Abe, M. Yasugi, H. Takeuchi, E. Watanabe, Y. Kamei, H. Yamamoto, "Development of omnidirectional aerial display with aerial imaging by retro-reflection (AIRR) for behavioral biology experiments," *Optical Review* **26**, 221–229 (2019).

LDC2020 | Oral Presentation

Imaging / Lighting -Display Technologies-

2020年4月22日(水) 10:45 ～ 12:30 301 (Conference Center)

[LDC5-03] Near-eye CGH display with Holographic Waveguide Element

*Wei-Chia Su[1], Wen-Kai Lin[2], Shao-Kui Zhou[2], Bor-Shyh Lin[2] （1. Graduate Institute of Photonics, National Changhua University of Education, 2. College of Photonics, National Chiao Tung University）

The near-eye holographic display systems based on waveguide type holographic combiners are analyzed. The astigmatism aberration will be induced by the holographic waveguide combiner. The astigmatism performance can be predicted with the ray-tracing technology and it can be verified experimentally. Astigmatism induced by the holographic waveguide element is corrected by using an improved iteration CGH algorithm.

Near-eye CGH display with Holographic Waveguide Element

Wei-Chia Su[1],[*], Wen-Kai Lin[2], Shao Kui Zhou[2], and Bor-Shyh Lin[2]

[1],[*]*Graduate Institute of Photonics, National Changhua University of Education, No. 1, Jin-De Road, Changsha City 50007, Taiwan*
[2]*College of Photonics, National Chiao Tung University, No.301, Gaofa 3rd Rd., Tainan City 71150, Taiwan*
Author e-mail address: wcsu@cc.ncue.edu.tw

Abstract: *The near-eye holographic display systems based on waveguide type holographic combiners are analyzed. The astigmatism aberration will be induced by the holographic waveguide combiner. The astigmatism performance can be predicted with the ray-tracing technology and it can be verified experimentally. Astigmatism induced by the holographic waveguide element is corrected by using an improved iteration CGH algorithm.*

1. Introduction

In order to provide natural 3D images, many teams focus on head-mounted displays (HMD) based on computer-generated hologram (CGH) technology in recent years. Among them, the holographic waveguide is a suitable element to be the combiner because of the lightweight. Generally, a pair of symmetric HOEs is employed to be the in-coupling element and out-coupling element. In this case, the waveguide element causes astigmatism which is independent of the distance of images [1]. On the other hand, replacing the in-coupling HOE with a geometric structure can enhance energy efficiency. However, the asymmetric structure causes the anamorphic effect and astigmatism which is dependent on the distance of images [2]. In this paper, we reviewed the above combiners and analyzed the aberration.

2. Holographic waveguide combiner

In this paper, the holographic waveguide combiners based on the asymmetric structure as shown in Fig. 1(a) and the symmetric case as shown in Fig. 1(b) were discussed. The information light in the asymmetric structure was coupled into waveguide via a wedge surface and coupled out via a HOE.

In the symmetric structure, the information light couple-in and couple-out via a pair of symmetric HOEs with same period. The phase-only spatial light modulator (SLM) and the probe beam were utilized to provide the information light. The lights will be redirected at the in-coupling surface and the out-coupling surface. However, the angle variations in the x-z plane and the y-z plane are different. It caused serious astigmatism in these two cases.

3. Aberration analysis and correction

In order to correct astigmatism, the aberration was analyzed via ray-tracing software Zemax. An intermediate image with astigmatism can be obtained at the SLM side when the information of an aberration-free virtual image propagates from the observer to the out-coupling HOE inversely. The observer can obtain the aberration-free image if the SLM provides the corresponding intermediate image accurately. The simulation results were shown in Fig. 2 where L is the distance from the out-coupling HOE to virtual images. Δd was defined as $d_x - d_y$ where d_x and d_y are the distance from SLM to the image plane in the x-z and y-z plane separately.
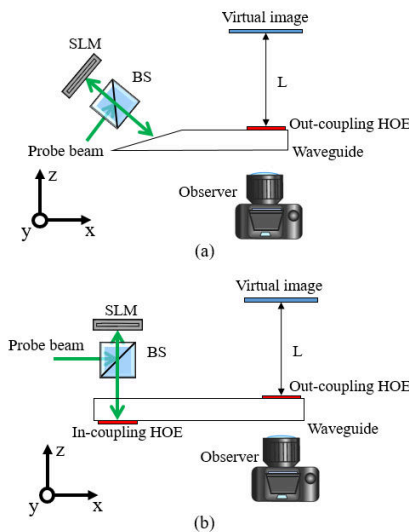

Fig. 1. The experimental configurations were utilized to obtain images of CGH system with an (a) asymmetric and (b) symmetric holographic waveguide combiner.
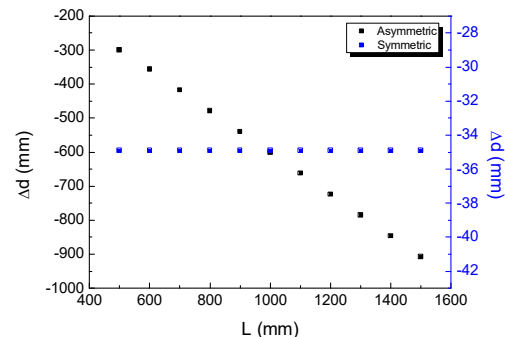

Fig. 2. The separation between the image planes in x-z plane and y-z plane corresponds to the distance of virtual images.

The complex amplitude distribution of an astigmatism intermediate image $u_h(x, y)$ can be described as

$$u_h(x, y) = u_i(x, y) \otimes exp\left[\frac{-i\pi}{\lambda}\left(\frac{x^2}{d_x} + \frac{y^2}{d_y}\right)\right] \quad (1)$$

where $u_i(x, y)$ is the complex amplitude distribution of the target image, λ is the wavelength of the probe beam. Then the phase-only CGH can be inferred from $u_h(x, y)$.

4. Experimental results

In this paper, the target image as shown in Fig. 3(a) and 3(c) were employed to test the asymmetric and symmetric structure separately. The resulting images were shown in Fig. 3(b) and 3(d) separately. The horizontal lines and vertical lines can be clearly obtained simultaneously. It shows the astigmatism was compensated. However, the resulting image of the asymmetric system was shrunk in horizontal. The shrinkage is dependent on the image distance L as shown in Fig. 4.
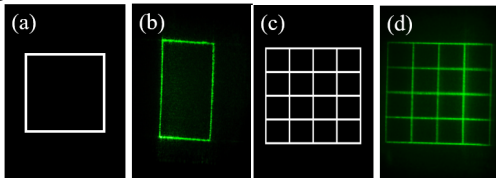

Fig. 3. The resulting images with astigmatism correction was obtained with the (b) asymmetric combiner and (d) symmetric combiner. (a) target image of (b); (c) target image of (d).
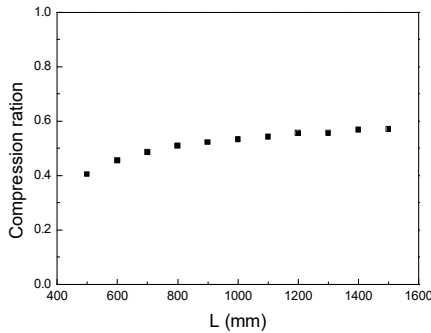

Fig. 4. The anamorph of astigmatism-free images depends on the images distance in the system with the asymmetric combiner.

5. Discussion

In these two cases, the astigmatism was analyzed and was corrected. However, astigmatism should be reanalyzed if any parameters such as thickness, refractive index, etc. are changed. In order to simplify the ray-tracing process, astigmatism of the asymmetric system can be approximated as

$$\Delta d = \left(Lcos^2(\theta_m) - \frac{D}{n}\right) \frac{cos^2\left(asin(nsin(\theta_m - \theta_t))\right)}{cos^2(\theta_m - \theta_t)} - L - \frac{D}{n} \quad (2)$$

where θ_m is the angle between the reference ray and signal ray of the out-coupling HOE, D is the propagated distance in the waveguide, n is the refractive index, θ_t is the tilt angle of the wedge. In this case, θ_t is 17.7°, θ_m is 42.67°, D is about 63mm, n is 1.5. The comparison between the results of software Zemax and the simplified formula was shown in Fig. 5.
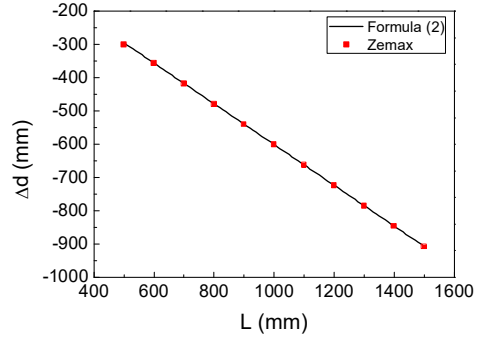

Fig. 5. The Δd corresponded to different image distance was computed by the traditional ray-tracing method and the simplified formula.

The astigmatism aberration of the symmetric system can be approximated as

$$\Delta d = \frac{Nt}{ncos(\theta_m)} \left(1 - \frac{1}{cos^2(\theta_m)}\right) \quad (3)$$

where N is the bounce times, t is the thickness of waveguide. In our case, N is 3, t is 8mm θ_m is 50°. The results of software Zemax and the simplified formula matched to each other as shown in Fig. 6.
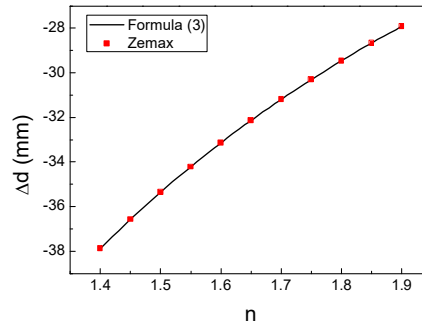

Fig. 6. The Δd corresponded to different refractive index was computed by the traditional ray-tracing method and the simplified formula.

6. Conclusions

In this paper, the aberration of two kinds of the holographic combiner was analyzed and corrected. For the asymmetric system, astigmatism was varied corresponding to the image distance. On the opposite, it is a constant corresponding to the distance in the symmetric system. Furthermore, astigmatism can be predicted according to the proposed simplified formulas.

References

[1]   H.-J. Yeom et al., "3D holographic head mounted display using holographic optical elements with astigmatism aberration compensation," Opt. Express 23, 32025-32034 (2015).

[2]   W.-K. Lin et al., "Astigmatism and deformation correction for a holographic head-mounted display with a wedge-shaped holographic waveguide," Appl. Opt. 57, 7094-7101 (2018).

LDC2020 | Oral Presentation
# Imaging / Lighting -Display Technologies-
2020年4月22日(水) 10:45 ～ 12:30 301 (Conference Center)

[LDC5-04] Effective Speckle Reduction Method Based on a Rotating Ball Lens

*Linxiao Deng[1], Yuwei Fang[1], Yuhua Yang[1], Tianhao Dong[1], Chun Gu[1], Lixin Xu[1] （1. University of Science and Technology of China）

A novel design for speckle reduction based on a rotating ball lens is investigated. In addition, a standardized speckle measurement method is also developed and the parameters mainly accord with characteristics of human eyes. This method could open up an avenue to the practical speckle measurement application.

Effective Speckle Reduction Method Based on a Rotating Ball Lens

Linxiao Deng, Yuwei Fang, Yuhua Yang, Tianhao Dong, Chun Gu, and Lixin Xu [*]

Department of Optics and Optical Engineering, University of Science and Technology of China, Hefei, Anhui 230026, P. R. China.
*xulixin@ustc.edu.cn

Abstract: *A novel design for speckle reduction based on a rotating ball lens is investigated. In addition, a standardized speckle measurement method is also developed and the parameters mainly accord with characteristics of human eyes. This method could open up an avenue to the practical speckle measurement application.*

1. Introduction

The laser as a light source in displays can provide high brightness, superior color gamut, high optical efficiency, and long lifetime [1-4]. However, one of the most serious problems for laser projection is speckle, which deteriorates the image quality.

In consideration of speckle caused by high coherence, these techniques include suppressing spatial and temporal coherence of laser. In some studies [1,5], similar methods are called angle and wavelength diversity. Besides, some studies use a diffuser and always combined with a light pipe [2] in the spatial light path. Nevertheless, such diffuser will add to extra light consumption.

In this paper, an effective speckle reduction method based on a rotating ball lens is proposed and demonstrated. The utilization of this lens in a practical laser projection system can vastly reduce the speckle with multiple speckle reduction mechanisms. Besides, according to the previous procedure outlined in [3], a standardized speckle measurement method based on human eye characteristics is proposed. In detail, a specific measuring system with a charge-coupled device (CCD) camera is set to make accurate, fast and objective measurement.

2. Theoretical analysis of laser speckle

2.1 Definition of speckle contrast

The severity of speckle phenomenon is obtained by the speckle contrast as follows [4]:

$$C = \frac{\sigma_I}{\bar{I}} = \frac{\sqrt{<I^2>-<I>^2}}{<I>},$$

where σ_I is the standard deviation of the light intensity *I*. Sometimes the speckle contrast is multiplied by 100% for a unified unit. In a projection system, the speckle must be reduced to a contrast value below 4% to eliminate the annoying spots observed by human eyes.

2.2 Statistical properties of Integrated speckle

In the experiment, when the speckle size is so tiny that multiple granules fill the same pixel in the detector, thus the speckle contrast is reduced in spatial integration. In other words, the value depends on the average speckle size and detector's pixel size. Our measurement setup includes a chromatic CCD camera with the pixel size A_p of 4.4 × 4.4 μm². The distance between the circular clear aperture of 3.2 mm and CCD chip is 17.21 mm. In addition, the

human average cone size is about 5.24 μm². This mismatch of the pixel size A_p has to be compensated [3]. Therefore, the measured speckle contrast must be multiplied with a compensating factor. In consideration of the central wavelength of our practical laser source, the value is 1.34 for red, 1.43 for green, and 1.50 for blue.

2.3 Speckle reduction by the ball lens

The ball lens is driven by a motor. It should be noted that its rotating shaft slightly deviates from the center of the ball lens. Fig. 1 illustrates the details of rotation and a specific beam is plotted to show the beam modulation with rotation. When the center of the ball lens goes through O$_1$, O$_2$, O$_3$, and O$_4$, its focus correspondingly passes O$_1$', O$_2$', O$_3$', and O$_4$'. This leads to an optical path difference between different beams of light, which suppresses the spatial coherence of the incident beam.
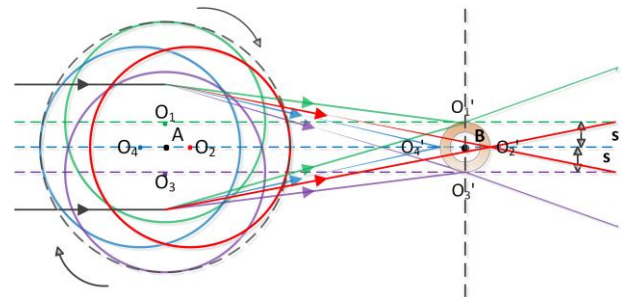

Fig. 1. Rotating process of the ball lens. On account of the deviation of the rotating shaft, the focus of the ball lens changes with its rotation. A denotes the rotating shaft, s = 0.5 mm denotes the deviation distance from the ball center, and the radius of the ball lens is 5.0 mm.

3. Experimental setup

Our experimental setup is shown in Fig. 2, which is composed of the projection system, the screen, and the measuring system.

The details of the tailored laser diodes are shown in table 1. For a projection system, the multi-mode fibers (MMFs) and combiner are used to combine three beams

Table 1. Laser diode

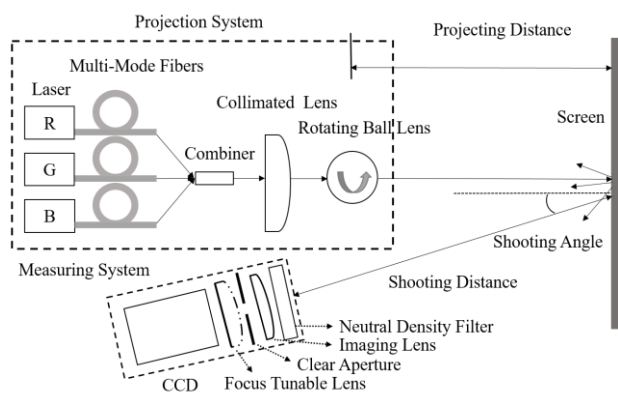| Type	Red	Green	Blue
Central wavelength (nm)	638	520	455
Power (W)	3.1	2.0	2.5

Fig. 2. The schematic layout of the preliminary experimental setup. R, G, and B represent Red, Green, and Blue.

from RGB light sources into one beam. The projecting distance is fixed to 2.4 m and the shooting distance is 1.25 m. Besides, the projecting light is vertical to a common white matte screen, which has a view angle of 150° and a peak gain of 0.85.

To record the image on the screen, a specific measuring system based on human eye characteristics is established with a CCD camera. The chip is made by SONY. The focus tunable lens is made by Optotune. A neutral density filter (NDF) is used to ensure that the light intensity becomes a proper value so the CCD camera has a linear response. Moreover, to avoid recording CCD's shadow on the screen, the shooting angle is adjusted to a tiny value and thus the shooting direction is still approximately vertical to the screen.

4.   Results and discussion

The voltage of the motor is changed to adjust the rotating speed of the ball lens. Peculiarly, the motor will not start to work until the voltage reach 0.4 V. In Fig. 3, when the voltage is lower than 0.4 V, the speckle contrast is not a constant. This may result from the slight instability of the
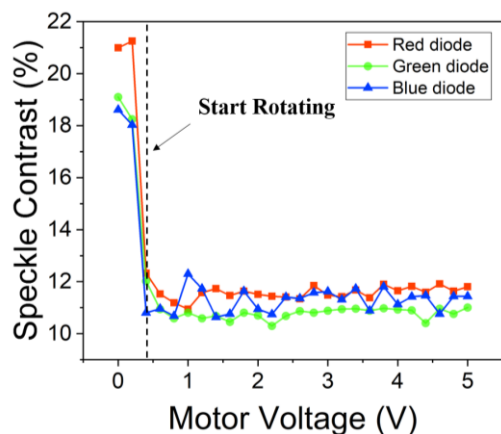

Fig. 3. The speckle reduction effect depends on different motor voltages with different laser sources. The motor will not start to rotate until the voltage reach 0.4 V.

laser source and slight vibration of screen. While the motor starts to rotate, the speckle contrast is rapidly reduced. In detail, the original speckle contrast is 20.99% (R), 19.10% (G), and 18.61% (B) at 0 V. When the motor voltage is 5 V, the value is 11.81% (R), 11.01% (G), and 11.44% (B).

It is worth noting that when the motor voltage is lower than 4 V, the light spot will oscillate on the screen, which deteriorates the image quality. In view of the nominal voltage of the motor is 5 V, the speckle contrast under this condition is used to calculate the speckle reduction factor $R_{\Omega rot}$ [1], which is 1.78 for red, 1.73 for green, and 1.63 for blue. Due to the motor voltage having a nonlinear influence on the rotating speed, if the motor voltage axis is changed to the rotating speed axis, the curve may become more gentle.

5.   Conclusion

In conclusion, we have fabricated a ball lens for speckle reduction. The speckle reduction factor through angle diversity is demonstrated, which is 1.78 for red, 1.73 for green, and 1.63 for blue. In addition, a standardized measurement system for speckle contrast is presented to ensure the results appropriate for human eye characteristics, which guides for practical speckle measurement application. In the future, our system can enable the integration of high power laser module with low speckle contrast, which could find potential application for high lumen laser projection.

Reference

1.   H. Yamada, K. Moriyasu, H. Sato, and H. Hatanaka, "Effect of incidence/observation angles and angular diversity on speckle reduction by wavelength diversity in laser projection systems," Opt. Express **25**(25), 32132-32141 (2017).
2.   J. W. Pan and C. H. Shih, "Speckle reduction and maintaining contrast in a LASER pico-projector using a vibrating symmetric diffuser," Opt. Express **22**(6), 6464–6477 (2014).
3.   S. Roelandt, Y. Meuret, A. Jacobs, K. Willaert, P. Janssens, H. Thienpont, and G. Verschaffelt, "Human speckle perception threshold for still images from a laser projection system," Opt. Express **22**(20), 23965–23979 (2014).
4.   J. W. Goodman, *Speckle phenomena in optics: theory and applications* (Roberts and Company, Englewood, 2007) Chap. 3-3.
5.   D. S. Mehta, D. N. Naik, R. K. Singh, and M. Takeda, "Laser speckle reduction by multimode optical fiber bundle with combined temporal, spatial, and angular diversity," Appl. Opt. **51**(12), 1894-1904 (2012).

LDC2020 | Short Oral Presentaion

Short Presentation for Poster Paper
Session Chair: Satoshi Ouchi(Hitachi)
Wed. Apr 22, 2020 12:30 PM - 12:33 PM 301 (Conference Center)

[LDCp-01] Reforming of Computer Generated Hologram Pattern through Angular Spectrum Domain Computation

*Chang Joo Lee[1], Woo Young Choi[1], Joong Ki Park[2], Kwan Jung Oh[2], Kee Hoon Hong[2], Ki Hong Choi[2], Seung Yeol Lee[1] （1. Kyungpook National University, 2. Electronics and Telecommunication Research Institute (ETRI)）

12:30 PM - 12:33 PM

LDC2020 | Short Oral Presentaion
Short Presentation for Poster Paper
2020年4月22日(水) 12:30 ～ 12:33 301 (Conference Center)

[LDCp-01] Reforming of Computer Generated Hologram Pattern through Angular Spectrum Domain Computation

*Chang Joo Lee[1], Woo Young Choi[1], Joong Ki Park[2], Kwan Jung Oh[2], Kee Hoon Hong[2], Ki Hong Choi[2], Seung Yeol Lee[1] （1. Kyungpook National University, 2. Electronics and Telecommunication Research Institute (ETRI)）

In this paper, we propose a hologram image resizing method through zero padding and cutting in spatial frequency domain for reducing computation time. This method is much faster than conventional CGH calculation method for reforming.

Reforming of Computer Generated Hologram Pattern through Angular Spectrum Domain Computation

Chang-Joo Lee[1], Woo-Young Choi[1], Joongki Park[2], Kwan-Jung Oh[2], Keehoon Hong[2],
Kihong Choi[2], and Seung-Yeol Lee[1]*

[1] School of Electronics Engineering, Kyungpook National University, Daegu, Republic of Korea
[2] Electronics and Telecommunication Research Institute (ETRI), Daejeon, Republic of Korea
Tel.:+53-950-6608, E-mail: seungyeol@knu.ac.kr

Abstract: *Since calculating a computer generated hologram pattern takes a long time, reduction of computation time in digital holography has been a great issue. Here, we propose a reforming method of hologram through simple calculations on the spatial frequency domain which has much faster computation speed.*

1. Introduction

Computer generated hologram (CGH) has an advantage compared to analogue hologram for its design flexibility. For example, it can reconstruct various virtual objects as well as real recorded objects. Various researches related to CGH calculation methods have been conducted since it does not need a complex recording process unlike analogue holography. However, the problem of CGH is that it consumes a lot of time to calculate. As technology advances, the resolution of the spatial light modulator (SLM) has been increased. As a result, it takes much more time to generate the CGH pattern. Even if the same object's CGH pattern is already recorded, if we want to change the size or the location of the object, we need to recalculate the whole CGH pattern from the beginning. If the resolution is small, it does not take much time to compute, but as the resolution increases over 10k by 10k the computation time of the CGH patterns increases exponentially. As the resolution of the SLM increases, large amount of computation time will become a big problem for application in the real-time hologram and mobile hologram using the conventional hologram calculation method.

Previously, there have been various studies on increasing the resolution of hologram images. For example, through zero-padding in the spatial frequency domain; or by using deep-learning algorithm were reported [1, 2]. However, the zero-padding based method was only restricted to simple scaling of the resolution of hologram, whereas the deep-learning based method cannot obtained uniform improvement for all situations. Moreover, to the best of our knowledge, studies to freely adjust the size and the position of the CGH image have not been published yet.

In this paper, we propose a hologram image resizing method through zero padding and cutting in spatial frequency domain for reducing computation time. This method is much faster than conventional CGH calculation method. We propose a calculation method in the spatial frequency domain to shift the focal length of the object. As shown in Fig. 1, the conventional holographic image magnification simultaneously changes the image size and focal length depending on the magnification factor of the CGH pattern. On the other hand, the proposed method has the advantage of changing the image size and focal length arbitrarily while maintaining the size of the CGH pattern.

2. Principle and result

Resizing method of hologram image can be divided into three major steps. First, the CGH pattern is resized through the calculation in the spatial frequency domain, and the second step is to modify the error in the resizing process. This step also calculates in the spatial frequency domain and not only corrects the error, but also adjusts the location where the hologram image is reconstructed. The final step is to bring the computed CGH pattern back into spatial domain and cut it to the desired resolution.

To enlarge the hologram image, the CGH pattern you want to magnify is Fourier-transformed into the spatial frequency domain. Then, to enlarge the image by α times, the Fourier-transformed pattern is zero-padded by α times to enlarge the pattern. After applying inverse Fourier-transform, the CGH pattern is cut to the desired resolution
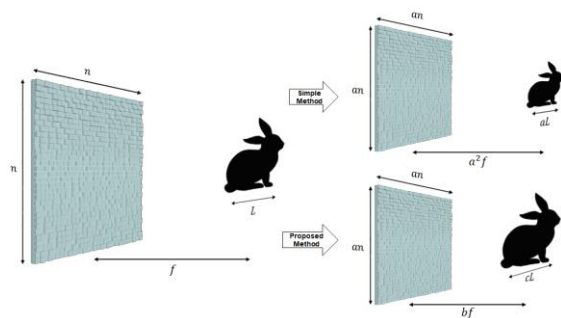

Fig. 1. Comparison of the proposed method with a simple magnification of CGH. Upper image shows image size and depth resulted by a simple magnification, whereas the image below shows the expected results obtained by using our configuration.

and reconstruction process is undergone to get a hologram image that is α times larger.

To scale down, the CGH pattern you want to magnify is Fourier-transformed into the spatial frequency domain. In order to scale down the image by $\frac{1}{a}$ times, the pattern is interpolated by α times using bicubic interpolation and then sliced by the size of $\frac{1}{\alpha}$ times. The sliced pattern then is inversed Fourier-transformed and undergoes the reconstruction process in which you can obtain a hologram image that is smaller by $\frac{1}{\alpha}$ times. If you want to obtain a holographic image with resolution β times larger than the initial CGH pattern and α times image size, interpolate αβ times when bicubic interpolating on the spatial frequency domain. After that, if you cut only by α times, you get a hologram image with a resolution of β times and an image size of α times.

However, when zero-padding or bicubic interpolation process is implemented in the spatial frequency domain, the focal length of the image changes. In order to compensate the unwanted error, additional calculations can be performed on the same spatial frequency domain to place the image in the desired focal length. The calculation method which can fix the axial error can be used to move the object in the x, y axis.
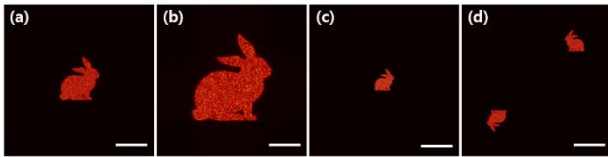

Fig. 2. Comparing the change of size and movement of the hologram image by using the proposed method. (a) Initial hologram image. (b) Simulation result of doubling the original hologram image using the proposed method. (c) Simulation result of the hologram imaged reduced by 1/2 times using the proposed method. (d) The result of moving two different images from their origin in different directions.

The method of moving the hologram image in the x, y axis and the focal length is to Fourier-transform the CGH pattern and multiply the exponential term by the distance you want to move in the spatial frequency domain as shown in the bottom equation.

$$H'_F = H_F e^{-2\pi i(x\dot{x}+y\dot{y}+z\dot{z})} \qquad (1)$$

where $H_F(f_x, f_y)$ is the Fourier transformed result of the CGH pattern $h(x,y)$, and $\dot{x} = f_x$, $\dot{y} = f_y$, $\dot{z} = f_z = \sqrt{\lambda^{-2} - \dot{x} - \dot{y}}$.

If the CGH pattern is interpolated α times over in spatial frequency domain, the focal length will change to α^2. By calculating the changed value and pulling it back to the position of the original focal length, you can not only correct the focal length even after interpolation, but also relocate it to the desired position by multiplying the x and y terms.

Table 1. shows the simulation results of the proposed method using the Matlab code produced by the laboratory. It took 30.03 seconds to calculate the 10K CGH hologram pattern from conventionally, but using our proposed method, it took 10.24 seconds when doubling the size of the image and took 11.58 seconds to reduce the time to 1/2 times. It is 61% faster computation time than conventional method. The specs of the computer running the simulation are CPU, inter (R) Xeon (R) E5-2680 v4 2.40GHz, 256GB of memory, and Geforce RTX 2080 Ti. The calculation was performed using the GPU.

Table 1. Comparison of the proposed method with a simple calculation CGH time.

10k	CGH	2x	0.5x
Conventional method	30.03(s)	30.21(s)	29.80(s)
Proposed method		10.24(s)	11.58(s)
Cutting time rate		66%	61%

3. Conclusions

In this study, we propose a method for resizing hologram images through zero-padding and cutting in the spatial frequency domain of a CGH pattern. We also propose a method of changing the image in *x, y* axis and focal length through additional calculations which is used to compensate for the error that occurs during resizing. This method is about 60% faster than the conventional method used to get the object with different positions and size.

References
[1] J. G. Shin, J. W. Kim, J. H. Lee, B. H. Lee, "Accurate reconstruction of digital holography using frequency domain zero padding" Institute of Electrical and Electronics Engineers, Jeju, 2017, pp. 1-4.
[2] H. J. Byeon, T. S. Go, S. J. Lee, "Deep learning-based digital in-line holographic microscopy for high resolution with extended field of view" Optics & Laser Technology, Volume 113, 77-86 (2019).

LDC2020 | Poster Presentation

Poster Session
Wed. Apr 22, 2020 2:00 PM - 3:30 PM Hall A (Exhibition Hall)

[LDCp-01] Reforming of Computer Generated Hologram Pattern through Angular Spectrum Domain Computation

*Chang Joo Lee[1], Woo Young Choi[1], Joong Ki Park[2], Kwan Jung Oh[2], Kee Hoon Hong[2], Ki Hong Choi[2], Seung Yeol Lee[1]　(1. Kyungpook National University, 2. Electronics and Telecommunication Research Institute (ETRI))

LDC2020 | Poster Presentation

Poster Session

2020年4月22日(水) 14:00 ～ 15:30 Hall A (Exhibition Hall)

[LDCp-01] Reforming of Computer Generated Hologram Pattern through Angular Spectrum Domain Computation

*Chang Joo Lee[1], Woo Young Choi[1], Joong Ki Park[2], Kwan Jung Oh[2], Kee Hoon Hong[2], Ki Hong Choi[2], Seung Yeol Lee[1] （1. Kyungpook National University, 2. Electronics and Telecommunication Research Institute (ETRI)）

In this paper, we propose a hologram image resizing method through zero padding and cutting in spatial frequency domain for reducing computation time. This method is much faster than conventional CGH calculation method for reforming.

Reforming of Computer Generated Hologram Pattern through Angular Spectrum Domain Computation

Chang-Joo Lee[1], Woo-Young Choi[1], Joongki Park[2], Kwan-Jung Oh[2], Keehoon Hong[2],
Kihong Choi[2], and Seung-Yeol Lee[1]*
[1] School of Electronics Engineering, Kyungpook National University, Daegu, Republic of Korea
[2] Electronics and Telecommunication Research Institute (ETRI), Daejeon, Republic of Korea
Tel.:+53-950-6608, E-mail: seungyeol@knu.ac.kr

Abstract: Since calculating a computer generated hologram pattern takes a long time, reduction of computation time in digital holography has been a great issue. Here, we propose a reforming method of hologram through simple calculations on the spatial frequency domain which has much faster computation speed.

1. Introduction

Computer generated hologram (CGH) has an advantage compared to analogue hologram for its design flexibility. For example, it can reconstruct various virtual objects as well as real recorded objects. Various researches related to CGH calculation methods have been conducted since it does not need a complex recording process unlike analogue holography. However, the problem of CGH is that it consumes a lot of time to calculate. As technology advances, the resolution of the spatial light modulator (SLM) has been increased. As a result, it takes much more time to generate the CGH pattern. Even if the same object's CGH pattern is already recorded, if we want to change the size or the location of the object, we need to recalculate the whole CGH pattern from the beginning. If the resolution is small, it does not take much time to compute, but as the resolution increases over 10k by 10k the computation time of the CGH patterns increases exponentially. As the resolution of the SLM increases, large amount of computation time will become a big problem for application in the real-time hologram and mobile hologram using the conventional hologram calculation method.

Previously, there have been various studies on increasing the resolution of hologram images. For example, through zero-padding in the spatial frequency domain; or by using deep-learning algorithm were reported [1, 2]. However, the zero-padding based method was only restricted to simple scaling of the resolution of hologram, whereas the deep-learning based method cannot obtained uniform improvement for all situations. Moreover, to the best of our knowledge, studies to freely adjust the size and the position of the CGH image have not been published yet.

In this paper, we propose a hologram image resizing method through zero padding and cutting in spatial frequency domain for reducing computation time. This method is much faster than conventional CGH calculation method. We propose a calculation method in the spatial frequency domain to shift the focal length of the object. As shown in Fig. 1, the conventional holographic image magnification simultaneously changes the image size and focal length depending on the magnification factor of the CGH pattern. On the other hand, the proposed method has the advantage of changing the image size and focal length arbitrarily while maintaining the size of the CGH pattern.

2. Principle and result

Resizing method of hologram image can be divided into three major steps. First, the CGH pattern is resized through the calculation in the spatial frequency domain, and the second step is to modify the error in the resizing process. This step also calculates in the spatial frequency domain and not only corrects the error, but also adjusts the location where the hologram image is reconstructed. The final step is to bring the computed CGH pattern back into spatial domain and cut it to the desired resolution.

To enlarge the hologram image, the CGH pattern you want to magnify is Fourier-transformed into the spatial frequency domain. Then, to enlarge the image by α times, the Fourier-transformed pattern is zero-padded by α times to enlarge the pattern. After applying inverse Fourier-transform, the CGH pattern is cut to the desired resolution
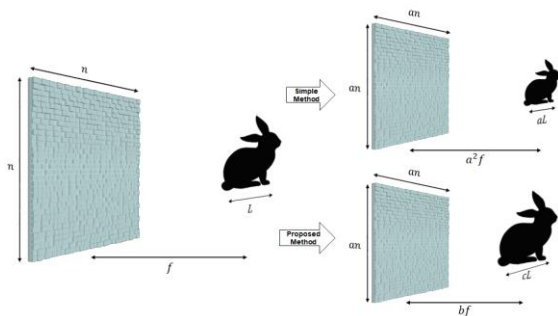

Fig. 1. Comparison of the proposed method with a simple magnification of CGH. Upper image shows image size and depth resulted by a simple magnification, whereas the image below shows the expected results obtained by using our configuration.

and reconstruction process is undergone to get a hologram image that is α times larger.

To scale down, the CGH pattern you want to magnify is Fourier-transformed into the spatial frequency domain. In order to scale down the image by $\frac{1}{a}$ times, the pattern is interpolated by α times using bicubic interpolation and then sliced by the size of $\frac{1}{\alpha}$ times. The sliced pattern then is inversed Fourier-transformed and undergoes the reconstruction process in which you can obtain a hologram image that is smaller by $\frac{1}{\alpha}$ times. If you want to obtain a holographic image with resolution β times larger than the initial CGH pattern and α times image size, interpolate αβ times when bicubic interpolating on the spatial frequency domain. After that, if you cut only by α times, you get a hologram image with a resolution of β times and an image size of α times.

However, when zero-padding or bicubic interpolation process is implemented in the spatial frequency domain, the focal length of the image changes. In order to compensate the unwanted error, additional calculations can be performed on the same spatial frequency domain to place the image in the desired focal length. The calculation method which can fix the axial error can be used to move the object in the x, y axis.
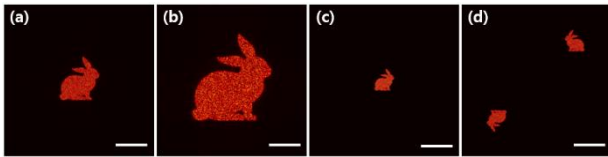

Fig. 2. Comparing the change of size and movement of the hologram image by using the proposed method. (a) Initial hologram image. (b) Simulation result of doubling the original hologram image using the proposed method. (c) Simulation result of the hologram imaged reduced by 1/2 times using the proposed method. (d) The result of moving two different images from their origin in different directions.

The method of moving the hologram image in the x, y axis and the focal length is to Fourier-transform the CGH pattern and multiply the exponential term by the distance you want to move in the spatial frequency domain as shown in the bottom equation.

$$H'_F = H_F e^{-2\pi i(x\dot{x}+y\dot{y}+z\dot{z})} \qquad (1)$$

where $H_F(f_x, f_y)$ is the Fourier transformed result of the CGH pattern $h(x,y)$, and $\dot{x} = f_x$, $\dot{y} = f_y$, $\dot{z} = f_z = \sqrt{\lambda^{-2} - \dot{x} - \dot{y}}$.

If the CGH pattern is interpolated α times over in spatial frequency domain, the focal length will change to α^2. By calculating the changed value and pulling it back to the position of the original focal length, you can not only correct the focal length even after interpolation, but also relocate it to the desired position by multiplying the x and y terms.

Table 1. shows the simulation results of the proposed method using the Matlab code produced by the laboratory. It took 30.03 seconds to calculate the 10K CGH hologram pattern from conventionally, but using our proposed method, it took 10.24 seconds when doubling the size of the image and took 11.58 seconds to reduce the time to 1/2 times. It is 61% faster computation time than conventional method. The specs of the computer running the simulation are CPU, inter (R) Xeon (R) E5-2680 v4 2.40GHz, 256GB of memory, and Geforce RTX 2080 Ti. The calculation was performed using the GPU.

Table 1. Comparison of the proposed method with a simple calculation CGH time.

10k	CGH	2x	0.5x
Conventional method	30.03(s)	30.21(s)	29.80(s)
Proposed method		10.24(s)	11.58(s)
Cutting time rate		66%	61%

3. Conclusions
In this study, we propose a method for resizing hologram images through zero-padding and cutting in the spatial frequency domain of a CGH pattern. We also propose a method of changing the image in *x, y* axis and focal length through additional calculations which is used to compensate for the error that occurs during resizing. This method is about 60% faster than the conventional method used to get the object with different positions and size.

References
[1] J. G. Shin, J. W. Kim, J. H. Lee, B. H. Lee, "Accurate reconstruction of digital holography using frequency domain zero padding" Institute of Electrical and Electronics Engineers, Jeju, 2017, pp. 1-4.
[2] H. J. Byeon, T. S. Go, S. J. Lee, "Deep learning-based digital in-line holographic microscopy for high resolution with extended field of view" Optics & Laser Technology, Volume 113, 77-86 (2019).

Novel Approach to Schwinger Field and Mega-Tesla Magnetic Field by Microbubble Implosion

M. Murakami[1], J. Honrubia[2], K. Weichman[3], A.V. Arefiev[3], S.V. Bulanov[4]

[1][1]*Institute of Laser Engineering, Osaka University, Suita, Osaka, Japan*
[2]*ETSI, Universidad Politecnica de Madrid, Madrid, Spain*
[3]*University of California San Diego, San Diego, USA*
[4]*Institute of Physics ASCR, ELI BEAMLINES, Czech Republic*

Murakami-m@ile.osaka-u.ac.jp

Recently we have proposed a novel scheme to generate ultrahigh electric field by using *microbubble implosion* [1, 2]. With a spherical bubble structure, it has been demonstrated ultrahigh field close to the Schwinger limit. In the present new work, we use microtube, and found that ultrahigh magnetic fields of the order of mega-Tesla can be achieved based on the similar principle to that of microbubble. First, we prepared a hollow cylindrical target surrounded by a solid material, which is then irradiated by ultrashort ultraintense laser pulse. Hot electrons generated by the laser irradiation launches plasma motion imploding toward the central axis. An important physical ingredient here is to prepare a seeding magnetic field along the target axis, which is of the order of kilo-Tesla. Owing to the gyro-motion, extremely high electric currents are generated of the order of 10^{15}A/cm^2. As a result, ultrahigh magnetic fields ~ 1-2 mega-Tesla have been demonstrated by the open source code EPOCH-2D.

[1] M. Murakami *et al*, "Generation of ultrahigh field by micro-bubble implosion",
Scientific Reports **8**, 7537 (2018).
[2] M. Murakami *et al*., "Relativistic proton emission from ultrahigh-energy-density nanosphere generated by microbubble implosion", *Phys. Plasmas* **26**, 043112 (2019).

LDC2020 | Oral Presentation

Keynote 2

Session Chair: Tetsuya Yagi(Mitsubishi Electric.Co.,)

Thu. Apr 23, 2020 9:00 AM - 9:45 AM 301 (Conference Center)

[LDC6-01(Keynote)] Indication of current-injection lasing from an organic semiconductor

*Chihaya Adachi[1], Toshinori Matsushima[1], Fatima Bencheikh[1], Shinobu Terakawa[1]
, William J. Potscavage[1], Chuanjiang Qin[1], Takashi Fujihara[1], Kenichi Goushi[1],
Jean-Charles Ribierre[1]　(1. Kyushu University)
 9:00 AM - 9:45 AM

Keynote 2

2020年4月23日(木) 09:00 〜 09:45 301 (Conference Center)

[LDC6-01(Keynote)] Indication of current-injection lasing from an organic semiconductor

*Chihaya Adachi[1], Toshinori Matsushima[1], Fatima Bencheikh[1], Shinobu Terakawa[1], William J. Potscavage[1], Chuanjiang Qin[1], Takashi Fujihara[1], Kenichi Goushi[1], Jean-Charles Ribierre[1] （1. Kyushu University）

We demonstrate the lasing properties of 4,4'-bis[(N-carbazole)styryl]biphenyl (BSBCz) thin films under electrical pumping. The device incorporates a mixed-order distributed feedback SiO_2 grating in an organic light-emitting diode structure and emit blue lasing.

Indication of current-injection lasing from an organic semiconductor

Atula S. D. Sandanayaka, Toshinori Matsushima, Fatima Bencheikh, Shinobu Terakawa, William J. Potscavage, Jr., Chuanjiang Qin,

Takashi Fujihara, Kenichi Goushi, Jean-Charles Ribierre, and Chihaya Adachi*

Center for Organic Photonics and Electronics Research (OPERA), Kyushu University, 744 Motooka, Nishi, Fukuoka 819-0395,

Japan

Abstract: *We demonstrate the lasing properties of 4,4'-bis[(N-carbazole)styryl]biphenyl (BSBCz) thin films under electrical pumping. The device incorporates a mixed-order distributed feedback SiO_2 grating in an organic light-emitting diode structure and emit blue lasing. The results provide an indication of lasing by direct injection of current into an organic thin film through selection of a high-gain organic semiconductor showing clear separation of the lasing wavelength from significant triplet and polaron absorption and design of a proper feedback structure to suppress losses at high current densities.*

1. Introduction

The properties of optically pumped organic semiconductor lasers (OSLs) have dramatically improved in the last 20 years as a result of major advances in both the development of high-gain organic semiconductor materials and the design of high Q-factor optical resonators.[1-3] While recent advances in low-threshold distributed feedback (DFB) OSLs by optical pumping have been demonstrated[4], the ultimate goal is electrically driven organic semiconductor laser diodes (OSLDs). In addition to enabling the full integration of organic photonic and optoelectronic circuits, the realization of OSLDs will open novel applications in spectroscopy, displays, lighting, medical devices and LIFI telecommunications.

The problems that have prevented the realization of lasing by the current excitation of organic semiconductors are mainly due to the optical losses from the electrical metal contacts and the triplet and polaron losses taking place at high current densities.[5] Approaches that have been proposed to solve these fundamental issues include the use of triplet quenchers[6] to suppress triplet absorption and singlet quenching by triplet excitons (STA) as well as the fabrication of small size and fine grating structures[7]. However, even with the advances that have been made in organic light-emitting diodes (OLEDs) and optically pumped OSLs,[1-3, 8-12] a current-injection OSLD has still not been conclusively demonstrated. Another promising laser architecture is based on an organic field-effect transistor (OFET),[13] which shows a great potential for solving electrode and polaron loss problems simultaneously. Much efforts have been focused to improve the performance of light-emitting OFETs by using single crystals[14-15], introducing multilayer structures to reduce charge density within an emissive layer,[16-17] a split gate structure for independent control of electron and hole injections,[18] and current confinement structures for increased local current density,[19] or utilizing microcavity effects originating from a gate electrode[20].

Previous studies have suggested that current densities over 1000 A/cm² would be required to achieve lasing from an OSLD if additional losses associated with the electrical pumping were completely suppressed.[21] One of the most promising molecules for the realization of an OSLD is 4,4'-bis[(N-carbazole)styryl]biphenyl (BSBCz) (chemical structure in Fig. 1a)[22] because of its excellent combination of optical and electrical properties such as a low amplified spontaneous emission (ASE) threshold in thin films (0.3 μJ/cm² under 800-ps pulse photoexcitation)[23] and the ability to withstand the injection of current densities as high as ~3 kA/cm² under 5 μs pulse operation in OLEDs with maximum external quantum efficiencies (η_{EQE}) of over 2%.[7] Furthermore, lasing at a high repetition rate of 80 MHz and under long pulse photoexcitation

of 30ms (q-CW) were recently demonstrated in optically pumped BSBCz-based DFB lasers.[23] Here, we report the lasing properties from an organic semiconductor film directly excited by electricity through the development and characterization of OSLDs based on a BSBCz thin film in an OLED structure with a mixed-order DFB grating.

The architecture of the OSLDs is schematically represented in Fig. 1a. A sputtered SiO_2 layer on indium tin oxide (ITO) glass substrates was engraved with e-beam lithography and reactive ion etching to create mixed-order DFB gratings with an area of 30×90 μm (Fig. 1b), and organic layers and a metallic cathode were vacuum deposited on the substrates. We designed the mixed-order DFB gratings to have an alternation of first- and second-order Bragg scattering regions, providing strong optical feedback and efficient vertical outcoupling of the laser emission, respectively.[16] Grating periods (Λ_1 and Λ_2) of 140 and 280 nm were chosen for the first- and second-order regions, respectively, based on the Bragg condition, $m\lambda_{Bragg} = 2n_{eff}\Lambda_m$, where m is the order of diffraction, λ_{Bragg} is the Bragg wavelength, which was set to the reported
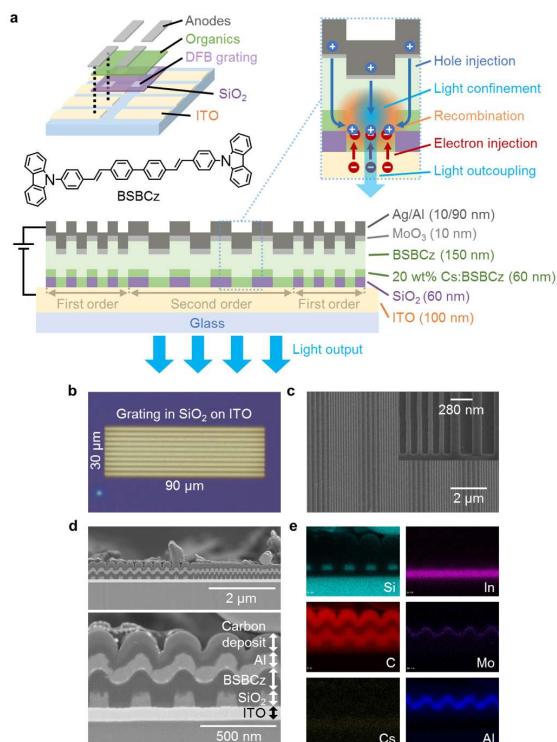

Fig. 1:Schematic view of OSLD and DFB structures

maximum gain wavelength (477 nm) for BSBCz, and n_{eff} is the effective refractive index of the structure, which was calculated to be 1.70.

2. Device characteristics of OSLDs

The OSLDs have an inverted OLED structure of ITO (100nm) / 20 wt.% Cs:BSBCz (60nm) / BSBCz (150nm) / MoO$_3$ (10nm) / Ag (10nm) / Al (90nm). Doping the BSBCz film with Cs in the region improves the electron injection into the organic layer, and MoO$_3$ is used as a hole injection layer. Figure 2 shows OSLD characteristics under pulse operation with the pulse width of 400 ns. Efficiency roll-off was well suppressed in the OSLDs under pulse operation, and the η_{EQE} was even found to substantially increase above 200 A/cm^2 to reach a maximum value of 2.9%. The output EL intensity height and full-width-at-half-maximum (FWHM) of an OSLD are plotted in Fig. 2c as a function of the current. While the FWHM of the steady-state PL spectrum of a neat BSBCz film is around 35 nm, the FWHM of the OSLD at high current densities decreases to values lower than 0.2 nm. Note that the second apparent transition point observed around 2 kAcm^{-2} is presumably due to the device instability at high current density. The slope efficiency of the output intensity abruptly changes with increasing current and can be used to determine a threshold of 600 A/cm^2 (8.1mA). Above 3.5 kA/cm^2, we observed significant emission of the broad EL in addition to the lasing emission. This might be induced by the partial breakdown of the SiO$_2$ grating due to the extremely high voltage and current. The output power as a function of the current density plotted in Fig. 3d is also measured using a power meter. The maximum output power measured with a power meter placed in front of an OSLD at a distance of 3 cm away from the ITO glass substrate was 0.50 mW at 3.3 kA/cm^2. These observed EL properties strongly suggest that light amplification occurs at high current densities and indicate that electrically driven lasing is achieved above a current density threshold.
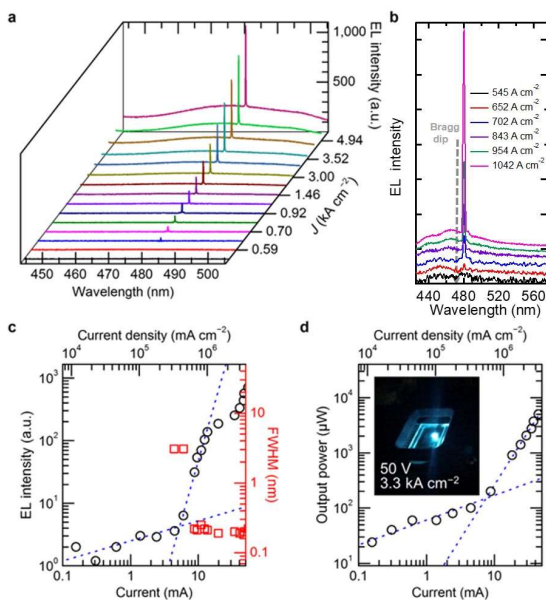

Fig. 2:OSLD characteristics

3. Conclusions

This study provided indication that lasing from a current-driven organic semiconductor is possible through proper design and choice of the resonator and organic semiconductor to suppress losses and enhance coupling. The low losses in BSBCz are integral to enabling lasing, so the development of strategies to design laser molecules with similar or improved properties is an important next step. We believe that this report opens opportunities in organic photonics and serves as a basis for the future development of an organic semiconductor laser diode technology that is simple, cheap, and tunable and can enable fully and directly integrated organic-based optoelectronic platforms.

Acknowledgement

References

1) I. D. W. Samuel, and G. A. Turnbull, Chem. Rev. **107**, 1272–1295 (2007).
2) S. Chénais, and S. Forget, Polym. Int. **61**, 390–406 (2012).
3) A. J. C. Kuehne, and M. C. Gather, Chem. Rev. **116**, 12823–12864 (2016).
4) G. Tsiminis, Y. Wang, A. L. Kanibolotsky, A. R. Inigo, P. J. Skabara, I. D. W. Samuel, and G. A. Turnbull, Adv. Mater. **25**, 2826–2830 (2013).
5) M. Baldo, R. Holmes, and S. Forrest, Phys. Rev. B, **66**, 3, 035321 (2002).
6) A. S. D. Sandanayaka, L. Zhao, D. Pitrat, J-C Mulatier, T. Matsushima, C. Andraud, J-H Kim, J-C Ribierre, and C. Adachi, Appl. Phys. Lett. **108**, 223301 (2016).
7) K. Hayashi, H. Nakanotani, M. Inoue, K. Yoshida, O. Mikhnenko, T-Q Nguyen, and C. Adachi, Appl. Phys. Lett. **106**, 093301 (2015).
8) E. B. Namdas, M. Tong, P. Ledochowitsch, S.R. Mednick, J. D. Yuen, D. Moses, and A. J. Heeger, Adv. Mater. **21**, 799 (2009).
9) C. Xiang, W. Koo, F. So, H. Sasabe, J. Kido, Light Sci. Appl. **2**, e74 (2013).
10) M. J. Jurow, C. Mayr, T. D. Schmidt, T. Lampe, P. I. Djurovich, W. Brütting, M. E. Thompson, Nature Mater. **15**, 85 (2016).
11) F. Chen, D. Gindre, J. M. Nunzi, Opt. Expr. **16**, 16746 (2008).
12) C. Gärtner, C. Karnutsch, and U. Lemmer, J. Appl. Phys. **101**, 023107 (2007).
13) M. Muccini, Nature Mater **5**, 605 (2006).
14) T. Takenobu, S. Z. Bisri, T. Takahashi, M. Yahiro, C. adachi, Y. Iwasa, Phys. Rev. Lett. **100**, 066601 (2008).
15) X. Zhang, H. Dong, W. Hu, Adv. Mater. **30**, 1801048 (2018).
16) R. Capelli, S. Toffanin, G. Generali, H. Usta, A. Facchetti, M. Muccini, Nat. Mater. **9** 496 (2010).
17) M. U. Chaudhry, K. Muhieddine, R. Wawrzinek, J. Li, S. C. Lo, E. B. Namdas, ACS Photon. **5**, 2137 (2018).
18) B. B. Y. Hsu, C. Duan, E. B. Namdas, A. Gutacker, J. D. Yuen, F. Huang, Y. Cao, G. C. Bazan, I. D. W. Samuel, A. J. Heeger, Adv. Mater. **24**, 1171 (2012).
19) K. Sawabe, M. Imakawa, M. Nakano, T. Yamao, S. Hotta, Y. Iwasa, T. Takenobu, Adv. Mater. **24** 6141(2012).
20) M. C. Gwinner, D. Kabra, M. Roberts, T. J. K. Brenner, B. H. Wallikewitz, C. R. McNeill, R. H. Friend, H. Sirringhaus, Adv. Mater., **24** 2728 (2012).
21) T. Aimono, Y. Kawamura, K. Goushi, H. Yamamoto, H. Sasabe, and C. Adachi, Appl. Phys. Lett. **86**, 71110 (2005).
22) A. S. D. Sandanayaka, K. Yoshida, M. Inoue, K. Goushi, J.-C. Ribierre, T. Matsushima, and C. Adachi, Adv. Opt. Mater. **4**, 834–839 (2016).
23) A. S. D. Sandanayaka, T. Matsushima, F. Bencheikh, K. Yoshida, M. Inoue, T. Fujihara, K. Goushi, J-C Ribierre, and C. Adachi, Science Adv. **3**, e1602570 (2017).

LDC2020 | Oral Presentation

Light sources and components 1
Session Chair: Tetsuya Yagi(Mitsubishi Electric.Co.,)
Thu. Apr 23, 2020 9:45 AM - 10:30 AM 301 (Conference Center)

[LDC7-01] Speckle Contrast Generated by 638-nm Broad Area Laser Diodes

*Kyosuke Kuramoto[1], Takuma Fujita[1], Takehiro Nishida[1], Tetsuya Yagi[1], Akira Takamori[2], Kazuhisa Yamamoto[2], Masahiko Kondow[3]　(1. Mitsubishi Electric Corporation, 2. Institute of Laser Engineering, Osaka University, 3. Graduate School of Engineering, Osaka University)

9:45 AM - 10:00 AM

[LDC7-02] Monolithic single-mode diode lasers at 633 nm with high coherence and reliability for holographic printing

*Katrin Paschke[1], G. Blume[1], J. Pohl[1], B. Sumpf[1], D. Feise[1], P. Ressel[1], A. Sahm[1], N. Werner[1], J. Hofmann[1]　(1. Ferdinand-Braun-Institut)

10:00 AM - 10:15 AM

[LDC7-03] High-direction and low-coherence semiconductor laser with dumbbell-type cavity

*Linhai Xu[1], Yufei Wang[1], Yufei jia[1], Wanhua Zheng[1]　(1. Institute of Semiconductors, CAS)

10:15 AM - 10:30 AM

Light sources and components 1

2020年4月23日(木) 09:45 ～ 10:30 301 (Conference Center)

[LDC7-01] Speckle Contrast Generated by 638-nm Broad Area Laser Diodes

*Kyosuke Kuramoto[1], Takuma Fujita[1], Takehiro Nishida[1], Tetsuya Yagi[1], Akira Takamori[2], Kazuhisa Yamamoto[2] , Masahiko Kondow[3]　(1. Mitsubishi Electric Corporation, 2. Institute of Laser Engineering, Osaka University, 3. Graduate School of Engineering, Osaka University）

Experimental investigation on speckle contrast generated by 638-nm broad-area laser revealed that increasing the emitter number reduced the speckle contrast, i.e. the triple emitter was better than dual one in the viewpoint of speckle reduction.

Speckle Contrast Generated by 638-nm Broad Area Laser Diodes

Kyosuke Kuramoto[1], Takuma Fujita[1], Takehiro Nishida[1], Tetsuya Yagi[1],
Akira Takamori [2], Kazuhisa Yamamoto [2], Masahiko Kondow[3]
[1] Mitsubishi Electric Corporation, 4-1 Mizuhara Itami 664-8641 Japan, Kuramoto.Kyosuke@aj.MitsubishiElectric.co.jp
[2] Institute of Laser Engineering, Osaka University, 2-6 Yamadaoka,Suita,Osaka 565-0871 Japan
[3] Graduate School of Engineering, Osaka University, 2-1 Yamadaoka,Suita,Osaka 565-0871 Japan

Abstract: Speckle contrast generated by 638-nm broad area single, dual and triple emitter laser diodes were experimentally investigated. In the single emitter, the wide stripe showed an advantage of speckle reduction. It was revealed that increasing the emitter number reduced the speckle contrast, i.e. the triple emitter was better than dual emitter in the viewpoint of speckle reduction.

1. Introduction

High-power red laser diode (LD) is a keystone for laser based displays, because the red LD shows poor characteristics compared with the GaN based blue LD [1]. One of the trend in the laser based displays is high brightness, and it requires highly-output LDs. Highest barrier to realize the high-power red LD is the sudden degradation in the long term aging. Mean time to failure (MTTF) due to the sudden one is proportional to the output power density at the front facet to the –n power, resulting that the wide stripe width is suitable to realize the high-power and the highly reliable operation [2]. We have developed high-power and highly reliable 638-nm broad area (BA) LDs. Multiple stripe structure is adopted in the LDs. The reason is described elsewhere [3-4].

In the actual display application, speckle contrast (Cs) is a one of important matter to be overcome. Goodman reported eight methods to reduce Cs [5]. In the methods, the wavelength diversity method is mainly used in the laser light source itself. Furukawa reported effect of the widening of the laser emission spectrum by tailoring the structures of 640nm band BA-LD arrays with 1cm width [6]. Murata reported Cs reduction by adopting the high-frequency superposition [7]. We did the new method by using the pulse driving current width and form with a narrow stripe (NS) red LD [8]. Also, the plural light source is widely used in the high lumen projector. The plural source works as independent speckle superposition and reduce Cs.

There is no report on the detail behaviour of Cs in red BA-LD including not only single emitter but also multi one so far to the best of our knowledge. In this paper, we will describe the Cs generated by the 638-nm single and multi-emitter BA-LD in detail.

2. LDs under evaluation

The 638-nm BA-LDs we have developed are single, dual and triple emitter assembled on a TO-can. They have almost same stripe structure. Only the differences are the stripe width and the stripe number. The chip structures are shown in Fig. 1. The details are described elsewhere [1-4]. In this study, the single emitters with the different stripe width (40 um: conventional, 60 um and 85 um) were additionally manufactured for evaluation. The dual emitter has 75 um stripes, and the triple 60 um, resulting in the total stripe width of 150 um in the dual one and 180um in the triple.

Figure 2 shows spectrum width dependence on operation current (Iop) normalized by threshold current. Usually the spectrum width is defined as the spectrum half width at a half maximum. But the LD's spectrum consisted of several fine peaks as depicted in Fig.2. Thus we used an integral half width (FWHI: full width at a half of integrated intensity) as the width, which was the difference between the wavelengths at which the cumulative integrated intensity of the spectrum shape is 25% and 75%. The spectrum width became higher as the normalized Iop (n-Iop) increased. Note that all the plots seemed to be on the same curve.
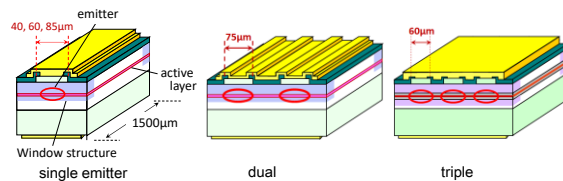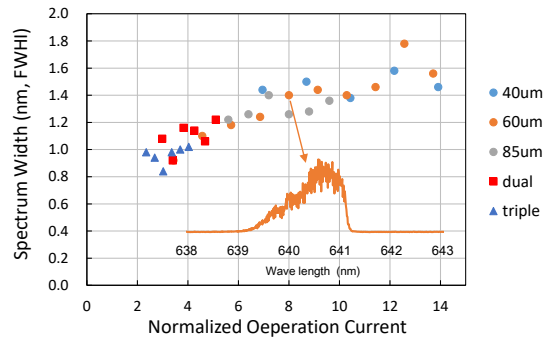

Fig. 1 BA-LD structures.

Fig. 2 Spectrum width dependence on normalized operation current.

3. Speckle contrast generated by the red LDs

The equipment for Cs measurement was SM01VS09 of Oxide, having an iris of 1.2 mm diameter which simulates modulation transfer function of human eye. The screen used in this study was conventional matte screen. A diffusion plate was inserted between the lens and the LD. The plate expanded the far field pattern (FFP) in the slow axis, resulting in the superimposition of multi emitter FFP on the screen. The image projected on the screen was strongly affected by FFP. Therefore the method proposed

by Kinoshita [9] was taken to extract the pure speckle pattern.

Speckle patters under operation current of 1.0 A for 60um stripe single emitter and 60um x 3 triple emitter are shown in Fig. 3. The former has Cs of 0.12, and the latter 0.074. The normalized intensity at the center line (shown as yellow arrows in the figure) for not only 60um and triple emitter but also 40um and 85um single emitter, 75um x 2 dual emitter under the condition are shown in Fig. 4. Cs values are described in the figure. Cs decreased as the stripe width increased, and that of triple emitter was smaller than those of the single emitter of the same stripe width and the dual emitter.
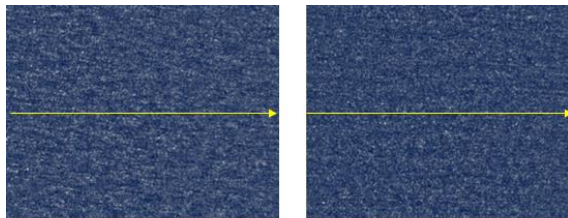
60um single emitter   60um x 3 Triple
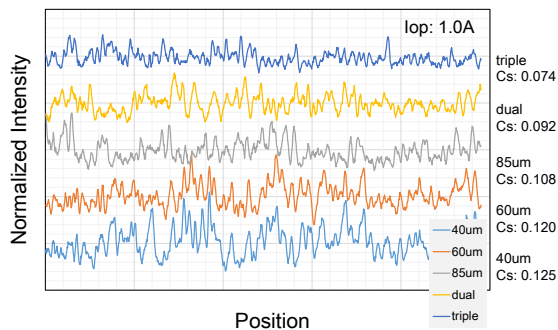Fig. 3 Speckle patters of single and triple emitter.

Fig. 4 Normalized intensity at the line for each emitters.

Cs dependence on the n-Iop is shown in Fig. 5. The 40 um and 60 um single emitters showed a tendency in which Cs decreased as the n-Iop increased. The tendency became clear under the high n-Iop higer than 10. The 85 um did not have a clear tendency. The measurement n-Iop range was 5 to 10. This lower range may make the tendency unclear. Under the same n-Iop, Cs decreased as the stripe width enlarged. As the stripe width widens, the number of lasing modes increases. This may bring the Cs improvement in the wider single emitter. Cs of 60 um single emitter in the n-Iop range less than 5 was approximately 0.12. On the other hand, that of triple emitter was 0.10, 83% of 60um value. The spectrum widths of both LDs under the same n-Iop were the same as shown in Fig.2. i.e., the Cs improvement by the spectrum width did not work in the same n-Iop. Therefore the improvement in the triple emitter may be due to the independent speckle superposition. Theoretically the Cs of the triple emitter is 58% of the single one. The difference between the experimental result and theory may come from the imperfection of the

superimposition of the triple emitter FFP. It was also revealed that the triple emitter showed lower Cs compared with the dual emitter.
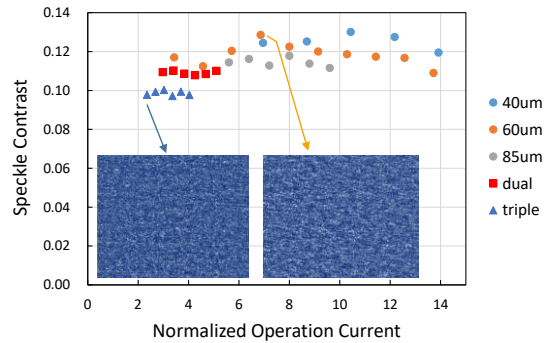

Fig. 5 Speckle contrast dependence on normalized operation current.

References

[1] T. Yagi, K. Kuramoto, T. Fujita, M. Kusunoki, and T. Nishida, "638-nm High Power Broad Area Laser Diodes for Display Applications" Proc. 154th Micooptics Meeting, 9-14 (2019) (in Japanese).

[2] H. Mitsuyama, T. Motoda, T. Nishida, K. Kadoiwa, and T. Yagi, "Reliability Study on High-Power 638nm Broad Stripe Laser Diode," Opt. Rev., **21** (1), 43–47 (2014).

[3] K. Kuramoto, T. Nishida, S. Abe, M. Miyashita, K. Mori, and T. Yagi, "High Power Operation of AlGaInP Red Laser Diode for Display Applications," Proc. of SPIE **9348**, 93480H (2015).

[4] T. Yagi, K. Kuramoto, K. Kadoiwa, R. Wakamatsu, and M. Miyashita, "Reliability study on high power 638-nm triple emitter broad area laser diode," Proc. of SPIE **9733**, 973305 (2016).

[5] J. W. Goodman, "Speckle phenomena in optics", Roberts &Co., Englewood (2006).

[6] A. Furukawa, N. Ohse, Y. Sato, D. Imanishi, K. Wakabayashi, S. Ito, K. Tamamura and S. Hirata, "Effective speckle reduction in laser projection displays," Proc. of SPIE **6911**, 69110T (2008).

[7] H. Murata, K. Shibasaki, K. Yamamoto, and K. Okamura, "Speckle control using high-frequency signal superposition to semiconductor laser", Opt. Rev. **21**, 79–82 (2014).

[8] T. Nishida, Y. Fujiwara, K. Yamamoto, A. Koizumi, and T. Yagi, "Speckle Reduction by Driving Current Modulation for Red Semiconductor Laser Diodes", IEEJ Trans. EIS **140**, 2, 181-186 (2020).

[9] J. Kinoshita, H. Aizawa, A. Takamori, K. Yamamoto, and H. Murata, "Angular dependence of screen speckle and fiber speckle of coupled output of nine high-power blue laser diodes through a multi-mode fiber", Opt. Rev. **23,** 121-132 (2016).

LDC2020 | Oral Presentation
# Light sources and components 1
2020年4月23日(木) 09:45 〜 10:30 301 (Conference Center)

[LDC7-02] Monolithic single-mode diode lasers at 633 nm with high coherence and reliability for holographic printing

*Katrin Paschke[1], G. Blume[1], J. Pohl[1], B. Sumpf[1], D. Feise[1], P. Ressel[1], A. Sahm[1], N. Werner[1], J. Hofmann[1]　(1. Ferdinand-Braun-Institut)

We will present redemitting DBR-tapered-diode-lasers at 633-nm which provide 200-300mW of optical power with coherence lengths of about 0.5m for more than 10,000h, which is suitable for holographic printing, interferometry or various types of spectroscopy.

Monolithic single-mode diode lasers at 633 nm with high coherence and reliability for holographic printing

K. Paschke, G. Blume, J. Pohl, D. Feise, P. Ressel, A. Sahm, N. Werner, J. Hofmann, B. Sumpf

Ferdinand-Braun-Institut, Leibniz-Institut für Höchstfrequenztechnik Gustav-Kirchhoff-Straße 4; 12489 Berlin; Germany

Abstract: *High coherence red-emitting light sources are required for laser applications such as holographic printing, interferometry or various types of spectroscopy. As many of such applications are moving out of the lab into real world environment there is a high demand for small sized, efficient and reliable laser sources, for which semiconductor lasers are preferred. We will present red-emitting DBR tapered diode lasers at 633 nm which provide 200 to 300 mW of optical power with coherence lengths of about 0.5 m for more than 10 000 h.*

1. Introduction

Diode lasers at 633 nm are in demand for a variety of applications due to their inherent advantages such as high visibility together with significant electro-optical conversion efficiency, small size, robustness, reliability and ease of use. However, when used in areas such as 3D holographic-based printers [1], holographic displays [2] or laser interferometry [3], red-emitting diode lasers must meet additional spectral and spatial coherence requirements such as a single spectral mode emission and diffraction limited beam quality. Also the optical output power should exceed a hundred milliwatts.

A promising concept to achieve a high output power with narrow spectral width and diffraction limited beam quality is the use of tapered diode lasers featuring a distributed Bragg reflector as wavelength selective rear-side mirror (see Fig. 1) [4].
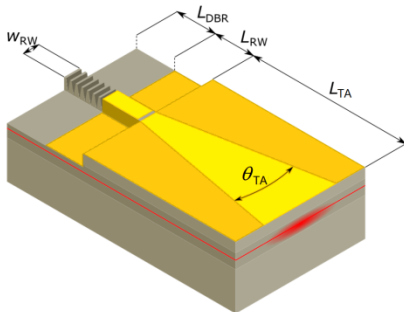

Fig. 1. Schematic of a distributed Bragg reflector tapered laser (DBR-TPL).

2. Concept and device manufacturing

While we have previously presented high power (up to 1 W) distributed Bragg reflector tapered diode lasers (DBR-TPL) at 635 – 639 nm [5], these lasers still lack the necessary spatial ($M^2 \sim 3$) and temporal coherence ($L_c = 5$ cm) as well as the lifetime ($\tau \sim 3000$ h) for the envisioned applications. Now, we present improved DBR-TPLs with higher electro-optical efficiency at reduced total power. Nevertheless, the devices feature better coherence properties and longer lifetimes at power levels of 200 to 300 mW. To achieve this we designed a laser structure with a single quantum well further away from the Matthew-Blakeslee critical thickness. The

length of the tapered section (L_{TA}) was reduced from 1500 to 1250 µm and the flare angle (θ_{TA}) was reduced from 4° to 3°. The width of the ridge waveguide (w_{RW}) was adapted from 5.0 µm to 7.5 µm to match the flare angle of the taper. The lengths of the RW and the DBR sections are $L_{RW} = 250$ µm and $L_{DBR} = 500$ µm, respectively. This gives a total device length of 2000 µm. The period of the DBR-grating Λ_{DBR} was set to 974 nm to match the desired lasing wavelength of 633 nm. The chip facets were passivated and coated to obtain a front facet reflectivity of $R_f = 5\%$ and an anti-reflection coating at the rear facet of better than 0.1%. The chips were mounted with the epitaxial side on a CVD diamond submount with a common p-contact for RW and TA section. The chip on submount was soldered onto a conductively cooled (CCP) heat sink with CS-type form factor (see inset in Fig. 2).

3. Device performance

Mounted devices were screwed onto a temperature controlled heat sink and driven with a laser diode driver. Forward voltage and optical output power are recorded as a function of current (see Fig. 2).
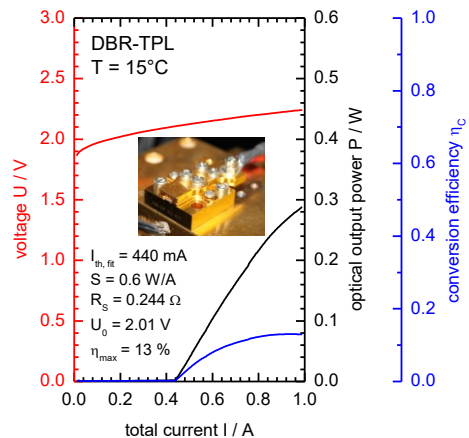

Fig. 2. Voltage-, power- and efficiency-current characteristics of a DBR-TPL. The inset shows a mounted laser on a CS-type CCP mount.

At a heat sink temperature of 15°C the threshold current is $I_{th} = 440$ mA and the slope efficiency $S = 0.6$ W/A. At $I = 1$ A the lasers emitted about 288 mW and required a

forward voltage of 2.24 V, giving an electro-optical conversion efficiency of about 13 %.

The spectrum is single mode in the whole current range with several mode hops typical for DBR-lasers (not shown). At 700 mA and an optical output power of 150 mW a spectrum was recorded with a high resolution spectrometer (LTB Elias II) with a resolution of about 100 pm (see Fig. 2).
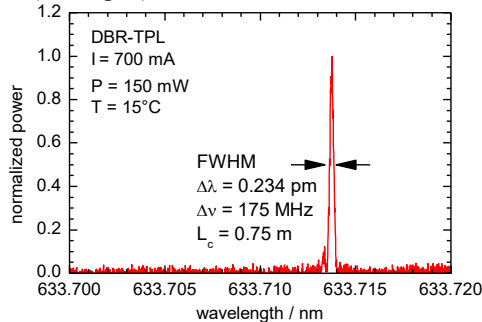

Fig. 3. High resolution spectrum of a DBR-TPL at 150 mW.

The emission shows a full width at half maximum (FWHM) of about 0.23 pm, which corresponds to a coherence length of 75 cm.

The spatial emission in the fast axis of an edge emitting laser is usually diffraction limited due to the small size of the vertical waveguide. The beam quality in the slow axis depends on the laser chip geometry and was recorded with a moving slit setup. The normalized intensity profiles are shown in Fig. 4.
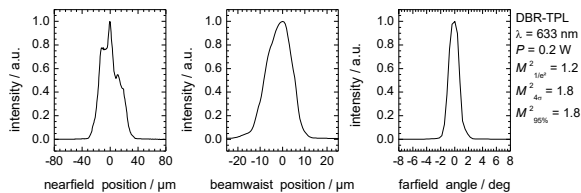

Fig. 4. Slow axis beam quality. Normalized intensity profiles at the facet (near field), the virtual beam waist within the chip and the far field.

The $1/e^2$ widths of the beam waist and the far field result in a beam quality factor M^2_{1/e^2} of 1.2, indicating an emission close to the diffraction limit. Using other diameter definitions, such as second order moments or 95% power content, result in a higher M^2 value of 1.8.
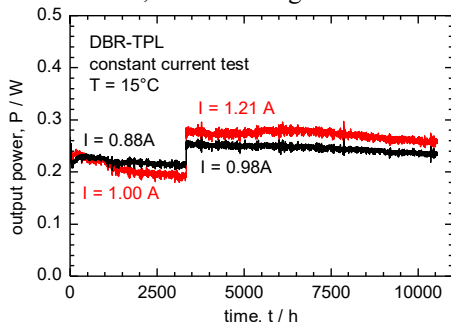

Fig. 5. Power transients at 200 - 300 mW of two DBR-TPL over more than 10 000 h.

The lifetime of two DBR-TPL devices was tested at a power level between 200 and 300 mW and they were operated for more than 10 000 h (see Fig. 5).

The DBR-TPL were also used to illuminate a holographic plate previously recorded with a HeNe laser (see Fig. 6).

Fig. 6. Picture of a hologram demonstrator using a 633 nm DBR-TPL for illumination.

7. Conclusions

We demonstrated the design and manufacturing of DBR-TPL at a wavelength of 633 nm. The output power, coherence properties and lifetimes are suitable for holography, so that these devices might be suitable light sources for interferometry and next generation holographic printers.

References

[1] Y. Gentet, and P. Gentet, "CHIMERA, a new holoprinter technology combining low-power continuous lasers and fast printing," Applied Optics **58** (34), G226-G230 (2019).

[2] S. Reichelt, R. Häussler, G. Fütterer, N. Leister, H. Kato, N. Usukura, and Y. Kanbayashi, "Full-range, complex spatial light modulator for real-time holography," Optics Letters 37 (11), 1955-1957 (2012).

[3] R. Yang, F. Pollinger, K. Meiners-Hagen, J. Tan, and H. Bosse, "Heterodyne multi-wavelength absolute interferometry based on a cavity-enhanced electro-optic frequency comb pair," Optics Letters 39 (20), 5834-5837 (2014).

[4] B. Sumpf, K. Paschke, "Spectrally stabilized high-power high-brightness DBR-tapered lasers in the VIS and NIR range," Proc. SPIE 10518, 1051817 (2018).

[5] D. Feise, W. John, F. Bugge, C. Fiebig, G. Blume, and K. Paschke, "High-spectral-radiance, red-emitting tapered diode lasers with monolithically integrated distributed Bragg reflector surface gratings," Opt. Express 20 (21), 23374-23382 (2012).

LDC2020 | Oral Presentation
Light sources and components 1
2020年4月23日(木) 09:45 ～ 10:30 301 (Conference Center)

[LDC7-03] High-direction and low-coherence semiconductor laser with dumbbell-type cavity

*Linhai Xu[1], Yufei Wang[1], Yufei jia[1], Wanhua Zheng[1] （1. Institute of Semiconductors, CAS）

We reported an electrically pumped dumbbell-type semiconductor laser with low-coherence and high-direction, which exhibits great potential application value in laser display.

High-direction and low-coherence semiconductor laser with dumbbell-type cavity

Linhai Xu[1,2,3], Yufei Wang[1,2,3], Yufei Jia[1,2,3], Wanhua Zheng[1,2,3]*

[1] Laboratory of Solid State Optoelectronics Information Technology, Institute of Semiconductors, CAS. Beijing 100083, China
[2] College of Future Technology, University of Chinese Academy of Sciences. Beijing 101408, China
[3] State Key Laboratory on Integrated Optoelectronics, Institute of Semiconductors, CAS. Beijing 100083, China
*whzheng@semi.ac.cn

Abstract: *We reported an electrically pumped dumbbell-type semiconductor laser with low-coherence and high-direction, which exhibits great potential application value in laser display.*

1. Introduction

Speckle produced by high spatial coherence can cause serious damage to the imaging quality of systems using lasers as illumination source. The amount of speckle is determined by the speckle contrast ratio C, which is defined by $\sigma/<I>$, where σ is a standard deviation of the intensity fluctuation, $<I>$ is an average intensity [1]. At present, there are two types of methods to solve the laser speckle problem, one is to add components outside the laser to eliminate speckles, and the other is to reduce the laser coherence [2]. The former requires complex systems and time-consuming, while the latter has poor directivity and power.

In this work, we fabricated an electrically driven laser with high directivity and low coherence at 635nm. The shape of the cavity is a dumbbell-type cavity structure. The laser with a horizontal far-field divergence angle of 7.7 °, a speckle contrast of 5%, and a maximum output power of 2.36 W was obtained.

2. Design and device fabrication

Fig. 1 shows the schematic diagram of the dumbbell-type cavity. As shown in Figure 1, the dumbbell-type cavity consists of three parts. Within the red box (areas I and III), two curved mirrors perpendicular to the cavity axis form a concentric cavity. And the left facet of the dumbbell-type cavity provides a straight sidewall mirror for the concentric cavity in area I. The right facet of the dumbbell-type cavity has the same effect for the concentric cavity of area III. FP cavity (area II) inside the blue box connects two concentric cavities. By adjusting parameters of the cavity properly, the cavity can form one-dimensional FP mode, two-dimensional chaotic mode and hybridized modes between them.
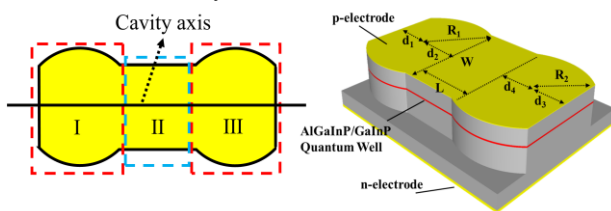

Fig. 1. Schematic diagram of the dumbbell-type cavity.

Fig. 2 shows the mode intensity distribution of the passive dumbbell-type cavity with parameters of $R_2=R_1=10$ μm, $d_1=d_2=d_3=d_4=0.5R_1$, $W=(R_1{}^2-d_1{}^2)^{1/2}$, $L=0.5W$. In the simulation, we can observe that the two-dimensional ring-shaped unstable modes generated by the concentric cavity expands significantly in the cavity and the number of modes greatly increases in the cavity. At the same time, the FP modes formed by the reflection of the cavity facets greatly improves the directivity of the laser. In experiments, we used lithography and ICP etching to prepare devices.
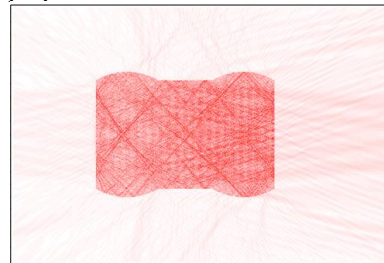

Fig. 2. Simulated mode intensity distribution of the passive dumbbell-type cavity

3. Experiment results

In the experiment, $R_1=R_2=250$ μm, other parameters are consistent with the simulation. Fig. 3(a) shows output power and voltage as a function of injection current for dumbbell-type cavity laser. Output power at 6A (40 μs 100 Hz and TEC 20 ℃) is 2.36 W. Fig. 3(b) shows lasing spectrum in the case of 2.36-W output power. The full width at half maximum of the spectrum is about 2nm, and there are many sharp peaks in the spectrum, which proves that our device has formed a large number of transverse modes.
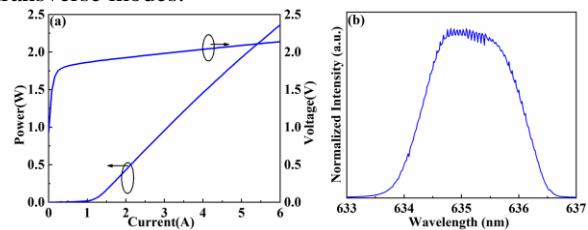

Fig. 3. (a) Output power and voltage as a function of injection current for dumbbell-type cavity laser.

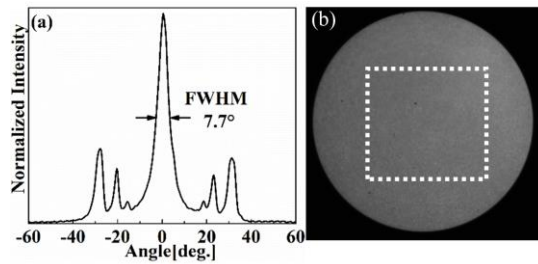(b) Emission spectrum of dumbbell-type cavity laser.

Fig. 4. (a) Horizontal far-field profiles of dumbbell-type cavity laser. (b) Speckle patterns of dumbbell-type cavity laser.

Fig. 4(a) shows horizontal far-field profiles of dumbbell-type cavity laser at 2.36 W. It is worth highlighting that the horizontal far-field divergence angle (FWHM) of our device is only 7.7 °. Fig. 4(b) shows speckle pattern of dumbbell-type cavity laser. Speckle contrast of the laser is as low as 5%.

4. Conclusions

In this work, we reported a dumbbell-type cavity laser with speckle contrast of 5% and horizontal far-field divergence angle of only 7.7 °. The maximum output power under pulse conditions also reached 2.36 W. This laser has huge potential application value in the field of laser display

References

[1] J. W. Goodman, *Statistical Properties of Laser Speckle Patterns* (Springer, 1975), pp. 9–75.

[2] H. Cao, R. Chriki, S. Bittner, A. A. Friesem, and N. Davidson, "Complex lasers with controllable coherence," Nature Reviews Physics 1, 156–168 (2019).

LDC2020 | Oral Presentation

Light sources and components 2
Session Chair: Tatsushi Hamaguchi(Sony)
Thu. Apr 23, 2020 10:45 AM - 12:15 PM 301 (Conference Center)

[LDC8-01] Progress in semipolar GaN-based VCSELs

*Jared A Kearns[1], Joonho Back[2], Nathan C Palmquist[1], Daniel A Cohen[1], Steven P DenBaars[1,2], Shuji Nakamura[1,2] (1. Materials Department University of California, Santa Barbara, 2. Department of Electrical and Computer Engineering, University of California, Santa Barbara)
10:45 AM - 11:15 AM

[LDC8-02] High Power Static Phosphor Light Source for Cinema Projectors

*Kenneth Li[1] (1. Optonomous Technologies Inc.)
11:15 AM - 11:30 AM

[LDC8-03] Interference Pattern Generation of Multi-wavelength Yellow-Orange Lasers Using Chi$^{(2)}$ Nonlinear Photonic Crystals

Bai-Wei Wu[1], Kai-Hsun CHANG[1,2], Safia Mohand Ousaid[2], Azzedine BOUDRIOUA[2], Hiroyuki YOKOYAMA[3], Chih-Ming Lai[4], *Lung-Han Peng[1,2,3] (1. National Taiwan University, 2. Université Paris 13, 3. Tohoku University, 4. Ming Chuan University)
11:30 AM - 11:45 AM

[LDC8-04] High-Frequency Modulation of RGB Semiconductor Lasers for High-Resolution Scanning Displays

*Kiyoshiro Yamanaka[1], Hiroshi Murata[1,2], Junichi Kinoshita[2], Kazuhisa Yamamoto[2] (1. Mie University, 2. Osaka University)
11:45 AM - 12:00 PM

[LDC8-05] 645 nm lasers with a low vertical divergence angle for laser display

*Yufei Jia[1], Yufei Wang[1], Linhai Xu[1], Wanhua Zheng[1] (1. Institute of Semiconductors, CAS)
12:00 PM - 12:15 PM

LDC2020 | Oral Presentation
Light sources and components 2
2020年4月23日(木) 10:45 ～ 12:15 301 (Conference Center)

[LDC8-01] Progress in semipolar GaN-based VCSELs

*Jared A Kearns[1], Joonho Back[2], Nathan C Palmquist[1], Daniel A Cohen[1], Steven P DenBaars[1,2], Shuji Nakamura[1,2] （1. Materials Department University of California, Santa Barbara, 2. Department of Electrical and Computer Engineering, University of California, Santa Barbara）

Semipolar vertical-cavity surface-emitting lasers with ion-implanted apertures and buried tunnel junction apertures are compared. The effect of changing the out-coupling mirror reflectivity is calculated to project the potential effect on output power.

Progress in Semipolar GaN-based VCSELs

Jared A. Kearns[1]*, Joonho Back[2], Nathan Palmquist[1], Daniel A. Cohen[1], Steven P. DenBaars[1,2], Shuji Nakamura[1,2]

[1] Materials Department, University of California, Santa Barbara, CA 93106, USA; [2] Department of Electrical and Computer Engineering, University of California, Santa Barbara, CA 93106, USA

*kearns@ucsb.edu

Abstract: *Blue semipolar ($20\bar{2}\bar{1}$) vertical-cavity surface-emitting lasers with ion-implanted apertures and buried tunnel junction apertures (BTJ) are fabricated and compared to show that the BTJ's reduced absorption improves device performance. The effect of changing the out-coupling mirror reflectivity is calculated to project the potential of these devices with minor structural changes.*

1. Introduction

Group III-Nitride vertical-cavity surface-emitting lasers (VCSELs), with their low threshold currents, circular beam profile, and 2D arraying capabilities, are advantageous for applications ranging from lighting and displays, to communications or optical sensing. While research has predominately occurred on c-plane based devices, semipolar planes provide several advantages for blue emission and potentially provide a pathway for efficient green VCSELs. Compared to c-plane, semipolar planes show a reduced quantum confined Stark effect; higher theoretical material gain; a lower transparency current density; inherently polarized emission parallel to the a-direction; and, in some cases, higher indium incorporation [1]. Few demonstrations of semipolar VCSELs have been reported and understanding their device characteristics is important for moving forward.

Two device structures are considered, one with an Al ion implantation (IIA) defined aperture, and one with a buried tunnel junction (BTJ) defined aperture.

2. Method

The ion implanted aperture (IIA) devices used a dual-dielectric DBR design with substrate removal via selective photoelectrochemical etching of a sacrificial layer as described in Ref [2]. To define the aperture, Al ion implantation was performed after an initial MOCVD growth. TJs were grown by MOCVD prior to further processing, with the end result shown in Fig. 1 (a).

The majority of the processing for the BTJ devices was similar to that of the IIA design and is described in more detail in Ref [3]. Unlike the top-hat design of the IIA electron blocking layer (EBL), the BTJ devices utilized a 10 nm total EBL with the last 5nm of AlGaN graded to GaN on the p-side. To form the aperture in these devices, a thin n++GaN layer was grown to form a tunnel junction. Afterwards, the TJ layers were etched away everywhere outside the apertures, leaving only lightly doped p-GaN. The third MOCVD growth of n-GaN provided the current spreader.

3. Results

Fig. 2(A) shows that for the IIA devices the peak power was 1.85 mW and the threshold current density and voltage were 4.6 kA/cm^2 and 7 V, respectively. The differential efficiency was 2.4% for the mode at 445 nm. The emission was nearly 100% polarized parallel to the a-axis direction. Using a 1D transmission matrix model, the internal loss (13 cm^{-1}), the mirror loss (1.2 cm^{-1}), and the relative power out of each side of the device (93% from the top) were estimated for an ideal device. Assuming an injection efficiency of 60%, as seen in comparable semipolar ($20\bar{2}\bar{1}$) edge emitting lasers [4], an
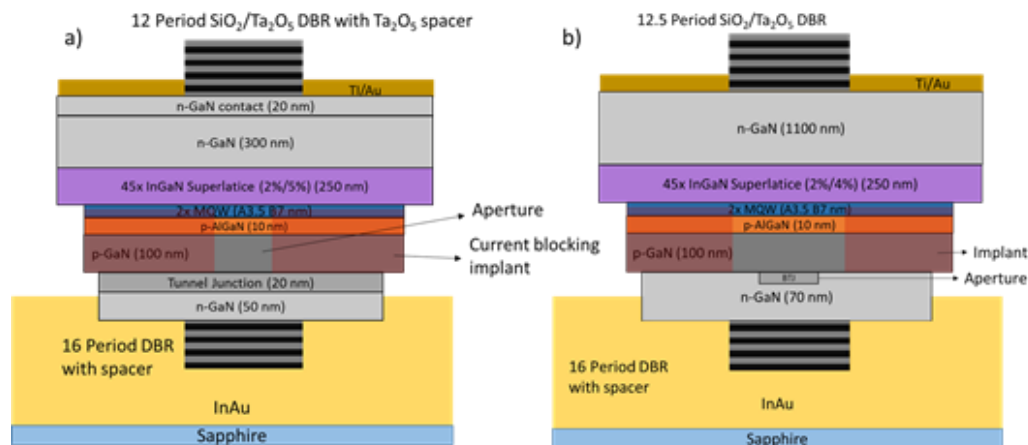

Fig 1. Shows the device structure of the IIA (a) and the BTJ (b) device designs. The implant present in the BTJ design is used to protect the active region during PEC etching and is placed far enough from the aperture to ensure there is no overlap with the mode.
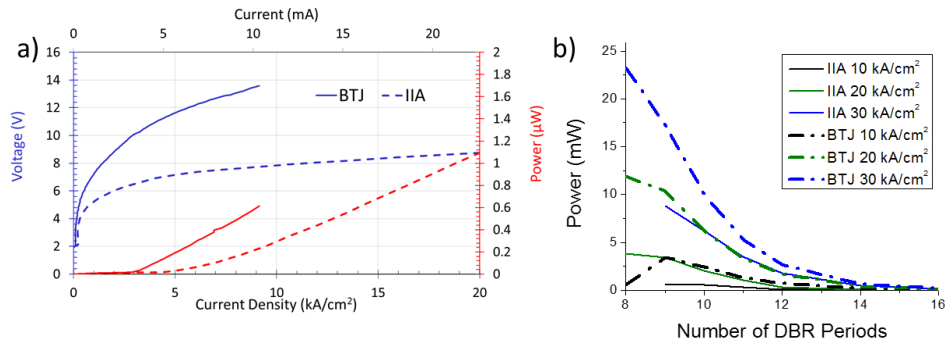
Fig 2. (a) The light-current-voltage (LIV) for the IIA and BTJ VCSELs under pulsed operation. (b) The output power vs number of DBR periods at several current densities.

additional 15 cm^{-1} of loss was estimated to exist based on the measured differential efficiency. This additional loss is likely due to a misalignment of the standing wave with the TJ, roughness induced scattering, overlap of the mode with the metal contact and the implanted area, as well as absorption in the DBR.

As shown in Ref. [2], the misalignment of the mode introduced ~0.6 cm^{-1} (0.3-1 cm^{-1}) of loss due to overlap with the implant and 6 cm^{-1} (3-12 cm^{-1}) of loss from the metal. The rest of the excess loss was likely due to roughness propagating from the GaN interface into the DBR or absorption loss in the DBR layers. The loss is quite sensitive to both of these parameters, so a small increase in either could cause the extra loss.

The BTJ samples were analyzed under both pulsed and CW operation, with LIV characteristics of a 12 μm aperture diameter VCSEL shown in Figure 2 (a). Under CW operation, the threshold current was 2.7 mA, the differential efficiency was 4%, and the maximum output power was 256 μW for a lasing mode at 452 nm. Using a TMM to estimate the sources of loss, as done for the IIA VCSELs, resulted in an expected 10 cm^{-1} of internal loss, 0.7 cm^{-1} of mirror loss, and almost no excess loss. The EBL design was improved for the BTJ devices by introducing a composition grade on the p-side to improve hole transport. This likely improving the injection efficiency. If an upper bound on the injection efficiency of 90% is assumed, similar to that obtained in high performance c-plane lasers, then the analysis predicts an upper bound on the excess loss of 6.5 cm^{-1}, similar to that observed in the IIA VCSEL. The pulsed differential efficiency improved by 20% relative to the IIA devices, likely due to the elimination of the absorption losses of the mode outside the aperture, in conjunction with an improvement in the injection efficiency by changing the EBL design. The BTJ devices suffered from high operating voltage that is believed to be due to incomplete activation of the buried p-type region and limited the maximum output power.

A key design consideration for VCSELs lies in the compromise between threshold current density and differential efficiency, primarily controlled by the number of layer pairs in the out-coupling DBR to affect its reflectivity. The effect of changing the number of periods in the top DBR on the output power for the BTJ and IIA samples was calculated using the reflectivity values found using TFCalc, and the gain curve found for semipolar edge emitting laser diodes with a similar active region. Figure 2 (b), shows that as the number of periods is decreased the output power increases, up to a certain extent. For the BTJ devices at 20 kA/cm^2, the output power with a 9 period DBR would be less than for a 10 period DBR due to the higher threshold current density of 9 period devices. Moving to a 10 period DBR is expected to lead to a 250 % increase (2.4 mW) in the output power at 10 kA/cm^2 for the BTJ devices, and 85% (0.6 mW) for the IIA devices, while increasing the threshold current density by 25% and 40%, respectively.

4. Conclusion

In conclusion, semipolar IIA VCSELs were fabricated and were analyzed to determine the main sources of loss. The BTJ devices showed an improved η_d of 4% under CW operation, but were limited in output power by their high operating voltage. The effect of changing the number of DBR periods was calculated to show that using a 10 period DBR should have increased the pulsed power by 280% at 30 kA/cm^2 for the BTJ devices.

References

1. L. Schade, U. T. Schwarz, T. Wernicke, M. Weyers, and M. Kneissl, "Impact of band structure and transition matrix elements on polarization properties of the photoluminescence of semipolar and nonpolar InGaN quantum wells," Phys. status solidi **248**, 638–646 (2011).

2. J. A. Kearns, J. Back, D. A. Cohen, S. P. DenBaars, and S. Nakamura, "Demonstration of blue semipolar (202̄1̄) GaN-based vertical-cavity surface-emitting lasers," Opt. Express **27**, 23707 (2019).

3. J. A. Kearns, J. Back, N. C. Palmquist, D. A. Cohen, S. P. DenBaars, and S. Nakamura, "Inhomogeneous Current Injection and Filamentary Lasing of Semipolar (2021̄) Blue GaN- Based Vertical- Cavity Surface- Emitting Lasers with Buried Tunnel Junctions," Phys. status solidi 1900718 (2019).

4. D. L. Becerra, D. A. Cohen, S. Mehari, S. P. DenBaars, and S. Nakamura, "Compensation effects of high oxygen levels in semipolar AlGaN electron blocking layers and their mitigation via growth optimization," J. Cryst. Growth **507**, 118–123 (2019).

LDC2020 | Oral Presentation
# Light sources and components 2
2020年4月23日(木) 10:45 ～ 12:15 301 (Conference Center)

[LDC8-02] High Power Static Phosphor Light Source for Cinema Projectors

*Kenneth Li[1] （1. Optonomous Technologies Inc.）

This paper describes a compact static phosphor system in which the static phosphor plate could be mounted on traditional heat sinks by which the heat can be removed effectively. The effective emission area is increased by a lightweight rotating optics scanning for focused spot onto the phosphor plate while maintaining the original etendue of the focused spot. The resulting high output can be used for cinema projectors and other high power applications.

High Power Static Phosphor Light Source for Cinema Projectors

Kenneth Li

Optonomous Technologies Inc., 30330 Rainbow View Ct., Agoura Hills, CA 91301, USA, +1-661-803-9939,
kenli@optonomous.com

Abstract: This paper describes a compact static phosphor system in which the static phosphor plate could be mounted on traditional heat sinks by which the heat can be removed effectively. The effective emission area is increased by a lightweight rotating optics scanning for focused spot onto the phosphor plate while maintaining the original etendue of the focused spot. The resulting high output can be used for cinema projectors and other high power applications.

1. Introduction
Laser excited phosphor systems have been used extensively for digital projectors overcoming the issues with power compared with LEDs and issues with lifetime compared with arc lamps. Due to the low temperature operation of the phosphor materials and the tendency to burn at high power, most system uses a phosphor wheel in which the phosphor materials could not be heat sunk effectively. Higher temperature materials such as ceramic phosphor, glass phosphor, and crystal phosphor have been developed, which increase the ceiling of the maximum output. On the other hand, they are still not sufficient for the power levels required by high power spotlight and digital cinema applications without a phosphor wheel. This paper describes a compact static phosphor system in which the static phosphor plate could be mounted on traditional heat sinks by which the heat can be removed effectively. The resulting high output can be used for cinema projectors and other high power applications..

2. Phosphor Wheel versus Static Phosphor
Figure 1(a) shows a traditional phosphor wheel used in high power laser phosphor light sources. As the phosphor wheel is rotation, the excitation laser will be scanning the phosphor wheel effectively increasing the exciting areas of the phosphor lowering the average temperature of the phosphor. Figure 1(b) shows a static phosphor system in which the phosphor material is place on top of a heat sink, which would be mounted on a larger heat sink for heat removal. Due to the limit of the maximum damage threshold of the phosphor and rate of heat dissipation, the power limit will not be high enough for high power applications.
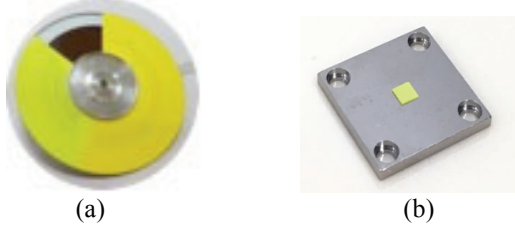

(a)   (b)

Figure 1 – Phosphor Wheel versus Static Phosphor

A typical static phosphor system disclosed in a patent as shown in Figure 2, describes a rotating system in which the excitation laser beam and the output white light beam are at the axis of a rotating system. The input and output are reflected to the perimeter of the rotation in which a system of collimating lens is used to scan the phosphor along the path and at the focus of the collimating lens. The output is collected by the collimating lens and transmitted back to the axis of rotation and directed to the output. There are many parts need to be rotated making the system bulky and expensive.

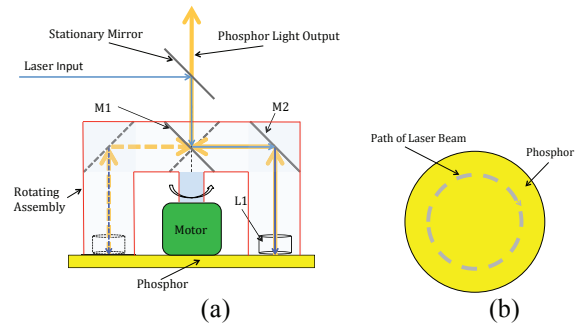(a)   (b)

Figure 2 – A typical static phosphor scanning system and its corresponding laser path

3. Compact OTI™ Scanning Focus Beam System
In this paper, a compact patent pending scanning focus beam static phosphor system as shown in Figure 3 is presented in which the static phosphor plate could be mounted on traditional heat sinks by which the heat can be removed effectively.
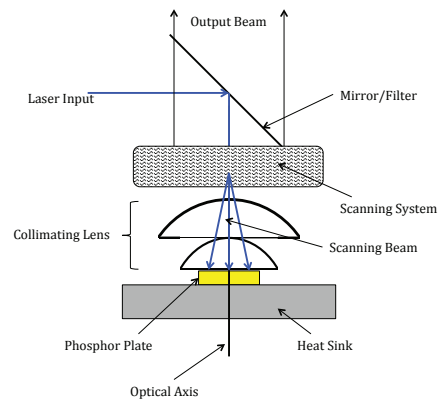

Figure 3 – An OTI Scanning Focus Beam Static Phosphor System

The system consists of a beam scanning module in which the input laser beam will be made scanned in a circular, raster scanned, and other random fashion as required by the design. The output beam is then focused onto the static phosphor by the collimating lenses, which will collimate the excited phosphor emission to the output as a parallel beam. After passing through the scanning module, the output beam will have the same optical axis as the input laser beam. The optical path of the scanning laser beam is shown in Figure 4 with a specific example of operation. The key to the design is that when the laser beam scans the phosphor plate, it creates a much larger effective focused spot such that the power density is lower and it provides as larger area for heat sinking. At the same time, the scanning system allows the output beam to be stationary such that the etendue of the system is determined by the focused spot alone, and not the full size of the scanned path.
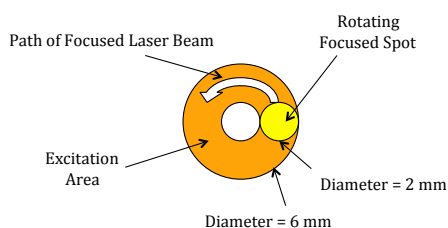

Figure 4 – Scanning Path of the Laser Beam

4. Expected Performance of the Example System

The limit for using a static phosphor plate as shown in Figure 1(b) is the limit of heat sinking of the intrinsic phosphor material and the power threshold in which the phosphor conversion efficient reaches a maximum. Such limits are usually in the range of about 40 to 60 optical watts per sq. mm. This severely limits the applications of static phosphor to higher power applications such as digital cinema projectors. To overcome such limitations, the OTI scanning focus beam system is used to produce a scanned phosphor pattern as shown in Figure 4, resulting in a much larger effective area while maintaining the output beam being stationary, keeping the same etendue as a non-scanning laser beam.

To demonstrate the applicability of such a system, the follow target system is evaluated and to be built for demonstration. In this example, a focused spot size of 2 mm is assumed, which is the requirement from most high power projector manufacturers. With a power density limit of 50 lm/W and an efficiency of 300 lm/W, the total output is 15,000 lumens, which will be sufficient for a projector with screen output in the 3,000 to 5,000 ranges without a scanning focus beam system. With this scanning focused beam system, assuming the scanned circle is 6 mm in diameter, the total focused area is 8 times the size of the original 2 mm spot. As a result, the total output from the phosphor is 120,000 lumens allowing projectors to have screen lumens in the 24,000 to 40,000 lumens ranges. Allowing further increase in output power, an increase of scanned circle diameter will increase the output power. For example, if the outer diameter is increased from 6 mm to 8 mm, the screen lumen can be increased to by 12 times instead of 8 times. In this case, the projector output will be in the 36,000 to 60,000 lumens ranges. Again, further power increase can be achieved by further increase in outer diameter while the etendue remains to be the same as that of the 2 mm spot.

Preliminary experiments have been performed using a bench top system. The output beam is directed to a screen at a distance while the laser is being scanned onto the phosphor plate. Figure 5 shows the location of the output beam relative to the cross hair with the scanner OFF and with the scanner ON. This shows that the output beam remains the same during the focus beam scanning operation.
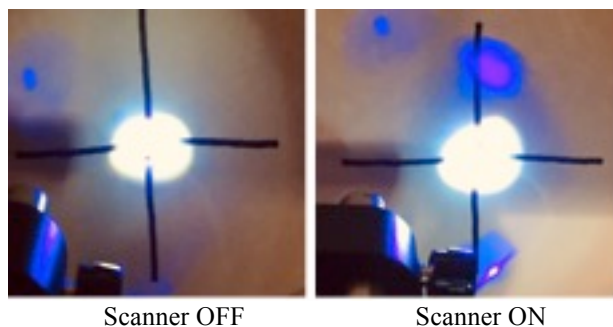

Scanner OFF   Scanner ON

Figure 5 – Location of Output Beam with the Scanner OFF and ON

Besides this system, several other systems are also designed and will be reported as they are developed. These systems are targeted to provide simpler architectures and higher overall conversion and collection efficiencies.

4. Conclusion

Using a compact patent pending OTI Scanning Focus Beam static phosphor system, it has been demonstrated that the scanned focused spot occupies a larger area for better heat sinking, thus increases the power handling capacity of the system. At the same time, the output beam remains stationary preserving the original etendue of the system. The system is flexible in design and will provide more than enough output power for the current cinema projector applications.

Light sources and components 2

2020年4月23日(木) 10:45 ～ 12:15 301 (Conference Center)

[LDC8-03] Interference Pattern Generation of Multi-wavelength Yellow-Orange Lasers Using Chi[(2)] Nonlinear Photonic Crystals

Bai-Wei Wu[1], Kai-Hsun CHANG[1,2], Safia Mohand Ousaid[2], Azzedine BOUDRIOUA[2], Hiroyuki YOKOYAMA[3], Chih-Ming Lai[4], *Lung-Han Peng[1,2,3] （1. National Taiwan University, 2. Université Paris 13, 3. Tohoku University, 4. Ming Chuan University）

We report tri-wavelength 580, 590, and 600nm yellow-orange lasers based on PPLT nonlinear photonic crystals composed of double-slit OPOs and chirped SHG structures. It enables coherent interference of SHG with a green to yellow-orange conversion slope efficiency >8% and an interference pattern with visibility of 0.61.

Interference Pattern Generation of Multi-wavelength Yellow-Orange Lasers Using χ(2) Nonlinear Photonic Crystals

Bai-Wei WU[1], Kai-Hsun CHANG[1,2], Sofia Mohand Ousaid[2], A. BOUDRIOUA[2], H. YOKOYAMA[3], C-M. Lai[4], L-H PENG [1,2,3]

[1] Inst. Photonics and Photonics, National Taiwan University, Taipei 106, Taiwan, R.O.C.

[2] Laboratoire de Physique de Lasers CNRS UMR 7538, Université Paris 13, Sorbonne Paris Cité, 93430Villetaneuse, France

[3] New Industry Creation Hatchery Center, Tohoku University, Sendai 980-8579, Japan

[4] Department of Electronic Engineering, Ming Chuan University, Taoyuan 333, Taiwan, R. O. C.

Phone: +886-2-33663700#439 Fax: +886-2-2367-7467 Email: r07941071 @ntu.edu.tw

Abstract: *We report tri-wavelength 580, 590, and 600nm yellow-orange lasers based on PPLT nonlinear photonic crystals composed of double-slit OPOs and chirped SHG structures. It enables coherent interference of SHG with a green to yellow-orange conversion slope efficiency > 8% and an interference pattern with visibility of 0.61.*

1. Introduction

Yellow-orange lasers cover a spectral range where oxyhemoglobin and melanin can find strong optical absorption [1]. Such properties make yellow-orange lasers valuable tools in ophthalmology and dermatology such as for vascular treatment and pigment removal. Yellow lasers can also facilitate scientific research in the STED (stimulated emission depleted) microscopy for bio-imaging with improved resolution [2].

Yellow lasers can be pursued by using atomic transitions in Dy or Tb doped crystals but the latter are still under-development [3]. Commercial yellow lasers were known to adopt optical pumped Nd:YAG [4] or semiconductor VCSEL [5] to generate NIR followed by intra-cavity SHG for yellow emission. It not only encounters complicated optics deign but suffers from the low efficient nonlinear crystals like LBO.

To improve the optical power to watt level and increase the energy conversion efficiency, conventional wisdom has resorted to a use of $\chi^{(2)}$ nonlinear photonic crystal (NPC) such as PPLN or PPLT. The latter can be directly pumped by high power NIR fiber- or diode-amplifiers [2, 6-7]. In this work, we report an approach of using PPLT-NPC to achieve coherent generation of tri-wavelength yellow-orange lasers. It can emit more than 20mW output power with a green to yellow-orange conversion slope efficiency > 8% from an uncoated PPLT made of cascaded OPO-SHG structures.

2. Experiment setup and results

To generate NIR wavelength in the 1150-1200nm spectral range for wavelength conversion, we adapted a design of having tri-QPM-OPO gratings in parallel but spaced with a double-slit like non-inverted structure. A combination of such OPO structure with a chirp QPM-SHG section enables interference pattern generation of 580, 590, and 600nm SHG yellow-orange light in the far field. Such spatial overlapping of multi-wavelength SHG yellow-orange beams, compared with single-wavelength yellow laser, can enhance light absorption in tissues containing oxyhemoglobin and melanin.

Shown in Fig.1 is a photograph of PPLT-NPC used in this work. For the tri-OPO part, it has a crystal length of 18mm and contains QPM periodicity of 7.67, 7.69, and 7.71 μm, respectively. In addition a double-slit region of non-inverted domains with 8 μm width and 22 μm distance was inserted between the QPM gratings. The aforementioned structure was monolithically cascaded with chirp-SHG segments composed of three QPM structures, each of 9.85, 10.49, and 10.84 μm period and 3 mm-length.
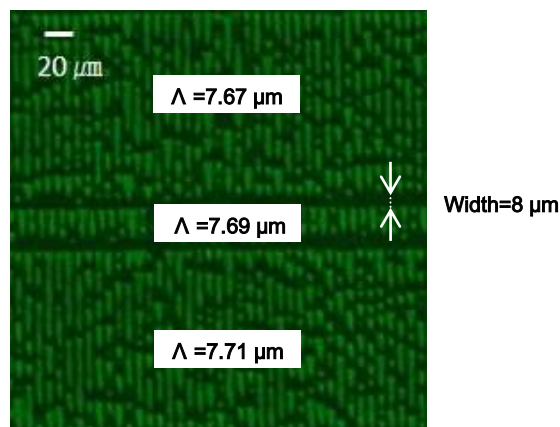

Fig. 1 Photograph of a QPM-OPO-SHG PPLT

Integration of PPLT-NPC with QPM-OPO-SHG structures offers a compact cavity design with reduced optical loss. It thus favours laser oscillation at low threshold. We illustrate in the inset of Fig.2 a layout of planar-concave SRO laser cavity to realize green to yellow-orange wavelength conversion. In this experiment, the green pump beam first passes through the SHG part followed by a double pass through the OPO segment due to reflection from the output planar mirror (ROC= −10m). This equivalently increases the nonlinear interaction length for NIR-OPO and results in a low threshold value of 15 MW/cm^2 peak intensity (corresponding to 84.5 mW average power) as referred from Fig. 2. On its return, the NIR beam also makes a double pass to the chirp QPM-SHG section by reflection

from the input concave mirror (ROC= −15cm). Finally the tri-colour yellow-orange lasers transmit out of the output planar mirror. The aforementioned processes results in a green to yellow-orange conversion slope efficiency greater than 8% as referred from Fig.2.
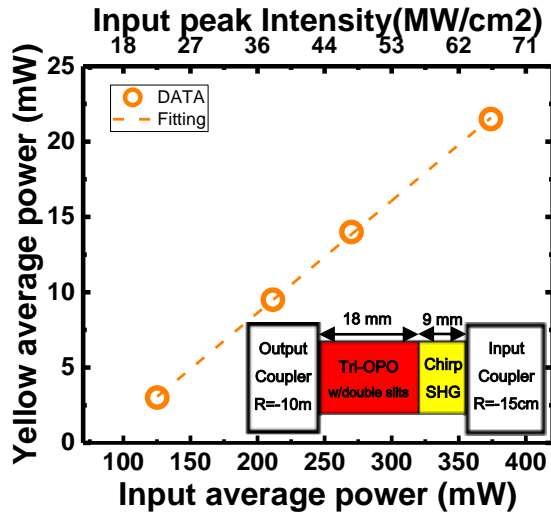

Fig.2 Green to yellow-orange conversion, Inset: layout

Overlaid in Fig.3 are the spectra of yellow-orange and NIR lasers generated from the QPM-OPO-SHG PPLT NPC. We note a one-to-one correspondence between the wavelength doubling 580, 590, and 600nm peaks and their NIR counterparts. It verifies use of monolithic $\chi^{(2)}$ OPO-SHG NPC in achieving efficient operation of multi-colour yellow lasers when the nonlinear optics processes are involved.
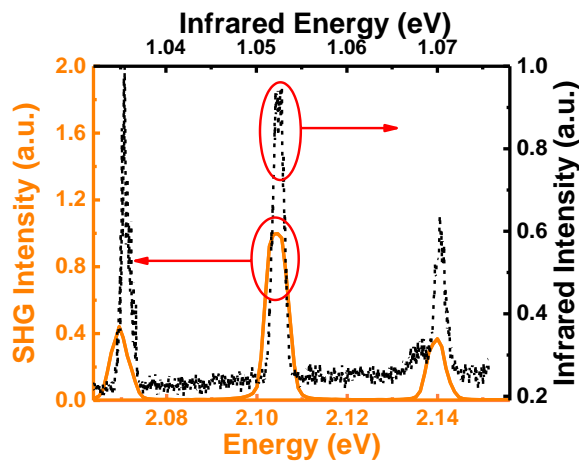

Fig.3 Spectral overlap of the yellow-orange and NIR lasers from the QPM-OPO-SHG PPLT

We further illustrate in Fig.4 the far field patterns of multi-colour yellow-orange lasers in the weak optical output power. We denote a mixing of *double slit-like* interference colour fringes versus only 580nm interference pattern in Fig.4. However, after adding a 580nm colour filter (FWHM=10nm) an interference visibility ~0.61 can be clearly resolved from Fig.4. The latter reveals the coherent properties of the 580nm SHG-

yellow laser inherent from its OPO-NIR counterpart of 1.53 nm spectral line width. On the other hand, for a multi-colour yellow-orange laser beam carrying the *double-slit* diffraction characteristics, its corresponding optical beam quality factor, M^2, would be deteriorated. The measured value for M^2_x and M^2_y is 1.9 and 4, respectively. The latter can be further improved by invoking a single mode fibre for mode shaping.
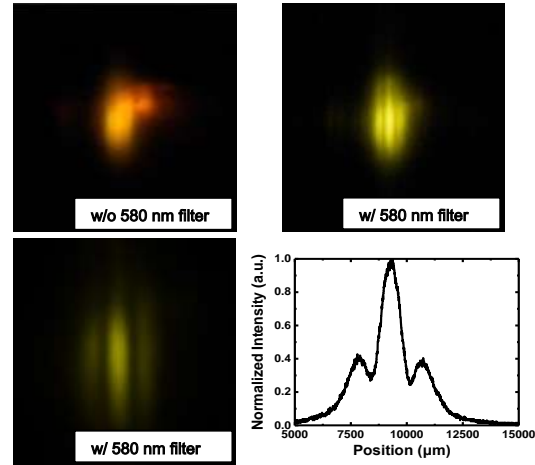

Fig.4 Far field patterns of yellow laser

4. Conclusions

We demonstrated a yellow-orange tri-color laser based on $\chi^{(2)}$ NPC made of QPM-OPO-SHG structures on PPLT. It offers a green to yellow-orange conversion slope efficiency > 8% and coherent interference from an uncoated PPLT.

References.

[1] M. A. Mainster, "Wavelength selection in macular photocoagulation," Ophthalmology **93** , 952 (1986)

[2]T. H. Runcorn et al., "Visible Raman-Shifted Fiber Lasers for Biophotonic Applications," IEEE Sel. Topics Quantum Elec. **24**, 1400208 (2018)

[3]C. Kränkel et al. "Out of blue: semiconductor laser pumped visible rare-earth doped lasers," Laser Photon. Rev. **10**, 548 (2016).

[4]J. Gao et al., "All-solid-state continuous-wave yellow laser at 561 nm under in-band pumping," J. Opt. Soc. Am. B, **30**, 95 (2013)

[5]E. Kantola et al, "High efficiency 20W yellow VCSEL," Opt. Exp. **22**, 6372 (2014)

[6]J.-H. Hung et al., "587 nm nanosecond optical pulse generation by synchronously-driven gain-switched laser diodes with optical injection locking," Appl. Phys. Exp. **12**, 082002 (2019)

[7] A. Sahm et al., "Compact Miniaturized Laser Module Emitting More Than 1.6 W of Yellow Light at 576 nm," IEEE Photon. Tech. Lett. **30**, 1878 (2018)

LDC2020 | Oral Presentation
Light sources and components 2
2020年4月23日(木) 10:45 ～ 12:15 301 (Conference Center)

[LDC8-04] High-Frequency Modulation of RGB Semiconductor Lasers for High-Resolution Scanning Displays

*Kiyoshiro Yamanaka[1], Hiroshi Murata[1,2], Junichi Kinoshita[2], Kazuhisa Yamamoto[2] （1. Mie University, 2. Osaka University）

Digital signal modulation characteristics of RGB pig-tailed laser modules were measured. Eye opening ratios over 80% were obtained in the frequency range of 100-600 MHz, which meet demands for the applications to 4-Mega-pixel displays.

High-Frequency Digital Modulation of RGB Semiconductor Lasers for High-Resolution Scanning Displays

Kiyoshiro Yamanaka[1]   Hiroshi Murata[1, 2]   Junichi Kinoshita[2]   Kazuhisa Yamamoto[2]

[1] Graduate School of Engineering, Mie University   1577 Kurima-Machiya-Cho, Tsu-City Mie 514-8507 Japan.

Phone: +81-59-231-9403   Fax: +81-59-231-9403   E-mail murata@elec.mie-u.ac.jp

[2] Institute of Laser Engineering, Osaka University   2-6 Yamadaoka, Suita, Osaka 565-0871 Japan.

Abstract: *Digital signal modulation characteristics of RGB semiconductor laser pig-tailed modules were measured in detail for the application to high-resolution scanning displays. Eye opening ratios over 80% were obtained in the repetition frequency range from 100 to 600 MHz, which meet demands for the applications to 4-Mega-pixel scanning displays.*

1. Introduction

Display/lighting systems using visible-wavelength semiconductor lasers have been attracting a lot of attention in opto-electronics research fields owing to the wide colour gamut, high colour reproduction range, high brightness, simple and compact optical circuits, and low power consumption. These advantages are due to the semiconductor laser's unique characteristic as a light source compared to conventional light sources; a narrow spectrum width and high spatial and temporal coherence owing to the light generation process based on the stimulated emission. Recently, several advanced displays and lighting systems utilizing RGB semiconductor lasers have been developed and come into the market [1].

One important visible laser application is a laser-beam-scanning display [2]. To realise an advanced high-resolution scanning display, high-speed control of RGB semiconductor lasers with arbitrary signal patterns are necessary. In this paper, high-speed modulation of RGB semiconductor laser modules using arbitrary digital sequence patterns are reported. Good modulation characteristics were obtained successfully for the pig-tailed RGB laser modules in the repetition frequency range from 100 to 600 MHz with an eye-opening ration over 80%, which are suitable for the application of 4-mega pixel resolution scanning displays.

2. Experimental set-up

The experimental set-up for the modulation of RGB semiconductor laser modules is shown in Fig. 1. A pig-tailed semiconductor laser module with a single-mode fibre for Red/Green/Blue light was installed in the temperature-controlled block with a bias-Tee circuit of a 2-GHz operational bandwidth. During the experiment, the temperature of each module was set at 20 degrees Centigrade.

Pseudo-random binary sequence (PRBS) signals of a $2^{31}-1$ bit stream were supplied to the installed laser module via the bias-Tee with an appropriate DC bias current, and the modulated light beam from the single-mode fibre was detected by use of a high-speed photo-diode with an operational bandwidth of ~ 2 GHz. The detected signal was measured by use of a digital oscilloscope. The optical spectrum of the output light from the module was also measured by use of an optical spectrum analyser.
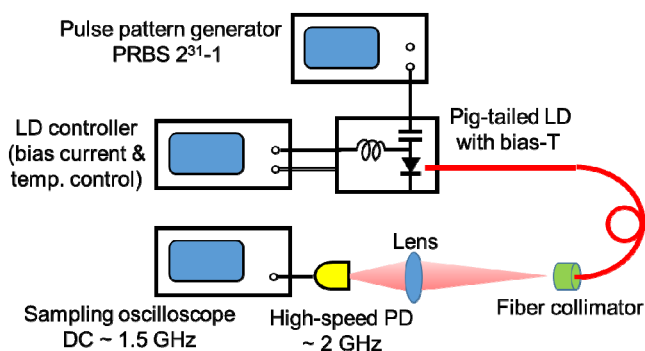

Fig. 1. Experimental set-up.

Table 1. Parameters of the RGB lasers.

	Red	Green	Blue
Operational wavelength λ (nm)	~ 636	~ 518	~ 452
Threshold current I_{th} (mA)	~37	~44	~21
DC bias current I_b (mA)	54	44	30

3. Measured results

Examples of the measured temporal waveforms from the Red semiconductor laser module are shown in Fig. 2. We can see that clear eye-openings are identified at the repetition frequencies of 100 and 300 MHz. For the Green and Blue laser modules, similar waveforms were obtained in the frequency range from 100 to 1200 MHz.

Figure 3 shows the frequency dependences of the eye-opening ratios obtained from the measured eye-patterns of the RGB laser modules. We can see that over 80% eye-opening ratios are obtained in the frequency range from 100 to 600 MHz for the three laser modules. In Fig. 3, the measured eye-opening values of the Green laser module show a little bit large variations compared to the Red and Blue module results, which is due to the

effect of the relaxation oscillation observed in the Green laser results. By adjusting the DC bias current to the laser, this variation can be reduced and better operational characteristics can be obtained, we believe.
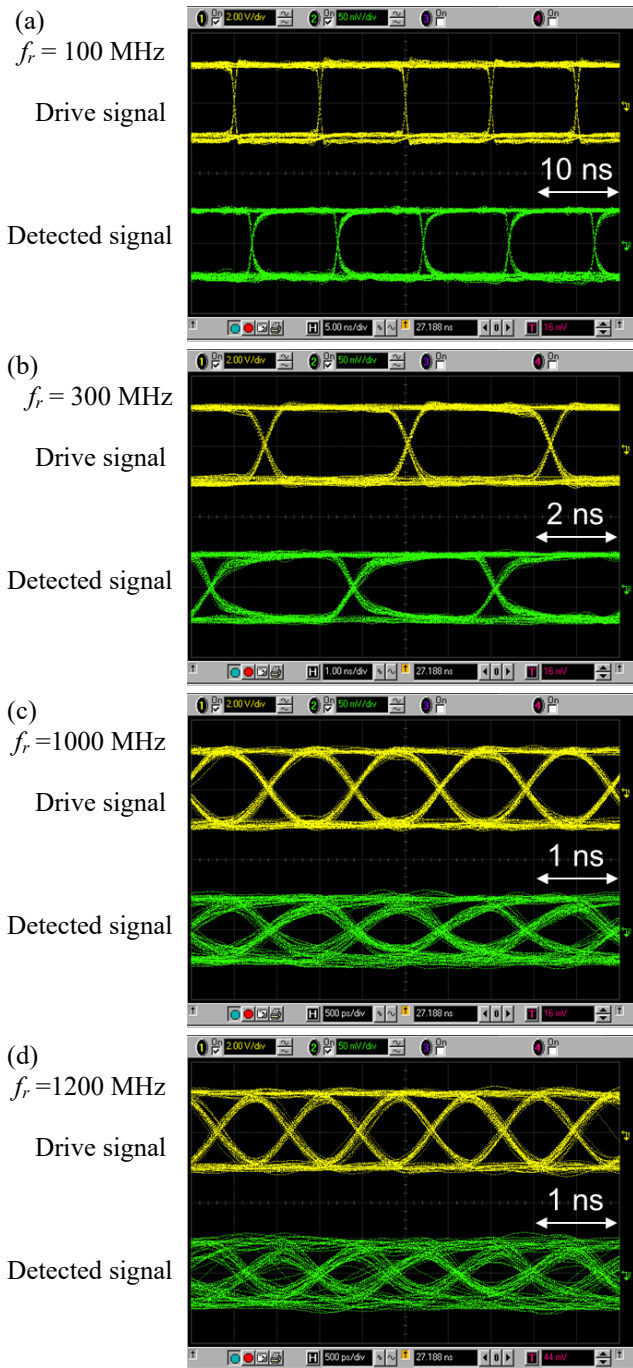
(a)
f_r = 100 MHz

Drive signal

10 ns

Detected signal

(b)
f_r = 300 MHz

Drive signal

2 ns

Detected signal

(c)
f_r =1000 MHz

Drive signal

1 ns

Detected signal

(d)
f_r =1200 MHz

Drive signal

1 ns

Detected signal

Fig. 2. Measured waveforms from the Red laser module under the PRBS digital signal modulation. (Wavelength λ = 635 nm. PRBS signal repetition frequency f_r = 100, 300, 1000, and 1200 MHz.)
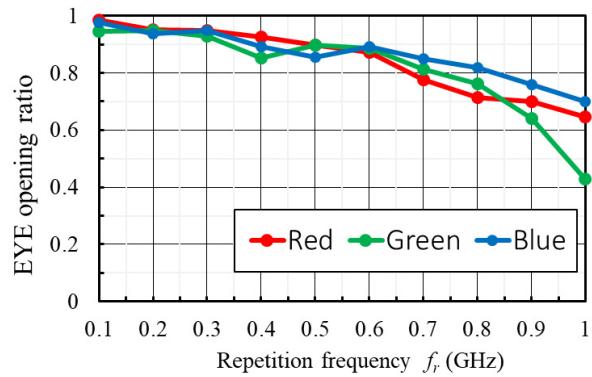
Fig. 3. Measured change in the eye-opening ratio versus the signal repetition frequency.

4. Discussion and conclusion

For the application to a high-resolution scanning display of 1920x1080 (~2-Mega pixel) with a frame rate of 60 Hz, clear digital modulation characteristics for arbitrary patterns with a repetition frequency of ~250 MHz are to be required for the light control with the laser direct modulation technique. For a 4-Mega pixel case, digital modulations with a repetition frequency of ~500 MHz are necessary. Therefore, the measured experimental results indicate that a compact high-resolution scanning display up-to 4-Mega pixels is realizable by use of the pig-tailed RGB laser modules used in the experiments.

The high-speed modulation technique of visible semiconductor lasers is also useful to reduce speckle noise patterns owing to the broadening of the spectrum width of the laser light by the modulation [3]. Discussions about speckle characteristics will be presented in the conference.

References
[1] K. Kuroda, K. Yamamoto and S. Kurimura, "Laser Display -from basics to applications-," ed. Optronics, Tokyo, Japan (2010).
[2] W. O. Davis, R. Sprague, and J. Miller, "MEMS-based pico projector display," *Proc. 2008 IEEE/LEOS International Conference on Optical MEMs and Nanophotonics*, Freiburg, Germany.
[3] H. Murata, K. Shibasaki, K. Yamamoto, and Y. Okamura, "Speckle Control Using High-Frequency Signal Superposition to Semiconductor Laser," *Opt. Rev.*, **vol.21**, no.1, pp.79-82 (2014).

LDC2020 | Oral Presentation
Light sources and components 2
2020年4月23日(木) 10:45 ～ 12:15 301 (Conference Center)

[LDC8-05] 645 nm lasers with a low vertical divergence angle for laser display

*Yufei Jia[1], Yufei Wang[1], Linhai Xu[1], Wanhua Zheng[1] （1. Institute of Semiconductors, CAS）

We design the 645 nm laser with a narrow vertical divergence. The measured vertical far-field divergence can be reduced from 18.3° to 14.7° (FWHM) without degrading the laser performance. In addition, the low coherence laser with 4% speckle contrast is presented for laser display.

645 nm lasers with a low vertical divergence angle for laser display

Yufei Jia[1,2], Yufei Wang[1,2], Linhai Xu[1,2], Wanhua Zheng[1,2,3,4]*

[1] Laboratory of Solid State Optoelectronics Information Technology, Institute of Semiconductors, CAS. Beijing 100083
[2] State Key Laboratory on Integrated Optoelectronics, Institute of Semiconductors, CAS. Beijing 100083, China
[3] College of Future Technology, University of Chinese Academy of Sciences. Beijing 101408, China
[4] Center of Materials Science and Optoelectronics Engineering, University of Chinese Academy of Sciences, Beijing 100049, China
*whzheng@semi.ac.cn

Abstract: *We design the 645 nm laser with a narrow vertical divergence. The measured vertical far-field divergence can be reduced from 18.3° to 14.7° (FWHM) without degrading the laser performance. In addition, the low coherence laser with 4% speckle contrast is presented for laser display.*

1. Introduction

Laser sources play a vital important role in the next generation display technology because of natural advantages. Laser based display can provide almost the full-color display, wide color gamut, large size and high contrast ratio compared with the conventional sources like lamps and light emitting diodes (LEDs). However, there are much effort to do for improving the laser performance like the vertical divergence angle, speckle. The low vertical divergence angle can increase the coupling efficiency and the other limiting factor, speckle, should diminish to improve the image quality. There are many types of designs for low vertical divergence angle including the super large optical cavity (SLOC) [1], mode expansion layers [2] and so on. In addition, we use the new optical cavity to realize the low coherence laser source [3].

In this paper, we present the 645 nm new epitaxy design to realize the vertical beam divergence angle as narrow as 14.7° at full width at half maximum (FWHM), compared with 18.3° of the conventional large optical cavity (LOC) epitaxy structure [3]. The low coherence laser with 4% speckle contrast is obtained, which is beneficial for improving the image quality in the laser display.

2. Laser structure design and simulation

Here we design the low vertical divergence angle by introducing the mode expansion layer in the n-doped region. It can expand the size of the transverse electrical field. In addition, we use the $Al_{0.5}In_{0.5}P$ as the p-doped cladding layer which can mainly restrict the optical field in the n-doped region. In the epitaxial direction, the active region consists of three quantum wells emitting in the 645 nm range. The thickness of each well is 5 nm, and the barrier layers are composed of the $(Al_{0.4}Ga_{0.6})_{0.51}In_{0.49}P$ with the thickness of 10 nm. Table 1 is the detailed structure of the low vertical divergence angle. Fig. 1(a) shows the refractive index distribution and the simulated nearfield pattern (NFP) in the fast axis. The far field pattern (FFP) is calculated by the Fourier transformation of near field amplitude, and we can obtain the vertical divergence of 13.5°, which is shown in Fig. 1(b).

Table 1 Laser structure of the low vertical divergence angle

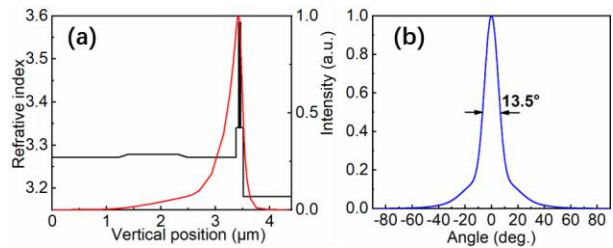| Material	Thickness (um)	Doping type
$Al_{0.5}In_{0.5}P$	1	p
$(Al_{0.4}Ga_{0.6})_{0.51}In_{0.49}P$	0.04	i
$3QW Ga_{0.45}In_{0.55}P$	0.005	i
$(Al_{0.4}Ga_{0.6})_{0.51}In_{0.49}P$	0.04	i
$(Al_{0.7}Ga_{0.3})_{0.51}In_{0.49}P$	1	n
$(Al_{0.68}Ga_{0.32})_{0.51}In_{0.49}P$	1.2	n
$(Al_{0.7}Ga_{0.3})_{0.51}In_{0.49}P$	1.2	n

Fig. 1 Refractive index distribution and simulated NFP (a) and the FFP (b) in the fast axis
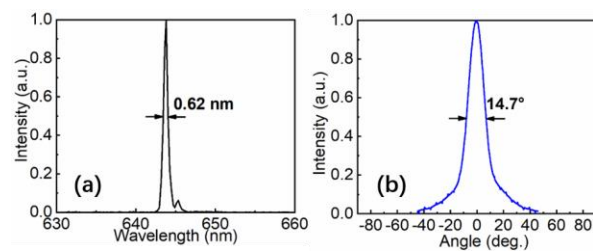
3. Experimental results

Fig. 2 Measured lasing spectrum (a) and the FFP in the fast axis (b) at 1.5 A CW

The epitaxy wafer was fabricated into the uncoated FP lasers with 100-μm width and lengths varying from 1 mm to 2.5 mm. The devices are measured under the pulsed condition with 40 μs at a repetition of 40 Hz. The obtained internal quantum efficiency η_i, the internal loss

α_i, the mode gain ΓG_0, and the transparent current density J_{tr} are 61.3%, 2.5 cm^{-1}, 27.79 cm^{-1} and 454.88 A/cm^2, respectively. Fig. 2 shows the peak wavelength of 643.8 nm and the vertical divergence angle of 14.7° at 1.5 A and length of 1.5 mm under continuous wave (CW) operation.

We also utilize the structure shown in Fig. 3 to realize the low coherence output under the pulsed condition. The parameters is R=500 µm, d=0.5R and L=1000 µm
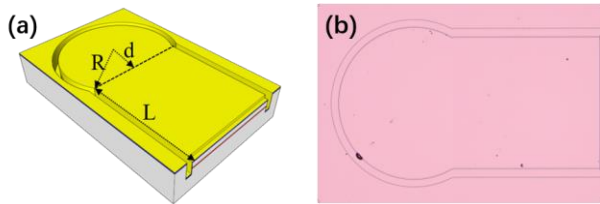

Fig. 3 Schematic of the low coherence laser (a) and the optical microscope image (b)
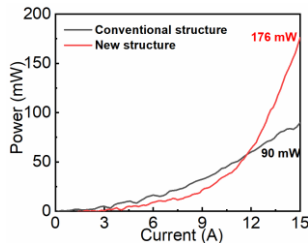

Fig. 4 L-I curves of conventional LOC structure (black line) and the new design structure (red line)

Fig. 4 shows the L-I curves of low coherence lasers in different epitaxy structures (black line: conventional LOC structure in Ref. 4; red line: structure in this article). The latter is mounted p-side down on the heatsink and they are both measured under the same pulsed condition. When at 15 A, the power of laser with new structure reaches 176 mW which is almost two times larger than that of the former.

Fig. 5 shows the speckle patterns of the low vertical divergence angle and low coherence laser and the conventional FP laser using the same wafer structure. The width and length of FP laser are 100 µm and 1.5 mm, respectively. The speckle contrast C is calculated by using the same size and location of sample areas, with the results of 4% for the low

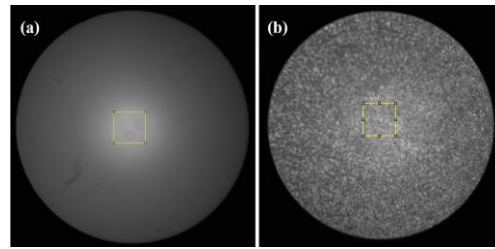vertical divergence angle and low coherence laser and 12% for the FP laser.

Fig. 5 Speckle patterns of the low vertical divergence angle and low coherence laser (a) and the conventional FP laser (b) using the same wafer structure

4. Conclusions

We present the 645 nm laser with low vertical divergence angle of 14.7°, which agree well with the theoretical calculations. In addition, we use this epitaxy structure to realize the low coherence laser diodes with speckle contrast of 4%, which can be utilized to improve the image quality and has a bright prospect in the future laser display.

References

[1] S. Zhao, A. Qi, M. Wang, H. Qu, Y. Lin, F. Dong and W. Zheng, "High-power high-brightness 980 nm lasers with >50% wall-plug efficiency based on asymmetric super large optical cavity," Optical Express., **vol. 26**, **no. 3**, pp. 3518-3526, 5 Feb. (2018).

[2] P. M. Smowton, G. M. Lewis, M. Yin, H. D. Summers, G. Berry, and C. C. Button, "650-nm lasers with narrow far-field divergence with integrated optical mode expansion layers," IEEE J. Sel. Topics Quantum Electron., **vol. 5**, **no. 3**, pp. 735-739, May/Jun. (1999).

[3] Y. Jia, Y. Wang, L. Xu and W. Zheng. "Low-spatial coherence electrically pumped semiconductor laser for speckle-free full-field imaging," LDC-5-01. (2019)

[4] M. V. Maximov, Y. M. Shernyakov etal. "High-performance 640-nm-range GaInP-AlGaInP lasers based on the longitudinal photonic bandgap crystal with narrow vertical beam divergence," IEEE J. Quantum Electron. **vol.41, no. 11**, 1341-1348. (2005)

LDC2020 | Oral Presentation

Novel and emerging technologies and applications 1
Session Chair: Hirotsugu Yamamoto(Utsunomiya University), Shiro Suyama(Tokushima University)
Thu. Apr 23, 2020 1:30 PM - 3:00 PM 301 (Conference Center)

[LDC9-01] Warp Square: A 360-degree Visual Experience in 4K Ultra-short-throw Projector Cave
*Norihiro Ohse[1] (1. Sony Corporation)
 1:30 PM - 2:00 PM

[LDC9-02] Trends and Prospects of Systems and Applications of Wireless Power Transmission Using Laser Light
*Tomoyuki Miyamoto[1] (1. Tokyo Institute of Technology)
 2:00 PM - 2:30 PM

[LDC9-03] Evaluation of the chromaticity of tricolor laser displays under the laser wavelength shifts depending on the operating currents
*Keisuke Hieda[1], Tomoyuki Maruyama[1], Fumio Narusawa[1] (1. HIOKI E.E. CORPORATION)
 2:30 PM - 2:45 PM

[LDC9-04] Forming Aerial Signage in front of LED Panel by Use of Retro-Reflector with Square-Shaped Holes
*Daiki Nishimura[1], Masaki Yasugi[1,2], Hirotsugu Yamamoto[1,2] (1. The University of Utsunomiya, 2. JST, ACCEL)
 2:45 PM - 3:00 PM

LDC2020 | Oral Presentation
# Novel and emerging technologies and applications 1
2020年4月23日(木) 13:30 〜 15:00 301 (Conference Center)

[LDC9-01] Warp Square: A 360-degree Visual Experience in 4K Ultra-short-throw Projector Cave

*Norihiro Ohse[1] （1. Sony Corporation）

We have developed Warp Square, a 360-degree projector cave using 4K ultra-short-throw projectors and a contrast screen. It has high spatial efficiency and delivers high-quality images with a high contrast ratio. This system has been applied to various multi-person VR experiences. We expect that it will eventually be installed in all homes in the future.

Warp Square: A 360-degree Visual Experience in 4K Ultra-short-throw Projector Cave

Norihiro Ohse

Tokyo Laboratory 01, R&D Center, Sony Corporation, Japan

Abstract: We have developed Warp Square, a 360-degree projector cave using 4K ultra-short-throw projectors and a contrast screen. It has high spatial efficiency and delivers high-quality images with a high contrast ratio. This system has been applied to various multi-person VR experiences. We expect that it will eventually be installed in all homes in the future.

1. Introduction

Augmented reality (AR), virtual reality (VR), and mixed reality (MR) provide novel experiences beyond those given by conventional flat-panel displays such as LCD and OLED. Several AR/VR/MR displays have been proposed and commercialized. For example, various VR head-mounted displays (HMDs) and headsets with a wide field of view (FOV) > 100° have been proposed and commercialized for VR applications [1]. While HMD provides VR experiences with immersive images and audio, the experience is limited to only one person, and the headgear can be difficult to wear for a long time or if the person is wearing makeup. To overcome these issues, the CAVE system, which was originally proposed by C. Cruz-Neira *et al.* [2], has been attracting interest recently. CAVE is a display system with an immersive panoramic view that surrounds multiple users with three to six display walls.

We have developed "Warp Square", which is a type of CAVE system that provides immersive experiences to multiple persons with high spatial efficiency and high image quality. In this paper, we describe the technology used to construct it and report some use cases in the real world.

2. System overview

The schematic configuration of Warp Square is shown in Fig. 1. It consists of four 4K ultra-short-throw projectors and surrounding contrast screens.
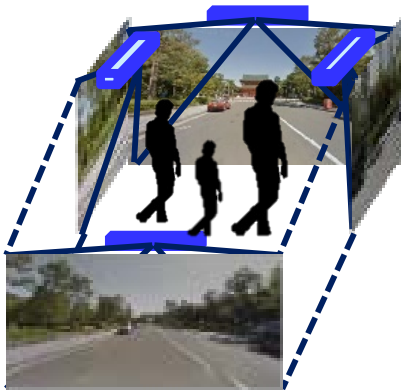

Fig. 1. Schematic diagram of Warp Square.

2.1 4K ultra-short-throw projector

The 4K ultra-short-throw projector was commercialized by Sony in 2014 [3]. Fig. 2 shows the 2014 model (LSPX-W1) and the 2017 model (VPL-VZ1000).
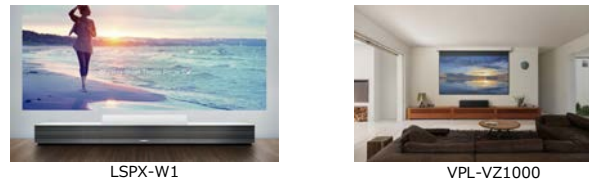

LSPX-W1   VPL-VZ1000

Fig. 2. Sony's 4K ultra-short-throw projector.

These projectors consist of laser light sources [4], a 4K-LCoS (Liquid Crystal on Silicon) panel/SXRD [5] and an ultra-short-throw projection lens. The laser light source has a long lifetime of more than 20,000 hours and can be turned on/off instantly. The 4K-LCoS panel has a small pixel gap and achieves a smooth image on the screen with no mesh. This is important for a CAVE system, since viewers look at images that are closer to the wall.

2.2 Contrast screen

When the light reflected by a wall illuminates other walls, it raises the background level of black images on those walls and the contrast of the images becomes lower. This has been a fundamental issue plaguing the conventional CAVE systems. In order to circumvent it, we introduce a high-contrast screen for Warp Square, as shown in Fig. 3. This high-contrast screen has an anisotropic reflecting property so that only the light from the ultra-short-throw projector is reflected to a person and the light from the other walls is reflected to the ceiling and absorbed there. As a result, we can achieve a high-contrast CAVE system.
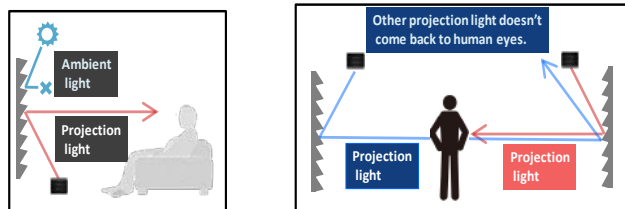

Fig. 3. High-contrast screen.
Left: Home theater use. Right: Warp Square use.

2.3. Sensing

Warp Square can be set up with conventional sensors such as Kinect, HTC VIVE, Motive, and so on. The Hokuyo ToF sensor is useful for touch sensing of the walls. We applied some of them in a demonstration of Warp Square at Sony's booth at SXSW2017 in Austin, Texas (Fig. 4).

Fig. 4. Warp Square at SXSW2017.

2.4. Compact form factor

A conventional CAVE system with normal-throw projectors has to use a rear projection setup, since a front projection setup with normal-throw projectors causes shadows of the person in front of walls. It therefore needs a very large space for rear projection typically about 2–5 times bigger than the inside of a CAVE system. Warp Square with its ultra-short-throw projector enables a front projection setup without the shadowing issue and therefore it does not need a large rear space and has a compact form factor. This is a big advantage for Warp Square because it can be installed in various places in a simple way.

3. Proof of concept

We envision several use cases for Warp Square and provide proofs of concept for each, as follows.

1: Entertainment use, such as for exhibitions, arts events, games, and animation. Visitors can get an immersive experience because they're surrounded by content that they can sense by touching as well as seeing. This will be a cool attraction for them.

2: Theme café or VIP room environment systems. Guests can have lunch or dinner in a unique environment, and VIPs can enjoy sports (e.g., football, soccer) or a live music event with a total view of the stadium with favorable cut scenes by picture in picture (PinP).

3: Enhanced education through the VR experience. We ran Google Street View inside Warp Square so children could gain a new awareness of the world (see Fig. 5).

Fig. 5. Google Street View in Warp Square at an elementary school.

4: Assistance in VR filming. Currently, most VR filming is done in front of a green screen, so the actors don't really have a good grasp of the intended field of action. Warp Square provides them with a virtual copy of the original, so the actors can perform with a more realistic sense of where they are.

5: Application to 5G. 5G telecommunication will soon bring us more powerful image transfer channels. Fig. 6 shows the 5G Demo Bus of NTT Docomo. This bus has Warp Square in its trailer and consists of five seats for viewing live sports or music events at locations distant from the stadium. The Demo Bus can go anywhere and demonstrate VR images.

Fig. 6. NTT Docomo's 5G Demo Bus.

4. Conclusion

We have developed Warp Square, a projector CAVE system with a high spatial efficiency and high-contrast images. Warp Square enables VR experiences with multiple persons. We expect this system will be applied in various scenarios such as entertainment, VIP private rooms, education scenes, and VR creation. We also feel that 5G telecommunications will boost its migration. Eventually, we hope that there will be Warp Square installed in every home, enabling all people to share the VR experience with each other.

[1] https://www.jp.playstation.com/psvr/
[2] C. Cruz-Neira, et al., in Proceedings of SIGGRAPH 1993, pp. 135–142 (1993).
[3] T. Mochizuki, et al., Proc.IDW'14, PRJ5-1 (2014).
[4] Y. Maeda, et al., SID Symposium Digest of Technical Papers, Vol. 46, Issue 1, pp. 362–364 (2015).
[5] S. Hashimoto, et al., SID Symposium Digest of Technical Papers, Vol. 36, Issue 1, pp. 1362–1365 (2005).

LDC2020 | Oral Presentation
# Novel and emerging technologies and applications 1
2020年4月23日(木) 13:30 〜 15:00 301 (Conference Center)

[LDC9-02] Trends and Prospects of Systems and Applications of Wireless Power Transmission Using Laser Light

*Tomoyuki Miyamoto[1]　（1. Tokyo Institute of Technology）

Optical wireless power transmission is attractive because of long-distance transmission, small size and light weight, and no electromagnetic interference. Applications for IoT terminals, consumer equipment, and mobilities are expected. The current status of features, systems, and applications will be reported, focusing on the author's results.

Trends and Prospects of Systems and Applications of Wireless Power Transmission Using Laser Light

Tomoyuki Miyamoto

FIRST, IIR, Tokyo Institute of Technology, 4259 Nagatsuta, Midori-ku, Yokohama 226-8503, Japan

Phone +81-45-924-5059, email tmiyamot@pi.titech.ac.jp

Abstract: *Optical wireless power transmission is attractive because of long-distance transmission, small size and light weight, and no electromagnetic interference. Applications for IoT terminals, consumer equipment, and mobilities are expected. The current status of features, systems, and applications will be reported, focusing on the author's results.*

1. Introduction

Optical wireless power transmission (OWPT) is a method of remotely and wirelessly supplying power using a laser light and a solar cell. Although the principle is simple, research to date has been limited. Similar to information communications, the existence of wiring restricts the installation of equipment, device functions, and the creation of applications and services. The realization of OWPT will bring about significant changes in society.

2. Optical wireless power transmission

As wireless power supply technology, several methods have been developed and put into practical use. However, these conventional methods suffer from short transmission distances, large and heavy modules, and electromagnetic interference (EMI) problems. Therefore, the application and available use cases are limited.

Optical wireless power transmission (OWPT) is an attractive novel method [1]. The OWPT has the advantages of long-distance transmission by laser beams, which are much less diffractive than radio-frequencies, and small size and light weight due to semiconductor devices of light sources and solar cells. The DC operation simplifies the circuit. The light beam and the DC circuit are advantageous for suppression of EMI. Although the concept of an OWPT has been discussed for about 50 years, there is limited research and demonstration, and sufficient knowledge and technologies have not yet been established.

As shown in Fig. 1, the practical OWPT system requires the integration of various functions, from the optical system to the control system. The system configuration is very similar to laser scanning display and advanced laser lighting. In the case of OWPT, the target of laser beam irradiation is a solar cell that moves its position and direction, and the light power covers wide range depending on the target system. In many cases, the power density of an irradiated light beam will be much larger than that of a display or lighting. Although visible light is not required, wavelength matching between the laser source and the absorption edge of the solar cell is important for efficient power transmission. OWPT can be expected as an important

laser based technology to accelerate the wireless society by improving the performance of devices such as efficiency and output power, and improvement of sensing technology based on IoT, and improvement of control technology based on progressed computer systems including deep learning technology.
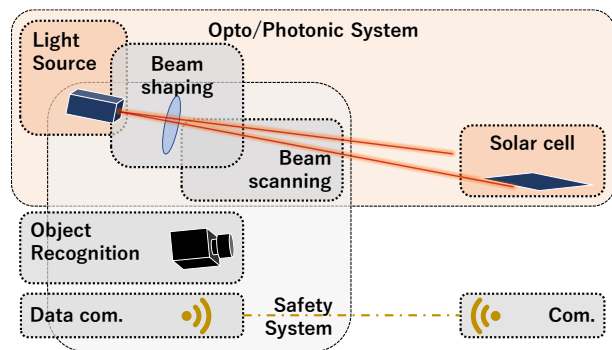

Fig. 1. Schematic configuration of OWPT system.

3. OWPT system configuration and demonstration

Since OWPT will be available of output power from mW to kW, it can be applied not only to charging IoT terminals and information devices, but also to mobility such as drones, robots, and vehicles.

In the case of IoT terminals consisting of numerous sensors, tags, and beacons, LED-based OWPT systems from their advantageous for safety have been investigated in order to provide supplying power and charging remotely from workers, robots, drones [2].

In the field of mobility applications, current drones and EVs have the problem of limited travel distance and time due to limited battery capacity. Since batteries already account for 20-50% of weight of the mobility, increasing the amount of battery is ineffective. Thus, dynamic charging will be an attractive solution. Currently, verification of operation from toy class mobilities is underway due to limitations in the applicable light output and control systems of the OWPT.

Figure 2 shows the dynamic charging of a moving toy car in view o the new EV society of the future. A high-power near-infrared (NIR) VCSEL array was used as the light source and a Si solar cell module was used as the receiver. Continuous moving becomes possible by

irradiating laser beam on a straight course. In the experiment, an electric double layer capacitor was installed in the car to charge power for moving on a non-irradiation course and initial start of the motor. In addition, toy-class micro drone was continuously floated by OWPT as shown in Fig. 3 [3]. Practical dynamic charging is expected by improving the laser output power and introducing a target tracking system which consists of an object recognition system and a beam steering system as well as a beam shaping/focusing systems.
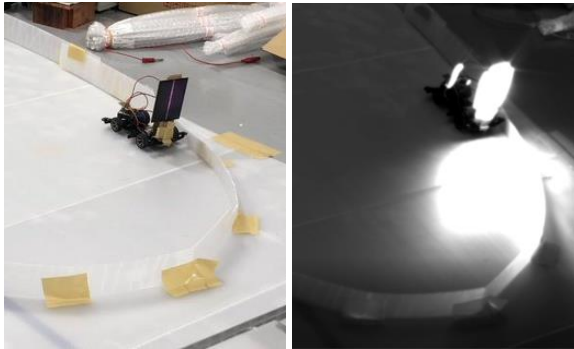
Fig. 2. Dynamic charging to toy-EV using VCSEL. (left) visible image, and (right) infrared image. Beam is irradiated on a straight course.

Fig. 3. Dynamic charging to toy-micro drone using VCSEL. Limited to a few cm floating due to fixed beam system.

Fig. 4. Multi-beam system.

For advanced OWPT system, multi-beam system are indispensable. By producing multi-beam systems, increase of beam intensity due to multiplexing of beams,

optimum beam irradiation suppressing beam deformation in oblique irradiation, and continuous irradiation even when one beam is blocked are expected. The safety of the system by the reduction of each beam power is also an advantage. In Fig. 4, an initial demonstration of multi-beams using two sets of a 2-axis rotatable light source and a 3D-depth camera was performed using in-house target recognition software/system [4].

In addition, the underwater operation has been investigated in order to expand the application field of OWPT. Although rf hardly transmits water due to large absorption, lightwave, particularly blue-green light, can transmit with a relatively small transmission loss. The OWPT from air to underwater has been investigated [5]. On the other hand, even if an OWPT system is introduced, appearance is also important for consumer equipment. Although ordinary solar cells have black surfaces, design controllability has been investigated in consideration of monochromatic light for OWPT [6].

4. Conclusions

Significance of the optical wireless power transmission system and current activities related to the OWPT were described. Although the basic configuration is simple, the devices and configuration methods suitable for the OWPT have not been sufficiently established, and it is expected to bring about a major change in equipment, services, and industries by progress of research and development.

References

[1] T. Miyamoto, "Optical wireless power transmission using VCSELs," Proc. SPIE **10682**, 1068204 (2018).

[2] Y. Zhou and T. Miyamoto, "200mW-class LED based optical wireless power transmission for compact IoT," Jpn. J. Appl. Phys. **58**, SJJC04 (2019).

[3] Z. Jiahe and T. Miyamoto, "Investigation of flying condition of drone powered by optical wireless power transmission," 40th annual meeting of Laser Society of Japan, G03-22a-X-04 (2020).

[4] J. Tang, K. Takahashi, J. Zhang and T. Miyamoto, "Design and build of OWPT system with multiple light sources," to be presented in OWPT2020.

[5] J. Li and T. Miyamoto. "Dynamic output power characteristics of optical wireless power transmission from air to underwater," to be presented in OWPT2020.

[6] Y. Liu and T. Miyamoto, "Oblique incidence characteristics of solar cells with controlled color and scattering appearance for OWPT," to be presented in OWPT2020.

LDC2020 | Oral Presentation

Novel and emerging technologies and applications 1

2020年4月23日(木) 13:30 ～ 15:00 301 (Conference Center)

[LDC9-03] Evaluation of the chromaticity of tricolor laser displays under the laser wavelength shifts depending on the operating currents

*Keisuke Hieda[1], Tomoyuki Maruyama[1], Fumio Narusawa[1] （1. HIOKI E.E. CORPORATION）

The wavelengths of red, green and blue laser diodes were measured while changing their operating currents. The wavelengths shifts observed in this experiment cause unintended color shifts in tricolor laser displays. To make the best use of tricolor laser displays, the wavelength shifts must be considered in their color management.

Evaluation of the chromaticity of tricolor laser displays under the laser wavelength shifts depending on the operating currents

Keisuke Hieda, Tomoyuki Maruyama, Fumio Narusawa,
HIOKI E.E. CORPORATION

Abstract: The wavelengths of red, green and blue laser diodes were measured while changing their operating currents. The wavelengths shifts observed in this experiment cause unintended color shifts in tricolor laser displays. To make the best use of tricolor laser displays, the wavelength shifts must be considered in their color management.

1. Introduction

In recent years, an increasing number of displays such as projectors, head up displays (HUD) and head mount displays (HMD) have been adopting lasers to benefit from their high color reproducibility, enhanced energy efficiency, and small size [1-4]. In order to make the best use of the advantages of a tricolor laser display, display manufacturers need to precisely control the color created by red, green, and blue (RGB) lasers. A well-known factor that affects the properties of laser diodes (LD) is temperature dependence. As the temperature increases, the bandgaps of semiconductors shrink, which lengthens an LD's oscillation wavelength [4]. Eventually, the wavelength shift causes unintended changes in the color of tricolor laser displays because the power ratio of RGB lasers to create a certain color depends on their wavelengths. In addition, since LDs have much narrower spectra than LEDs, the color change caused by the wavelength shift is more critical in tricolor laser displays. To eliminate the uncertainty caused by LDs' temperature dependence, the junction temperature (T_j), which is defined as the temperature of the active layer, must be kept constant because the T_j directly affects LDs' properties. The T_j is calculated as follows:

$$T_j = T_c + R_{th(j-c)} \times P$$

where T_c is the case temperature, and $R_{th(j-c)}$ is the thermal resistance between the junction and case, and P is the electrical power applied to the LD. Since the T_c is easily measurable and controllable using a thermometer and a Peltier device, the effect of the T_c on the T_j is removable. On the other hand, the P depends on the LD operating current, which changes based on the image the LDs are drawing, and the $R_{th(j-c)}$ also has different values in different setups so that the T_j can not be controllable. Furthermore, given that the active layer is inaccessible by a thermometer, the T_j is not measurable, either. In this regard, evaluating the actual T_j dependence of LD properties is very difficult. As a practical alternative, the operating current dependence, which is equivalent to the P dependence, of laser properties must be evaluated. The most commonly evaluated property is the operating current dependence of LD optical power.

However, as mentioned above, the wavelength is also indirectly affected by the operating current. In this paper, the effect of operating current dependence of laser wavelength on the chromaticity of tricolor laser displays was investigated for a better color management of tricolor laser displays.

2. Experiment

2.1 Measurement setup

The centroid wavelengths of RGB LDs, which are suitable for the chromaticity evaluation of RGB LDs [5], were measured by the optical meter TM6104 (HIOKI E.E. CORPORATION) while changing their operating currents. The TM6104 is an optical power meter specially designed for RGB laser measurement capable of measuring the centroid wavelength [6], the optical power, the luminous flux, the chromaticity of RGB lasers separately and simultaneously. A schematic diagram of the experiment setup is shown in Fig.1. In this experiment, can-package LDs were mounted in aluminum fixtures to release the heat of the LDs and driven by a DC current source. The operating current was swept from the threshold current to approximately the maximum operating current in each LD measurement. Their case temperature was kept at 25 degrees using a Peltier device. The laser light entered the TM6104 through a focusing lens.
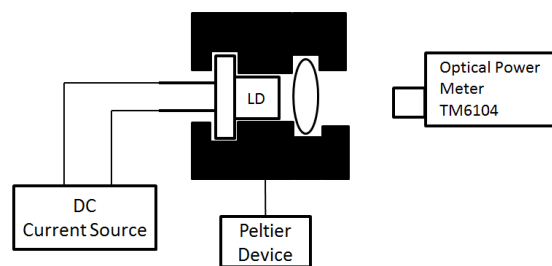

Fig. 1. Experiment setup.

2.2 Measurement results

As shown in Fig.2, the wavelength shifts accompanying the change of the operating current were 1.37nm, 1.34nm and 1.53nm in the blue, green and red LD respectively.
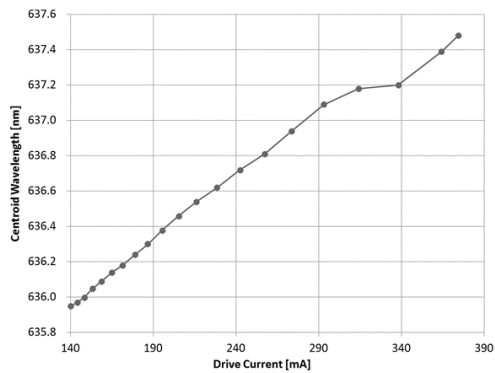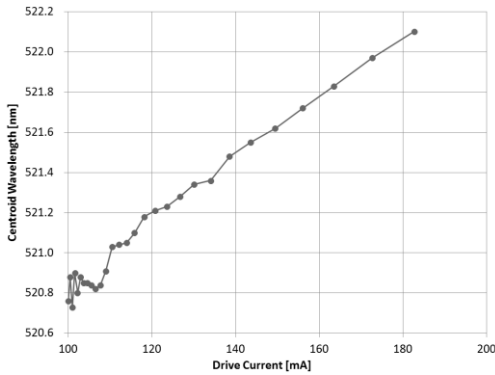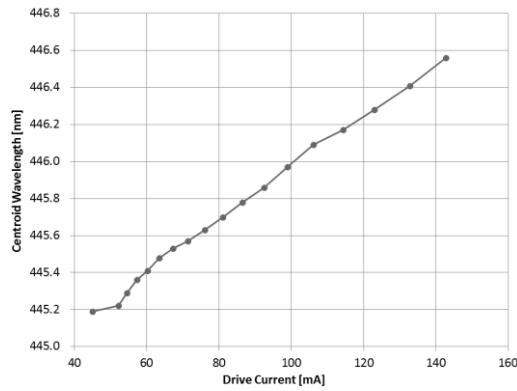
Fig. 2. Operating Current and Centroid Wavelength

Fig. 3. Color Shifts Caused by Wavelength Shifts

3. Analysis

To translate the wavelength shifts into the color shift of the tricolor LDs, the chromaticity values created by the tricolor LDs were calculated in each measurement point using the color matching functions. Since the LD optical power was increased by ten percent from one measurement point to another by adjusting the operating current, the power ratio of RGB LDs was constant throughout the experiment. Since the chromaticity values are determined by the power ratio and wavelengths of RGB LDs, the color would not change if their wavelength were unchanged. Therefore, the observed color shifts from one measurement point to another are attributed to the wavelength shifts. The chromaticity values in each measurement point are plotted in Fig.3. As shown in Fig.3, the chromaticity x shifted from 0.3275 to 0.3334 and y from 0.3068 to 0.3052 respectively.
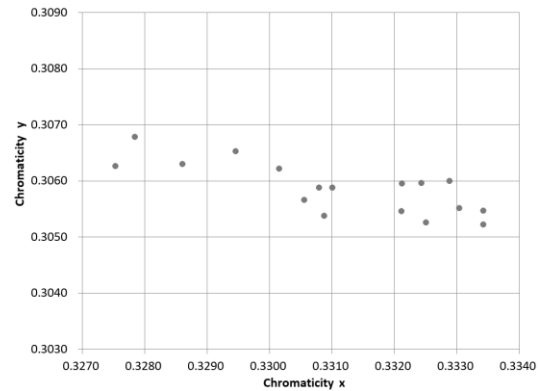
4. Conclusions

We have revealed that the wavelength shifts of RGB LDs depending on the operating current cause color shifts of tricolor laser displays, which will degrade their image quality. The wavelength shifts observed in this experiment are unavoidable even with Peltier devices because they can not control the junction temperature of LDs. Display manufacturers normally conduct white balance adjustment to obtain correction factors for a precise color reproduction. However, considering the wavelength shift above, the correction factors obtained in a certain condition can not be applied to other conditions. In order to eliminate the effect of the wavelength shift on the color of tricolor laser displays, the operating current dependence of the wavelengths, which is mostly not specified in LD datasheets, must be measured and applied to color management.,

References

[1] K. V. Chellappan, E. Erden, and H.Urey, "Laser-based displays: a review," Appl. Opt. 49, F79-F98 (2010).

[2] E. Buckley, "Laser wavelength choices for pico-projector applications," J.Disp. Technol.7, 402-406 (2011)

[3] Y.Zhang, H.Don, R.Wang, J.Duan, A.Shi, Q.Fan and Y.Liu, "Demonsration of a home projector based on RGB semiconductor lasers," Appl. Opt. 51, 3584-3589 (2012)

[4] J. Pankove "Temperature dependence of emission efficiency and lasing threshold in laser diodes," IEEE J. Quantum Electronics, vol. 4, issue 4, 119-122 (1968)

[5] K.Hieda, T.Maruyama, T.Takesako, and FNarusawa, "New Method Suitable for measuring chromaticity and photometric quantity of laser displays," Opt. Rev. 25, 175-180 (2018)

[6] IEC 61280-1-3:2010, "Fiber optic communication subsystem test procedures - Part 1-3: General communication subsystems - Central wavelength and spectral width measurement".

LDC2020 | Oral Presentation
# Novel and emerging technologies and applications 1
2020年4月23日(木) 13:30 ～ 15:00 301 (Conference Center)

[LDC9-04] Forming Aerial Signage in front of LED Panel by Use of Retro-Reflector with Square-Shaped Holes

*Daiki Nishimura[1], Masaki Yasugi[1,2], Hirotsugu Yamamoto[1,2] (1. The University of Utsunomiya, 2. JST, ACCEL)

We propose an optical system to form aerial signage over an LED panel. A beam splitter is placed in front of the LED panel that is covered with retro-reflector with square-shaped holes. The aerial image is formed in front of the LED panel, which is suitable for a large-scale installation.

Forming Aerial Signage in front of LED Panel
by Use of Retro-Reflector with Square-Shaped Holes

Daiki Nishimura[1], Masaki Yasugi[1, 2], Hirotsugu Yamamoto[1, 2]
[1]Utsunomiya University, 7-1-2 Yoto, Utsunomiya City, Tochigi, 321-0904 Japan,
[2]JST, ACCEL, 7-1-2 Yoto, Utsunomiya City, Tochigi, 321-0904 Japan,
+81 28 689 7074, hirotsugu@yamamotolab.science.

Abstract: *We propose an optical system to form aerial signage over an LED panel. A beam splitter is placed in front of the LED panel that is covered with retro-reflector with square-shaped holes. The aerial image is formed in front of the LED panel, which is suitable for a large-scale installation.*

1. Introduction

Aerial imaging by retro-reflection (AIRR) has been proposed as a method to form an aerial image for a wide range of viewing angle [1]. Prospective applications of aerial displays include aerial large-scale signage for traffics, advertisement, and amusements. However, the conventional optical design requires a large foot space to install the large aerial signage system. Recently, it has been demonstrated that an aerial light-field image can be formed in front of a mirror by inserting a slit array between a light-field display and a beam splitter [2]. However, moiré due to the slit array occurred in this design. This paper proposes a novel optical design that forms an aerial image without moiré that can be observed from the front of the LED panel.

2. Aerial imaging by retro-reflection (AIRR)

The principle of AIRR is shown in Fig. 1. AIRR is composed of three elements: a light source, a retro-reflector, and a beam splitter. Light from the light source goes to the beam splitter and splits in reflected light and transmitted light. The reflected light impinges the retro-reflector and go back to the beam splitter after the retro-reflection. The light splits again on the beam splitter. The transmitted light converges to the position of plane symmetry of the light source regarding the beam splitter. The observation results of focusing the aerial image with a screen is shown in the Fig. 2. The Luminance of the aerial image is less than 10% of the light-source display.
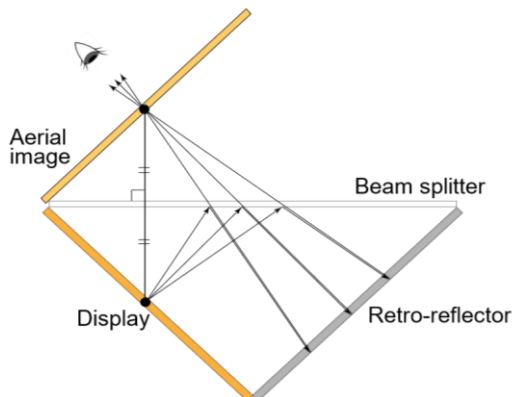

Fig. 2. Aerial image formed with AIRR.

3. Optical system to form the aerial signage in front of an LED panel

Fundamental structure to form aerial signage in front of an LED panel is shown in Fig. 3. A polarizer is attached to the surface of a dot matrix LED panel. A retro-reflector that is covered with a quarter-wave retarder film is placed between the LED pixels. To increase the visibility of aerial image, we make the LED invisible from the front by inserting a reflective polarizer in front of the LED panel in cross Nicol arrangement with the polarizer. In this case, the light from the LED panel transmits polarizer and reflects at the reflective polarizer. The polarization angle of the retro-reflected light is rotated by 90 degrees after penetrating the quarter-wave retarder twice. Therefore, the retro-reflected light transmits through the reflective polarizer and converges into the plane symmetric position of the light source regarding the reflective polarizer.

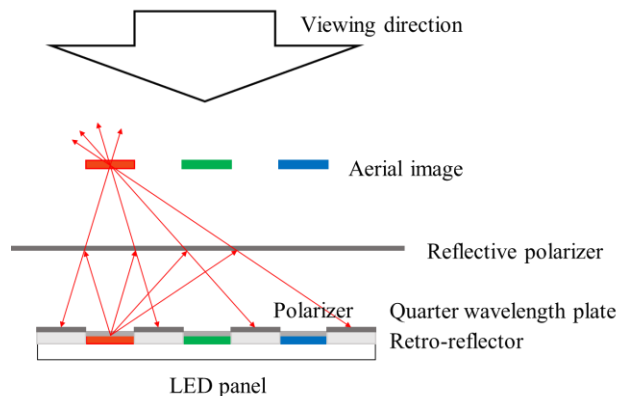Fig 1. Aerial imaging by retro-reflection (AIRR).

Fig 3. Optical system to form aerial signage by use of patterned retro-reflector.

4. Experiment

We have developed a preliminary prototype for experimental confirmation of our optical design. A 6-mm-pitch LED panel was used for the light source. The LED panel with a retro-reflector with square-shaped holes is shown in Fig. 4. When the holes are bigger, the transmittance of LED light improves. On the other hand, when the holes are made smaller, the area for retroreflection increases.
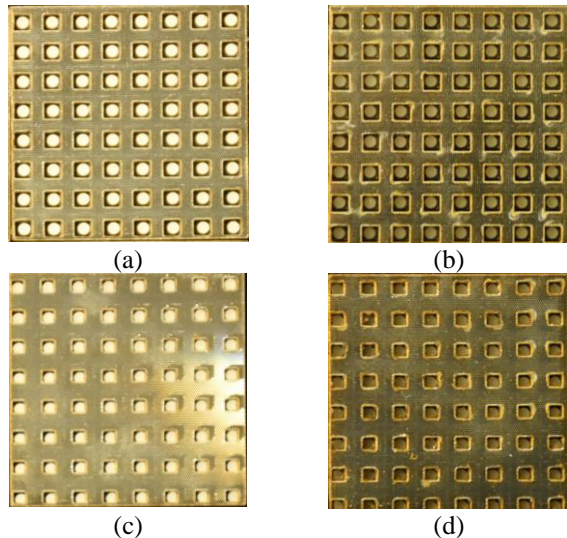

(a)　　　　　　　(b)

(c)　　　　　　　(d)

Fig 4. An LED panel that is covered with a retro-reflective sheet with square-shaped holes. (a) Hole size is 3mm × 3mm and without polarizer. (b) Hole size is 3mm × 3mm and with polarizer. (c) Hole size is 2mm × 2mm and without polarizer. (d) Hole size is 2mm × 2mm and with polarizer.

The displayed image used for experiments and the observation results of focusing the aerial image with a screen are shown Fig. 5. The aerial image is clearly formed at the aerial image position, which is the plane-symmetrical position of the light-source display regarding the beam splitter. Direct observation results of the aerial images formed with the setups of Fig. 4 are shown in Fig.6. In Fig.6 (a) and (c), the light-source LED panel was visible to the observer. However, in Fig.6 (b) and (d), the light-source LED panel became invisible. From results of this study, we have confirmed that the polarizer and the reflective polarizer inserted in a cross Nicol arrangement block the direct light from the LED panel. Furthermore, the luminance of aerial image in Fig. 5 (d) is more than that of aerial image in Fig. 5(b). From results of this study, we have confirmed that increasing the area of retro-reflector improves the light use efficiency and brightens the aerial image.
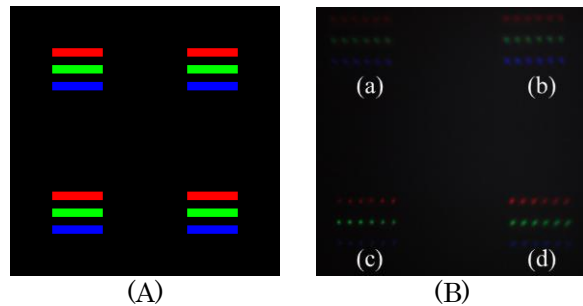

(A)　　　　　　　(B)

Fig 5. (A) A displayed image shown on the light-source LED panel. (B) Screen observation results of the formed aerial images.
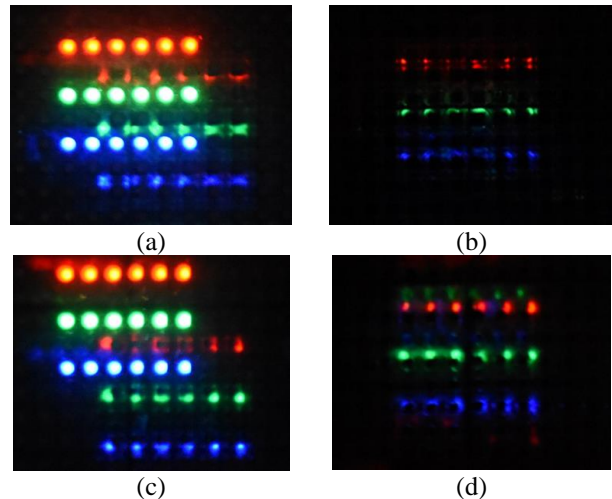

(a)　　　　　　　(b)

(c)　　　　　　　(d)

Fig 6. Viewed aerial images from the front. The aerial images were formed (a) by use of Fig 4 (a), (b) by use of Fig 4 (b), (c) by use of Fig 4 (c), and (d) by use of Fig 4 (d), respectively.

5. Conclusion

We have proposed an optical system for aerial signage over an LED panel without moiré. Showing aerial signage right in front of an LED panel reduces the foot space, which is suitable for a large-scale installation.

References

[1] H. Yamamoto, Y. Tomiyama, and S. Suyama, "Floating aerial LED signage based on aerial imageng by retro-reflection (AIRR)," Opt. Exp. 22, 26919 (2014).

[2] T. Kobori, K. Shimose, S. Onose, T. Okamoto, M. Nakajima, T. Iwane, and H. Yamamoto, "Aerial Light-Field Image Augmented Between You and Your Mirrored Image," Proc. SIGGRAPH ASIA'17, 08-0176 (2017).

LDC2020 | Oral Presentation

Novel and emerging technologies and applications 2
Session Chair: Masato Ishino(Osaka University), Norihiro Ohse(Sony)
Thu. Apr 23, 2020 3:30 PM - 4:45 PM 301 (Conference Center)

[LDC10-01] Large and Long-Viewing Distance DFD (Depth-Fused 3D) Display by using Transparent Polyethylene Screens and Short-Focus Projectors
*Shiro Suyama[1], Haruki Mizushina[1] (1. Tokushima University)
 3:30 PM - 4:00 PM

[LDC10-02] Subjective Super-Resolution by Use of High-Speed Multi-Color LED Display
*Kojiro Matsushita[1], Toyotaro Tokimoto[1,2], Hirotsugu Yamamoto[1,3] (1. Utsunomiya University, 2. DaoApp Technology Company Limited, 3. JST, ACCEL)
 4:00 PM - 4:15 PM

[LDC10-03] Improvement of Visibility of Aerial Image in See-Through AIRR by Cutting Off Ambient Light Using Polarization Modulation
*Kengo Fujii[1], Masaki Yasugi[1,2], Hirotsugu Yamamoto[1,2] (1. Utsunomiya University, 2. JST ACCEL)
 4:15 PM - 4:30 PM

[LDC10-04] Fabrication of SiO_2-based Binary Diffractive Lens with Controllable Focal Distribution for High-Power Laser Applications
*Atsushi Motogaito[1], Kazuki Matsuo[1], Kazumasa Hiramatsu[1] (1. Mie University)
 4:30 PM - 4:45 PM

# Novel and emerging technologies and applications 2
2020年4月23日(木) 15:30 〜 16:45 301 (Conference Center)

[LDC10-01] Large and Long-Viewing Distance DFD (Depth-Fused 3D) Display by using Transparent Polyethylene Screens and Short-Focus Projectors

*Shiro Suyama[1], Haruki Mizushina[1]　（1. Tokushima University）

We have developed large and long-viewing-distance DFD (Depth-fused 3D) display with deep 3D image by using transparent polyethylene screens with adequate transmittance and scattering and short-focus projectors. Blurring front image can successfully enlarge 3D-image depth.

Large and Long-Viewing Distance DFD (Depth-Fused 3D) Display by using Transparent Polyethylene Screens and Short-Focus Projectors

Shiro Suyama and Haruki Mizushina
Department of Optical Science & Technology, Faculty of Engineering, Tokushima University
2-1, Minamijousanjima, Tokushima, 770-8506 Japan, suyama.shiro@tokushima-u.ac.jp

Abstract: *We have developed large and long-viewing-distance DFD (Depth-fused 3D) display with deep 3D image by using transparent polyethylene screens, short-focus projectors and blurring front image. Transparent polyethylene screen has adequate transmittance and scattering characteristics for DFD display. We successfully enlarge 3D-image depth by blurring front images in long viewing distance.*

1. Introduction

3D display is attractive for a digital signage, such as applications in station, shopping mall or so. For large digital signage, 3D display with long viewing distance, glassless, large depth and large screen size is necessary.

In various 3D displays, DFD (Depth-fused 3D) display [1] as shown in Fig. 1 has merits of glassless, fatigueless, simple structure and etc. DFD display is composed of two conventional 2D displays. Two overlapped images with different depth can be fused and perceived as a single depth image. The perceived depth of the fused image continuously changes as the luminance ratio of the two images is changed.
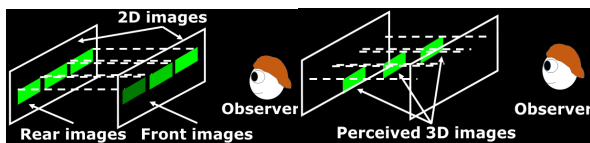

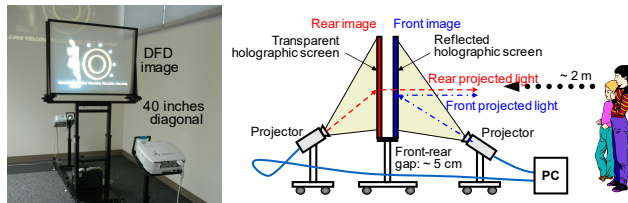Fig. 1. Principle of DFD display.

Fig. 2. Example of large DFD display by holographic screens.

Figure 2 shows an example of large DFD display with holographic screens [2, 3]. Because of small front-rear gap derived from depth fusion limit of about 4-5 arcmin. in DFD display [4] and necessity of non-interference between front and rear screens, expensive holographic screens are used as unavoidable choice. As scattering characteristics of these holographic screens are different by incident light angle differences, mutual non-interference between front and rear screens can be successfully achieved. However, two problems of (A) expensive screens for large 3D display and (B) small 3D image depth by small front-rear gap still remain.

(A) For low-cost screens with mutual non-interference in large and long-viewing-distance DFD display, we propose to use transparent polyethylene screens with adequate transmittance and scattering characteristics and short-focus projectors.

(B) To increase 3D image depth in long-viewing application in DFD display, we also propose to blur front image. In DFD display, enlarging viewing distance makes it easier to fuse front and rear images to one depth image. However, enlarging viewing distance has next two problems of necessity of deeper 3D image and difficulty to perceive small depth.

In this paper, we adopt transparent polyethylene screen and short-focus projector for DFD display, and enlarge perceived 3D-image depth by blurring front image in long-viewing distance DFD display.

2. Transparent polyethylene screens with adequate scattering & transparent characteristics

Figure 3 shows transmittance and scattering characteristics of transparent polyethylene screen. Transmittances of this polyethylene screen are high enough from 0.7 to 0.9 at all observation angles. On the other hand, scattering ratios are also high around 0.5 even at 20-60 degrees. This indicates that this transparent polyethylene screen is appropriate for large and long-viewing distance DFD display.
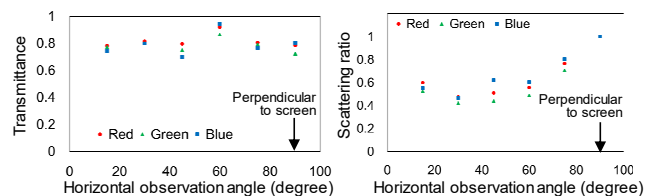

Fig. 3. Transparent polyethylene screen with adequate transmittance and scattering characteristics.

3. Large and long-viewing distance DFD display with two transparent polyethylene screens and short-focus projectors
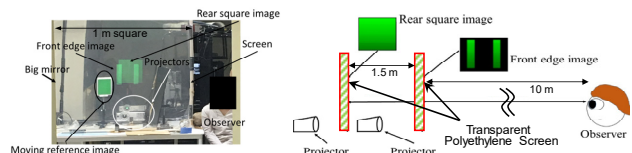

Fig. 4. Large and long-viewing distance DFD display with transparent polyethylene screens and shor-focus projectors.

We propose large and long-viewing distance DFD display with transparent polyethylene screens and short-

focus projectors [5, 6] as shown in Fig. 4. The distance between front and rear screen was 1.5 m and viewing distances was 10 m from front screen, in which viewing distance and distance between front and rear images was widely enlarged from conventional one.

Stimulus was rear green square, 26.5 cm each side and front green edge patterns of 19.5 cm by 4.8 cm with two blurring levels of 0 and 30 pixels (front edge-pattern image size: 737 by 181 pixels). The luminance of rear square image was fixed. Front edge-pattern image luminances were changed from 20% to 100% as compared to rear square-image luminance. Perceived depth was measured from rear plane position by matching the depth of moving reference image (16.2 cm by 12.3 cm) to stimulus perceived depth.

4. Enlarged 3D image depth and viewing distance by using blurred DFD display with two transparent polyethylene screens and short-focus projectors

Figures 5 and 6 show perceived depth dependences on front image luminance with non-blurring (0 pixel) and blurring front image of 30 pixels. Viewing distance of 10 m and front-rear screen distance of 1.5 m are equivalent to under but around depth fusion limit of front-rear gap [4].
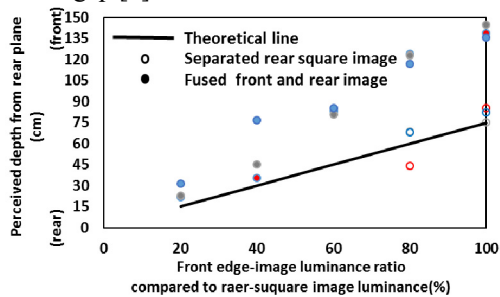

Fig. 5. Perceived depth dependences by non-blurring front images (0 pixel).
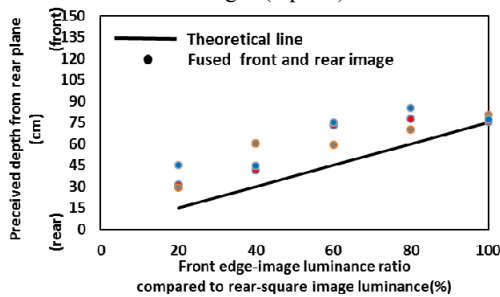

Fig. 6. Perceived depth dependence by blurring front images of 30 pixels.

In Fig. 5 with non-blurring edge-part images, front and rear images cannot be fused at high luminance region of 80-100% and perceived depths are widely scattered. At low luminance region of 20-60%, front and rear images can be fused. However, perceived depths have large deviations between trials and are apart from the theoretical line.

In Fig. 6 with blurring front images of 30 pixels, all images with edge-part image luminances of 20-100% can be fused and have almost the same perceived depths

as the theoretical line, in contrast to scattered perceived depths in Fig. 5 with non-blurring edge-part images. Moreover, their deviations between trials are small enough. This indicates that enlarging viewing distance together with increasing 3D image depth can be achieved by blurring front image in spite of their contrary effects on front-rear image fusion.

Thus, when the viewing distance of deep 3D image is enlarged and front image has appropriate blurring, perceived depth can be successfully fused to the one same depth as the theoretical line.

5. Summary

In order to achieve large and long-viewing distance 3D display, we evaluated perceived depth dependence with large viewing distance of 10 m and deep front-rear gap of 1.5 m by blurring front images in DFD display with two transparent polyethylene screens and short-focus projectors.

By long viewing distance with deep 3D image and appropriate blurring front image, the perceived depths can be successfully fused to the one same depth as a theoretical line and depth deviations between trials are small enough.

Thus, large and deep 3D image can be achieved by long-viewing distance and appropriate blurring front image. This method will be promising for many applications of a long-viewing distance 3D display.

References

[1] S. Suyama, S. Ohtsuka, H. Takada, K. Uehira and S. Sakai, "Apparent 3-D image perceived from luminance-modulated two 2-D images displayed at different depths", Vision Research, **44**(8), 785-793(2004).

[2] M. Date, H. Takada, S. Suyama, K. Tanaka and K. Nakazawa, "Projection-Type Depth Fused 3-D (DFD) Display", Proc. IDW'06, 3Dp-4, (2006).

[3] M. Date, S. Sugimoto, H. Takada and K. Nakazawa, "Depth-fused 3D (DFD) display with multiple viewing zones", Vol. 6778 of Proc. SPIE2007, 6778-42, (2007).

[4] H. Takada, S. Suyama and M. Date, "Evaluation of the Fusional Limit between the Front and Rear Images in Depth-Fused 3-D Visual Illusion", IEICE transactions on electronics, **89**(3), 429-433(2006).

[5] Y. Nagao, H. Mizushina and S. Suyama, "Enlarging Viewing Distance and 3D Image Depth at Large Edge-Based DFD Display by Blurring Edge Parts", Proc. IDW'17, 3Dp2-12L, (2017).

[6] H. Matsubara, H. Mizushina and S. Suyama, "3D Image Depth Enlargement in Large Edge-Based DFD Display with Long Viewing Distance by Blurring Edge Images", Proc. 3DSA/IDW'19, 3DSAp2/3Dp2-18, (2019).

LDC2020 | Oral Presentation
# Novel and emerging technologies and applications 2
2020年4月23日(木) 15:30 ～ 16:45 301 (Conference Center)

[LDC10-02] Subjective Super-Resolution by Use of High-Speed Multi-Color LED Display

*Kojiro Matsushita[1], Toyotaro Tokimoto[1,2], Hirotsugu Yamamoto[1,3] （1. Utsunomiya University, 2. DaoApp Technology Company Limited, 3. JST, ACCEL）

We have developed a novel multi-color LED display. The developed LED display shows images at a high frame rate to perform subjective super-resolution, which makes viewers perceive a higher resolution than the number of actual LED lamps. We have confirmed that subjective super-resolution effect is evoked in multi-color images.

Subjective Super-Resolution by Use of High-Speed Multi-Color LED Display

Kojiro Matsushita[1], Toyotaro Tokimoto [1, 2], Hirotsugu Yamamoto [1, 3]
[1] Utsunomiya University, Yoto 7-1-2, Utsunomiya City, Tochigi, 321-0904, Japan,
[2] DaoApp Technology Company Limited, Zhonshan North Road, Shihlin Didtrict, Taipei City, 11155, Taiwan,
[3] JST, ACCEL, Yoto 7-1-2, Utsunomiya City, Tochigi, 321-0904, Japan.

Abstract: *We have developed a novel multi-color LED display. The developed LED display shows images at a high frame rate to perform subjective super-resolution, which makes viewers perceive a higher resolution than the number of actual LED lamps. We have confirmed that subjective super-resolution effect is evoked in multi-color images.*

1   Introduction

Subjective super-resolution display is a display method that gives smoother perception than the physical number of pixels in a coarse LED panel [1, 2]. Previous systems showed only grayscale images [3]. From the principle of subjective super-resolution, it is considered that the super-resolution effect can be obtained even for multi-color images. In this work, we construct a system that supports multiple colors in combination of the three primary colors and demonstrate the super-resolution effect.

2   Subjective super-resolution

Human eyes are constantly moving unconsciously. This eye movement is called fixational eye movement and consists of three types of movements: microsaccade, drift, and tremor [4, 5]. Fig. 1 shows the movement of the viewpoint due to the fixation tremor. We do not perceive this shaking while the eyeball is moving due to fixational eye movement. This is because there is a circuit in the brain that corrects the movement due to fixational eye movement [6]. When correcting the image that comes into the eyes, it detects the presence or absence of relative movement. When viewing a stationary object, the visible image slides as the visual field shifts. On the other hand, when there is a moving object in a stationary background, there is a relative motion between the background and the moving object even if the visual field shifts. In other words, if there is no relative movement in the image that reaches the brain, the brain judges that the eyeball is just moving and is actually still.
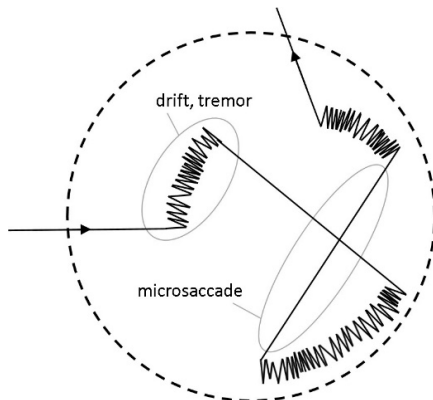
Subjective super-resolution display uses this fixation circuit for the motion caused by fixational eye movements. On the display, the image is moved to imitate fixational eye movement. The observer makes the illusion that the movement of the image is due to his or her own eye movements, and makes unconscious correction. Fig. 2 illustrates the subjective super-resolution display method. The original image with a higher resolution than the display resolution is divided into low-quality sub-frames. By dividing adjacent pixels of the original image so that they correspond to one pixel of the display, the resolution looks like the original image after correction. By switching the sub-frames at a high speed, the sway of the fixation is reproduced.
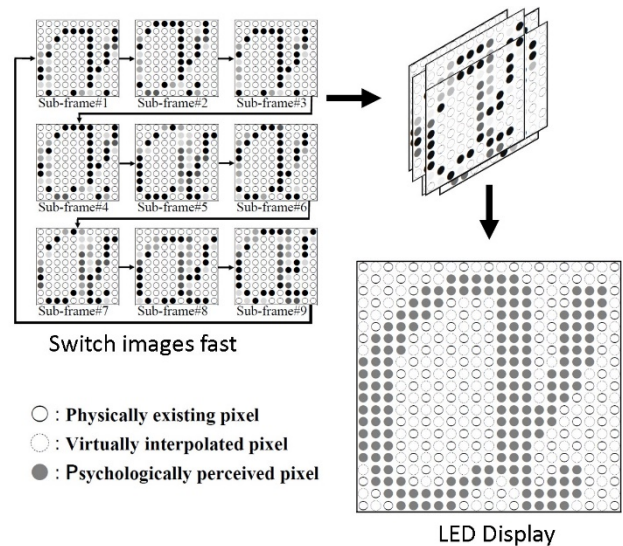

Fig. 2 Subjective super-resolution display.

3   High-Speed Multi-Color LED Display System

A system for subjective super-resolution display was developed by use of an FPGA (Field-Programmable Gate Array). Image data divided into subframes is stored in the memory. The number of colors that can be displayed by this system is a total of 8 colors, 1 bit each for RGB. The switching frequency of the subframes can be changed from 4 types of 1 Hz, 40 Hz, 64 Hz, and 90 Hz by a switch on the FPGA controller board. In addition, the display

Fig. 1 Fixational eye movements.

order and brightness of the sub-frames can also be adjusted with switches on the board.

The time required to scan one row in the LED panel is about 3.68μs . Since the LED display used in the experiment scans 32 lines, the update time for one screen is $3.68\mu s \times 32 lines = 117.76\mu s$ μs. A current flows through each pixel of the LED even when it is turned off. Ghosting is a phenomenon in which pixels that should not be lit by this small current are lit. In this system, in order to prevent unintended lighting of pixels by this ghosting, processing to stabilize the internal circuit is performed. Therefore, the maximum frequency of one screen update is about 8.5 kHz.

4   Experiment

In this work, we divided the original 129×129 pixels image into nine 64×64 pixels sub-frames. Fig. 3 shows the correspondence between the original image and each pixel in the subframe. Nine adjacent pixels of the original image correspond to one pixel of the subframe, and $n \times n$ pixels subframes are created from the $(2n + 1) \times (2n + 1)$ pixels original image. Fig. 4 shows the subframes used in the experiment. Nine slightly different subframes were created because of the division using the above method.
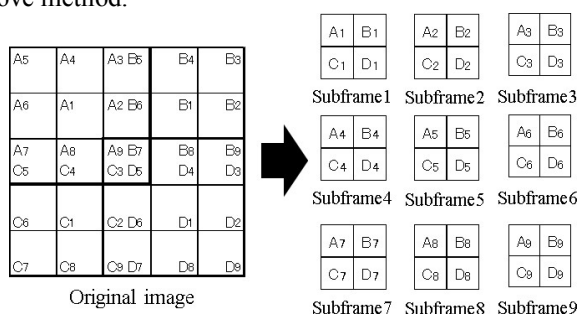

Fig. 3 Correspondence between the original image and 9 sub-frames for subjective super-resolution display.

Fig. 4 Displayed images of 9 sub-frames.

To confirm that the proposed method achieves the effect of subjective super-resolution, we prepare comparative evaluation images. Fig. 5 shows the reference image. For the reference image, the original image used in the experiment is compressed to 64×64 and displayed as a still image on the LED display. We have confirmed that the subjective super-resolution display looks smoother than the reference image.

If the correction processing was performed perfectly, the resolution would appear to be about 4 times, actually it was about 1.5 to 2.5 times. Since the correction function based on fixational eye movement is detection of relative motion, we infer that the observer may see the highest resolution near the boundary where sub-frame switching cannot be detected. Thus, our future work includes optimization of display speed.

Fig. 5 Reference image.

5   Conclusion

In this work, we constructed a system for subjective super-resolution LED display corresponding to 8 colors. We have experimentally confirmed that subjective super-resolution effect was evoked in multi-color images. Further studies are needed in order to verify the effectiveness of subjective super-resolution display in full color and super-resolution effects in natural scene images. A part of this work was supported by JST ACCEL Grant Number JPMJAC1601, Japan.

References

[1]   T. Tokimoto, S. Tokimoto, K Fujii, S. Morita, and H. Yamamoto, "Subjective Super-Resolution Model on Coarse High-Speed LED Display in Combination with Pseudo Fixation Eye Movements," IEICE Trans. Electron., vol. E102-C, No. 11, pp. 780-788 (2019).

[2]   T. Tokimoto, K. Fujii, S. Morita, and H. Yamamoto, "A novel super-resolution display technique by use of spatiotemporal coding," Proc. IDW '18, DESp3/VHFp7-3L (2018).

[3]   K. Matsushita, T. Tokimoto, K. Fujii, and H. Yamamoto, "Spatio-Temporal LED Driving for Subjective Super-Resolution of Grayscale Images," Proc. IDW '19, VHFp4/DESp1-1 (2019).

[4]   H. Kaneko, "Fixational eye movement", Journal of The Institute of Image Information and Television Engineers, vol. 63, pp. 1538-1539(2010)[in Japanese].

[5]   S. Martinez-Conde, S. L. Macknik, and D. H. Hubel, "The role of fixational eye movements in visual perception," Nature Reviews Neuroscience, vol. 5, pp. 229–240 (2004).

[6]   NTT Technical Journal Editorial Department, "Q&A What is fixational eye movement?", NTT Technical Journal, vol. 16, pp. 60-61 (2004)[in Japanese].

LDC2020 | Oral Presentation
# Novel and emerging technologies and applications 2
2020年4月23日(木) 15:30 〜 16:45 301 (Conference Center)

[LDC10-03] Improvement of Visibility of Aerial Image in See-Through AIRR by Cutting Off Ambient Light Using Polarization Modulation

*Kengo Fujii[1], Masaki Yasugi[1,2], Hirotsugu Yamamoto[1,2] (1. Utsunomiya University, 2. JST ACCEL)

An aerial image can be superimposed and displayed on the real world by using a see-through structure by AIRR. In this paper, we improve the visibility of aerial images in see-through AIRR.

Improvement of Visibility of Aerial Image in See-Through AIRR by Cutting Off Ambient Light Using Polarization Modulation

○Kengo Fujii[1], Masaki Yasugi [1), 2)], Hirotsugu Yamamoto [1), 2)]
[1)] Utsunomiya University, Yoto 7-1-2, Utsunomiya City, Tochigi, 321-0904, Japan,
Tel: +81-28-689-6137, E-mail: k_fujii@yamamotolab.science
[2)] JST ACCEL, Yoto 7-1-2, Utsunomiya City, Tochigi, 321-0904, Japan

Abstract: *In aerial imaging by retro-reflection (AIRR), an aerial image can be superimposed and displayed on the real world by using a see-through structure. In this paper, we show a method to make an aerial image brighter by combining a beam splitter with a polarizer.*

1. Introduction

Aerial imaging by retro-reflection (AIRR) is an aerial-image-forming technique [1]. Advantages of aerial image include high sense of reality, no physical contact and precise position. Use of polarization modulation in AIRR, called polarized AIRR (pAIRR), increases visibility of the formed aerial image [2]. The aerial image formed by AIRR has a wide viewing angle horizontally and vertically. On the other hand, in the conventional setup, the visible region was limited to the front of the AIRR device. Thus, we have realized a see-through aerial display system that makes the aerial image and the user's gesture visible from the opposite side [3].

The see-through structure AIRR is used not only for the user to see the aerial image from both the front and back of the display device, but also to see the real scene through the beam splitter behind the aerial image reflected in the user's front view. Here, when the surrounding environment is very bright, there is a problem that the brightness of the aerial image is insufficient, and it is difficult for the user to observe.

In this paper, the visibility of the aerial image is improved by combining a see-through structure AIRR with a polarizer.

2. PRINCIPLE

2.1. Aerial Imaging by Retro-Reflection (AIRR) [1]

Fig. 1 (a) shows the principle of AIRR. This setup consists of a light source, a beam splitter, and a retro-reflector. The beam splitter reflects rays from the light source. The reflected rays are retro-reflected, that is, reflected reversely at the incident positions on the retro-reflector. The retro-reflected rays are converged to the position of the plane-symmetrical of the light source with respect to the beam splitter.

2.2. Polarized AIRR [2]

In order to increase luminance, we utilize polarization modulation. We call this a pAIRR. Fig. 1 (b) shows the principle of pAIRR. This structure is composed of a light source, a reflective polarizer, a quarter-wave retarder film, and retro-reflector. We locate the reflective-polarizer and the linearly polarized light of the display in

crossed-nicol arrangements. In this case, the light from the display reflects at the reflective polarizer. The polarization angle of the retro-reflected light is rotated by 90 degrees after penetrating the quarter-wave retarder twice. Therefore, the retro-reflected light transmits through the reflective polarizer and converges into the plane symmetric position of the light source regarding the reflective polarizer. In the standard AIRR, there was a loss of rays forming an aerial image due to transmission and reflection in the beam splitter. In pAIRR, loss can be reduced in this way, and a brighter aerial image can be formed.
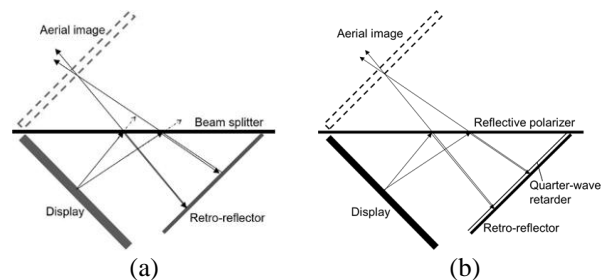

Fig. 1 Principle of (a) AIRR and (b) pAIRR.

2.3 See-Through AIRR [3]

The conventional AIRR had a wide view angle in front of the AIRR device. The see-through AIRR makes it possible to see an aerial image from the opposite side of the AIRR device. Fig. 2 shows the principle of the see-through AIRR.
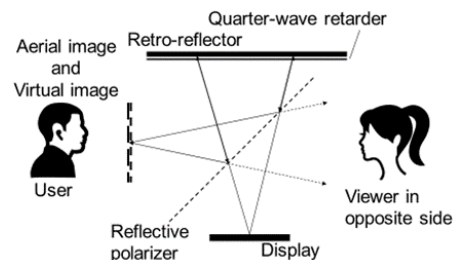

Fig. 2 Principle of see-through AIRR.

In the see-through type AIRR, the arrangement of retro-reflector is different from the conventional AIRR

configuration. Of the light emitted from the light source, the light transmitted through the beam splitter enters the retro-reflector and is retro-reflected by it. The retro-reflected light is reflected by the beam splitter and forms an aerial image for the user in front of the device. On the other hand, the light reflected by the beam splitter from the light source shows a virtual image to the user view from the opposite side of the device. The apparent position of this virtual image coincides with the position of the aerial image seen from the front. As a result, the aerial image with a wider view angle can be realized by combining the view angle from the two directions opposite and front.

3. Experiments
In a see-through AIRR, the ambient light enters the user's field of view through the beam splitter from the back of the aerial image, reducing the visibility of the aerial image. In this experiment, the visibility of the aerial image when viewed from the user is improved by combining a see-through type AIRR with a polarizer.

Fig. 3 shows the insertion position of the polarizer in this experiment. The polarizer is installed between the user and the beam splitter, and on the opposite side. The transmission axis of the polarizer is crossed-Nicol or parallel-Nicol arrangement between the polarizer and the reflective polarizer, and the visibility of the aerial image is changed.
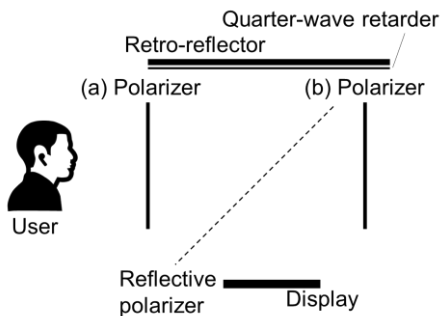

Fig. 3 Experiment of combining polarizer (a) in front user and (b) opposite side of user with see-through structure AIRR

4. Results
Fig. 4 shows an aerial view of a see-through AIRR without a polarizer. Fig. 5 show the experimental results when the polarizer was installed at the position shown in Fig. 3 (a). the transmission axes of the polarizer and the reflective polarizer are Fig. 5 (a) crossed Nicol arrangement and Fig. 5 (b) parallel Nicol arrangement. When each transmission axis was cross, the scene behind the beam splitter was cut, and the aerial image was clearly observed. On the other hand, when the transmission axes were parallel, the aerial image was not visible, and the scenery through the beam splitter was clearly observed.

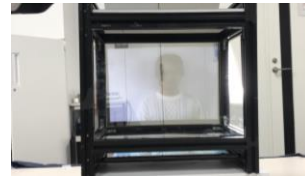Fig. 6 show the experimental results when the polarizer was installed at the position shown in Fig. 3 (b).

Fig. 4 A standard aerial display of see-through AIRR.

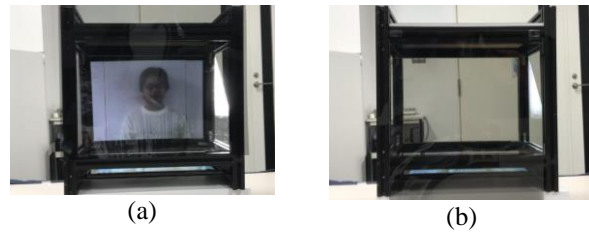(a)   (b)

Fig. 5 A polarizer was installed between the user and the device. The transmission axes of the polarizer and the reflective polarizer are (a) crossed Nicol and (b) parallel Nicol arrangement.

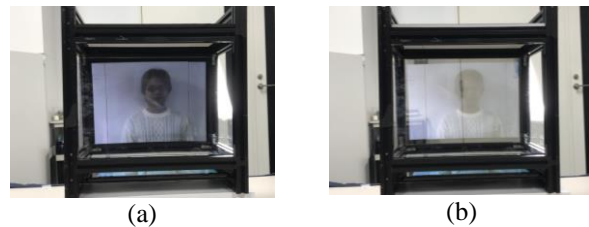(a)   (b)

Fig. 6 A polarizer was installed opposite side of the user. The transmission axes of the polarizer and the reflective polarizer are (a) crossed Nicol and (b) parallel Nicol arrangement.

The transmission axes of the polarizer and the reflective polarizer are Fig. 6 (a) crossed Nicol arrangement and Fig. 6 (b) parallel Nicol arrangement. When each transmission axis was cross, the appearance of the aerial image was the same as when the polarizer was in front. When each transmission axis was crossed, the aerial image was observed as usual.

5. Conclusions
The brightness of the aerial image in the see-through structure AIRR was improved by using polarization modulation.

References
[1] H. Yamamoto, Y. Tomiyama, and S. Suyama, "Floating aerial LED signage based on aerial imaging by retro-reflection (AIRR)," Opt. Exp. 22, pp. 26919-26924 (2014).

[2] M. Nakajima, K. Onuki, I. Amimori and H. Yamamoto," Polarization State Analysis for Polarized Aerial Imaging by Retro-Reflection (PAIRR)," Proc. IDW, Vol. 22, pp429-432 (2015).

[3] R. Kakinuma, M, Yasugi, S. Ito, K. Fujii and H. Yamamoto, "Aerial Interpersonal 3D Screen with AIRR that Shares Your Gesture and Your Screen with an Opposite Viewer," Proc. IMID 2018, P3-103(2018).

LDC2020 | Oral Presentation
# Novel and emerging technologies and applications 2
2020年4月23日(木) 15:30 ～ 16:45 301 (Conference Center)

[LDC10-04] Fabrication of SiO_2-based Binary Diffractive Lens with Controllable Focal Distribution for High-Power Laser Applications

*Atsushi Motogaito[1], Kazuki Matsuo[1], Kazumasa Hiramatsu[1] （1. Mie University）

A binary diffractive lens with controllable focal distribution owing to the adjustable zone radius and interval was fabricated by electron beam lithography and reactive ion etching. The measured intensity distribution was consistent with the simulation.

Fabrication of SiO$_2$-based Binary Diffractive Lens with Controllable Focal Distribution for High-Power Laser Applications

Atsushi Motogaito, Kazuki Matsuo, Kazumasa Hiramatsu

Graduate School of Engineering, Mie University, 1577 Kurima-machiya-cho, Tsu, Mie 514-8507, Japan

Tel & Fax: +81-59-231-9399, and Email: motogaito@elec.mie-u.ac.jp

Abstract: *A binary diffractive lens with controllable focal distribution owing to the adjustable zone radius and interval has been fabricated by electron beam lithography and reactive ion etching. The measured intensity distribution was consistent with that of the simulation.*

1. Introduction

The application of laser beams can be utilized in various fields such as communication, recording, processing, display, lighting, and measurement, owing to their high directivity. Thus, optical elements for controlling laser light have attracted immense research attention. Optical lenses such as convex lenses and axicon lenses, are often employed to arbitrarily control the distribution of laser light by refraction.

The focal length of a lens is a function of its refractive index and radius of curvature. Cylindrical or ring-shaped beams can be obtained focusing a laser beam with an axicon lens. A wide variety of beam patterns can be generated through a combination of lenses. When a laser beam is incident on a convex lens, light is focused at a single point. In contrast, the wavefront of a laser beam transmitted through an axicon lens results in a conical surface with the propagation axis given by the axis of rotational symmetry. A region of high light intensity is generated through interference on the propagation axis. Additionally, axicon lenses have a high depth of focus. It is not necessary to implement the exact control of the focal length for axicon lenses; their depth of focus is controlled using the size of the apex angle of the conical surface.

Optical lenses are difficult to downsize because of their curvatures. In contrast, the focal length of diffractive lenses is independent of the refractive index and radius of curvature and can be controlled using the structure formed on the surface of the lens. Thus, diffractive lenses have a greater degree of freedom for controlling the focal length than optical lenses. Furthermore, because diffractive lenses do not have curvatures, they can be made thinner than optical lenses.

We propose a binary diffractive lens for controlling focal distribution. For most diffractive lenses, the phase shift that is proportional to the square of the ring radius, is used to focus the incident light on the focal point; however, it provides only a fixed light-focusing characteristic. Our method comprises a diffraction grating and diffractive lens that are proportional to the ring radius and square of the ring radius, respectively. Changing the structure of the lens alters the phase shift, focal length, and depth of focus. Therefore, the focal distribution (intensity distribution) can be controlled using diffractive lenses to axicon lenses. Using a quadratic polynomial to express the phase shift and other functions of the ring radius, various focal characteristics can be realized.

In this study, a durable SiO$_2$-based lens for high-power laser applications such as laser processes or laser lighting was fabricated by electron beam lithography by etching glass instead of a resist [1]. Further, the focal distribution of the fabricated lens was characterized and compared with simulation.

2. Design and fabrication

2.1 Design

We designed a binary diffractive lens with a controllable focus based on an ideal Fresnel diffractive lens that deploys both grating and diffractive lenses. Fig. 1 shows schematic diagrams of the cross-sectional and top views of the designed lenses. This structure is based on the Fresnel lens and comprises binary structures. We have demonstrated a conversion method from the Fresnel lens structure to the binary structure in our earlier work [2, 3]. In this figure, the annular zone interval, ΔR_1, at the center of the initial zone interval and the annular zone interval, ΔR_M, at the terminal position, representing the *Mth* zone of the lens, are independent variables used in the simulation, where R_M is the radius of the lens. The wavelength of the incident light is $\lambda_0 = 532$ nm; h is the height of the lens. The design method has been discussed at length in Reference 1 [1].
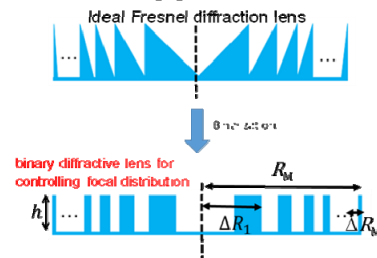

Fig. 1. Schematic of the fabricated lens.

2.2 Fabrication

Figure 2 shows the lens fabrication process. First, chromium was sputtered on an SiO$_2$ substrate. Further,

the resist was spin-coated on the chromium film that acts as a mask for reactive ion etching. Then, electron beam lithography, development, and wet etching of the chromium layer of the developed region, and reactive ion etching by CF$_4$ were carried out in the same order. Finally, the remaining chromium and resist layer were removed.

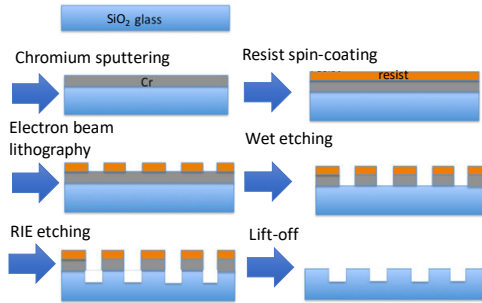Fig. 2. Schematic of the fabrication process.

3. Results and discussion

The atomic force microscopy (AFM) image of the center of the fabricated lens is shown in Fig. 3. The period of the first zone is 27.9 μm, and the depth of the structure is 507 nm. The period of the edge is 7.4 μm, and the depth of the structure is 510 nm. So the lens structure can be fabricated as designed.
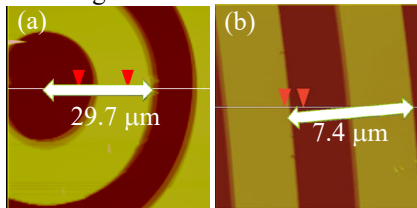
Fig. 3. AFM image of the fabricated lens: (a) center, (b) edge

Then, simulation and measurement results for the focal distribution in the Z direction that is the depth from the fabricated lens along the optical axis, are shown in the Fig. 4. The wavelength of the incident light is 532 nm. The parameters ΔR_I and ΔR_M are 30 μm and 8 μm, respectively. The peak is obtained at the focal point of the fabricated lens at $Z = 6$ mm. The intensity distribution of the measurement agrees well with that of the simulation result. This result is almost the same as that of the resist lens [1].

The focal distribution of the fabricated lens in the X direction that is parallel to the surface of the glass substrate is shown as a function of depth (Z) by using the knife-edge method (Fig. 5). The intensity is maximum at the focal point ($Z = 6$ mm). When moving away from the focal point where the first-order diffraction light is focused, the intensity drops rapidly. These results agree well with the simulation results. Additionally, the fabricated SiO$_2$ lens shows excellent focal distribution as that of the resist lens [1].
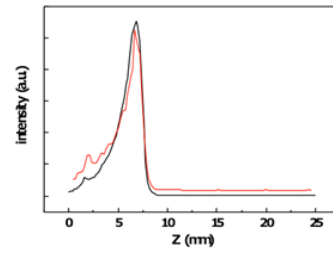

Fig. 4 Simulation (black) and measurement (red) results of the focal distribution in the Z direction.
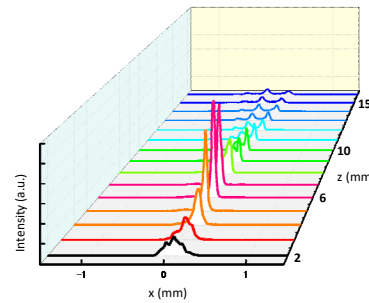

Fig. 5. Focal distribution in the X direction.

4. Conclusions

SiO$_2$ binary diffractive lens has been fabricated by electron beam lithography and reactive ion etching for focal distribution control. The fabricated lens demonstrates an excellent focal distribution that is nearly the same as that of the resist lens, and the experimental results agree well with the simulation data.

References

[1] A. Motogaito, Y. Iguchi, S. Kato and K. Hiramatsu, "Fabrication and characterization of a binary diffractive lens for controlling focal distribution," Appl. Opt. **59**, 742-747 (2020).

[2] A. Motogaito, N. Machida, T. Morikawa, K. Manabe, H. Miyake and K. Hiramatsu, "Fabrication of a binary diffractive lens for controlling the luminous intensity distribution of LED light," Opt. Rev. **16**, 455-457 (2009).

[3] A. Motogaito and K. Hiramatsu, "Fabrication of binary diffractive lenses and the application to LED lighting for controlling luminosity distribution," Opt. Photon. J. **3**, 67-73 (2013).

LDC2020 | Oral Presentation

Laser Technology for Automotive Applications - Phosphor Light Source-

Session Chair: Masaru Kuramoto(Stanley Electric)

Fri. Apr 24, 2020 9:15 AM - 10:30 AM 301 (Conference Center)

[LDC11-01] AlInGaN laser diodes for automotive applications

*Takashi Miyoshi[1], Masanobu Tanaka[1], Shin-ichi Nagahama[1] （1. Nichia Corporation）

 9:15 AM - 9:45 AM

[LDC11-02] Laser Light Sources for Automotive Front Lighting Applications

*Meng Han[1], Julian Carey[1], Paul Rudy[1] （1. SLD Laser）

 9:45 AM - 10:00 AM

[LDC11-03] Design parameters for light engines with static ceramic luminescent converter assemblies

*Volker Hagemann[1], Albrecht Seidl[1] （1. SCHOTT AG）

10:00 AM - 10:15 AM

[LDC11-04] Ce:YAG composite ceramic phosphors for laser lighting

*Kenta Yagasaki[1], Hisashi Minemoto[1], Kana Fujioka[1], Hiroshi Fuji[1], Kazuhisa Yamamoto[1] （1. Osaka University）

10:15 AM - 10:30 AM

LDC2020 | Oral Presentation

Laser Technology for Automotive Applications - Phosphor Light Source-

2020年4月24日(金) 09:15 ～ 10:30 301 (Conference Center)

[LDC11-01] AlInGaN laser diodes for automotive applications

*Takashi Miyoshi[1], Masanobu Tanaka[1], Shin-ichi Nagahama[1] （1. Nichia Corporation）

GaN-based multi-mode blue laser diodes (LDs) were fabricated on c-plane GaN substrates. The wall plug efficiency was 40.7 % at 2.3A. These LDs were integrated to white LDs with luminous flux and luminance over 1300 lm and 700 cd/mm$^{2.}$

AlInGaN laser diodes for automotive applications

Takashi Miyoshi, Masanobu Tanaka, Shin-ichi Nagahama

Nichia Corporation, 491, Oka, Kaminaka-cho, Anan-shi, Tokushima 774-8601, Japan

Phone: +81-884-22-2311

Email: takashi.miyoshi.2@nichia.co.jp

Abstract: *GaN-based multi-mode blue laser diodes (LDs) were fabricated on c-plane GaN substrates. The wall plug efficiency was 40.7 % at 2.3A. These LDs were integrated to white LDs with luminous flux and luminance over 1300 lm and 700 cd/mm$^{2.}$*

1. Introduction

Since the first commercialization of 405 nm GaN-based laser diodes (LDs) for Blu-Ray Disc, there has been numerous developments in laser chips for improving the optical output power and widening lasing wavelength [1]. Realization of high power and wide wavelength range has been expanding the application of GaN-based LDs. Laser displays, e.g. projectors and laser TVs using blue/green LDs have been growing to the major market in GaN-based LDs over the past decade. Also, not only a laser chip itself, but the white LDs which are the combination of laser chip and phosphor have developed . They have the same beam radiation characteristics as white light emitting diodes (LEDs) and could apply to various applications like medical, lighting or automotive. In this work, we report latest development of blue and white LDs for automotive applications.

2. Structure of blue LD chip

Figure 1 shows the schematic structure of a multi-mode blue LD. AlInGaN epitaxial layers were grown on free-standing n-type c-plane GaN substrates by metal organic chemical vapor deposition. The ridge waveguide structure with 45 μm stripe width was formed on p-side. P-side and n-side electrodes were deposited on each side of the laser chip. Dielectric mirrors were deposited on both facets, which were obtained by cleavage along m-plane. These were mounted on the heat sink by the junction down. Conventional TO-ø9.0 mm package was applied for the evaluation of blue LDs.
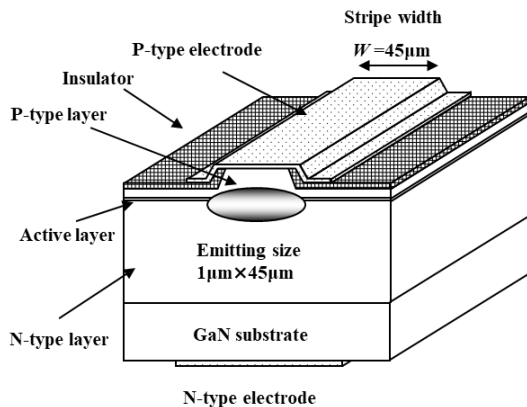

Fig. 1. Schematic structure of LDs.

3. Blue LDs

Figure 2 shows the voltage-current (V-I) and the optical output power-current (L-I) at 25 ºC under direct current (DC) with a wavelength of 450 nm. The threshold current was about 0.2 A. The optical output and the forward voltage at 2.3 A were 3.65 W and 3.9 V, corresponding to the wall plug efficiency (WPE) of 40.7 %. Improvement of WPE contributed to suppress the heat generation due to energy conversion losses and decreased thermal load at high temperature operation which was required for automotive applications.
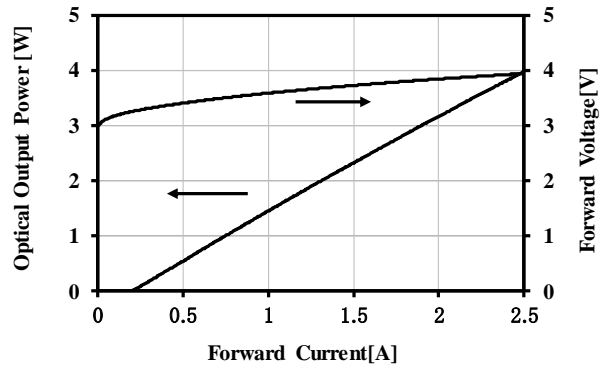

Fig. 2. L-I and V-I characteristics of a blue LD.

Figure 3 shows the temperature dependence of the relative optical output power of our developed blue LD and conventional one by operating pulse currents. In the automotive application, stabilization of optical output power against temperature is important considering usage environment, especially high temperature range.
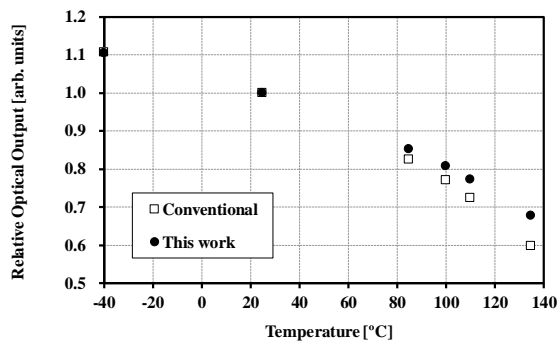

Fig. 3. Temperature dependence of optical output power

Developed LDs have customized structure and realized stable characteristics compared to conventional one.
 The operating test condition was at the temperature of 110 °C under DC and automatic current control (ACC) condition with the forward current of 2.5A assuming automotive exterior applications (Fig. 4). From 1,000 hours operation, it was confirmed that degradation of the optical output was very little. This indicates that our developed blue LDs have the enough durability even under high temperature operation.
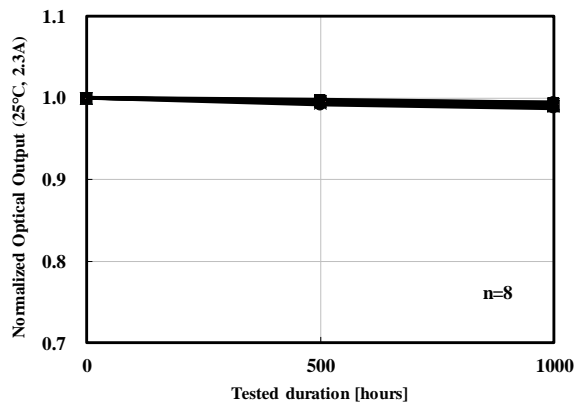

Fig. 4. Result of operating test with forward current of 2.5A under DC operation.

4. White LDs

 White LDs which were composed of blue chip and yellow phosphor have an advantage in that they have more luminance than LEDs in general. These products were already commercialized as the light sources for high-beam spot in automotive headlight [2]. However, high-flux is required for expanding the application of white LDs. In this work, two developed blue LD chips described in previous section were applied for new generation white LDs. As a result, when the forward current was 2.3 A under pulse operation at 25 °C, the luminous flux and the luminance were 1360 lm and 710 cd/mm^2 from the phosphor (size: 1.0 x 0.5 mm), respectively. These results were considered to indicate that our new white LDs would be the light sources for high-beam spot as well as low/high-beam use. Moreover, very high-luminance would contribute for the realization of efficient thinner height headlamps.
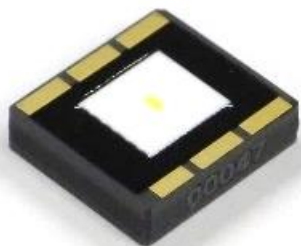

Fig. 5. Appearance of white LD.

7. Conclusions

 Efficient blue multi-mode LDs with stable temperature characteristics were fabricated. The optical output and

the WPE were 3.65 W and 40.7 %. By integrating two blue LD chips, the luminous flux of 1360 lm and the luminance 710 cd/mm^2 of white LDs were realized. We believe that the performance of these LDs is suitable for automotive applications.

References

[1] Y. Nakatsu, Y. Nagao, K. Kozuru, T. Hirao, E. Okahisa, S. Masui, T. Yanamoto, S. Nagahama, " High-efficiency blue and green laser diodes for laser displays," Proc. SPIE 10918, 109181D-1 (2019).

[2] T. Miyoshi, "8th Laser Display Conference", Yokohama, Japan (2018).

LDC2020 | Oral Presentation
# Laser Technology for Automotive Applications - Phosphor Light Source-
2020年4月24日(金) 09:15 ～ 10:30 301 (Conference Center)

[LDC11-02] Laser Light Sources for Automotive Front Lighting Applications

*Meng Han[1], Julian Carey[1], Paul Rudy[1] （1. SLD Laser）

Progress in development of blue laser diodes and their integration with phosphors enabled a new category of solid state light sources for automotive lighting. In this paper, a dynamic laser light module consisting of blue laser diode, a MEMS scanner and remote phosphor for adaptive driving beam and future intelligent lighting will be introduced.

Laser Light Sources for Automotive Front Lighting Applications

Meng Han[1], Julian Carey[1], Paul Rudy[1]
[1] SLD Laser, 6500 Kaiser Driver, Fremont, CA 94555, USA

Abstract: *Progress in development of blue laser diodes and their integration with phosphors enabled a new category of solid state light sources for automotive lighting. In this paper, a dynamic laser light module consisting of blue laser diode, a MEMS scanner and remote phosphor for adaptive driving beam and future intelligent lighting will be introduced.*

1. Introduction

Most recently automotive OEMs have spent great efforts to develop next generation high resolution adaptive driving beam to improve driving safety and to enable novel functionalities related to autonomous driving and Car-to-X communications, however, conventional techniques including LCD, DLP, MicroLED encounter technical challenges associated with harsh automotive environment and stringent system reliability and efficacy requirements. The objective of our study is to investigate the feasibility of utilizing a MEMS based laser scanner consisting of a high power 450nm LD, a remote phosphor and a biaxial MEMS mirror for adaptive automotive lighting applications.

2. Laser light source technology

By fabricating a blue laser diode on semi-polar Gallium Nitride (GaN), blue laser light is produced at high levels of optical output power of 3 watts and more due to the high gain in the device [1]. As importantly, these laser diodes show minimal droop characteristics, meaning that, high power lasers with very small scale are being implemented in automotive lighting applications which require high brightness light source with a peak luminance value exceeding 1000cd/mm². As illustrated in Fig.1, unlike a blue LED that emits a few watts of diffuse optical energy per square millimeter, several watts of light produced from the laser diode emanate from a light emitting area only tens of microns in width, and can therefore illuminate a tiny spot at phosphor surface that is hundreds of microns in diameter [2].

To complete the spectrum for white light illumination, the blue radiation is partially converted to longer wavelengths by a phosphor element. Innovations in high temperature phosphors and special binding materials have enabled phosphors to convert light efficiently at the elevated power densities and temperatures that result from the laser light radiation. It's worth mentioning that most of previously developed phosphor converted laser light sources utilize a transmissive architecture, namely, blue laser is focused at the rear surface of a laser phosphor layer and white light is emitted from the other side of laser phosphor. Although it involves relatively less efforts to develop a transmissive laser light source, proper heat management of laser phosphor material is challenging since heat is more difficult to be dissipated

from transmissive laser phosphor comparing with reflective phosphor which is directly mounted on a thermally conductive substrate. As a result, the minimum laser spot size on transmissive phosphor would be larger than that of reflective phosphor to avoid excessive heat generated by focused laser beam, which leads to lower peak luminance of laser light source with transmissive phosphor.
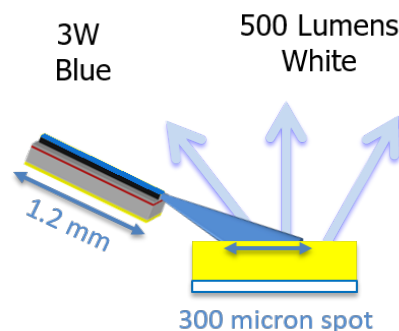

Fig. 1. Schematic drawing of a high luminance laser white source consisting of a high power GaN blue laser diode and reflective phosphor.

Except of advantages of high peak luminance, reflective laser light architecture also enables higher level of laser safety. Assuming failure of laser phosphor material either due to shock or degradation, leakage of coherent blue laser radiation from failed transmissive phosphor can induce severe eye injuries. In contrast to transmissive laser light, specular reflection of blue laser in reflective laser light can be readily blocked with a beam dump, direct radiation from blue laser diode has virtually no chance to damage human eye, therefore a laser light source with reflective phosphor can be classified as a class I laser.

As shown in Fig.2, a fiber coupled laser light module with reflective phosphor has been developed especially for automotive lighting applications. This fiber coupled laser light is composed of a high power blue laser diode, a multi-mode glass fiber of 30 cm up to 1,000 cm of length to transport blue light to a distal end and a reflective phosphor element enclosed in a metal head.

Fig. 2. A fiber coupled laser light module for automotive front lighting applications, which is composed of a high power 450nm wavelength blue laser module, a transporting multi-mode optical fiber and a remote reflective laser phosphor packaged in a metal head.

Typical optical fiber carrying 450nm laser radiation operates at a transport efficiency of approximately 99.8 per cent per meter thus losses are neglectable even for significant fiber lengths. As described in previous session, a remote phosphor platelet located at distal end of the optical fiber is operated as a reflecting element. This placement offers the advantage of straightforward heat sinking of the phosphor element which is important due to the high levels of power density. Blue laser module which is more sensitive to heat can be placed in a low ambient temperature environment, for example, at the back side of a laser headlamp or at a mounting position far away from engine components. As a passive component which is much more thermally robust than laser diode, the phosphor metal head will be placed inside headlamp. Since the thermal power of phosphor metal head is 1.7W only, a highly compact system design can be realized by eliminating of active cooling components such as cooling fans.

The laser spot size on phosphor of fiber coupled laser light module is 270um in diameter, which generates luminous flux of 450lm at 50^0C operating temperature and peak luminance exceeding 1400cd/mm^2, which is one order of magnitude higher than the peak luminance of typical automotive high power LEDs and two times brighter than the first generation automotive laser white light sources. Reflected blue laser radiation is blocked by a beam dump which ensures that coherent laser light is never released. Additional safety and performance monitoring features are included in the blue laser module, where the optical power of blue laser and phosphor converted yellow light and case temperature of high power blue laser diode are actively monitored with integrated detectors located in the blue laser module. With this arrangement, the white light emitting element may be sealed in a location remote from the laser and its electronics which may be placed in another location that has more favorable physical and thermal characteristics.

3. Laser scanner for ADB

3.1 Automotive adaptive driving beam
Automotive Adaptive Driving Beam (ADB) is an intelligent front lighting solution which can maximize beam range to targeted illumination area and minimize undesired glares to oncoming and preceding traffic. In pace with continuous performance improvement of ADAS sensors and image processing algorithm, there is clear tendency towards pixelized ADB or matrix beam with higher angular resolution, illuminance and contrast. Recently there were several techniques under development for next generation ADB ranging from LCD, DLP, MicroLED to Laser scanner, besides normal photometric requirements including resolution, illuminance and contrast, overall system efficacy is an import metric to assess those next generation ADB technologies. It is known that a halogen bulb consumes approximately 60W of electric power to fulfill low and high beam requirements, the power consumption was reduced to less than 15W in the past decade through wide adoption of LED but it was again raised to 50W – 60W as demonstrated by some most recent high resolution ADB prototypes. How to further improve system optical efficacy turned out to be a major focus for development of next generation ADB [3].

3.2 Laser dynamic scanner for ADB
Among various techniques of high resolution ADB, a laser scanning approach appears promising by offering high illuminance, design flexibility, compact system size and low power consumption. As shown in Fig.3, a laser scanning ADB unit consists of a fiber coupled high power blue laser, a MEMS scanner as beam steering component and a reflective phosphor as light conversion part. High power blue laser beam is coupled into a glass fiber, after passing though collimating and folding optics, it is reflected by a millimeter size biaxial MEMS scanning mirror driven by electrostatic force. The MEMS mirror steers the laser beam angle with kHz scanning rate before the laser beam reaches a reflective laser phosphor plate. A dynamic scanning pattern on phosphor generated by flying laser spots will be projected onto road with aspherical projection lens and relay optics.

System architecture of laser scanning ADB is quite similar to static laser fiber module which has been introduced in previous session, heat management of blue laser diode is decoupled from laser scanner unit and reflective phosphor, no active cooling or sophisticate heat management such as heat pipe is required for laser scanning ADB. Total electric power consumption of complete laser scanning module as demonstrated in Fig.3 is 12W only, average illuminance value on road at 25m distance exceeds 200lx. A typical laser scanning range covers +/- 20 degrees in both horizontal and vertical directions with an angular resolution less than 1 degree. The minimum pixel number of laser scanning ADB exceeds 400 and can be further increased by reducing laser spot size on phosphor. The whole scanning system is quite compact with a footprint of less than 2 x 2 inch.
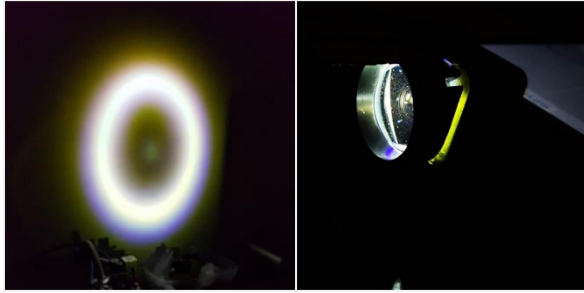
Fig. 3. A dynamic laser scanning unit for automotive adaptive beam. Blue laser is coupled into an optical fiber, reflected by a bi-axial MEMS mirror and focused at a reflective phosphor. A dynamic light distribution pattern is projected on the road through a 2inch diameter projection lens.

4. Discussions and conclusions

Comparing with previous laser light sources with transmissive phosphor, fiber coupled laser light module with reflective phosphor nearly doubles those key photometric metrics in terms of luminous flux and peak luminance, it is an ideal laser light source for static automotive front lighting application such as high beam assistant based on its unique advantages of passive cooling, high luminance and class 1 laser safety. Integration of a biaxial MEMS scanner with fiber coupled reflective phosphor allows further extension of laser light applications from a static high beam to a dynamic scanning ADB. A compact size laser scanning ADB prototype has demonstrated long beam range, reasonable angular resolution with a total electric power consumption of 12W only.
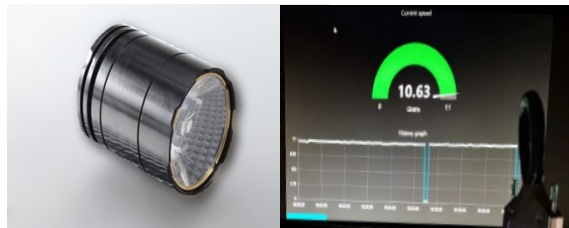

Fig. 4. A laser light LiFi prototype demonstrates a real time date transfer rate of 10.63 Gbit per second. Laser light from a GaN laser diode is modulated to encode data transfer after collimation with a 35mm diameter lens.

In addition to conventional automotive lighting functionalities such as high beam, low beam and ADB, the unique characteristics of GaN laser light allow new types of applications which go beyond illumination. To put a number in perspective, the pulse rise time of GaN laser diode is approximately 0.5ns, high speed modulation of laser output power can be implemented to integrate either laser ranging or light communication functions into a laser light automotive illumination unit. Some of the recent studies conducted in our group in 2019 have demonstrated a real time data transfer rate of 10.63 Gbit per second with a laser LiFi (Light Fidelity) prototype designed for wireless data transmission, the laser light source and real time data rate are shown in Fig.4. Another investigation related to LiDAR (Light Detection and Ranging) based on both simulation and experimental measurements has proven that a laser light headlamp is capable to measure range information by detecting of back reflected laser pulses emitted from an automotive illumination laser light source, in other words, both illumination and sensing can be realized with a single laser source.

Laser lighting technology has grown more mainstream in automotive applications which were the first to harness its high luminance characteristics in forward lighting like high beam. With new progress in MEMS scanner, fiber coupled laser scanning approach is attracting significant interests in developing high system efficacy ADB, which enables the transition of laser light applications from static to dynamic lighting functionalities. Besides conventional automotive front lighting applications, development is ongoing to integrate directional white-light laser sources into next-generation lighting applications such as LiFi for light-based wireless data transmission, LIDAR for range detection and Car2X communications.

References

[1] S. Nakamura, S. Pearton and G. Fasol, "The Blue Laser Diode; the Complete Story", Springer, ISBN 3-540-66505-6, (2000)

[2] J. J. Wierer, J. Y. Tsao and D. S. Sizov, "Comparison between blue lasers and light-emitting diodes for future solid-state lighting"; Laser Photonics Rev. Vol. 7, No. 6, pp. 963-993 (2013)

[3] International Symposium on Automotive Lighting ISAL 2015, Proceedings of the Conference: Volume 16

LDC2020 | Oral Presentation

Laser Technology for Automotive Applications - Phosphor Light Source-

2020年4月24日(金) 09:15 ～ 10:30 301 (Conference Center)

[LDC11-03] Design parameters for light engines with static ceramic luminescent converter assemblies

*Volker Hagemann[1], Albrecht Seidl[1]　(1. SCHOTT AG)

Laser pumped phosphor light sources overcome the luminance limit of LEDs, that restricts the use of solid state lighting in etendue limited applications such as digital projection. This paper investigate static converter properties such as light diffusion and temperature dependence of the irradiance limit that is necessary to fully utilize the benefits of these components in optimized light engines.

Design parameters for light engines with
static ceramic luminescent converter assemblies

Volker Hagemann, Albrecht Seidl

SCHOTT AG, Hattenbergstr. 10, 55122 Mainz, +49 6131 66-7318, volker.hagemann@schott.com

Abstract: *Laser pumped phosphor light sources overcome the luminance limit of LEDs, that restricts the use of solid state lighting in etendue limited applications such as digital projection. The improved irradiance limit of static ceramic converter assemblies will accelerate the transition to those sources. A good understanding of the static converter's properties such as light diffusion and temperature dependence of the irradiance limit is necessary to fully utilize the benefits of these components in optimized light engines. Measurements of these properties are reported and their impact on the light engine design is discussed in this paper.*

1. Introduction

Cerium doped garnet phosphors [1] have revolutionized the general lighting industry, that has almost fully adopted to solid state lighting (SSL) by now. For general lighting applications, the limited luminance that LEDs offer is not of any concern, since flux is easily scaled by increasing the emitting area. But for digital projection and other etendue limited applications, even the luminance of several 100 cd/mm², that is achieved by high brightness LEDs is in most cases not sufficient to replace high intensity discharge lamps.

Laser pumped phosphors (LPP) are the SSL-solution of choice for these applications and digital projectors that make use of laser pumped phosphor wheels gain an increasing market share. Ceramic phosphor wheels that enable light engines with several 100 Watts of laser power have been reported [2]. But also so called static ceramic phosphors, that are soldered onto a heatspreader can provide luminances of 2000 cd/mm² and more [3] in a light engine.

Fig. 1. Static ceramic converters

Although there is no strict definition to the term, a light engine usually includes electronics, optics and means for heat dissipation. Just as a combustion engine needs to have a perfect match to the electronic, thermal and mechanical interfaces of a vehicle, a light engine needs to meet the electronic, thermal and optical requirements of the respective application. We investigate some of the thermal and optical properties of static ceramic converters that may be leveraged to fully utilize their benefits for perfectly designed light engines.

2. Experimental setup

A versatile setup that irradiates a sample with a blue laser of well defined power and spot size is used for the experiments (figure 1).

Details on how to derive irradiance and luminance profiles from the recorded camera images are reported elsewhere [3].
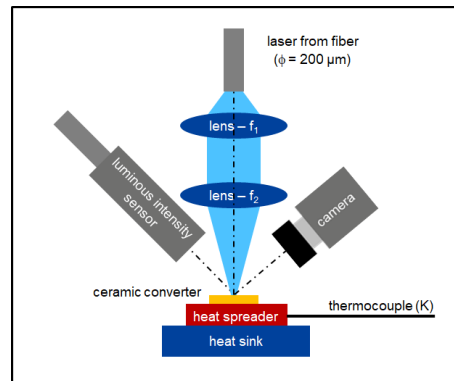

Fig. 1. Experimental setup for irradiance measurement.

3. Experimental Results

For the reported experiments, the blue laser light output from the D = 200 µm fiber core is imaged onto the sample with a magnification factor of 2.8, yielding a nominal spot size of 560µm.

At room temperature, a power of up to 21 W can be delivered onto the sample before the light output dropped due to "thermal roll-over" [3].
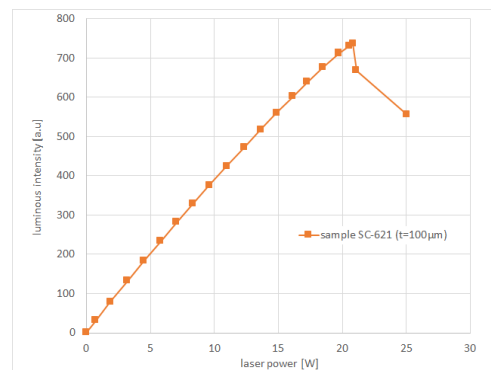

Fig. 2. Measurement of a 100µm thick ceramic at a heat spreader temperature of 24 °C yields a power limit of 21 W.

If the temperature of the heat sink is increased via a thermoelectric cooler (TEC), the power limit drops in a linear fashion and an increase of the power limit to almost 23 W for cooling the sample to 0°C can be anticipated from extrapolation.
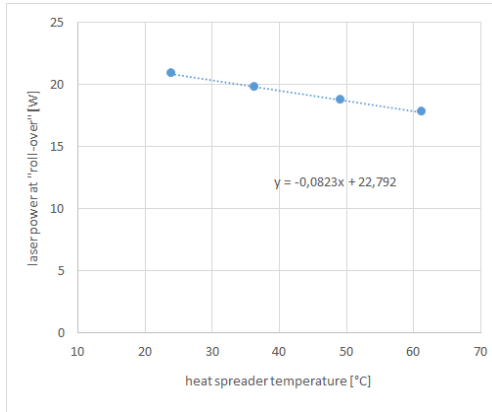

Fig. 3. Temperature dependency of power limit

From the normalized blue light irradiance profile in figure 4 an irradiance limit of ~60 W/mm² can be calculated from the 21 W power limit at room temperature and figure 3 can be scaled accordingly.
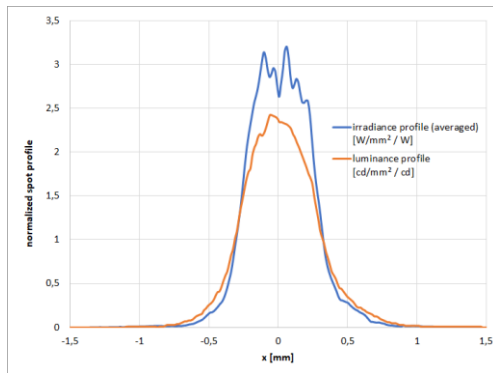

Fig. 4. Spot profile of blue laser irradiation and of luminescent emission.

Figure 4 also shows the normalized luminance profile, which is wider than the irradiance profile. This is due to light diffusion in the phosphor [3, 4]. For a measured luminous intensity of 1188 cd that is emitted in normal direction, we calculate a peak luminance of about 2.8 kcd/mm². Depending on the etendue of the optical system that the light engine is supposed to "drive", light from a certain spot area of the emitting phosphor surface is coupled into the optical system. The dependency of flux and average luminance within this spot on the spot size is calculated from the luminance distribution and depicted in figure 5.
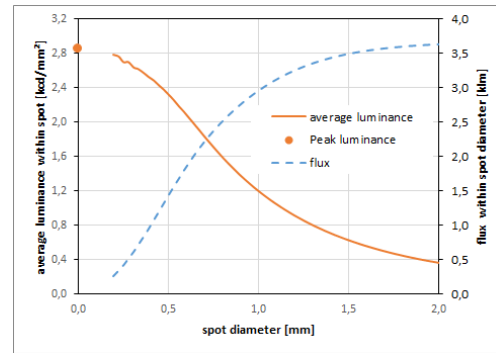

Fig. 5. Dependency of average luminance and luminous flux on the diameter of the spot that the light is collected from.

4. Discussion

As an example for reading the graph in figure 5, we assume that a light engine only collects light from an D = 0,5 mm spot. In this case, the phosphor delivers a very high average luminance of 2400 cd/mm², but only about 40% of the total flux is collected. Increased ambient temperature will reduce the flux and cooling will increase it according to figure 3.

7. Conclusions

Static ceramic phosphors deliver high luminance and high flux in laser pumped phosphor light sources. But only with throughout knowledge of the thermal properties as well as the light diffusion characteristics, a light engine design that fully utilizes these benefits can be designed.

Optimizing shape and extension of the blue laser spot provides a further, very important degree of freedom for optimizing the light engine. This can be addressed by measurements with different magnification factors in our setup, but is also supported by a powerful numerical model, that is able to predict light diffusion as well as power limits for any given irradiance profile.

References

[1] Z. Xia and A. Meijerink, "Ce3+-Doped garnet phosphors: composition, modification, luminescence properties and applications", Chem. Soc. Rev. 46, 275.299 (2017)

[2] V. Hagemann, A. Seidl and K. Inoguchi "Utilizing the unique properties of ceramic fluorescent converters for laser pumped phosphor light-engines in digital projection." The 7th Laser Display and Lighting Conference 2018 (LDC'18), Yokohama, Japan, Apr. 24 - Apr. 27 (2018)

[3] V. Hagemann, A. Seidl and G. Weidmann, „Static ceramic phosphor assemblies for high power, high luminance SSL-light sources for digital projection and specialty lighting", Proc. SPIE 11302 (2020) – to be published

[4] Prahl, S.A., "Light transport in tissue", PhD Thesis, Univ. of Texas at Austin (1988).

LDC2020 | Oral Presentation

Laser Technology for Automotive Applications - Phosphor Light Source-

2020年4月24日(金) 09:15 ～ 10:30　301 (Conference Center)

[LDC11-04] Ce:YAG composite ceramic phosphors for laser lighting

*Kenta Yagasaki[1], Hisashi Minemoto[1], Kana Fujioka[1], Hiroshi Fuji[1], Kazuhisa Yamamoto[1] （1. Osaka University）

We succeeded in suppression for thermal-quenching of phosphors using AlN-Ce:YAG composite ceramics for the first time. The ceramics have excellent thermal conductivity, so that the generated heat by the focused beam of a Laser Diode (LD) diffuses efficiently. This technology contributes to the improvement of a high-power head lamp.

Ce:YAG composite ceramic phosphors for laser lighting

Kenta.Yagagasaki[1], Hisashi Minemoto[1], Kana Fujioka[1], Hiroshi Fuji[1], Kazuhisha Yamamoto[1]
[1] Osaka University 2-6 Yamadaoka Suita-shi Osaka 565-0871 Japan
Phone +81-6-6879-8735, email yagasaki-k@ile.osaka-u.ac.jp

Abstract: *We succeeded in suppression for thermal-quenching of phosphors using AlN-Ce:YAG composite ceramics for the first time. The ceramics have excellent thermal conductivity, so that the generated heat by the focused beam of a Laser Diode (LD) diffuses efficiently. This technology contributes to the improvement of a high-power head lamp.*

1. Introduction

Laser lighting composed of blue Laser Diodes (LDs) and phosphors enabled to reduce the size of lighting devises and saved its energy, because the LD was higher brightness source than conventional one, e.g. halogen lamp and light emitting diode (LED). In addition, its high directivity had an advantage of further illumination for practical use in various fields [1]. While the high brightness LD beam was focused on the surface of phosphor, the focused spot heated the phosphor and its temperature significantly rised. It quenched the luminescence with the thermal ionization [2-5] in the phosphor for example, Ce-doped yttrium aluminium garnet (Ce:YAG) as shown in Fig1. To decrease the quenching, the thermal conductivity of the phosphor had to be enough to dissipate the heat generated from relaxation process. Aluminium nitride (AlN) for an additive to the phosphor has high thermal conductivity and high refractive index as shown in Table1. These properties definitely induce the phosphor temperature to decrease. In this study, we propose AlN-Ce:YAG composite ceramics so as to decrease the luminescent quenching by suppressing phosphor temperature rising and evaluate its luminescent properties. This is the first AlN-Ce:YAG composite ceramics phosphor, and we aim to establish new energy-saving laser lighting technology

Table 1 Thermal conductivity and refractive index [6,7]

Material	Thermal conductivity[W/m・k]	Refractive index
Al_2O_3	32	1.8
AlN	150	2.2
YAG	14	1.8

2. Experimental procedure

The composite ceramics were obtained by a solid-state reaction method. We mixed Ce:YAG with 10wt%, 20wt%, and 50wt% of AlN. Green bodies were sintered at 1700 ° C for 12 h in an air atmosphere or a nitrogen one. Figure 2 shows the experimental setup for measurement of luminescent properties. The sample was placed on a hot plate, which changed the environment temperature from room temperature to 150°C, the spectra and luminescence properties were measured by an illuminometer with changing the maximum optical power from a blue LD (wavelength 445 nm) up to 1.1 W. Figure 3 shows the obtained sample and the light emission. In addition, the temperature at surface of the sample was measured by a thermo camera. Moreover, the composite structure of the sample was evaluated by X-ray diffractometer (XRD) and Scanning Electron Microscope (SEM).
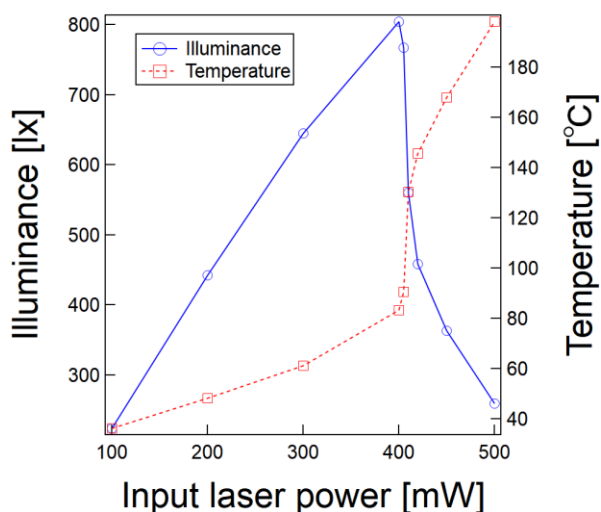

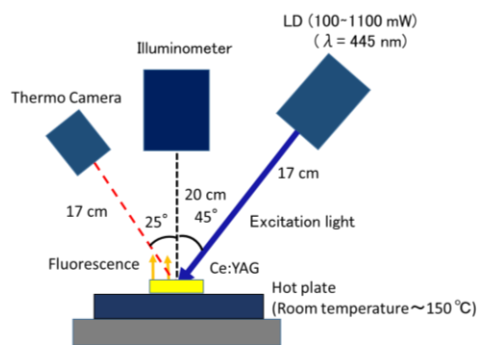Fig. 1. Thermal quenching of Ce:YAG powder at high excitation

Fig. 2. The experimental setup

Fig. 3. Sample and light emission

3. Results and discussion

Figure 4 shows the temperature change on the surface of samples sintered in an air atmosphere as the excitation laser power rises up to 1.1 W. It is confirmed that the temperature rise is suppressed by the AlN-Ce:YAG composite at the high-excitation laser power in comparison to the only Ce:YAG. However, the added AlN is oxidized during sintering in an air atmosphere, and turn into Al_2O_3 as shown XRD peak pattern (Fig. 5a) It is considered that the effect of suppressing the temperature rise is caused by the thermal conductivity of Al_2O_3. We improved sintering conditions in order to leave AlN phase. As a result, Fig. 5b shows that AlN peaks is clearly confirmed and the AlN-Ce:YAG composite ceramic is successfully synthesized. This ceramic has the excellent thermal conductivity and contributes to the improvement of a high-power head lamp.
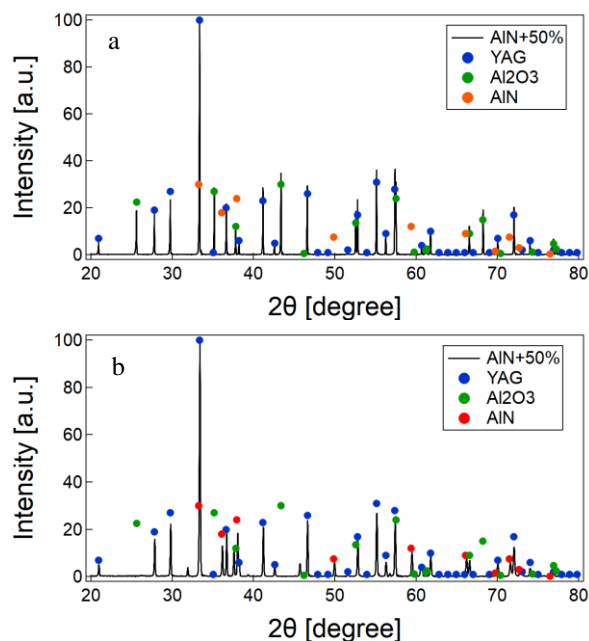
4. Conclusions

We confirmed the improvement of the performance of the thermal property by the composite ceramics. Moreover, we also demonstrated the AlN phase in Ce:YAG ceramics, which had been conventionally considered difficult to sinter, and the possibility of manufacturing composite ceramics of Ce:YAG and AlN. In the next step, we aim to produce AlN-Ce:YAG composite ceramics with higher purity by optimizing sintering conditions, and aim to realize innovative energy-saving technologies that reduce temperature quenching by using composite ceramics.

References

[1] Jonathan J. Wierer, Jr., Jeffrey Y. Tsao,Dmitry S. SizovJ. "Comparison between blue lasers and light-emitting diodes forfuture solid-state lighting"Laser Photo. Rev.**7**,963-993, (2013)

[2] Shuxing Li, Qiangqiang Zhu, Daiming Tang, Xuejian Liu, George Ouyang et al, J. Mater. Chem. C "Al2O3–YAG:Ce composite phosphor ceramic: a thermally robust and efficient color converter for solid state laser lighting"Mater. Opt. Electron. Devices. **4**, 8648 (2016)

[3] N. C. George, Kristin A. D, R. Seshadri "Phosphors for SolidState White Lighting". Annu. Rev. Mater. Res. **43**, 481−501. (2013)

[4] Bachmann V., Ronda C., Meijerink A." Temperature Quenching of Yellow Ce3+ Luminescence in YAG:Ce." Chem. Mater. **21**, 2077−2084 (2009)

[5] J. Ueda, Dorenbos, Bos, A. J., Meijerink, A.Tanabe, S. "Insight into the Thermal Quenching Mechanism for Y3Al5O12:Ce3+ Through Thermoluminescence Excitation Spectroscopy." J. Phys. Chem. C. **119**, 25003−25008 (2015)

[6] Kyocera, "characteristics of Kyocera fine ceramics", https://www.kyocera.co.jp/prdct/fc/list/tokusei/denndou/index.html

[7] M.R. Krames, O.B. Shchekin, R. Mueller-Mach, G.O. Mueller, L. Zhou, G. Harbers, and M.G. Craford: Status and future of highpower light-emitting diodes for solid-state lighting. J. Disp. Technol. 3(2), 160 (2007).
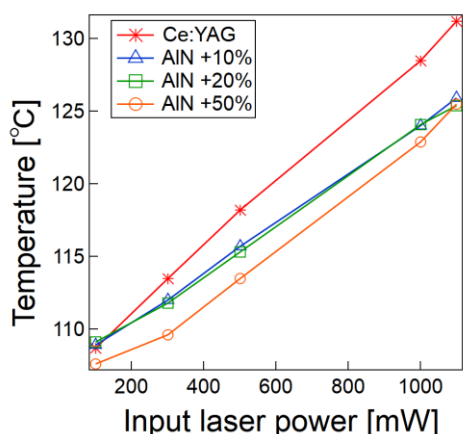
Fig. 4. The dependence of the temperature of phosphors on input laser power

Fig. 5. XRD patterns of the sample sintered in an air atmosphere (a) and a nitrogen atmosphere(b)

LDC2020 | Oral Presentation

Laser Technology for Automotive Applications - Systems-

Session Chair: Satoshi Ouchi(Hitachi)
Fri. Apr 24, 2020 10:45 AM - 12:15 PM 301 (Conference Center)

[LDC12-01] Automotive Laser Headlamps using DMD Technologies

*Kenneth Li[1], Yung Peng Chang[2] (1. Optonomous Technologies Inc., 2. Taiwan Color Optics, Inc.)

10:45 AM - 11:15 AM

[LDC12-02] Sokuiki-Sensor (LiDAR) System and Applications

*Keisuke Inoue[1], Katsumi Kimoto[1], Naohiro Shimaji[1], Masanori Hino[1], Toshihiro Mori[1] (1. Hokuyo Automatic co., ltd.)

11:15 AM - 11:45 AM

[LDC12-03] Wide Angle Multi-Shift Stereo Camera with Monocular Detection

*Masayuki Kobayashi[1], Kazuyoshi Yamazaki[1], Felipe Gomez Caballero[2], Takuma Osato[2], Takeshi Endo[2], Masayuki Takemura[2], Takeshi Nagasaki[3], Takeshi Shima[3] (1. Central Research Laboratory, Hitachi Ltd., 2. Hitachi Research Laboratory, Hitachi Ltd., 3. Hitachi Automotive Systems Ltd.)

11:45 AM - 12:15 PM

LDC2020 | Oral Presentation
Laser Technology for Automotive Applications - Systems-
2020年4月24日(金) 10:45 ～ 12:15 301 (Conference Center)

[LDC12-01] Automotive Laser Headlamps using DMD Technologies

*Kenneth Li[1], Yung Peng Chang[2] （1. Optonomous Technologies Inc., 2. Taiwan Color Optics, Inc.）

This paper presents a laser excited phosphor automotive headlight combining the high efficiency of the white LEDs and the high intensity spot of the laser, producing a non-uniform, hot spot intensity profile on the DMD. The output intensity profile on the roadway can be controlled providing the low beam, high beam, ultra-long-range spot light, and controlled dimming for various detected objects from a single DMD

Invited Paper

Automotive Laser Headlamps using DMD Technologies

Kenneth Li [1)], Yung Peng Chang [2)]

1)   Optonomous Technologies Inc., 30330 Rainbow View Ct., Agoura Hills, CA 91301, USA, +1-661-803-9939,
kenli@optonomous.com
2)   Taiwan Color Optics, Inc., 4F., No.32, Keya Rd., Daya Dist., Taichung City, Central Taiwan Science Park, 42881, Taiwan,
+886-916-369-588, ypchang@tcog.com.tw

Abstract: *This paper presents a laser excited phosphor automotive headlight combining the high efficiency of the white LEDs and the high intensity spot of the laser, producing a non-uniform, hot spot intensity profile on the DMD. With the spatial intensity modulation capability of the DMD, the output intensity profile on the roadway can be controlled providing the low beam, high beam, ultra-long-range spot light, and controlled dimming for various detected objects from a single DMD.*

1. Introduction

For intelligent automotive headlight applications, a digital projector type of architecture is commonly used such that the illumination on the roadway can be controlled by the pixels of the imager, such as a DMD. Selective areas can be illuminated or dimmed such that it provides better illumination for the driver and less blinding glares for the on-coming vehicles. In order to provide a wide field of view (FOV) for low beam and high on-center brightness for high beam, the illumination source luminance for the on-center portion of the FOV must be much higher than the rest of the area. Simply increasing the overall brightness for illuminating the DMD would be very inefficient as most of the illuminated area around the hot spot will be dimmed electronically, which is wasting power. Effectively, the area dilution of the brightness from increasing the FOV must be counteracted by an increase in source luminance (for the center hot spot section only). This paper discloses an optical configuration in which the center portion of the light source, e.g. a LED, is pumped using a laser such that a hot spot is formed in the center section, with a sharp roll-off to a relatively lower luminance in outer section of the light source.

2. All-in-One Headlight Intensity Requirements

Multiple headlights are being used in automobiles. Most common are the low beam and high beam headlights and traditionally, they are placed inside the same lamp housing. Recently, most of the headlight systems consist of multiple modules with one or more modules for low beams and high beams. Ideally, the output intensity profile of the final output is as shown in Figure 1.
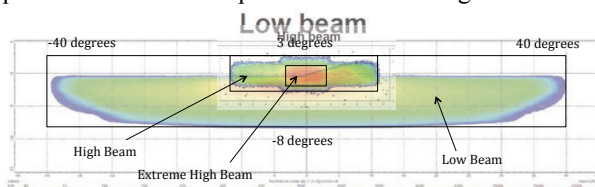

Figure 1 – Intensity Profile of a All-in-One Headlight

In order to provide such intensity profile using a DMD, if the DMD is illuminated in the traditional manner with a uniform intensity profile, the intensity will have to be equal to the highest, i.e. the peak, intensity required for the ultra-long-range beam as the DMD can modulates the output intensity by reduction. If the average intensity is the peak intensity, the total amount of light required will be many times higher and will be impossible to implement. As a result, a non-uniform intensity profile as shown in Figure 2 will be required with low intensity for the main area, higher intensity for hot spot 1, and the highest intensity for hot spot 2. With such configuration, a minimum amount of light will be wasted due to the modulation of the DMD.
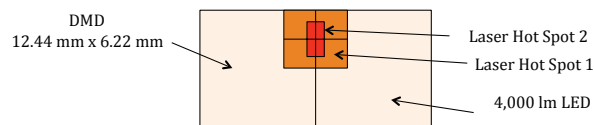

Figure 2 – Target Intensity Profile on DMD

In order to provide the higher intensity profile of hot spot 1 and hot spot 2, a layer of crystal phosphor as shown in Figure 3, the hybrid LED/laser light source, is required for converting the laser light into visible light as the original phosphor layer of the white LED will be damaged by such high laser power.
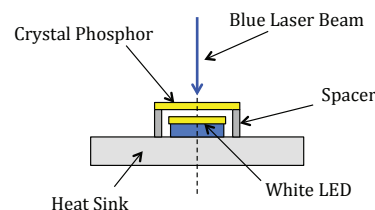

Figure 3 – Hybrid LED/Laser Light Source

Figure 4 shows a graphical representation of the intensity profile. The peak intensity can be 5 to 10 times higher than the rest of the area. Using the DMD, the output can be modulated to provide the low beam only, the high beam only, the ultra-long-range beam only, or a combination of all. In addition, the modulation and the laser output can be coordinated providing the lowest power consumption possible for the various lighting configurations.
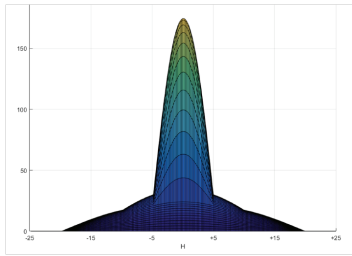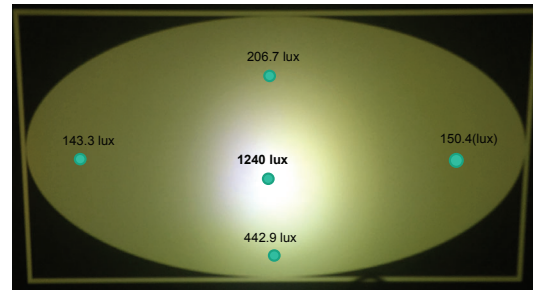
Figure 4 – Intensity of a Hot-Pot Light Source

Figure 6 – Output Intensity of a Hot-Spot Headlight

3. A Hybrid LED/Laser Light Source Headlight

Figure 5 shows a schematic diagram of a DMD headlight using a hybrid LED/Laser light source such that the intensity profile as shown in Figure 1 can be achieved.
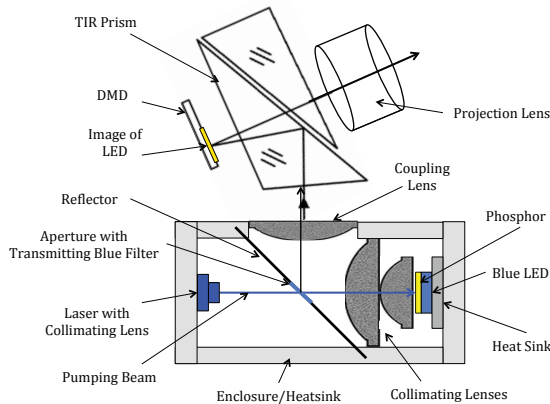

Figure 5 – Schematic Diagram of a Hybrid Light Source DMD Headlight

As shown in the figure, a white LED with phosphor excited with a blue LED is used as the large area light source for the general illumination of the DMD. This LED can also be replaced by the LED as shown in Figure 3 with the crystal phosphor plate for laser excitation. The output from the LED is collimated by the collimated lenses and directed to the TIR lens with DMD for projection. On the other side of the light source, the collimated output beams from one or more laser diodes are directed towards the collimating lens through apertures in the reflector such that the beams are focused onto the crystal phosphor plate through the collimating lenses. The resulting white light output is collimated and directed to the DMD together with the output of the LED. With the proper arrangements, the intensity profile of the light output to the DMD can be tailored to produce the desired output pattern of the headlight. An initial hot spot prototype was built using such hybrid LED/laser light sources and a TI's DLP® DMD imager and the output is as shown in Figure 6, which is the projected output onto a screen demonstration the relative output of the system. It clearly shows a hot spot in the output profile with the center intensity about 5 to 6 times the intensity around the hot spot. Another prototype is being built with higher intensity white LED and with multiple lasers and the results will be reported.

4. A Novel All-in-One DMD Headlight.

Although the normal DMD is used in the ON/OFF mode where the output is produced when the mirrors is turned to ON, the -12° position with the illumination light source placed at the -24° position. When the mirrors are turned to the OFF +12° position, the reflected light will reflected to the +48° position where a light dump is place to collect the stray light. In this novel structure, the DMD is used with the mirrors in both the -12° and the +12° position utilizing both the ON and OFF positions of the DMD. In this case, the normal light source is place at -24° position such that the light is directed to the output when the DMD is ON. In addition, the hot-spot light source is placed at the +24° position such that the light output is directed to the output when the DMD is OFF. The output of this headlight can be controlled by the DMD to produce a output pattern that is a combination of the full area light source and the hot-spot light source.
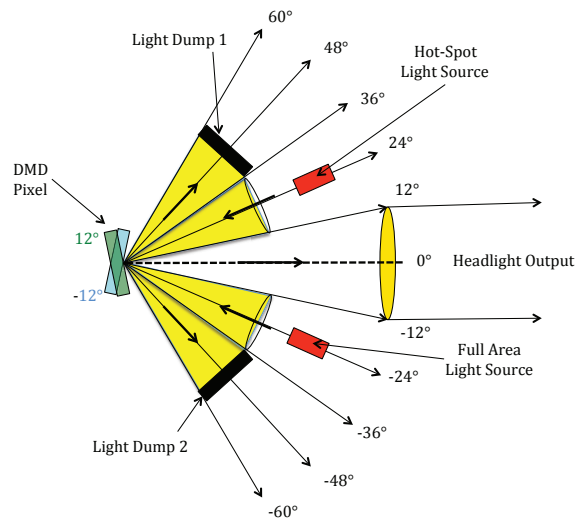
5. Conclusion

A prototype of the hot-spot headlight was built showing the principle of a all-in-one headlight operation using a hybrid LED/laser light source. A novel DMD system using both the ON/OFF positions of the DMD mirrors is also described.

LDC2020 | Oral Presentation
# Laser Technology for Automotive Applications - Systems-
2020年4月24日(金) 10:45 ～ 12:15 301 (Conference Center)

[LDC12-02] Sokuiki-Sensor (LiDAR) System and Applications

*Keisuke Inoue[1], Katsumi Kimoto[1], Naohiro Shimaji[1], Masanori Hino[1], Toshihiro Mori[1] （1. Hokuyo Automatic co., ltd.）

The authors have developed various types of Sokuiki-sensors that is fundamental technology for autonomous robots, autonomous driving car. In this paper, we have introduced the structure and application of such Sokuiki-sensors.

Sokuiki-Sensor (LiDAR) System and Applications

Keisuke Inoue, Katsumi Kimoto, Naohiro Shimaji, Masanori Hino and Toshihiro Mori

Hokuyo Automatic co., ltd., 1-37, Kamisu-cho, Toyonaka-shi, Osaka, Japan

561-0823, +81-6-6333-8635, k-inoue@hokuyo-aut.jp

Abstract: *LiDAR for surrounding environment recognition is an important fundamental technology for autonomous service robots, autonomous driving car and so on. The authors have developed various types of Sokuiki-sensors for over a decade. In this paper, we have introduced the structure and application of such Sokuiki-sensors.*

1. Introduction

In past decade, scanning laser range sensors such as, LiDAR (Light Detection and Ranging) and Sokuiki-sensor, have been used in various robotic applications. They serve as an eye of service robots and detect obstacle for the robots used in factories. Recently it has also attracted attention as an important technology for the autonomous driving car. Many companies around the world are actively developing it (see [1] for the review). Sensor manufactured by Velodyne Inc is one of the most widely used sensor for autonomous driving car. It can measure distances over 100 m with a 360° FoV (Field of View). To achieve this, it uses many pairs of emitters and receivers methodically arranged in the device. Such design requires complicated adjustment during the assembly and to realize it with small size and low cost is difficult. Solid-state Lidar has important advantage over such design due to the possibility of miniaturization and high reliability, but such LiDAR are yet to be developed by any companies.

We have developed variety of user friendly LiDAR (named as Sokuiki-sensor) which are compact, less-power consuming and economical. In this paper, we describe about our Sokuiki-sensor and its applications.

2. Two-Dimensional Sokuiki-sensor

2.1 General application

Three dimensional LiDAR is developed by many companies, however, there are many situations where two-dimensional LiDAR are used because of its compactness and low costs, for example, the indoor AGVs and delivery robots. Two-dimensional sensor mounted at 150～400 mm height on the robots can avoid collisions with people and obstacles while capturing the environment data to be used for SLAM. In such application, wide FoV and high accuracy in short range are the most important factors. Fig.1 shows the product appearance of Hokuyo's very small sized Sokuiki-sensor UST-20LX suitable for the usage in AGV application.

2.2 Advanced application

In the near future it is expected that the autonomous mobile robots will be deployed as home delivery robots, construction robots, farm work robots, and infrastructure inspection robots. Most of these robots are expected to work outdoors. In such applications, the requirements of
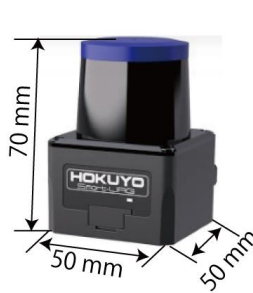

Fig. 1 : Small size of Sokuiki-sensor (UST-20LX)

Fig. 2 : Outdoor type of Sokuiki-sensor (URM-40LC-EW)

LiDAR are, stable operation under the wide temperature difference, strong sunlight, rainy, snowy, and foggy conditions. Fig. 2 shows the product appearance of Hokuyo's two-dimensional Sokuiki-sensor URM-40LC-EW that is suitable for outdoor usage. URM-sensor has intelligent technology, such as, rain and fog filters, and control of gain for different ambient light conditions.

2.3 Structure of two-dimensional Sokuiki-sensor

Fig. 3 shows basic structure of Hokuyo's two-dimensional Sokuiki-sensor [2]. Laser beam is generated by the laser diode and emitted outside through the emitting lens and the emitting mirror. When the laser beam bounces off the object, the reflected light is captured by an APD (Avalanche Photo Diode) via a light receiving lens and light receiving mirror. Two-
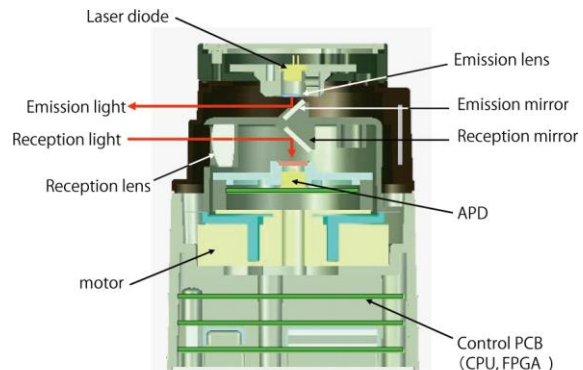

Fig. 3 : Structure of two-dimensional Sokuiki-sensor

dimensional distance with a wide FoV is realized by an optical scanner that rotates optical assembly with a motor. Pulse Laser diode with wavelengths around 780-950 nm are used in the device.

3. Three-dimensional Sokuiki-sensor

3.1 Advantages of Three-Dimensional Sokuiki-sensor
In outdoor environments, there are many objects that cannot be detected by a two-dimensional Sokuiki-sensor, such as curbs, or handrails at position of about 1 m height. In addition, the road is not flat, so a three-dimensional range sensor is indispensable. Fig. 4 shows the product appearance of Hokuyo's three-dimensional Sokuiki-sensor. It has wide FoV and high vertical resolution, e.g. 40 degree and 45 points. Fig. 5 shows the output image of three-dimensional Sokuiki-sensor. As shown in Fig. 5, the height information of trees and walls can be measured in an outdoor environment.

3.2 Structure of three-dimensional Sokuiki-sensor
Fig. 6 shows basic structure of Hokuyo's three-dimensional Sokuiki-sensor [3]. While maintaining the simplicity and advantages of the two-dimensional scanning method, three-dimensional scanning is achieved by mounting a resonant mirror (ReM) on the horizontal scanning motor (Fig. 6). ReM vibrates at a few kHz to achieve vertical scanning. Since the ReM is very small and lightweight, it is operated by the same motor with two-dimensional Sokuiki-sensor. To supply power to the ReM fixed to the rotating part, a non-contact power supply module is incorporated inside the scanner. Thus, the line of power supply to the ReM does not hinder rotation of the motor. The laser light is emitted outside through the ReM. The reflected light is also received by the APD through the ReM. The time difference between light emission and light reception is calculated with same method as two-dimensional Sokuiki-sensor and distance to the point is estimated.

4. Conclusion
In this paper, we introduced some of the Sokuiki sensors. In the future, demand of such sensors with higher specification is expected to rise. For example, customers have requirements for longer distances, higher resolution, and smaller size.

To achieve these, re-development of some of the basic technology is vital. For example, designing a laser
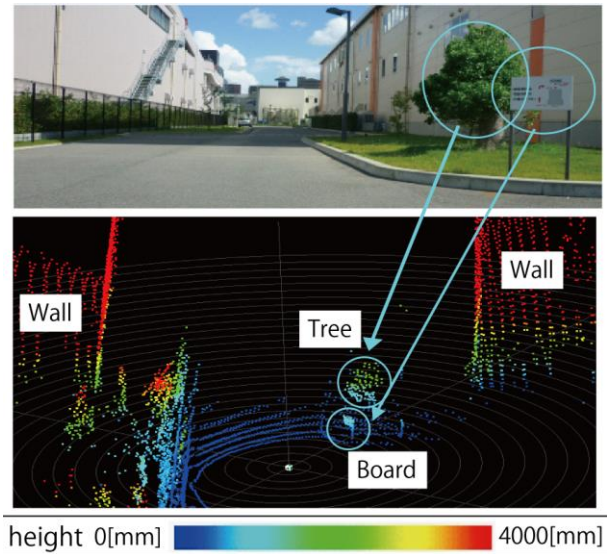

Fig. 5 : Output image of tree-dimensional Sokuiki-sensor
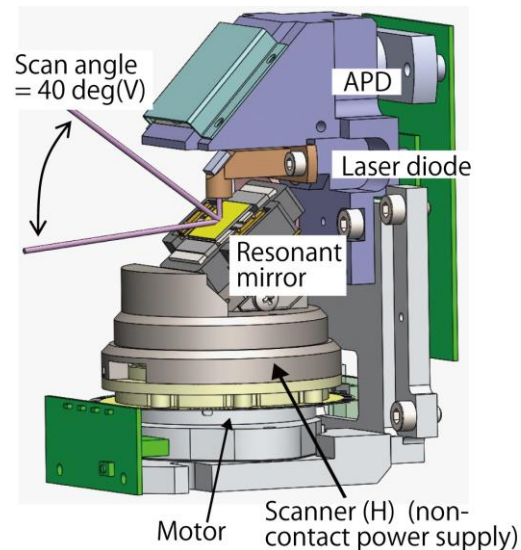

Fig. 6 : Structure of three-dimensional Sokuiki-sensor

with a small spot, a photodetector with high sensitivity with stable output, and non-mechanical scanning device for the Sokuiki-sensor can dramatically improve its performance. This will in turn enhance the functionality of autonomous robots.

References

[1] Nikkei electronics, "LiDAR price destruction" (*in Japanese*), 49-61 (2017).

[2] H. Kawata, et.al, "Advanced functions of the scanning laser range sensor for environment recognition in mobile robots," in Multisensor Fusion and Integration for Intelligent Systems, 2006 IEEE International Conference on. IEEE, pp.414-419, (2006)

[3] Katsumi Kimoto, et, al "Development of Small Size 3D LIDAR", Proc. of ICRA 2014, pp. 4620-4626, (2014)

Fig. 4 : Three-dimensional Sokuiki-sensor
(YVT-35LX)

LDC2020 | Oral Presentation
# Laser Technology for Automotive Applications - Systems-
2020年4月24日(金) 10:45 ～ 12:15 301 (Conference Center)

[LDC12-03] Wide Angle Multi-Shift Stereo Camera with Monocular Detection

*Masayuki Kobayashi[1], Kazuyoshi Yamazaki[1], Felipe Gomez Caballero[2], Takuma Osato[2], Takeshi Endo[2], Masayuki Takemura[2], Takeshi Nagasaki[3], Takeshi Shima[3] （1. Central Research Laboratory, Hitachi Ltd., 2. Hitachi Research Laboratory, Hitachi Ltd., 3. Hitachi Automotive Systems Ltd.）

The developed stereo camera system combines stereo and monocular vision for far-distance detection and wide-angle FOV. Moreover, we improved detection accuracy by compensating the monocular vision with the road disparity calculated from the stereo vision.

Wide Angle Multi-Shift Stereo Camera with Monocular Detection

Masayuki Kobayashi[1], Kazuyoshi Yamazaki[1], Felipe Gomez Caballero[2], Takuma Osato[2], Takeshi Endo[2], Masayuki Takemura[2], Takeshi Nagasaki[3], Takeshi Shima[3]

[1] Central Research Laboratory, Hitachi Ltd., 1-280, Higashi-koigakubo Kokubunji-shi, Tokyo, Japan, +8170-4880-8040, masayuki.kobayashi.tx@hitachi.com, [2] Hitachi Research Laboratory, Hitachi Ltd., [3] Hitachi Automotive Systems Ltd.

Abstract: *The developed stereo camera system combines stereo and monocular vision for far-distance detection and wide-angle field of view. Moreover, we improved detection accuracy by compensating the monocular vision with the road disparity calculated from the stereo vision.*

1. Introduction

Automobiles are one of most convenient mobilities. On the other hand, they are causing many traffic accidents every year. Recently, advanced driver assistance systems (ADAS) had been developed to achieve both convenience and safety. Our research focuses on the creation of next generation stereo cameras that can contribute to improve safety of ADAS.

A stereo camera system uses a set of two cameras from which obtained images can be used to measure the distance to a target object by calculating the object's disparity between the two images. Several car manufacturers let cars equip stereo camera systems that support automatic braking system (AEB) and adaptive cruise control (ACC) [1, 2].

In order to increase the safety performance, there is a need for an extended field of view (FOV) stereo camera that can detect crossing cyclists and pedestrians while turning at intersections [3-5]. On the other hand, detection and distance measurement of far preceding vehicles is also required for high-speed range ACC. If the stereo camera FOV is simply extended, resolution of CMOS image sensors becomes insufficient.

In this paper, we describe the developed multi-shift stereo camera system which combines stereo and monocular vision, as well as the monocular detection technique implemented in the monocular vision region which employs road disparity.

2. Wide angle by multi-shift method

Fig. 1 shows the concept of the FOV for a stereo camera using the multi-shift method.
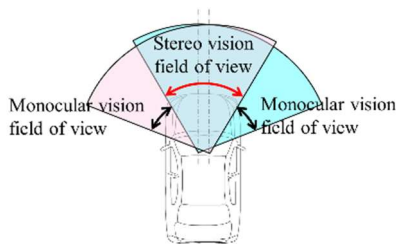

Fig. 1. FOV of multi-shift stereo camera.

It can be seen above that the FOV for each camera is extended to the outer side. Therefore, the center area of the FOV becomes a stereo vision region since both left and right camera images are available, while the right and left areas of the FOV are monocular vision regions.

Fig. 2 shows example images obtained by the multi-shift stereo camera. The left view camera image has a monocular vision at left of stereo vision, and the right view camera image has a monocular vision at right of stereo vision.
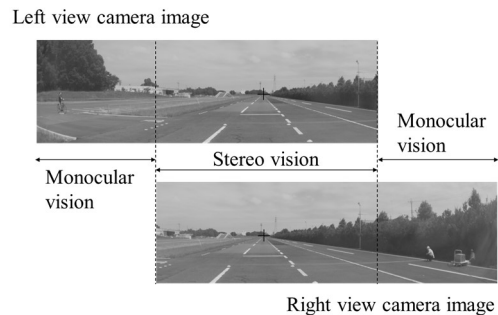

Fig. 2. Example of multi-shift stereo camera image set.

Therefore, in comparison with the outer-angle area, the center FOV has many CMOS image sensor pixels assigned, which ensures that required resolution for far detection is available.

3. Monocular detection with stereo vision

Monocular object detection for the multi-shift stereo camera is described in this section. We developed a monocular detection technique employing the top-view image subtraction method combined with a camera posture estimation by road disparity obtained from the stereo vision. Fig. 3 shows the top-view image subtraction method detection concept. In the top-view image subtraction, the camera images of current and previous time frames are affine-transformed to create top-view images, then the resulting images are subtracted to obtain a differential top-view image. The created top-view images can be moved in a way that the road on both images overlap, resulting on an image where only the differentials between the three-dimensional objects and the moving objects remain. Therefore, even if the own car is moving, this technique will enable easy detection of the objects. Further, this technique is possible to measure the distance of the object by calculating the length from the camera to the object on the top-view image.
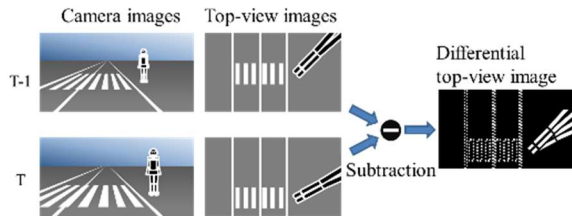
Fig. 3. Monocular view detection using differential top-view image.

In order to create an accurate top-view image in situations where the camera posture changes dynamically, it is important to estimate the posture of the camera at any given time. Fig. 4(a) shows the concept of camera posture estimation using disparity from the road surface. Fig. 4(b) shows a road disparity on the camera image. We utilize the road disparity [7] to estimate the camera posture parameters, e.g., camera height, tilt, and roll angles. In our technique, the road surface is assumed flat, we can estimate the parameters by fitting the road disparity to a flat plane. Then, the compensated top-view image with the estimated parameters can accurately detect the objects and measure the distance.
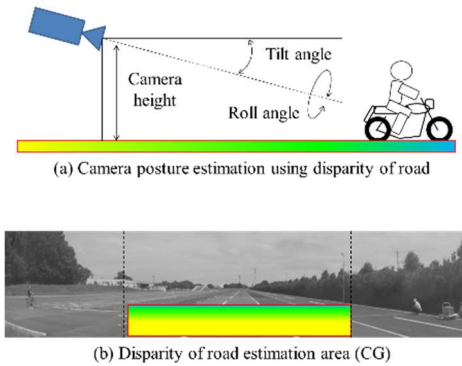

(a) Camera posture estimation using disparity of road

(b) Disparity of road estimation area (CG)

Fig. 4. Camera pose estimation using disparity of road.

4. Result

Fig. 5 shows an experimental result of the monocular detection. In this condition, the target was a crossing cyclist from the right side, the own vehicle mounted the stereo camera traveled towards a collision point. At the moment, the distance between the cyclist and the camera was 16 m.

(a) Test scenario

(b) Camera image

(c) Result without camera posture estimation

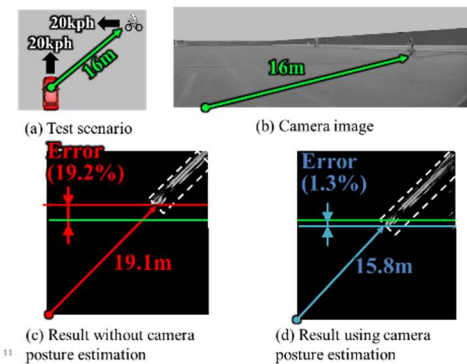(d) Result using camera posture estimation

Fig. 5. Experimental result of monocular detection.

Fig. 5(c) shows the differential top-view image without the camera posture estimation, and the white pixels indicate subtraction differentials. The measured distance was 19.1 m, and the error was 19.2%. In the same manner, Fig. 5(d) shows the result using the estimation. The measured distance was 15.8 m, and the error was 1.3%.

As the result, the developed estimation method reduced the distance measurement error from 19.2% to 1.3% because the top-view image was compensated with the estimated parameters. Therefore, we have confirmed the effect of the technique.

5. Conclusions

We developed a stereo camera employing the multi-shift method which can achieve both far-distance detection and wide-angle FOV.

The multi-shift method creates monocular vision on the outer part of the stereo camera FOV and expands its FOV. Moreover, the method can suppress the resolution reduction of the center FOV by using many pixels for the stereo vision field, preserving the detection distance performance in the stereo vision field.

In addition, the developed monocular detection technique using the top-view image subtraction method with camera posture estimation was able to achieve high-accurate detection in the monocular vision field by estimating the camera posture using disparity of the road surface. In this way, it became possible to realize AEB for wide-angle FOV targets. We expect that the spread of this low-cost and wide-angle multi-shift stereo camera, will contribute to further reduce traffic accidents.

References

[1] S. Katahira, E. Shibata, and T. Monji, "Development of an Advanced Stereo Camera System," SAE Tech. Paper, 2007-01-3591, (2007).
[2] T. Sugawara, H. Altmannshofer, and S. Kakegawa, "Applications of Road Edge Information for Advanced Driver Assistance Systems and Autonomous Driving," Advanced Microsystems for Automotive Applications 2017, pp. 71-86, (2017).
[3] World Health Organization, "Global Status Report on Road Safety 2018," (2018).
[4] Euro NCAP, "AEB VRU Test Protocol v3.0.2," (2019).
[5] Euro NCAP, "Euro NCAP 2025 Roadmap," (2017).
[6] C. Yang, H. Hongo, and S. Tanimoto, "A New Approach for In-Vehicle Camera Obstacle Detection by Ground Movement Compensation," International IEEE Conference on Intelligent Transportation Systems, (2008).
[7] S. Kakegawa, H. Matono, H. Kido, and T. Shima, "Road Surface Segmentation based on Vertically Local Disparity Histogram for Stereo Camera," International Journal of Intelligent Transportation Systems Research 16 [2], pp. 90–97, (2018).

LDC2020 | Oral Presentation

Visible light communication (VLC) technologies and systems
Session Chair: Hidekazu Hatanaka(Ushio)
Fri. Apr 24, 2020 1:00 PM - 2:30 PM 301 (Conference Center)

[LDC13-01] Location-based Services using Visible Light Communication

*Shinichiro Haruyama[1] （1. Keio University）

1:00 PM - 1:30 PM

[LDC13-02] Laser-based LiFi for 6G: Potential and Applications

*Volker Jungnickel[1], Julian Hohmann[1], Dominic Schulz[1], Peter Hellwig[1], Jonas Hilt[1], Christoph Kottke[1], Ronald Freund [1]   （1. Fraunhofer Heinrich Hertz Institute）

1:30 PM - 2:00 PM

[LDC13-03] The Future Prospects of Robot-Photonics:Visible Light Communication and Sensing with the Plasmonic Mirror

*Kensuke Murai Murai[1]   （1. National Institute of Advanced Industrial Science and Technology）

2:00 PM - 2:30 PM

LDC2020 | Oral Presentation
# Visible light communication (VLC) technologies and systems
2020年4月24日(金) 13:00 ～ 14:30 301 (Conference Center)

[LDC13-01] Location-based Services using Visible Light Communication

*Shinichiro Haruyama[1] （1. Keio University）

Visible light communication can be used for location-based services by sending location information from visible light sources. Typical light sources of visible light communication are LED lights, but we proposed the use of DMD (Digital Micromirror device) projectors to send different data in different directions. Combinations of different types of transmitters and receivers are shown with various location-based services.

Location-based Services using Visible Light Communication

Shinichiro Haruyama

Graduate School of System Design and Management, Keio University
4-1-1, Hiyoshi, Kohoku-ku, Yokohama, 223-8526, Japan,
Telephone: +81-45-564-2467
Fax: +81-45-564-2541,
Email: haruyama@sdm.keio.ac.jp

Abstract: Visible light communication can be used for location-based services by sending location information from visible light sources. Typical light sources of visible light communication are LED lights, but we proposed the use of DMD (Digital Micromirror device) projectors to send different data in different directions. Combinations of different types of transmitters and receivers are shown with various location-based services.

1. Introduction

Visible light communication is generally line-of-sight communication, which means that communication is possible only when there is no obstacle between a transmitter and a receiver. This line-of-sight property means that positional relationship between a transmitter and a receiver can be detected. This positioning technology makes it possible to realize various location-based services.

2. Types of transmitters and receivers for visible light communication

Typical visible light transmitters for communication are LED lights which emits visible light in all directions [1]. DMD (Digital Micromirror device) projector can also be used as a visible light transmitter. A DMD projector can send different data in different directions. On the receiver side, typical visible light receivers for communication are photo diodes that receive optical signal and convert it into an electric current. An image sensor can also be used as a receiver [2]. By performing image processing on an image, it is possible to receive data from an optical transmitter and detect the direction of the incoming light.

3. Location-based services using different types of transmitters and receivers

Table 1 shows the combination of different transmitters and receivers and explains the advantages/disadvantages of different combinations. Each combination and its use for location-based service will be explained in the following subsections.

3.1. Location-based services using LED light and photo diode

Figure 1 shows a use case of location-based services using LED light and photo diode, where an LED light is used as a data transmitter and a terminal with a photo diode is used as a data receiver.

Table 1. Combination of different types of transmitters and receivers

A receiver can detect not only the room location, but it can also detect the position in the room where the receiver is located. Its prototype [3] was made as shown in Figure 2, where the visually impaired in the middle of the photo was able to walk with the audio guidance. The location accuracy is a few meters which is the illuminated range of an LED light.
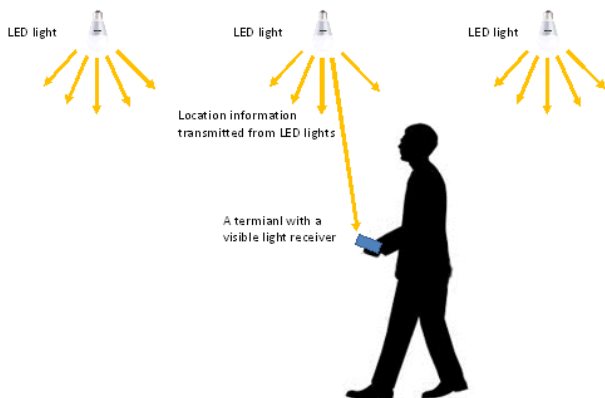

Figure 1: Use case of location-based services using LED light and photo diode

Figure 2: Navigation Prototype for the Visually Impaired using LED light and photo diode

3.2. Location-based services using LED light and image sensor

An image sensor can not only receive data from an optical transmitter but also detect the direction of the incoming light as shown in Figure 3.
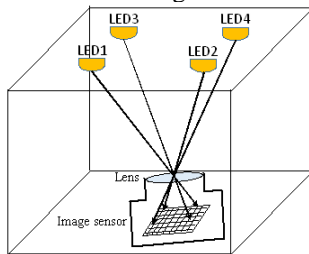

Figure 3: Concept of position detection by using LED light and image sensor

An image sensor can do simultaneous image acquisition and data reception, which conventional photo diode cannot do. When an image is taken by an image sensor and the position of the pixel where LED is projected onto, it is possible to calculate the three-dimensional position and the pose of a receiver with computer vision techniques.

Figure 4: Robot position control prototype using LED light and image sensor

Figure 4 shows one application of this method, where a robot with an image sensor receives optical signals from four LED lights on the ceiling and calculates its own position with an accuracy of a few centimeters [4].

3.3. Location-based services using DMD projector and photo diode

A DMD projector sends different positional data from each different pixel, and a photo diode receiver receives the signal as shown in the classroom application in Figure 5 where each student at different location receives different data. A DMD projector can send different data in different directions with a few millimeter accuracy [5]. By using a modulation method with a constant average

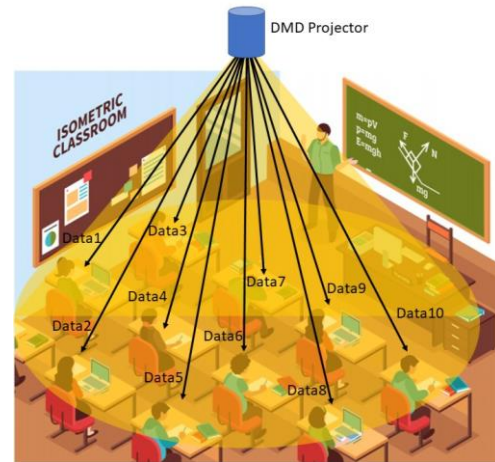optical power, it is possible to produce an illumination light without uncomfortable flickering.

Figure 5: Concept of location-based service using DMD projector and photo diode

3.4. Location-based services using DMD projector and image sensor

An intelligent transport system using DMD projector and image sensor was proposed in [6] where a projector projects an image on the road and a camera on a car receives the projected image.

References

[1] Shinichiro Haruyama, "Progress of visible light communication", IEEE 2010 Conference on Optical Fiber Communication (OFC/NFOEC), San Diego, USA (March 2010).

[2] Takaya Yamazato, Shinichiro Haruyama, "Image sensor based visible light communication" in a book "Visible Light Communication" by Shlomi Arnon, Cambridge University Press (March 2015)

[3] Madoka Nakajima, Shinichiro Haruyama, "Indoor navigation system for visually impaired people using visible light communication and compensated geomagnetic sensing", 2012 1st IEEE International Conference on Communications in China (ICCC 2012), pp. 524–29 (August 2012)

[4] Toshiya Tanaka, Shinichiro Haruyama, "New Position Detection Method using Image Sensor and Visible Light LEDs", IEEE Second International Conference on Machine Vision (ICMV), pp. 150 – 153, Dubai/United Arab Emirates (December 2009)

[5] Motoi Kodama, Shinichiro Haruyama, "A Fine-Grained Visible Light Communication Position Detection System Embedded in One-Colored Light Using DMD Projector", Mobile Information Systems, Volume 2017, Article ID 9708154 (March 2017)

[6] T. Arisue, T. Yamazato, H, Okada, M. Kinoshita, S. Arai, T. Yendo, K. Kamakura, T. Fujii, "An Experiment of Image Sensor Communication Using Digital Micromirror Device Projector as a Vehicle Headlight", IEICE Workshop on Optical Wireless Communication for Smart City (OWC2), pp.1-4, Toyota, Japan (December 2019)

LDC2020 | Oral Presentation
# Visible light communication (VLC) technologies and systems
2020年4月24日(金) 13:00 〜 14:30 301 (Conference Center)

[LDC13-02] Laser-based LiFi for 6G: Potential and Applications

*Volker Jungnickel[1], Julian Hohmann[1], Dominic Schulz[1], Peter Hellwig[1], Jonas Hilt[1], Christoph Kottke[1], Ronald Freund [1] （1. Fraunhofer Heinrich Hertz Institute）

LiFi uses the light for mobile communications. Advantages of laser- compared to LED-based LiFi systems are better energy efficiency and higher modulation bandwidth, yielding enhanced mobility, higher data rates, more precise positioning and reduced latency in promising 6G applications like mobile backhaul, secure meeting rooms and industrial or medical wireless.

Laser-based LiFi for 6G: Potential and Applications

Volker Jungnickel, Julian Hohmann, Dominic Schulz, Peter Hellwig, Jonas Hilt, Christoph Kottke and Ronald Freund
Fraunhofer Heinrich Hertz Institute, Einsteinufer 37, 10318 Berlin, Germany (volker.jungnickel@hhi.fraunhofer.de)

Abstract: *LiFi uses the light for mobile communications. Advantages of laser- compared to LED-based LiFi systems are better energy efficiency and higher modulation bandwidth, yielding enhanced mobility, higher data rates, more precise positioning and reduced latency in promising 6G applications like mobile backhaul, secure meeting rooms and industrial or medical wireless.*

1. Introduction

Light fidelity (LiFi) is a new wireless communication system using optical signals for mobile communications. Compared to radio frequencies (RF), LiFi operates in the previously unused optical spectrum being much wider than the whole radio spectrum used nowadays. LiFi can be confined in one room and re-used next door, thus offering enhanced privacy. LiFi is robust against (and will not create) electro-magnetic interference, what is wanted in medical and industrial scenarios. It is well established that LiFi can complement RF systems, which offer wireless coverage for users in large areas [1]. LiFi can be deployed in the same area, serving few users nearby each optical access point. By using a grid of LiFi access points each covering a smaller area, spectrum is reused more frequently in space, i.e. LiFi can be considered as a future capacity upgrade for RF. LiFi started with high-power LEDs as transmitters and large-area photodiodes as receivers. High-power LEDs are available for low cost in modern luminaires enabling visible light communication (VLC) [2]. But LiFi is more efficient when using it in the near infrared (780-1000 nm). At the baseband, experts learned to handle illumination and communication separately to simplify the protocol stack for LiFi and make it similar to other systems. But still, reuse of WiFi chips is cumbersome. Signals have to be up-converted to an intermediate frequency (IF) equal to half of the signal bandwidth, approximately. But modern WiFi chips integrate baseband and RF tightly so that signals are inaccessible. LiFi vendors use home networking protocols nowadays, based on the ITU-T recommendation G.9991 using OFDM with adaptive bitloading in 200 MHz bandwidth.

2. Advantages of laser compared to LED

The promises of using lasers instead of LEDs for LiFi relate to stimulated emission. Next to spontaneous emission, due to the statistical recombination of electron-hole pairs, which convert into photons, laser light is based on stimulated emission being enforced by photons, fed back into the active zone via two mirrors arranged as a resonator. Being an additional radiative side-path for spontaneous recombination, stimulated emission reduces the lifetime of electron-hole pairs and thereby increases the modulation bandwidth. Moreover, stimulated emission reduces the impact of non-radiative Auger
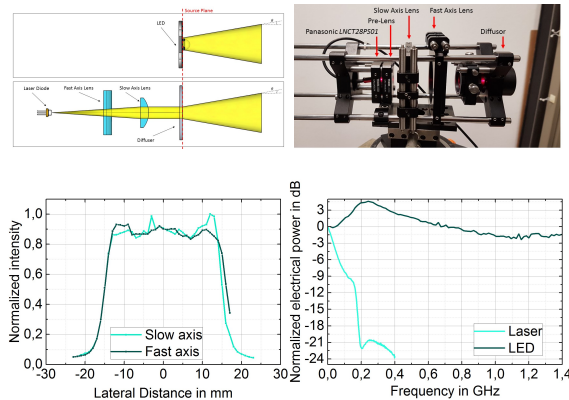

Fig. 1. Top left: Comparison of transmitter designs for LED and laser-based LiFi. Top right: Eye-safe laser-based LiFi Tx setup. Bottom left: Beam profiles after the diffuser. Bottom right: Measured frequency response of LED and laser.

recombination. As a result, more light is output, i.e. *lasers have better energy efficiency compared to LEDs*. For the same reason, lasers have a more linear characteristics between drive current and output power.

3. Eye-safety for laser-based LiFi

LEDs support eye safety by nature. The active zone of a high-power LED is a large radiating area emitting high optical power into a wide beam. It is hardly possible to focus that light onto a smaller spot size and, thereby, eye-safety is less critical than for lasers. The resonator of a laser directs the light towards the optical axis. Reflectivity of mirrors in edge-emitting semiconductor lasers is low and the active zone is long and thin. Therefore, lasers act as a point source and additional effort is needed to fulfil eye safety regulation similar to an LED. There are recent developments towards vertical cavity surface-emitting lasers (VCSELs), using a thin but short active zone with mirrors having high reflectivity. VCSELs emit a nearly circular beam with low power. By arranging hundreds of VCSELs in an array, all of them radiating into the same direction, one can form a large radiating area, which is similar to a LED [7, 8]. VCSEL arrays may become useful as a compact, eye-safe laser-based LiFi transmitter that can be easily integrated into next-generation mobile devices.

3. Experimental results

In our experiments, we characterize eye-safe transmitter design and modulation bandwidth when using LEDs and lasers for LiFi. We have used an LED SFH4451 from OSRAM, having 55 mW optical output power at a drive current of 100 mA (0.55 W/A) at 850 nm and a laser LNCT28PS01 from Panasonic having 170 mW output power at a drive current of 210 mA (0.8 W/A) at 780 nm. While the LED light comes from an area of 0.3x0.3 mm² with a symmetric beam with 34° FWHM, the laser is a point source radiating an elliptical beam with 6.5° and 22° FWHM for fast and slow axis, respectively. For the laser, therefore, we have used two cylindrical lenses with the same focal point in order to form a collimated, circular beam, next sent onto an engineered holographic diffuser. The collimated beam and the diffuser form a large radiating area with similar beam characteristics compared to the LED (Fig. 1). We have measured the modulation bandwidth of the LED and the laser by using a ZFBT-4R2GW+ bias-T from Mini Circuits, a FEMTO HSPR-X-I-1G4 photo-receiver and a standard vector network analyser. While the high-power LED has a 3-dB cut-off frequency of 30 MHz, the laser has a resonance peak around 200 MHz and its 3-dB cut-off frequency is not even reached at 1.4 GHz (Fig. 1). According to these results, when operated well above the threshold current, the laser provides better energy efficiency than the LED and has a significantly higher modulation bandwidth.

4. Benefits in use cases for LiFi

Recent research has identified promising use cases for LiFi such as point-to-point wireless backhaul [3], mobile access in secure meeting rooms [4], industrial [5] and medical wireless [6], see Fig. 2. Here, we highlight some benefits of using laser-based LiFi in these promising applications for next-generation WiFi and 6G systems. Higher bandwidth yields higher data rates in general, although signal-to-noise ratio (SNR) reduces. Bandwidth is a pre-log factor in Shannon's formula for the capacity limit of communication links, while SNR scales logarithmic. According to our results, laser-based LiFi could provide around 5x higher data rate compared to LEDs. The best LED-based LiFi systems offer more than 1 Gbit/s today, hence it is expected that up to 10 Gbit/s can be achieved in mobile scenarios, what qualifies laser-based LiFi for future WiFi and 6G requirements. For industrial and medical applications, it is important to integrate positioning with communication. By using time-of-flight measurements, positioning resolution, same as latency and jitter, will improve by factor 5 with lasers. Energy-efficiency improves due to two effects: Improved efficiency of the laser and higher bandwidth i.e. shorter packet duration both lead to reduced power consumption which are important in battery-powered mobile devices [8]. While our edge-emitting lasers still resulted in a relatively bulky setup, one can expect similar results with VCSEL arrays which become available soon for integration into mobile devices (laptops, smartphones, tablets) [9, 10].
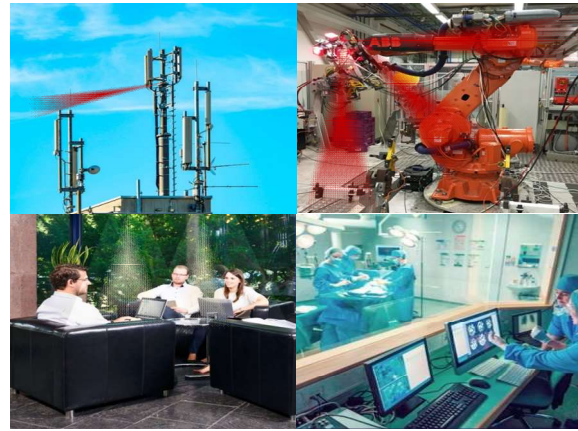

Fig. 2 LiFi use cases: Mobile backhaul, secure meeting room, industrial and medical wireless.

5. Conclusions and outlook

Our experiments indicate that laser-based LiFi enables better energy efficiency and significantly higher modulation bandwidth compared to LED-based systems. Therefore, lasers enhance the capabilities of LiFi in many promising applications. Further research is needed to develop a new generation of laser-based LiFi qualifying for the next-generation WiFi and 6G systems.

References

[1] M. Ayyash *et al*., "Coexistence of WiFi and LiFi toward 5G: concepts, opportunities, and challenges," in *IEEE Commun. Mag.*, vol. 54, no. 2, pp. 64-71, 2016.

[2] L. Grobe *et al*., "High-speed visible light communication systems," in *IEEE Commun. Mag.*, vol. 51, no. 12, pp. 60-66, 2013.

[3] D. Schulz *et al.*, "Outdoor measurements using an optical wireless link for fixed-access applications," *J. Lightw. Technol.*, 37, 634-642, 2019.

[4] A. Paraskevopoulos *et al.* "Pilot Li-Fi installation in a conference room in Mainau-lake constance: Realization and outlook," *2018 Global LiFi Congress*, Paris, 2018.

[5] P. W. Berenguer *et al*., "Real-time optical wireless mobile communication with high physical layer reliability," in *J. Lightw. Technol.*, vol. 37, no. 6, pp. 1638-1646, 2019.

[6] S. Maravanchery Mana et al., "LiFi experiments in a hospital", OFC 2020, San Diego, paper M3I.2

[7] M. Hinrichs et al. "Pulsed modulation PHY for power-efficient optical wireless communications," ICC 2019, Shanghai, China.

[8] V. Jungnickel *et al*., "Enhance lighting for the internet of things," *2019 Global LiFi Congress*, Paris, France, 2019. Online: https://www.eliot-h2020.eu/

[9] https://www.trumpf.com/en_US/products/vcsel-solutions-photodiodes/vcsel-module-sensors/

[10] http://vixarinc.com/products/vcsel-modules

LDC2020 | Oral Presentation
# Visible light communication (VLC) technologies and systems
2020年4月24日(金) 13:00 ～ 14:30 301 (Conference Center)

[LDC13-03] The Future Prospects of Robot-Photonics:Visible Light Communication and Sensing with the Plasmonic Mirror

*Kensuke Murai Murai[1]　（1. National Institute of Advanced Industrial Science and Technology）

Photonics are essential for present robot systems. Photonic devices are more important not only for distance and image but also for environmental communication and sensing. The plasmonic mirror with the metal-insulator-metal (MIM) structure has the potential to sense such information with the LED/LD driven white light.

The Future Prospects of Robot-Photonics:
Visible Light Communication and Sensing with the Plasmonic Mirror

Kensuke Murai [1]

1) National Institute of Advanced Industrial Science and Technology (AIST), AIST-Kansai, Ikeda, Osaka 563-8577, Japan

Abstract: Photonics are essential for present robot systems. Photonic devices are more important not only for distance and image but also for environmental communication and sensing. The plasmonic mirror with the metal-insulator-metal (MIM) structure has the potential to sense such information with the LED/LD driven white light.

1. Introduction

It has been about 100 years since the word "robot" was used by Mr. Karel Capek. The system "robot" had been developed from a mechanical system to an intelligent system with information technology. Therefore, "robotics" is based on the integration of various technologies such as mechanics, electronics and information technology such as IoT (internet of things) and AI (artificial intelligence). In Japan, it is defined that "robot" is an intelligent system with three major elements which are actuators, sensors and intelligent controllers [1]. Furthermore, communications, materials as well as batteries are also important parts of the systems.

On the other hand, "photonics" has also about 100 years history. Most photonic devices are based on the photoelectric effect which is the emission of electrons when light shines on a material. Photonic devices are essential in present robot systems. Even in robotic cleaners, more than half of sensors are photonic ones. They are based on photonics such as optical communication, PSDs (position sensing detectors) and visible/infrared cameras. Auto-driving cars employ LiDARs (light detection and ranging) or a stereo camera system in order to detect 3D information around the car. Photonic sensors are also used inside the robot system sensing condition of actuators and motors.

Useful robot systems are requested for the connected factories in Industry4.0. As Japan is going in an aging society with a low birthrate, useful robot systems would be required for future Japanese society called Society 5.0 [2]. The 17 goals of the Sustainable Development Goals (SDGs) [3] should be all achieved by 2030, all over the world.

2. Robot-Photonics

The 21st century is called "the robotic century" and "the photonic century". Photonics is already essential for recent robot systems. Therefore, the 21st century would be "a century for robot-photonics". In 2018, the Laser Society of Japan (LSJ) started a technical committee concerning "robot-photonics". (See Fig.1) The word "robot-photonics" means a fusion of research between robotics and photonics. In this committee, we discuss innovation through robot-photonics toward an aging society with a low birthrate in Japan. As shown in Fig.1, basic research (seeds) in cooperation of researchers

related to robotics and photonics are necessary, and various applications (needs) exist to be matched in the views of academy and industry toward the fields of agriculture, infrastructure, food, factory and so on. Advanced robot systems and innovative applications are expected in this committee. We had held several technical meetings on research topics with laboratory tours, some symposiums at the annual meetings of OSJ (the Optical Society of Japan) and that of LSJ (the Laser Society of Japan), some invited talks at international conferences [4] in OPIC (the Optics and Photonics International Congress) held at Pacifico Yokohama. Furthermore, the special issue related to robot-photonics had been published in the LSJ magazine (Laser Kenkyu) in July 2019. Examples of directions are photonic maintenance of old infrastructures, harmful birds, animals and insects, and advanced photonic communication (Li-Fi). Several research topics related to robot-photonics were discussed. They are related to basic research on photonic and robotic technologies such as hyperspectral cameras, high-speed cameras, laser range finders, laser projectors and deep learning, manipulation as well as application such as destruction of old power plants and control of harmful birds, animals, insects.
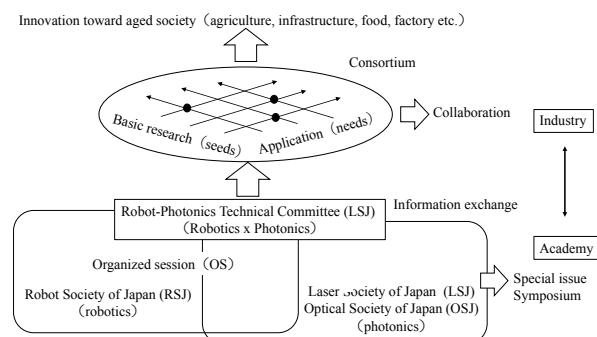

Fig. 1 Concept of the Robot-Photonics Technical Committee of the Laser Society of Japan (LSJ).

3. Visible Light Communication and Sensing with the Plasmonic Mirror

Though the wireless communication is established by radioactive frequency such as Wi-Fi (wireless fidelity), light-based communication called Li-Fi (light fidelity) is also desired for both ecological and economic reasons. Wireless communication between robots and their

environment is more important than ever in the era of cloud computing. For example, autonomous vehicles could communicate by a laser-driven head light. Photonic communication could be possible between their LED/LD-based head lights and active mirrors on traffic marks. However, the Li-Fi has some issues to be solved such as bi-direction and obstruction. Possible solution for the bi-direction issue is dual color communication. The active mirror is another solution using an active mirror.

Normal white LED consists of the yellow phosphor equipped on the blue LED, the blue LED can be blinked electronically and the yellow phosphor follows the blue LED blinking. Laser-driven white light can also be achieved using blue LDs which are much faster in switching speed than the blue LED.

As shown in Fig. 2, a plasmonic spectral filter (plasmonic mirror) [5-7] consists of a metal-insulator-metal (MIM) structure. The total thickness of the MIM structure is within 1 micrometer which is too thin to stand without a substrate. The MIM structure shows strong absorption at a certain wavelength of white LED spectra. As the absorption wavelength is determined by the refractive index or by the thickness of the insulator layer, the absorption wavelength of the insulator layer could be shifted electrically or mechanically. The electrical control would be achieved by changing the refractive index of electro-optic (EO) materials. For this purpose, we have discussed some EO materials as the insulator layer. We chose the PLZT ceramics and the EO polymer for this EO material. On the other hand, the mechanical control would be achieved by changing the thickness of the insulator layer. Real-time photonic sensing could be achieved to detect acoustic and vibration information for future robot systems.

4. Conclusions

Photonics is essential for new robot systems. In the robot-photonics technical committee in the LSJ, we use several items related to robot-photonics in order to match basic research (seeds) and application (needs). White LED communication and sensing via the plasmonic mirror with the metal-insulator-metal (MIM) structure will give us more information for future robot systems.
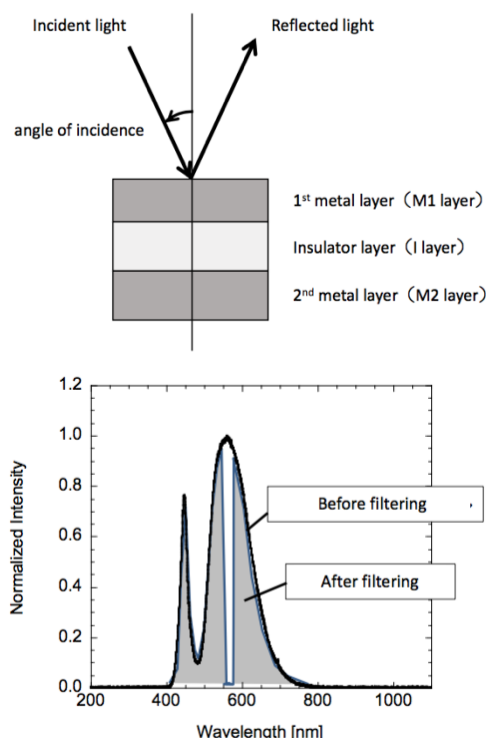
Acknowledgement

Fig. 2 A plasmonic spectral filter (a plasmonic mirror) with the metal-insulator-metal (MIM) structure (upper) and white LED spectra before and after filtering (bottom).

References

[1] Report of 'Robot Policy Research Council' (METI, 2006); https://www.jara.jp/various/report/img/robot-houkokusho-set.pdf (in Japanese)

[2] Society 5.0; https://www8.cao.go.jp/cstp/society5_0/index.html

[3] Sustainable Development Goals (SDGs); https://www.un.org/sustainabledevelopment/sustainable-development-goals/

[4] K. Murai, "White LED Communication via the Plasmonic Spectral Filter with the MIM Structure as Robot-Photonics", IoT-SNAP9-01(invited), IoT-SNAP2019 (Pacifico Yokohama, 2019.4.25).

[5] Y. Oshikane, K. Murai, T. Higashi, F. Yamamoto, M. Nakano, H. Inoue, "Plasmonic active spectral filter in VIS-NIR region using metal-insulator-metal (MIM) structure on glass plate", Proc. SPIE 8463, Nanoengineering: Fabrication, Properties, Optics, and Devices IX, 846303 (15 Oct. 2012); doi: 10.1117/12.929201.

[6] K. Murai, Y. Oshikane, T. Higashi, F. Yamamoto, M. Nakano, H. Inoue, "Design and fabrication of active spectral filter with metal-insulator-metal structure for visible light communication", Proc. SPIE 8632, Photonic and Phononic Properties of Engineered Nanostructures III, 863223 (21 Feb. 2013); doi: 10.1117/12.2003637.

[7] K. Murai, Y. Oshikane, F. Yamamoto, K. Hattori, S. Mochizuki, T. Mihara, M. Nakano, "Fabrication and evaluation of active spectral filter with metal-insulator-metal structure for visible light communication", Proc. SPIE 8994, Photonic and Phononic Properties of Engineered Nanostructures IV, 89941T (19 Feb. 2014); doi: 10.1117/12.2038250.

Smart Systems

Session Chair: Junichi Kinoshita(Osaka University)
Fri. Apr 24, 2020 3:15 PM - 4:30 PM 301 (Conference Center)

[LDC14-01] Vertical View Human Action Recognition from Range Images

*Akinobu Watanabe[1], Keiichi Mitani[1] （1. Hitachi, Ltd.）
 3:15 PM - 3:45 PM

[LDC14-02] High-Speed Projection for Augmenting the World

*Yoshihiro Watanabe[1] （1. Tokyo Institute of Technology）
 3:45 PM - 4:15 PM

[LDC14-03] Color LiDAR using RGB visible laser diodes

*Tomoyuki Ohashi[1], Masato Ishino[1], Kazuhisa Yamamoto[1], Kana Fujioka[1] （1. Institute of
Laser Engineering, Osaka University）
 4:15 PM - 4:30 PM

[LDC14-01] Vertical View Human Action Recognition from Range Images

*Akinobu Watanabe[1], Keiichi Mitani[1] （1. Hitachi, Ltd.）

We developed the human joints' position estimation technique and the person tracking technique from looking-down-view range image of TOF sensor, and confirmed the correct prediction ratio of hands' position is 97%, upper-front view angle is suitable for hands' position estimation, and confirmed the person tracking error is reduced to 1/7.

Vertical View Human Action Recognition from Range Images

Akinobu Watanabe [1], Keiichi Mitani [1]

[1] Hitachi, Ltd. , Research & Development Group, 1-280, Higashi-koigakubo Kokubunji-shi, Tokyo, 185-8601 Japan, +81-80-2097-8607, akinobu.watanabe.fz@hitachi.com, keiichi.mitani.jj@hitachi.com

Abstract: *We developed the human joints' position estimation technique and the person tracking technique from looking-down-view range image of TOF sensor, and confirmed the correct prediction ratio of hands' position is 97%, upper-front view angle is suitable for hands' position estimation, and confirmed the person tracking error is reduced to 1/7.*

1. Introduction

In the analyses of the operation of workers in the manufacturing premise and the customer action in the retail store, the inflection of provided range image data by TOF (Time of Flight) sensor is expected. Many techniques are suggested as a person posture estimate using range image data, but, as for the use case in the point of view looking down, examination does not advance enough.

1.1 Background

A sensor apparatus and an IT system have been developed and become low price. An IoT (Internet of Things) market using Information collected with them from a machine, a vehicle and a building, to use the information for analysis and control is spreading. It is predicted that the market size of IoT grows up to approximately 1,300 billion dollars from approximately 700 billion dollars of 2015 in 2019 [1].

With progress of IoT, there is the movement that is going to feed back the result of future prediction by collecting the data of a machine and the facilities which are on-site physically, and reappearing as "digital twin" within the cyber world of the IT system, using an information processing technology. Siemens and GE stimulate research and development in conjunction with the digital twin, too and have begun to already send information in a general medium [2][3].

Furthermore, sensing object is being extended to "a Human being" from "a Thing". The detection, the reduction of the improvement, efficiency and work error that I included the movement of the person in is enabled by reproducing the spot that the Homo sapiens included as digital twin. In order to realize it, it is necessary to detect existence and the movement of the person, and to process it to convert it a fixed form as digital information. Microsoft announced Kinect for a game in the consumer market [4]. Kinect can not only capture the movement of the player as an animation, but also acquire three dimensions of joint positions of the subject as coordinate data in the space. In addition, there is movement to apply for industry because available SDK is provided on a PC [5].For example, Kinect is used for the study of the system for fields of industry to detect the deviation action of the shop floor worker [6].

On the occasion of the use of Kinect, one PC equipped with GPU is necessary for one Kinect sensor. Furthermore, it is assumed the viewpoint of Kinect is the front view. Then in the production line floor, it is hard to keep a field of vision because of shielding, and it is an issue that there is much limitation for sensor setting.

1.2 Purpose

It was aimed for the establishment of the posture detection technology suitable for an available industrial use with the general-purpose 3D sensor including the TOF sensor in order to solve the problem mentioned above.

1.3 Target

In this study, we intend for processing to extract a joint position (skeleton) of the human body from the range image which photographed the human body. Particularly, high precision of the technique that can extract a skeleton with the viewpoint looked down from upper position at intends for suggestion of making it and an evaluation of the precision is our target.

2. Experiment

As shown in the prior publication, we developed vertical view human skeleton recognition method [7]. And we improved a correct rate of sequential joint searching method, and developed human model selection method to choose the most appropriate model from various models for various target bodies. In this study, we improve the accuracy of detection ratio of human joints and person position.

2.1 Previous method

Previous method is first to detect the head as the starting point and search the joints from a shoulder to a hand in a human body model sequentially [7].

Regarding people tracking, there are many open SDKs which have various algorithms that detect the person position from 2D images or 3D range images, point cloud. In which, a commonly procedure of that person detections is to classify person as move body after clustering point cloud., e.g. [8].

2.2 Issue of correct ratio

The correct ratio of human joints position by the previous method is shown in Table 1. , which is reported in [7].

In previous method, average correct ratio for detected frames is 93 [%]. Hands' correct ratio for detected frames are 88[%] and 83[%].

Table 1. Correct Ratio

[%]	Shoulder		Elbow		Wrist		Hand	
	R	L	R	L	R	L	R	L
Detected	99	88	95	97	94	98	88	83

Then we decided the issue is the correct ratio of the hands.

2.3 Issue of people tracking
The current algorithms have several issues: (1) coalescence with other clusters, (2) occlusion caused by a person hiding behind the others, (3) undetected human pillages an ID of an already been detected and so on. In this work, we count the number of people tracking errors related to (3), shown in Fig. 18.

2.4 Developed method
We developed the hybrid approach using (1) image creation from IR image and depth data, (2) image recognition method and (3) 3D position estimation method. The flow of this approach is shown in Fig. 1.
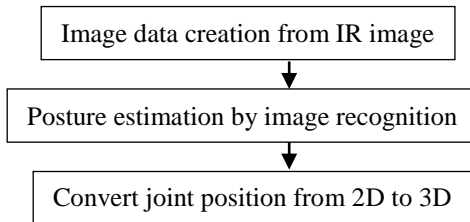
Image data creation from IR image
↓
Posture estimation by image recognition
↓
Convert joint position from 2D to 3D

Fig. 1. Hand position detection flow

2.5 Image creation
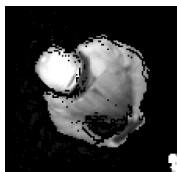From Fig. 2, to 6 are the examples of evaluation images of this work.
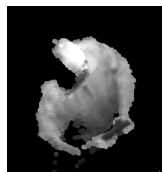

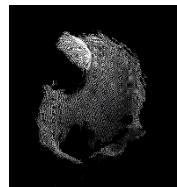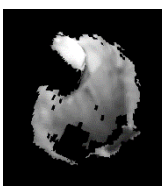Fig. 2. 2D IR   Fig. 3. Large pixel

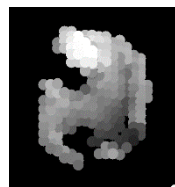Fig. 4. Mesh   Fig. 5. Polygon   Fig. 6. Voxel

In order to improve detection ratio, we assumed the displaying method is important. Then we compared such cases as (1) the size of pixel is enlarged, (2) adding the line next to each other (to say, "mesh" or "wire frame"),

(3) painting the triangle plane of 3 adjacent pixels as 3 vertex of it (to say, "polygon") and (4) voxel spheres instead of pixels.
IR images may include unnecessary information, for example, background. Then we create evaluation image not including other information than human appearance. 3D range image can be projected to any plane of any angle. Then we created 3D range images of X axis rotation chopping its rotation angle from top view to front view.

2.6 Image recognition method
We applied OSS to recognize human body joints from IR images and estimate joint position in 2D coordinates on IR images.

2.7 3D position estimation method
When we got 2D position on IR images, then it can be converted to 3D position in world coordinates.

2.8 View angle comparison
We measured joint detection ratio and correct ratio for 3 different view angle 2D IR images. They are (a) Front view, (b) Upper-front view and (c) Top view. Fig. 7 , 8 and 9 are the examples of each images.

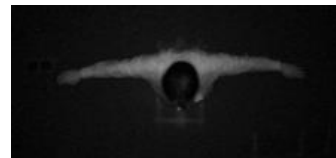
Fig. 7. Front view

Fig. 8. Upper-front view

Fig. 9. Top view

2.9 People tracking method
We developed cluster-to-person classification method aiming to solve the problem (3) of subsection 2.3 in this work.

3. Results

We developed techniques that detect human actions, such as posture and position, from 3D range image of TOF sensor. And we confirmed the improvement.

3.1 Reference data of joint position
Table 2 shows reference evaluation data to measure detection ratio and correct ratio in this study. This data is same as the one in previous study.

Table 2. Reference data

Model	Behavior	frame
1	A	231
2	B	61
3	C	355
4		321
5	D	97
6		123
Total	-	1188

Table 3 shows reference evaluation data to measure detection ratio and correct ratio for different view angle comparison in this study.

Table 3. Reference data of different view angle

Model	View Angle	frame
7	Front	5701
	Upper-Front	5442
	Top	5342
Total	-	16485

3.2 Joint detection ratio

By applying OSS joint detection software, we got joint position in 2D coordinates on evaluation image.
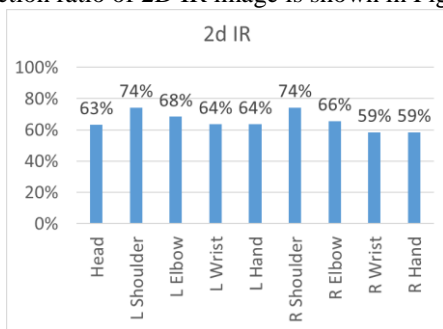The detection ratio of 2D IR image is shown in Fig. 10.

Fig. 10. Detection ratio

In this case, hands' detection ratios are 64% and 59%. The correct ratio of 2D IR image is shown in Fig. 11.
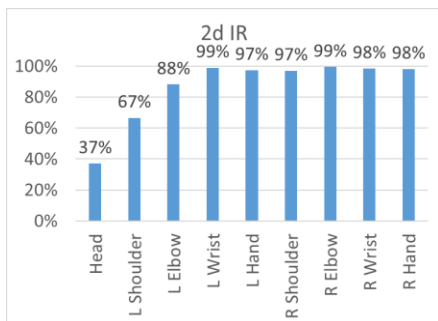

Fig. 11. Correct ratio

In this case, hands' detection ratios are 97% and 98%.

The detection ratio of 3D rotated image are shown in from Fig. 12 to Fig. 15.

Fig. 12 shows large pixel case. In this case, the 9 degrees rotation marks the best result. And it is better than simple 2D IR image case.

Fig. 13 shows mesh case and Fig. 14 shows polygon case. In these cases, the detection ratio is lower than 2D IR image case.

Fig. 15 shows voxel sphere case. In this case, the detection ratio is almost zero in every rotation degree.
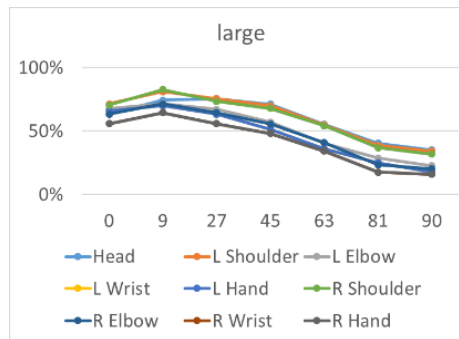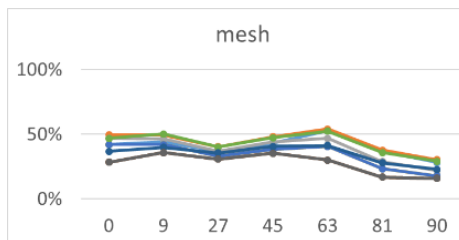

Fig. 12. Large pixel
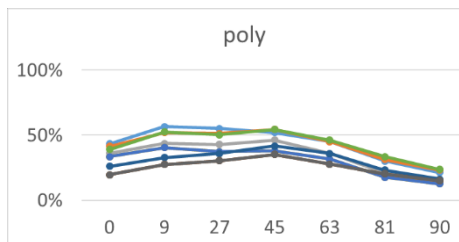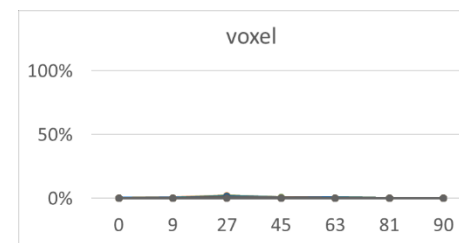

Fig. 13. Mesh

Fig. 14. Polygon

Fig. 15. Voxel sphere

Comparing among these displaying methods, joint detection ratio improvement from 2D IR of both left and right hands is shown in Fig. 16.
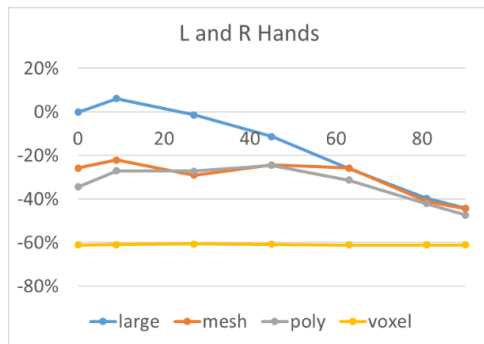

Fig. 16. Hands detection improvement

Fig. 17 shows correct ratio for detected frames of hand joints for 3 different view angels. In this Fig. 17, "correct (x y)" indicates the ratio of frames which the distance between reference joint position and detected joint position in horizontal plane is smaller than 200[mm], and "correct (z) means vertical distance. In upper-front case, detect ratio is low, but correct ratio is high.
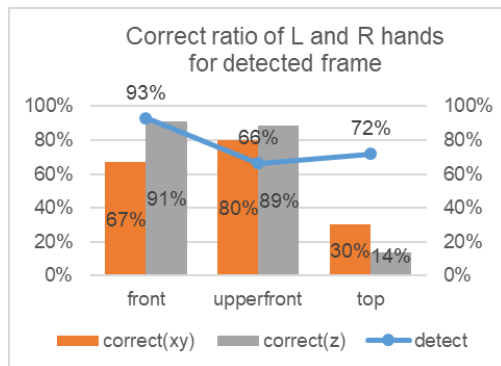

Fig. 17. Comparison among 3 view angles

3.3 Person tracking ratio
We performed the people tracking method of this work to evaluate the improvement under the situations that cause the error undetected human pillages an ID of an already been detected; the results of the above are shown in Fig. 18. The x-axis means the scene pattern and y-axis means number of people tracking error.
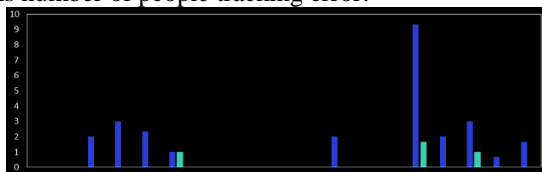

Fig. 18. Person tracking improvement
Each blue and green bar indicates previous and this work.

4. Discussion

4.1 Joint detection

In Fig. 16, we confirmed that the 3D rotation method have the possibility to improve hands' detection ratio.

We will evaluate other rotation variations and displaying methods.
In Fig. 17, upper-front case is the best in failure ratio, even detect ratio is the worst. Then we confirmed upper-front view angle is better than other angels in low failure and high precision points of view.
We think the reason why correct ratio is low comparing with the result for reference data shown in Table 2 is the quality of 2D IR images, for example low resolution and low luminance, especially around hands

4.2 Person tracking
In Fig. 17, the number of errors at the previous (blue bar) reduced to 1/7 at the error undetected human pillages an ID of an already been detected.

5. Conclusions
Hand position estimation is confirmed the correct prediction ratio of hands is 97%, upper-front view angle is suitable for hands' position estimation and people tracking is improved that misdetection count is reduced to 1/7.

References

[1] Worldwide Internet of Things 2016-2019 Forecast: Market Opportunity by Region and Narrowing the Lens on Use Cases, IDC, 2016

[2] Digitalization in machine building - The digital twin (http://www.siemens.com/customer-magazine/en/home/industry/digitalization-in-machine-building/the-digital-twin.html)

[3] 'Digital Twin' Technology Changed Formula 1 and Online Ads. Planes, Trains and Power Are Next (http://www.gereports.com/digital-twin-technology-changed-formula-1-online-ads-planes-trains-power-next/)

[4] Kinect (https://developer.microsoft.com/ja-jp/windows/kinect/hardware)

[5] Kinect for Windows SDK (https://msdn.microsoft.com/ja-jp/library/dn799271.aspx)

[6] Hitachi and Daicel Develop Image Analysis System to Detect Signs of Facilities Failures and Deviations in Front-line Worker Activities (http://www.hitachi.com/New/cnews/month/2016/07/160713.html)

[7] A. Watanabe, et al. 'Optimization of Vertical View Human Skeleton Recognition from Range Images', Proceedings of IDW '18, pp. 1182 (PRJ5-3) (2018/12).

[8] M. Munaro, F. Basso and E. Menegatti, "Tracking people within groups with RGB-D data", IEEE/RSJ Int'l Conf. on Intelligent Robots and Systems, 2101-2107 (2012).

Smart Systems

2020年4月24日(金) 15:15 ～ 16:30 301 (Conference Center)

[LDC14-02] High-Speed Projection for Augmenting the World

*Yoshihiro Watanabe[1] （1. Tokyo Institute of Technology）

This paper introduces the progress of high-speed projection technology and how this technology opens new possibilities of augmenting the world based on dynamic projection mapping.

High-Speed Projection for Augmenting the World

Yoshihiro Watanabe

Tokyo Institute of Technology, 4259, Nagatsuta, Midori-ku, Yokohama, Kanagawa 226-8502

+81-45-924-5474

watanabe.y.cl@m.titech.ac.jp

Abstract: *This paper introduces the progress of high-speed projection technology and how this technology opens new possibilities of augmenting the world based on dynamic projection mapping.*

1. Introduction

In recent years, the application range of projectors has been remarkably expanded. With the introduction of projectors for advanced displays and measurements, the required functions are not just limited to projection on a fixed flat screen [1]. Such developments have brought out new technical challenges.

One of the most important among them is the requirement for increased projection speed. To meet this requirement, it is necessary to increase the updating frequency of videos and reduce the latency from video transmission to projection.

Based on such demand, we have tackled on the research exploring a new type of high-speed projector and the applications of dynamic projection mapping. Dynamic projection mapping, not limited to stationary objects, was created as an evolution of projection mapping. Dynamic projection mapping enables the spatio-temporal blending of projected images against real-world change and is expected to create a new type of reality. Our development history based on such concept is shown in Fig. 1. The details are described in the remaining sections.

2. DYNAFLASH: 1000-fps high-speed projector

Conventional projectors are premised on the projection of an image onto a stationary target object such as a screen, and whilst excellent in terms of image quality, projectors with a frame rate of 30 fps - 120 fps have been the norm. This lack of performance has hindered new development. The keys to performance are a high projection frame rate, rapid transfer of images from the computer, low delay prior to the beginning of projection of the image, and projection of a multi-gradated image, and all of these requirements must be satisfied simultaneously.

Based on this background, in 2015, we developed a single-chip digital light processing (DLP) high-speed monochrome projector capable of projecting 8-bit images at 1000 fps with a 3-ms delay [2]. We call this high-speed projector DynaFlash. DynaFlash enables such high-speed performance by closely coordinating mirror control based on a Digital Micromirror Device (DMD) with the high-speed modulation of a LED. We also developed the prototype of a high-speed color projector capable of 947-fps projection, DynaFlash v2, in 2018 [3]. Moreover, we developed a high-speed and high-brightness color projector with a single-chip-DLP configuration that meets the demands for compactness and speed by introducing light sources based on luminescent concentration from LEDs and an optimized optical system [4]. This is the latest version of our high-speed projector, DynaFlash v3.

This type of high-speed projector can maximize its value when it is integrated with high-speed visual sensing and the projected image is manipulated in real time. Next section introduces the achieved examples.

3. Dynamic Projection Mapping

By using DynaFlash with high-speed vision, dynamic projection mapping, which completely blends a dynamically changing real world with projected virtual information at a human sensory level, becomes possible.

There are reported examples of projection mapping onto non-rigid curved surfaces such as a deformed paper surface or T-shirts [5]. In this case, this also incorporated technology for the high-speed tracking of non-rigid deformation. It was confirmed that image projection onto deformed paper and flexing T-shirts could be performed and the projected image was kept existing as if it were printed on the surface.

Furthermore, examples have been reported about achieving dynamic projection mapping onto faces [6]. In this example, a new visual work "INORI (prayer)" was created through collaboration between the researchers, the artists, and the dancers. Recently this example was extended so as to be fit in various facial expressions [7]. The projected virtual images closely connecting with the dynamic real motion are unified with bodies as if it were the parts of skin and realize advanced representations in which body is metamorphosed.

The next target is the material appearance. Human can perceive the material visually from the specular gloss. This perception can easily be hacked by using dynamic projection mapping [8, 9]. In these examples, the specular appearance was augmented according to the three-dimensional object surface and motion. Moreover, we also have shown that even the unevenness of non-existing materials could be reproduced freely [3]. The physical motion and the appearance projected with low latency was perfectly consistent under the physical law of reflection. Then, it becomes hard to separate the real object and the unreal projected appearance.
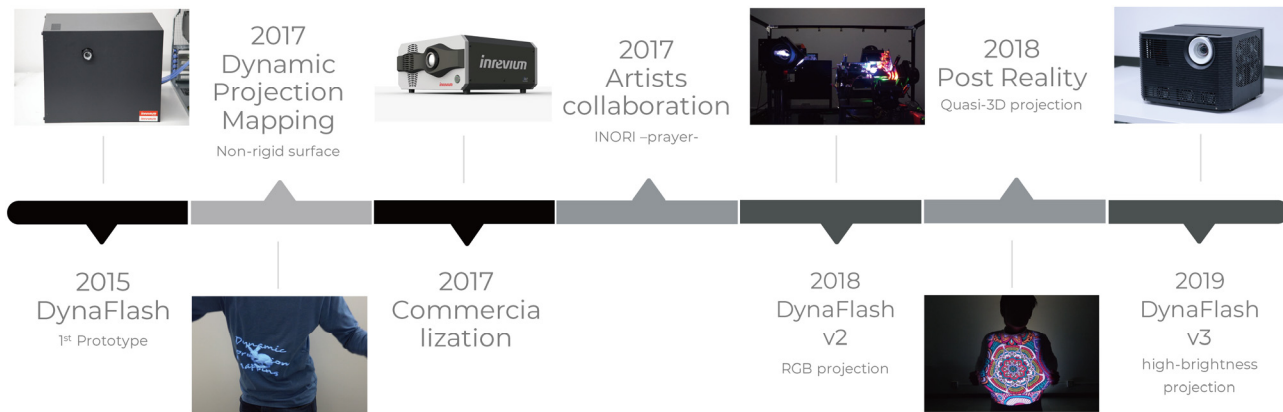
Fig. 1. Development history of high-speed projectors and its applications

4. Conclusions

This paper has introduced the progress of high-speed projection technology and how this technology open new possibilities of augmenting the world based on dynamic projection mapping. This type of technology is expected to have a wide application range, which includes advertisements, man–machine interactions, work support, automobile applications, interiors, and measurements. The potential market size is large. Toward this future, we can expect significant developments in this field.

References

[1] A. Grundhöfer, D. Iwai, "Recent Advances in Projection Mapping Algorithms, Hardware and Applications," Computer Graphics Forum, Vol. 32, No. 2, 2018.

[2] Y. Watanabe, G. Narita, S. Tatsuno, T. Yuasa, K. Sumino, M. Ishikawa, "High-speed 8-bit image projector at 1,000 fps with 3 ms delay," International Display Workshops, pp.1064-1065, 2015.

[3] DynaFlash v2 and Post Reality, 2018. http://www.vision.ict.e.titech.ac.jp/projects/dynaflashv2/

[4] Y. Watanabe, M. Ishikawa: "High-speed and high-brightness color single-chip DLP projector using high-power LED-based light sources," International Display Workshops, pp.1350-1352, 2019.

[5] G. Narita, Y. Watanabe, and M. Ishikawa, "Dynamic projection mapping onto deforming nonrigid surface using deformable dot cluster marker," IEEE Transactions on Visualization and Computer Graphics, vol.23, no.3, pp.1235-1248, 2017.

[6] INORI -PRAYER-: Collaboration with WOW, TOKYO, and AyaBambi, 2017. http://www.vision.ict.e.titech.ac.jp/projects/WOW_TOKYO_AYABAMBI/

[7] Dynamic Facial Projection Mapping -Basic Test-, 2018. http://www.vision.ict.e.titech.ac.jp/projects/faceDPM/

[8] Y. Watanabe, T. Kato, M. Ishikawa: "Extended Dot Cluster Marker for High-speed 3D Tracking in Dynamic Projection Mapping," IEEE International Symposium on Mixed and Augmented Reality, pp. 52-61, 2017.

[9] L. Miyashita, Y. Watanabe, M. Ishikawa: MIDAS Projection: Markerless and Modelless "Dynamic Projection Mapping for Material Representation," ACM Transactions on Graphics, Vol.37, No.6, pp.196:1-196:12, 2018.

LDC2020 | Oral Presentation
Smart Systems
2020年4月24日(金) 15:15 〜 16:30 301 (Conference Center)

[LDC14-03] Color LiDAR using RGB visible laser diodes

*Tomoyuki Ohashi[1], Masato Ishino[1], Kazuhisa Yamamoto[1], Kana Fujioka[1] （1. Institute of Laser Engineering, Osaka University）

We propose color LiDAR using RGB visible LDs that can obtain color information as well as position information. From results of the Time-of-Flight(ToF) measurements and received light characteristics for color chart, the feasibility of the color LiDAR was verified.

Color LiDAR using RGB visible laser diodes

Tomoyuki Ohashi, Masato Ishino, Kazuhisa Yamamoto, Hiroshi Fuji and Kana Fujioka
Institute of Laser Engineering, Osaka University, 2-6 Yamada-Oka, Suita Osaka 565-0871 Japan
TEL +81-6-6879-8784 Fax +81-6-6879-8951 email ohashi-t@ile.osaka-u.ac.jp

Abstract: *We propose color LiDAR using RGB visible LDs that can obtain color information as well as position information. From results of the Time-of-Flight(ToF) measurements and received light characteristics for color chart, the feasibility of the color LiDAR was verified.*

1. Introduction

In recent years, much attention has been paid to automatic driving and autonomous robots [1-2]. These systems need to handle hazard sensing and small 3D mapping. To get these information, we need both color and position information, and systems with sensor fusion of camera and infrared LIDAR are currently mainstream. However, these fusion systems have three problems. First, the use of two devices increases the size of the device. Secondly, a separate light source is required for nighttime and dark places, and the equipment becomes larger. Finally, the composition process is complicated because the scanning method is different between scanning LIDAR and camera.

By the way, if we employ RGB visible LDs to LIDARs [3-4], it may be possible that color information is obtained without a camera as well as an illumination light for dark places.

This time, we propose color LIDAR with RGB visible LDs instead of the infrared LD used for the conventional LIDAR. And the feasibility of color LIDAR was successfully verified from basic research including TOF measurement using RGB visible LDs.
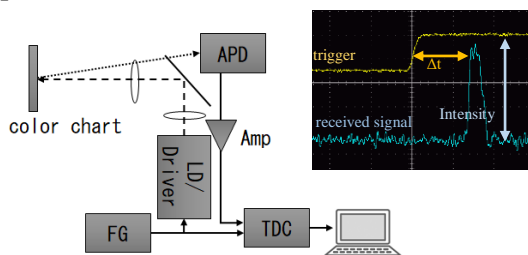
2. Experimentals

Fig. 1 Schematic drawing showing TOF measurement system

In order to verify fundamental characteristics of color LiDAR, we performed ToF experiment using RGB-LDs for color charts (white, black, red, two blue, green, yellow). The configuration of ToF measurement system is shown in Fig. 1. The spectral reflection characteristics of color charts as a target are shown in Fig. 2. A laser beam under with about 15 ns pulses, based on the signal from Function Generator (FG) was illuminated to the color chart, and the reflected light from a color chart was detected by avalanche photodiode (APD).

The electric signal from the APD was amplified and measured by using an oscilloscope. Also, the time difference between this signal and the trigger signal of FG was determined by a Time to Digital Converter (TDC) board. The wavelength of the LD under investigation were 638 nm for red, 520 nm for green, and 450 nm for blue, respectively. And the average pulse light output was 0.5 mW.
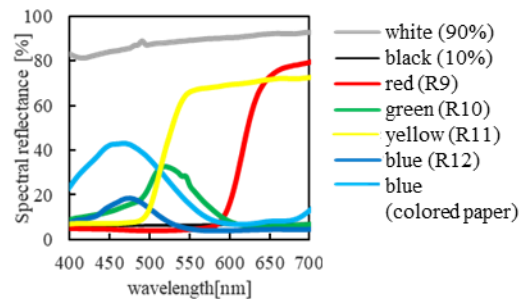

Fig. 2 Spectral reflection characteristics

3. Result and Discussions

3.1 Distance measurement for RGB LDs.

ToF measurements using TDC were carried out for RGB LDs. In the experiment, a white color chart was used as the target, and the time differences for the distance from 6m to 13m were measured at 0.5m intervals.

The results are shown in Fig. 3. It can be seen that for all RGB LDs, the time difference linearly increases with distance and the distance over 12m could be measured.
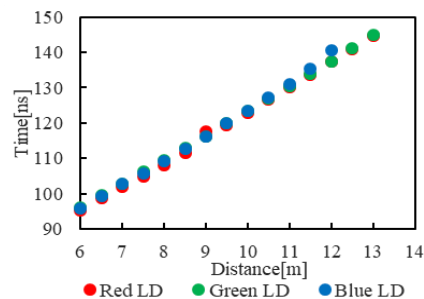

Fig. 3 Distance measurement by ToF

3.2 Receiving characteristics for different color charts
To verify the possibility of color discrimination by LiDAR, RGB-light receiving characteristics with respect to the distance for 5 color charts (white, black, red, blue,

green) were measured by each RGB-LD. Fig. 3 shows the distance dependences of received signal intensity for each color chart, in which the light sources are red LD(a), blue LD(b), and green LD(c), respectively.

From Fig. 3(a), in the case of red LD, the received signal intensity from the green / blue / black color chart was as low as about 1 to 2 V. On the other hand, that from white / red color chart was as high as the amplifier was saturated below 9m. Similarly, that of white / green was higher in the case of green LD, and only white was higher in the case of blue LD. The reason why the signal intensity of only white was high is considered that as shown in Fig.2 the spectral reflectance of the blue color chart at 450 nm was only 15.1% although that of the red color chart at 640 nm was 68.4%, and that of the green color chart at 520 nm was 32.8%.
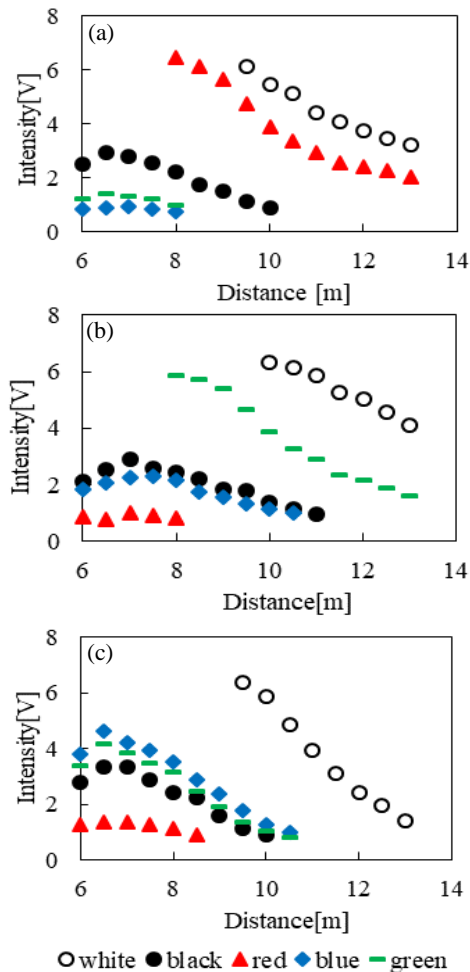

○ white ● black ▲ red ◆ blue ─ green

Fig.3   Distance dependences of received signal intensity for each color chart, where the light sources are red LD(a), blue LD(b), and green LD(c)

To investigate color discrimination in more detail, a blue colored paper having high spectral reflectance of 42.3% at 450 nm and a yellow color chart as an intermediate color were added to target charts. Table 1 shows the summary of signal intensity from different color charts for RGB-LDs received, in which the distance is 8 m.

From the table, in the case of white /black, the difference in RGB signals is small, and signal intensity corresponding to the shade of each chart is obtained. The red chart has a high intensity when a red LD is used, and also the green has a high intensity with a green LD. The yellow chart has a relatively high intensity with both red LD and green LD, so it can be judged yellow as an intermediate color of the two. In the two blue cases, the both intensities are relatively high, and when comparing the two colors, intensity for blue LD are different according to the shading. Also, the results of the receiving characteristics of each LD at each color chart correspond well to the spectral reflection characteristics of the color chart shown in Fig.2.

From these results, it was found that by using RGB-LD as the light source of LiDAR, not only RGB colors but also intermediate colors and shades can be distinguished.

Table. 1 Signal intensity from different color charts for each RGB-LD at 8m and color judgment (unit: volt)

color chart	red LD	green LD	blue LD	color judgement
white(90%)	6.73	6.70	6.72	white
black(10%)	2.20	2.45	2.41	black
red(R9)	6.47	0.801	1.11	red
green(R10)	1.00	5.85	3.53	green
yellow(R11)	6.56	4.80	1.39	yellow
blue(R12)	0.775	2.14	3.14	blue
blue (colored paper)	1.13	4.30	6.21	light blue

4. Conclusions

In this report, feasible study of color LiDAR was verified. From the ToF measurement, it was found that each color charts could be distinguished in addition to the distance information. From these results, it has been proved that the present method is effective not only for acquiring a color 3D image but also for realizing high-precision discrimination of a person or an object with a very simple configuration.

References
[1] K. Osugi and K. Miyauchi:Proc. Symposium of Advanced Vehicle Control 98 (AVEC '98)(1998)p.735
[2] H. Kawata, A. Ohya, S. Yuta, W. Santosh, and T. Mori: Proc. IEEE/RSJ Int. Conf. on Intelligent Robots and Systems(IROS), (2005) p.3277
[3] M. Ishino, T. Kitamura, A. Takamori, J. Kinoshita, N. Hasegawa, M. Nishikino and K. Yamamoto: Optical Review, 26(2019)213
[4] M. Ishino, T. Kitamura, A. Takamori, J. Kinoshita and K. Yamamoto; The 8th Laser Display and Lighting Conference 2018 (LDC'18), 2-5

Post Deadline and Closing
Session Chair: Sunao Kurimura(NIMS)
Fri. Apr 24, 2020 4:30 PM - 5:00 PM 301 (Conference Center)

[LDC-CL]   Closing Remarks
4:30 PM - 5:00 PM